Cation and Anion Doping Effects in Brownmillerites $Ba_2In_2O_5$ & $A_2Fe_2O_5$ (A = Ca, Sr & Ba) through Structural and Electrochemical Characterizations

Thesis Submitted to AcSIR for the Award of the Degree of

DOCTOR OF PHILOSOPHY

In Chemical Sciences

By

C. P. Jijil

Enrollment Number: 10CC12A26047

Under the guidance of

Dr. R. Nandini Devi

Catalysis and Inorganic Chemistry Division

CSIR- National Chemical Laboratory, Pune - 411008, India

February 2017

.....Dedicated to my Father &
Jia Kutty.....

सीएसआईआर - राष्ट्रीय रासायनिक प्रयोगशाला
(वैज्ञानिक तथा औद्योगिक अनुसंधान परिषद)
डॉ. होमी भाभा मार्ग, पुणे - 411 008, भारत
CSIR - NATIONAL CHEMICAL LABORATORY
(Council of Scientific & Industrial Research)
Dr. Homi Bhabha Road, Pune - 411 008, India

CERTIFICATE

This is to certify that the work incorporated in this Ph.D. thesis entitled "**Cation and Anion Doping Effects in Brownmillerites $Ba_2In_2O_5$ & $A_2Fe_2O_5$ (A = Ca, Sr & Ba) through Structural and Electrochemical Characterizations**" submitted by **Mr. C. P. Jijil** to Academy of Scientific and Innovative Research (AcSIR) in fulfillment of the requirements for the award of the Degree of **Doctor of Philosophy in Chemistry,** embodies original research work under my supervision/guidance. I further certify that this work has not been submitted to any other University or Institution in part or full for the award of any degree or diploma. Research material obtained from other sources has been duly acknowledged in the thesis. Any text, illustration, table etc., used in the thesis from other sources, have been duly cited and acknowledged.

Student
C. P. Jijil

Research Guide
Dr. R. Nandini Devi
Senior Scientist, CSIR-NCL, Pune, India
Assistant Professor, AcSIR, New Delhi, India

Date: 27th February 2017
Place: CSIR-NCL, Pune

Communication Channels
NCL Level DID : 2590
NCL Board No. : +91-20-25902000
EPABX : +91-20-25893300
: +91-20-25893400
FAX
Director's Office : +91-20-25902601
COA's Office : +91-20-25902660
SPO's Office : +91-20-25902664
WEBSITE
www.ncl-india.org

DECLARATION

I hereby declare that the thesis entitled "**Cation and Anion Doping Effects in Brownmillerites $Ba_2In_2O_5$ & $A_2Fe_2O_5$ (A = Ca, Sr & Ba) through Structural and Electrochemical Characterizations**" submitted for the award of the Degree of Doctor of Philosophy in Chemistry to the Academy of Scientific & Innovative Research (AcSIR), New Delhi, has been carried out by me at Catalysis & Inorganic Chemistry Division, CSIR-National Chemical Laboratory, Pune-411008, India, under the guidance of **Dr. R. Nandini Devi**. Research material obtained from other sources has been duly cited and acknowledged in the thesis. The work is original and has not been submitted as a part or full by me for any degree or diploma to this or any other university.

C. P. Jijil

Enrollment Number: 10CC12A26047

Date: 27th February 2017

Place: CSIR-NCL, Pune

Acknowledgement

I express my deep sense of gratitude to my research guide Dr. R. Nandini Devi, who has always been very affectionately concerned, creatively helpful, and meticulously careful at every stage in the progress of my work. Her discretion and originality of thinking have significantly contributed to shaping my ideas in this thesis. I am indebted to her for giving me liberty to carry out my research work independently throughout the course. I gratefully acknowledge her constant encouragement and support in the successful completion of this work. Working with her was really a great pleasure and fetched me a lot of learning experience.

I am thankful to Dr. Sreekumar K. (CSIR-NCL, Pune) and his students Dr. Sreekuttan M. U. and Mr. Siddheshwar N. B. for their valuable opinions and effective collaboration.

I am deeply indebted to Dr. Bhalchandra K. (SRM University, Chennai) for his timely help, insightful suggestions and fruitful collaboration. I am also thankful to his students Mr. Moorthi L. and Mr. Indrajit M. P. for their helping hands and hospitality provided during my stay in SRM.

I would like to express my gratitude to Dr. S. N. Jha, Dr. D. Bhattacharyya and Ms. Chandrani N. (RRCAT, Indore) for EXAFS analysis.

I would like to acknowledge Dr. P. D. Babu and Dr. Rajarajan (BARC, Mumbai) for the neutron diffraction experiments.

I would also like to acknowledge Dr. K. Krishnamoorthy K. (CSIR-NCL, Pune) and his student Mr. Chithiravel S. for conductivity experiments.

I am thankful to my Doctoral Advisory Committee (DAC) members Dr. Paresh L. Dephe, Dr. Sreekumar K. and Dr. Benudhar Punji for continuously monitoring the progress of the research work and for scientific discussions.

I sincerely acknowledge the help provided by Dr. C. V. V. Satyanarayana, Dr. P. A. Joy and Dr. T. Raja at various stages of my PhD work.

I am also thankful to Dr. K. R. Patil and Mr. S. S. Deo for XPS, Ms. Violet Samuel for PXRD (also for those delicious fish fry), Ms. Richa Bobade for Raman spectroscopy, Mr. Dama Srikanth for BET analysis. I acknowledge Mr. P. K. Mane and Mr. S. S. Deo for technical support during my Ph.D. Timely help from Madhu chettan is gratefully acknowledged.

I wish to thank former Directors Dr. Sourav Pal & Dr. Vijayamohanan K. Pillai and Dr. Ashwini Kumar Nangia, Director, CSIR-National Chemical Laboratory, for allowing me to carry out my

research work by providing all possible infrastructural facilities, and for permitting me to submit this work in the form of a thesis for the award of Ph.D. degree. I also thank CSIR, Government of India, for awarding the research fellowship.

It gives me immense pleasure to acknowledge Dr. Rose-Noelle (University of Lille, France), and her group member, Dr. Aurelie, Dr. Xavier and Dr. Ibtissem for their whole hearted support and hospitality during my stay at Lille.

I am forever indebted to all my former teachers as they built the foundation for this achievement. Special thanks go to Dr. Raju Francis with whom I started my research career.

My deepest and heartiest thanks go to all my seniors Dr. Kala Raj, Atul, Anupam, Rajesh & Soumya. I am overwhelmed by the friendly atmosphere and support provided by my labmates Leena, Shibin, Pavan, Sourik, Anurag, Priyanka, Shunottara, Emmanuel, Chinnu, Jishna, Anjumol, Sumona, Monojit, Satej, Pranav, Santosh & Drubha. I am also thankful to the project trainee students Mohit, Sabna, Vineetha, Fessy, Akhil, Ajay, Shivesh, Saranya, Sandhya, Anantha, Rajith, Ali and Surya for creating a happily environment in lab.

I also acknowledge the homely environment provided by Reji, Rahul, Renny, Hari, Sadiq, Mufsir, Vijayadas, Mithra Aany, Yamuna, Jima, Manoj chettan, Shijo chettan, Manaf ikka, Mamta, Anjali, Dhanya, Divya, Neeta, Anumon, Arun, Tony, Lenin, Mohan, Manjunath, Bihag, Biyas, Anup, Geethu, Naren, Pandiraj, Anuj, Ketan, Khaja, Rekha, Sijin & Ratesh during my stay in NCL.

I am thankful to my colleagues and friends, Sanoop, Vidyanand, Pranav, Ranjeesh, Shebeeb, Munavar, Fayis, Sandeep, Vipin, Khayum, Rashid, Sharath K., Sarath, Srikanth, Richa Bobade, Laxmi, Pranjal, Dheeran, Siva, Vipul, Seema, Kalpana, Nishitha, Narshimha Kanan, Jay, Amlan, Mangesh, Tanusree, Richa, Neha, Maneesha, Sagar, Sandeep, Nilesh, Presnjit, Ramakanta Sahu, Betsy, Aneesh, Prithi, Trupthi, Swathi, Vidya, Atul, Prakash Chandra, Vyshakh, Sunil, Sreedhala, Anju, Ashok, Aswathi, Periyasami, Manikandan, Prabu K., Prabu M., Edwin, Uniikrishanan, Roshna, Vijay, Mangesh, Anantharamaiah, Ram Sunder, Prajitha, Vishal, Suman Devi, Jaya C. Jose, Megha, Bhaskar, Harshal. Pritish for their indispensable help and for allowing me to spend wonderful time with them.

In this occasion I would like thank my friends, Mahesh, Roshan, Sanal, Nijith, Jidhilish, Vijin, Soniya, Lekha, Anu, Anusha, Linet, Jilu, Lallu, Chandan for their constant support and help.

I would like to express my deep sense of gratitude to my parents and my sister for their enthusiastic encouragement, advice and moral support and selfless love. I find no words to express the love of my amma who has always given me the best of everything. Her love, support and blessings has

always been my strength. I am deeply indebted to my brother-in-law for his constant support and help. Due adoration to my niece Shivananda & Amaya and nephew Devang for their innocent love and affection.

Words are not enough to express my gratitude to a very special person, my wife, Beena, for her support, endless care, unconditional love and understanding throughout. It gives me great pleasure to thank her family for their constant support. I am thankful to my beloved daughter, my knuju vava, Jia kutty for the bundle of love she brings and innocent smile that gives me inspiration and always cheers me up. I thank all family members for their constant encouragement to finish this work.

Though, many have not been mentioned, none is forgotten.

C. P. Jijil

Table of Contents

Abstract

The current scenario of increasing energy demand has led to the depletion of conventional fuels at an alarming rate and also combustion of these fuels has led to high levels of pollution in spite of the regulatory measures in place. Hence search for alternative source for energy with minimal impact on environment is the need of the hour. Various alternatives and techniques are proposed, but one of the major challenges in front of the research community is to design materials capable of harvesting these energy sources as well as to catalyze some of the key reactions involved in these techniques.

Perovskites (ABO_3) based oxide materials have gained considerable attention as a potential material for various applications, owing to their low cost, high chemical and thermal stability and a wide window available for doping in the lattice and thereby tuning the properties of the compound. They have been widely studied in various energy sectors such as cathode materials in solid oxide fuel cells (SOFC), as mixed ionic and electronic conducting membranes (MIEC) for in situ separation of O_2 from air in high temperature reactors etc. Oxygen vacancies in the lattice of these oxides play an important role in enhancing the activity. Recently it has been observed that these materials exhibit good oxygen reduction reaction (ORR) under alkaline medium and can be a potential cathode material in alkaline fuel cell (AFC). The presence of oxygen vacancy will enhance the O_2 adsorption, facilitating the B-O_2 bond formation which is an important step in ORR on perovskite type oxides. Hence, in general oxygen vacancies in the lattice of perovskite help to improve the activity. So compounds having inherent oxygen vacancies in the lattice can be considered as potential candidates for these kinds of applications. In the present thesis we have selected brownmillerite based materials which have inherent oxygen vacancy in the lattice and doping in the cationic and anionic sites are attempted. Structural and electrochemical characterizations were performed to study the effect of doping in the lattice and the potentiality of these materials in low and high temperature electrochemical applications.

The thesis will be presented in five chapters, a brief description of which is as follows.

Chapter 1 presents a general introduction to perovskite based oxide materials and its application in the field of MIEC membranes, SOFC and AFC for ORR catalysts. The role of oxygen vacancies in the perovskite lattice for all these applications are highlighted in this chapter. Further it explains the structural properties of oxygen deficient brownmillerites, which has a structure similar to that of perovskite with inherent oxygen vacancies in the lattice. Finally the scope and objective of the thesis are stated.

Chapter 2 is divided into two parts.

Chapter 2A describes the synthesis of $Ba_2In_2O_5$ brownmillerites in which In site is progressively doped with Ce. 25% doping retains the ordered structure of brownmillerite with alternate layers of tetrahedra and octahedra whereas further increase in Ce concentration creates disorder in oxygen vacancies. Ce doped samples exhibited ORR activity under alkaline conditions. Structures with disordered oxygen atoms/vacancies are found to be better catalysts for ORR; $Ba_2In_{0.5}Ce_{1.5}O_{5+\delta}$ was the best among the series of compounds. Stoichiometric perovskite, $BaCeO_3$ with the highest concentration of Ce shows very poor activity emphasizing the importance of oxygen vacancies, which facilitate O_2 adsorption, in tandem with catalytic sites in ORR. High temperature conductivity also improved with Ce doping, which also brings down the order-disorder transition temperature as evident from high temperature XRD measurements. These results suggest that the material can be a potential candidate for MIEC membranes and as cathode material in SOFC.

Chapter 2B presents an attempt to study the role of oxygen vacancies in the lattice on ORR activity under alkaline medium and on high temperature conductivity. Aliovalent doping by relatively stable metal in the In site of $BaCe_{0.5}In_{0.5}O_{3-\delta}$ was performed to vary the oxygen vacancies in the lattice. Zirconium was used as the dopant owing to its stable oxidation state. A series of compounds viz. $BaCe_{0.5}In_{0.5-x}Zr_xO_{3-\delta}$ was synthesized by gradually doping Zr(IV) in place of In(III), which will cause a decrease in the oxygen vacancies present in the lattice. The concentration of Ce which is a redox active metal was kept constant throughout the series. Electrochemical measurements indicated that the ORR

activity and conduction at higher temperatures decreased with decrease in oxygen vacancies.

Chapter 3 describes the synthesis and electrochemical characterization of a series of compounds with cobalt doping in indium site of $Ba_2In_2O_5$ brownmillerites. Coblat is used as dopant to increase the conductivity of the sample. 25% doping retains the brownmillerite structure with disorder in oxygen site of alternate layers. Further substitution of cobalt in indium site leads to the loss of brownmillerite structure and the compound attains perovskite structure. These compounds were stable under inert and oxidative atmosphere at higher temperature. Cobalt doped samples exhibited far better ORR activity when compared to the parent $Ba_2In_2O_5$ brownmillerite. Among the series of compounds, $BaIn_{0.25}Co_{0.75}O_{3-\delta}$ with highest Co doping and oxygen vacancies randomly distributed in the lattice exhibited best ORR activity. Also these compounds exhibited better conductivity at higher temperature with increase in Co doping, suggesting that they can be used as MIEC membranes and as cathode materials for SOFC.

Chapter 4 describes the anionic substitution by nitrogen doping in $A_2Fe_2O_5$ (A = Ca, Sr, Ba) brownmillerites to get Fe-N_x active site in the lattice. Fe-N_x site along with the inherent oxygen vacancy of brownmillerite is envisaged to present synergistic effect to improve the ORR activity under alkaline medium. This is conceptualized in this chapter through enhanced activity of N doped brownmillerites when compared to its oxide parents. N-doping in the lattice was proved using neutron diffraction, UV-Vis spectroscopy, X-ray photoelectron spectroscopy and X-ray absorption spectroscopy. Electrochemical characterizations using cyclic voltammetry, rotating disc electrode and rotating ring disk electrode indicates an improved ORR activity in N-doped brownmillerite. N-doped compounds exhibited 4-electron reduction pathways with lower H_2O_2 production and had better stability. These observations will enable in better designing of ORR catalysts which are stable and cost effective.

Chapter 5 summarizes the results and conclusions based on the work reported in the thesis. Altogether, this thesis reports cation and anion doping in $A_2B_2O_5$ brownmillerites. The effect of doping is investigated by a thorough structural

characterization. Further the electrochemical properties of the samples have been evaluated under alkaline medium in room temperature to know its applicability as ORR catalyst in AFC. Also high temperature impedance measurements and high temperature PXRD data tells about the potentiality of these compounds for MIEC membranes and as cathode materials in SOFC.

List of Figures

List of Tables

List of Abbreviation

AFC	Alkaline Fuel Cell
BET	Brunauer-Emmett-Teller
CMR	Catalytic Membrane Reactor
CPE	Constant Phase Element
CV	Cyclic Voltammetry
DMFC	Direct Methanol Fuel Cell
EIS	Electrochemical Impedance Spectroscopy
EXAFS	Extended X-ray Absorption Fine Structure
GC	Glassy Carbon
HTXRD	High Temperature X-ray Diffraction
ICSD	Inorganic Crystal Structure Database
JCPDS	Joint Committee on Powder Diffraction Standards
LSV	Linear Sweep Voltammogram
MCFC	Molten Carbonate Fuel Cell
MIEC	Mixed Ionic and Electronic Conduction
ORR	Oxygen Reduction Reaction
OTM	Oxygen Transport Membranes
PAFC	Phosphoric Acid Fuel Cell
PEMFC	Proton Exchange Membrane Fuel Cell
PXRD	Powder X-ray Diffraction
RC	Randle Circuit
RDE	Rotating Disk Electrode
RRDE	Rotating Ring Disk Electrode
SOFC	Solid Oxide Fuel Cell
TGA	Thermogravimetric Analysis
XAS	X-ray Absorption Spectroscopy
XANES	X-ray Absorption Near Edge Structure
XPS	X-ray Photoelectron Spectroscopy

Chapter 1

Introduction and Literature Survey

1.1. Introduction

The major energy sources of today's world are fossil fuels which are non-renewable. As the name suggests, these are the derivatives of plant and animal fossils that are millions of years old. They are primarily formed from the remains of the decayed plants and animals of the carboniferous era. Fossil fuel in the form of coal, natural gas and oil/petroleum meet the majority of energy demand of the current era. An increasing demand of energy has caused spiralling consumption of these fuels which has led to serious environmental issues such as global warming, pollution, and climate change. Any process using fossil fuels produces carbon dioxide, a well known green house gas and also other contaminants such as nitrogen oxides, sulphur oxides and ash. Also the increasing energy demand has caused mankind to face the issue of resource limitation due to depletion of fossil fuel supplies. So it is imperative to look towards alternatives for fulfilling the rising global energy demand. The alternative source of energy should be scientifically possible, environmentally acceptable and technologically promising. Renewable means of producing and storing electricity are expected to be increasingly important for fulfilling the global energy demand. Various alternative sources such as solar, wind, hydroelectric, geothermal, biomass and nuclear energies are envisaged to play an important role in future energy demands. Remarkable developments are taking place in the technologies such as fuel cells and solar cells which use renewable energy sources. To make these technologies commercially competitive, the main challenge is material designing for a reliable way of storing energy and catalyzing some of the key reactions involved in these technologies. New materials hold the key to fundamental advances in energy conversion and storage, both of which are essential in order to meet the challenges such as the finite resource of fossil fuels and impact on environment because of these conventional fuels.

Among the vast families of materials, oxide based compounds have gained considerable attention. There has been a steady increase in research related to oxide materials for energy technology in the past few decades owing to their abundant sources, low cost and high chemical and thermal stability. Both simple and complex oxides are studied extensively and their properties are tuned as per the requirement. Among the oxides, perovskite based systems are of great interest in multiple catalytic

reactions due to its unique structure and a wide window available for doping and thereby tuning the properties of the compound.

1.2. Perovskites and related compounds

1.2.1. Perovskites

The mineral perovskite ($CaTiO_3$) is named after a Russian mineralogist, Count Lev Aleksevich von Perovski, and was discovered and named by Gustav Rose in 1839 from samples found in the Ural Mountains. Goldschmidt who prepared the first synthetic perovskite in 1926 used the term perovskite to describe a class of compounds with same stoichiometry and connectivity as those in $CaTiO_3$. The crystal structure of a $BaTiO_3$ type orthorhombic perovskite was solved by H. D. Megaw in 1945 [1]. Perovskite type oxides have shown potential candidature as materials for various energy related technologies such as fuel cells, solar cells, high temperature oxygen transport membranes (OTM) etc. Owing to their high thermal and chemical stability, perovskite oxides can be applied to various types of reactions involving gas and solid reactions at higher temperatures, liquid reactions at ambient conditions, and even those conducted under irradiation [2-5]. Also they have a wide range of technological applications such as in sensors, memory devices (RAM), superconductors, amplifiers, and electro-optical devices. They exhibit many interesting properties such as colossal magnetoresistance, ferroelectricity, superconductivity, charge ordering, spin dependent transport, high thermopower and the interplay of structural, magnetic and transport properties [6]. Synthetic organic iodide perovskites are suggested as possible inexpensive base materials for high-efficiency commercial photovoltaics.

The broad diversity of properties exhibited by these compounds are because of the fact that more than 90% of the metallic elements from the periodic table are known to be stable in a perovskite type oxide structure. Perovskite has a general formula of ABO_3 where A site cations can be lanthanides, alkali or alkaline earth metal ions while the B site cations are in general transition metal ions. Based on the valences of the cations and the electroneutrality of the compound, different charge distributions among the A and B site cations are possible. Various compositions viz., $A^{I}B^{V}O_3$ (e.g. $NaWO_3$), $A^{II}B^{IV}O_3$ ($CaTiO_3$) or $A^{III}B^{III}O_3$ (e.g. $LnBO_3$, Ln being a trivalent lanthanide and B a transition metal) are possible [7].

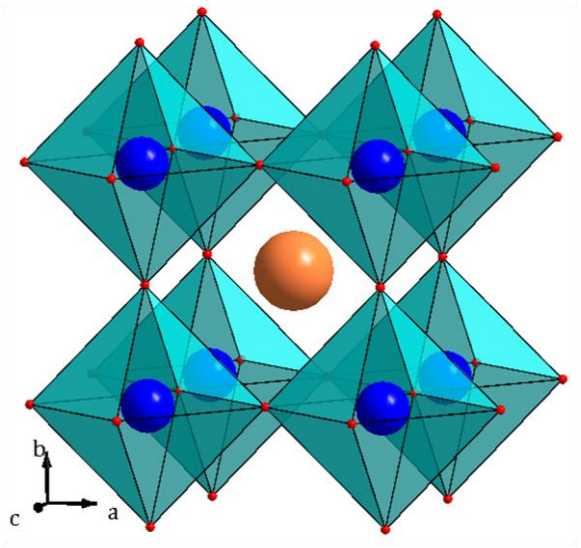

Figure 1.1. Polyhedral representation of perovskite (ABO_3). Orange sphere represent A site cation, blue sphere is for B site cation and red sphere is for oxygen atom.

It is possible to adopt a wide range of compositions in perovskite structure by partial substitution of cations in both A and B site with isovalent or aliovalent cations resulting in a general formula of $A_{1-x}A'_xB_{1-y}B'_yO_{3\pm\delta}$. This kind of substitution in perovskite lattice gives rise to stable mixed oxidation states or unusual oxidation states in the crystal structure. The ideal crystalline unit cell of perovskite has a cubic structure with Pm3m space group, where the larger A-site cations occupies the centre of the cube formed by the relatively smaller B cations, and the oxygen ions are located in the middle of the edges formed by the B cation as shown in Figure 1.1. The B cation is in octahedral coordination with oxygen whereas the A cation is in dodecahedral coordination [7]. Many doped oxides have shown interesting properties [8], the unique structure of perovskites and the versatility of their composition make them remarkable materials for numerous applications.

For an ideal cubic structure with a unit cell parameter of "a", the B-O distance will be equal to a/2, while the A-O distance will be $a/\sqrt{2}$; the following relationship between the ionic radii will hold

$$r_A + r_O = \sqrt{2}(r_B + r_O)$$

But it was observed that, few perovskite compounds still exhibited cubic structure even though this equation was not exactly obeyed. As a measure of the

deviation from the ideal situation, Goldschmidt introduced a term called tolerance factor (t), defined by the equation [9]

$$t = (r_A + r_O) / \sqrt{2}(r_B + r_O)$$

and is applicable at room temperature to the ionic radii of A (r_A), B (r_B) and oxygen (r_O).

For an ideal cubic structure, the tolerance factor, "t" is unity; nevertheless the cubic structure is maintained if the tolerance factor lies between 0.9 to 1 [4]. However lower symmetry structures (e.g. orthorhombic structure of $CaTiO_3$ and $GdFeO_3$) are formed if the value is in between 0.71 to 0.9. If the value of t further drops below 0.71, the compound adopts a trigonal ilmenite structure ($FeTiO_3$). On the other hand, for a higher t values ($1.00 < t < 1.13$), the crystal will exhibit a hexagonal symmetry.

Further, the presence of oxygen vacancies (δ) in the lattice of perovskite plays a pivotal role in many applications. A real crystal often contains intrinsic defects like oxygen vacancies due to equilibrium between lattice oxygen and gas phase oxygen. According to Kroger-Vink notation

$$2O_O \leftrightarrow O_2\,(g) + 2V^{ii}_O + 4e'$$

where O_O represents lattice oxygen, O_2 (g) is gas phase oxygen, V^{ii}_O is an oxygen vacancy, and e' is an electron in the conduction band.

The concentration of oxygen vacancies in a pure perovskite material depends generally on factors like temperature, total pressure and oxygen partial pressure [10]. Extrinsic vacancies in these compounds can be introduced by doping A and B-site ions with lower valence ions. These oxygen vacancies in the lattice are known to influence the properties of the perovskite considerably.

The two main applications of perovskite based oxides which have gained immense attention in the past are as mixed ionic and electronic oxide ion conductor membranes (MIEC) and as cathode and electrolyte materials in solid oxide fuel cell (SOFC). Very recently researchers have shown great interest on perovskites as oxygen reduction reaction (ORR) catalyst in alkaline fuel cell (AFC). These are discussed in the following sections.

1.2.1.1. Applications of perovskite

1.2.1.1.1. Mixed ionic and electronic conductors

Catalytic membrane reactor (CMR) is considered to be a potential approach to attain green and sustainable chemistry with less energy consumption and lower pollution. A CMR carries out separation and reaction in a single unit, thereby enhancing performance in terms of separation, selectivity and yield [11-14]. The concept of CMR was first introduced by Gryaznov and co-workers in 1960 [15]. One of the widely studied inorganic membranes for CMR are the dense mixed conducting ceramic membranes especially MIEC membranes. Many of the petrochemical processes such as oxidative coupling of methane to C2 (ethylene and/or ethane) (OCM), partial oxidation of methane to syngas (POM), partial oxidation of heptane to hydrogen (POH), selective oxidation of ethane to ethylene (SOE), selective oxidation of propane to propylene (SOP), and oxidation of ammonia into NO in nitric acid manufacturing process [16-24] are reported to be achieved in single step with the help of such MIEC membrane integrated reactors when compared to low yield conventional technologies.

In general MIEC membranes are useful in reactions which take place at higher temperatures; this enhances the oxide ion conduction through the membrane. Also the membranes are exposed to different atmospheres at both sides, usually one side has highly reducing gases and the other side has oxidizing gases. Hence the most important criterion for a material to be used as MIEC membrane is that it should be thermally and chemically stable at higher temperatures under reducing (H_2, CO etc.), oxidizing (CO_2, air etc.) and sometimes high steam atmospheres along with high ionic conductivity for oxygen separation. Hence immense amount of work has been carried out for the development of highly stable MIEC materials with considerable oxygen permeation flux [25].

The ionic conductivity in ZrO_2 (Y_2O_3) solid solution was reported long back in 1899 by Nernst [26] but it took a long time for the research community to realize the novel application of these solid solutions for oxygen separation until Takahashi et al.'s initial development of mixed ionic and electronic conduction in Bi_2O_3-BaO ceramic oxide materials [27].

Dense membranes of perovskite based structures above 800 °C have shown excellent oxygen flux ensuring that only pure oxygen exists in the permeate stream, resulting in theoretically infinite selectivity [28]. A schematic representation of a MIEC membrane used for the partial oxidation of methane to obtain syngas is shown in Figure 1.2. Pure oxygen can be filtered from the air during the reaction using MIEC membrane which will selectively pass oxide ions through its lattice via. oxygen vacancies. The mechanism of oxygen transport through the MIEC membranes basically involves three steps (i) dissociation of molecular oxygen and reduction on the membrane surface, (ii) incorporation of oxygen anion into the crystal lattice and its migration through the lattice via oxygen vacancies and (iii) the combination of oxygen anions on the membrane sweep side. Hence the presence of oxygen vacancies in the lattice plays an important role in oxygen separation as evident from the second step [29].

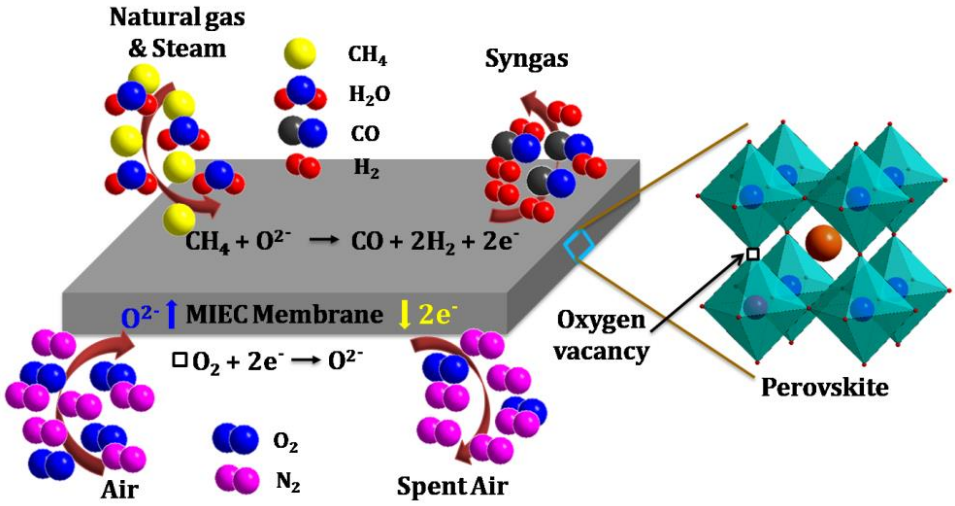

Figure 1.2. Schematic representation of a MIEC membrane made of perovskite for the partial oxidation of methane to syngas.

1.2.1.1.2. Fuel cells

A fuel cell is an electrochemical cell which converts the chemical energy stored in a given fuel into electrical energy with high efficiencies and environmentally benign by-products [30-32]. The thermodynamic efficiency of fuel cell is around 80% which is much higher than the Carnot efficiency (~ 40%) of conventional combustion engine [33]. In a fuel cell, anode and cathode are electronically separated by an electrolyte which works as a path for the ionic conduction and the circuit is closed by the flow of electrons externally. At anode, electrons are produced by the oxidation of fuels such as

H_2, CH_4, CH_3OH etc., which are then transferred to the cathode through an external circuit where the reduction of oxygen takes place [34]. Depending upon various parameters such as nature of electrolyte employed, fuel required and temperature range in which the cell operates, fuel cells are classified into alkaline fuel cell (AFC), proton exchange membrane fuel cell (PEMFC), direct methanol fuel cell (DMFC), phosphoric acid fuel cell (PAFC), molten carbonate fuel cell (MCFC) and solid oxide fuel Cell (SOFC) [35]. An overview of different fuel cell types is given in Table 1.1.

Table 1.1. An overview of different types of fuel cell.

	AFC	PEMFC	DMFC	PAFC	MCFC	SOFC
Operating temp. (°C)	<100	60-120	60-120	160-220	600-800	600-1000
Anode reaction	$H_2 + 2OH^- \rightarrow 2H_2O + 2e^-$	$H_2 \rightarrow 2H^+ + 2e^-$	$CH_3OH + H_2O \rightarrow CO_2 + 6H^+ + 6e^-$	$H_2 \rightarrow 2H^+ + 2e^-$	$H_2 + CO_3^{2-} \rightarrow H_2O + CO_2 + 2e^-$	$H_2 + O^{2-} \rightarrow H_2O + 2e^-$
Cathode reaction	$½O_2 + H_2O + 2e^- \rightarrow 2OH^-$	$½O_2 + 2H^+ + 2e^- \rightarrow H_2O$	$3/2\ O_2 + 6H^+ + 6e^- \rightarrow H_2O$	$½O_2 + 2H^+ + 2e^- \rightarrow H_2O$	$½O_2 + CO_2 + 2e^- \rightarrow CO_3^{2-}$	$½O_2 + 2e^- \rightarrow O^{2-}$
Charge carrier in the electrolyte	OH^-	H^+	H^+	H^+	CO_3^{2-}	O^{2-}
Power	10 - 100 kW	1 W - 500 kW	100 mW – 1 kW	< 10 MW	100 MW	<100 MW
Efficiency (%)	60	25-58		>40	45-47	35-43

Perovskite based oxides have shown immense potential as electrode and electrolyte materials for fuel cells. They have been widely studied for SOFC due to their high thermal and chemical stability at higher temperatures. Very recently researchers have shown immense interest in perovskite type oxides for ORR in alkaline medium. A brief literature survey of the application of perovskite based materials in SOFC and AFC is given below.

1.2.1.1.2.1. Solid oxide fuel cell

SOFC is a highly promising fuel cell and an excellent alternative for the high power applications including industrial and large-scale central electricity generating stations, and as large-scale megawatt power plants in rural areas. SOFCs also allow flexible operation with various fuels, such as hydrocarbons, coal, syngas, or impure hydrogen [36-41]. The basic elements of SOFC are shown in Figure 1.3. It consists of an

electrolyte, an anode and a cathode generally made of ceramic materials. The oxide ion produced at the cathode after the reduction of oxygen travels to the anode through the oxide ion conducting electrolyte. Reduction of the fuel at the anode takes place to give electrons, which flow through the external circuit and the by product is usually water if H_2 is used as fuel. One of the attractive features of SOFCs is that hydrocarbons can be directly used without any external reformers for hydrogen generation. The exhaust gas, which has high temperature, can be used in other power generating systems (e.g. gas turbines) thereby providing a high overall electrical efficiency (up to 70% in a combined cycle system).

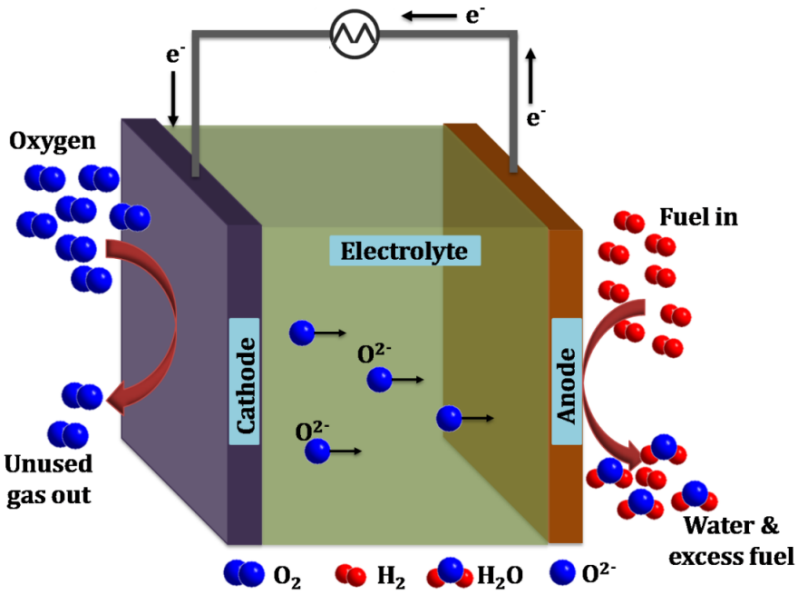

Figure 1.3. Schematic representation of a typical solid oxide fuel cell.

In general, SOFC operates at higher temperatures and hence ceramic electrodes and electrolytes are preferred in order to provide proper stability in the oxidized and reduced atmospheres, chemical compatibility with other components and suitable ionic and electronic conductivity. Yttria-stabilized zirconia (YSZ) is one of the most reliable electrolytes used in SOFCs, it has reasonably high oxygen-ion conductivity and suitable chemical and physical stability in oxidizing and reducing atmospheres [42]. Nickel/yttria-stabilized zirconia (Ni/YSZ) cermet (ceramic–metal mixture) is the state-of-the-art material for anode component in SOFC. Nickel is preferred over other elements owing to its high conductivity, enhanced catalytic activity in reducing atmosphere at higher temperatures and low cost [43]. The SOFC cathode must have high ORR activity on the surface and high diffusivity of oxide ions through the bulk. Also

the thermal expansion coefficient of the cathode should be similar to that of electrolyte material which in turn will reduce fatigue from thermal stress due to mismatch in the thermal expansion coefficient of the components in SOFC. The widely used cathode material is lanthanum strontium manganite (LSM), due to its excellent compatibility with YSZ electrolyte and its moderate electric conductivity [44].

Although LSM is used as cathode material, the main drawback of this material is poor transport of ions limiting the electrochemical reaction to occur only at the triple phase boundary (TPB) which is the gas/electrolyte/electrode interface. Hence materials which can conduct both electrons and oxygen ions (MIEC materials) are proposed as better cathode materials. Perovskites such as $Ba_{0.5}Sr_{0.5}Co_{0.8}Fe_{0.2}O_{3-\delta}$ and $La_{0.6}Sr_{0.4}Co_{0.2}Fe_{0.8}O_{3-\delta}$ and layered perovskite type oxides such as $LnBaCoO_5$ (Ln=La, Pr, Nd, Sm, and Gd) which exhibits MIEC properties have been studied as cathode materials. All these materials have oxygen vacancies in their lattice which facilitates the ionic conductivity [45-49].

Further lowering the operating temperature of SOFC to 600-800 °C will make the technology affordable and commercially viable for long term operation [50]. With the current state-of-the-art materials, a sharp increase in the polarization resistance in the cathode part is observed at these temperatures, resulting in rapid loss of SOFC performance [51, 52]. A high concentration of oxygen vacancies in the lattice will enhance the mobility of oxygen species and thereby increase the oxygen ion conductivity and ORR activity of the compound [53, 54]. Hence materials exhibiting oxygen vacancies in the lattice and improved conductivity at relatively lower temperatures can be envisaged as better alternatives for cathode materials in SOFC.

1.2.1.1.2.2. Alkaline fuel cell

Among the different types of fuel cells, AFC has the highest electrical efficiency and offers an alternative for reducing the cost by replacing Pt with noble metal free catalysts for ORR [55, 56]. AFC's are the oldest fuel cell technology; they have been used in the U.S. space program to produce electrical energy and water on-board spacecrafts. AFCs were extensively studied during 1960's to 1980's, nevertheless, a wide spread commercialisation of this technology at that time failed because of the prohibitive price of the electrode materials used and some technical barriers such as electrolyte leakage,

need of high purity fuels, susceptibility to CO_2 poisoning etc [57]. But with the advent of alkaline anion exchange membranes, which replaced the conventional liquid electrolytes of AFC, most of the issues associated with the AFCs were solved and hence AFC has gained considerable attention in the past decade [58]. A schematic representation of AFC is shown in Figure 1.4. AFC uses an electrolyte through which hydroxyl ion can migrate from cathode to anode; oxidation of hydrogen to water and reduction of oxygen to hydroxide takes place at anode and cathode respectively.

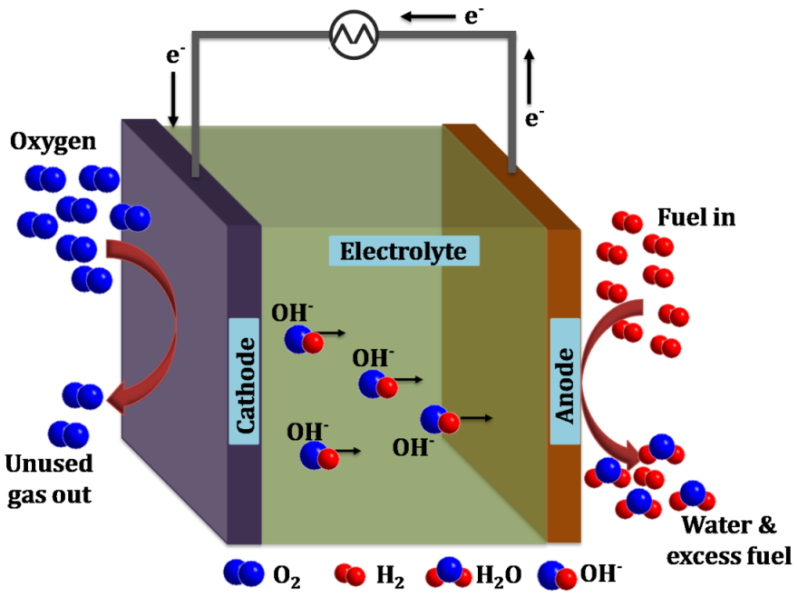

Figure 1.4. Schematic representation of a typical alkaline fuel cell.

The half cell reaction and overall reaction can be written as follows.

At anode: $2H_2+4OH^- \rightarrow 4\ H_2O+ 4e^-$

At cathode: $O_2 + 2H_2O + 4e^- \rightarrow 4OH^-$

Overall reaction: $2H_2+O_2 \rightarrow 2H_2O$ + electricity + heat

Some of the advantages of AFC when compared to other types of fuel cell are as follows [59]

1. The ORR is more facile in the alkaline medium in both thermodynamic and kinetic aspects leading to a smaller activation overvoltage for ORR resulting into higher electrical efficiency.

2. As a result of this improved ORR kinetics, wide range of non noble metal based materials can be used as cathode material. The use of such non noble metal catalysts can bring down the cost of AFC technology [60, 61].
3. Due to the high p^H environment, a much wider variety of materials which are unstable in the acidic conditions can also be used as electrode components in AFC.
4. Since the anion exchange membranes are free from metal ions, the chances of formation of metal carbonates or bicarbonates can be completely excluded even with impure gas feeds.

Despite these facts, even with the current AFC technology running on the anion exchange membranes, some critical issues remain unresolved. Among many constraints on the overall AFC performance, the major restriction comes from the sluggish kinetics of ORR. It is widely known that the kinetics of ORR is substantially poor as compared to that of the anodic hydrogen oxidation and other electrochemical processes occuring in these systems. As a result of this kinetic over potential losses associated with the ORR, precious metals such as Pt, Ag and Pd are used in the cathode to drive the reduction of oxygen. A broad range of other non precious materials are also screened for catalysing ORR. However, most of these cathode materials exhibit poor performance and only a handful of non noble metal catalysts are reported to show comparable ORR activity to that of the noble metal based catalysts. While the poor performance of non noble metal catalysts causes overall efficiency loss, noble metal catalysts on the other hand, though reported to show excellent activity, enhance the total system cost and possess the problem of stability under alkaline medium [62-64]. Thus, the cathode catalyst is one of the critical components which determines the overall performance of AFC.

ORR at the cathode is a highly complex, multi electron reaction and proceeds through a number of adsorption/desorption steps. Apart from this, it is highly influenced by a number of parameters such as the nature of electrode material, catalyst, electrolyte, temperature, pH etc [65]. The ORR at cathode can proceed either by 4 - electron or 2 - electron reduction pathway. The 4 electron pathway is more preferred since it produces a high voltage for H_2-O_2 fuel cell. Steps involved in these pathways are as follows

In a 4-electron pathway, direct hydroxyl ion formation takes place

$O_2 + 2H_2O + 4e^- \rightarrow 4OH^-$ $E^o = 0.401$ V

Whereas a 2-electron pathway involves the peroxide species as the intermediate compound.

$O_2 + H_2O + 2e^- \rightarrow HO_2^- + OH^-$ $E^o = -0.065$ V

$HO_2^- + H_2O + 2e^- \rightarrow 3OH^-$ $E^o = 0.867$ V

HO_2^- formed can also decompose via

$2HO_2^- \rightarrow 2OH^- + O_2$

The state-of-the-art ORR catalyst for fuel cell is Pt or Pt based composites [66, 67]. The key steps involved in ORR are the O-O bond dissociation and the formation of surface absorbed -OH groups [68]. Hence an effective catalyst should follow Sabatier's principle which states that the interactions between the catalyst surface and reactant or product should be neither too strong nor too weak. Pt with its suitable electronic structure, low d-band centre and d-orbital vacancy along with its favourable surface geometric structures of Pt-Pt inter spacing is the best ORR catalyst [69]. These characteristic features help in improved O_2 bond weakening and eases the formation of surface -OH groups on the catalyst surface.

The thermodynamic and kinetic feasibility of ORR in alkaline medium has opened up the possibility of exploiting a wide variety of materials as electrocatalysts, provided they fulfil the prerequisites such as high electronic conductivity, easy adsorption of reactants and desorption of products, availability of multiple valance states etc. A variety of non-precious metals such as carbon nanotubes supported metal particles [70, 71] graphitic carbon nitride/carbon composite [72], N/B/P/S doped carbon nanotube (CNT) and graphene [73-75] and metal oxides including perovskites and spinels [61, 76] are reported as electrocatalyst for ORR at the cathode of AFC. Among these, perovskite type oxides have attracted significant attention in the past few years owing to their low cost, high stability under strong alkaline conditions, high corrosion resistance, facile synthesis procedure and variable stoichiometries [61].

Electrocatalytic activity of perovskite $LaNiO_3$ for cathodic reduction of oxygen was first reported by Matumoto et. al. in the year 1975 [77]. Later catalytic activity of perovskite oxides, $La_{1-x}Sr_xBO_3$ (B = Co, Mn, Fe) as electrocatalysts in oxygen evolution reaction was reported in 1984 by Bockris and Otagawa [78]. They investigated oxygen evolution reaction on eighteen substituted perovskites and explained the results on the basis of molecular orbital theory. It was observed that the electrocatalytic properties increased with increase in the occupancy of the antibonding orbitals of M^z-OH. Although there were only few studies on perovskite based oxides as electrocatalysts for oxygen evolution/reduction from 70's to 90's, it is only in the past decade that considerable interest in these compounds for electrocatalysis evolved.

The electrocatalytic activity of perovskites for ORR is dependent on a number of parameters such as microstructure, electronic conductivity, surface adsorption characteristics etc. These features can be easily tuned by controlling the size, morphology and phase of the materials. Hammouche et. al. has reported enhanced oxygen reduction activity of $La_{1-x}Ca_xCoO_3$ (with $0 \leq x \leq 0.6$) prepared by sol-gel method in propanol medium than in those prepared in water [79]. The enhancement was attributed to the single-phase oxide formation, grain-to-grain chemical homogeneity and good electrical conductivity when synthesised in propanol medium. Singh et. al. has reported the ORR activity of the electrode prepared by embedding the perovskite $La_{1-x}Sr_xMnO_3$ into a polypyrrole (PPy) layer, which was then sandwiched between two pure PPy films and electrodeposited on a graphite support [80]. They observed that the porosity of PPy matrix increased in presence of oxide particles and the ORR activity exhibited by the composite electrode was better than a non-composite electrode made from the same oxide. Later, Tulloch et al. observed an interesting correlation between the ORR activity and the structural transformation of perovskite from one crystal system to another. They have demonstrated the ORR activity of perovskite-based series, $La_{1-x}Sr_xMnO_3$ (where x = 0, 0.2, 0.4, 0.6, 0.8 and 1.0) under ambient temperature in 1M KOH electrolyte [81]. The structural transition from cubic $LaMnO_3$ to hexagonal $SrMnO_3$ was correlated with the ORR activity of the catalyst. The reason for the structural transition is attributed to the change in the oxidation state of manganese from +3 in $LaMnO_3$ to +4 in $SrMnO_3$. The unit cell volume decreases from x = 0 to x = 1 in $La_{1-x}Sr_xMnO_3$, indicating that manganese oxidation state determines the unit cell rather

than the ionic size of A-site cation. $La_{0.4}Ca_{0.6}MnO_3$ exhibited the highest activity for ORR in this series which was ascribed to the structural transition, a minimum in crystallite size and a maximum in BET surface area around this composition. Suntivich et al. later developed a new methodology to compare the ORR activities of submicron sized transition metal oxides; $LaNiO_3$, $LaCu_{0.5}Mn_{0.5}O_3$, and $La_{0.75}Ca_{0.25}FeO_3$ which were synthesised by co-precipitation method [82]. They have adopted a method wherein a thin film of oxide material is adhered on glassy carbon (GC) disk electrode using sodium ion-exchanged Nafion solution as binder. The ORR activity of this catalyst coated electrode was measured. This method to an extent overcomes the O_2 mass transport resistance observed within the porous pellet oxide electrodes and also lessens the risk of corrosion to the catalyst material by using an ion exchanged Nafion solution. Among the catalyst examined, $LaNiO_3$ exhibited the best ORR activity and was comparable to that of the commercial Pt/C catalyst. Sunarso et al. studied the ORR activity of $LaMO_3$ and $LaNi_{0.5}M_{0.5}O_3$ (M = Ni, Co, Fe, Mn and Cr) using the rotating disk electrode (RDE) and rotating ring disk electrode (RRDE) techniques [83]. Interestingly they observed that $LaCoO_3$ exhibited the largest ORR current density and most positive onset potential in $LaMO_3$ (M = Ni, Co, Fe, Mn and Cr) series. A 50% substitution of Ni in $LaNiO_3$ with Co, Fe, Mn and Cr exhibited better positive onset potential than $LaNiO_3$, thereby indicating the beneficial catalytic effect of two transition metals. These observations also support the fact that ORR activity of perovskite oxides is strongly correlated with the valence state of transition-metal cation including its change during redox reaction. Wang et al. has performed a comparative study of the ORR mechanism on $LaBO_3$ (B = Mn, Fe and Cr) surfaces by first-principle calculations based on density functional theory (DFT) [84]. They observed that Cr in $LaCrO_3$ was a better adsorption site for atomic oxygen in comparison with the other two, but such a strong binding does not favour the ORR process. On the other hand the oxygen adsorption on $LaFeO_3$ was very weak which is again not favoured for a good ORR activity. The results calculated from the theoretical studies suggest that the ORR activity increases in the order of $LaFeO_3$ < $LaCrO_3$ < $LaMnO_3$. These findings were in agreement with the e_g filling model deduced from experiments conducted by Suntivich et al [76], where the authors have observed that too little and too much filling of e_g electrons will lead to strong and weak B-O_2 bond formation respectively; neither cases are desirable for ORR activity. An e_g filling of ~1 was suitable for the adsorption and desorption of O_2 on B through B-O_2 bond formation.

Oxygen reduction on double perovskite, Sr_2MMoO_6 (M = Fe and Co) was reported by Mabrouk et al [85]. Oxygen reduction on Sr_2CoMoO_6/C proceeded via four electron pathway whereas it proceeded by a two electron peroxide pathway in Sr_2CoFeO_6/C composite. This difference in behaviour was related to the nature of the adsorbed oxygen on Fe and Co cations. Poux et. al. has reported the dual role of carbon in the catalytic layers of perovskite (either $LaCoO_3$ or $La_{0.8}Sr_{0.2}MnO_3$)/carbon composite [86]. Electrode prepared from the perovskite layer exhibited high ohmic losses and led to poor catalyst utilization. In order to increase the performance, carbon is mixed with the perovskite oxide and a composite made of these two are used to prepare the electrode. Carbon increases the electrical contact between the perovskite particles and the current collector, thereby enhancing the utilization of perovskite structure. They observed that in the case of $LaCoO_3$ composite electrodes, carbon reduces O_2 to H_2O_2 and the role of $LaCoO_3$ is limited to the decomposition of H_2O_2 produced in the first step. On the other hand in the case of $La_{0.8}Sr_{0.2}MnO_3$ composite electrode, along with the decomposition of H_2O_2 produced by the carbon, the perovskite contributed to the first step of ORR. Very recently Jing et al. reported the role of oxygen vacancies in ORR [87]. They have carried out electrocatalytic studies on non stoichiometric $CaMnO_{3-\delta}$ and observed that oxygen defective $CaMnO_{2.75}$ with an average Mn valence near ~3.5 displays the highest ORR activity. This supports the fact that oxygen vacancies in perovskite type oxides enhance the ORR activity.

Since electrochemical processes are inevitably associated with the efficient flow of electrons, high electrical conductivity is always preferred for a material to exhibit electrocatalytic activity. As a result electrical conductivity is vital to exhibit ORR activity. However, most of the perovskites exhibit inherently poor electrical conductivity and their performance is limited by high ohmic losses. In pursuit of improving their electronic conductivity, integrating with conducting carbon substances such as carbon black, carbon nanotube, carbon nanofiber, graphene etc. are generally adopted. Such materials can provide electrons to the perovskites during the ORR and increases the electrical contact between the perovskite particles and the current collector, enhancing the activity.

Among non-oxide systems, N doped C and related materials have also shown immense potential as cost effective alternatives of Pt for ORR catalysis [88-90]. These

systems exhibit excellent ORR activity owing to their unique electronic properties resulting from the conjugation between the nitrogen lone pair electrons and graphene π system [91]. A detailed understanding of the active sites and the role of nitrogen atom is yet to be achieved; however, the generally accepted mechanism is that a net positive charge is created on the carbon atoms adjacent to nitrogen in the matrix, which readily attracts electrons from the anode and also facilitates the O_2 adsorption in the ORR process [88]. Further development has shown that N and transition metal (Fe & Co) co-doped carbon morphologies exhibit better ORR activity under both acidic and alkaline conditions [70, 92]. Among the transition metals, Fe containing systems are widely studied. In general it is observed that Fe-N-C site is active for ORR and enhances the activity of the catalyst [93, 94].

Anionic substitution in particularl by nitrogen in iron containing perovskites can also be considered as an approach to change the electronic structure of the oxide, thereby bringing forward a catalytically active Fe-N centre in the lattice. Anion substitution in the lattice of perovskite has shown considerable increase in the photo catalytic activity [95]. The increase in the activity can be attributed to the reduction in the band gap after N-doping. In N doped oxides, N-2p orbitals present impurity acceptor states above the valence bands consisting of O-2p orbitals consequently reducing the band gap [96]. This increases the conductivity of the compound. Nevertheless studies on anion substituted perovskites are not yet reported in the literature.

Hence in general it can be understood that perovskite based systems with high chemical and thermal stability along with oxygen vacancies in the lattice are cost effective materials for various energy sectors. Hence compounds having inherent oxygen vacancies in the lattice can be envisaged as potential materials for these types of applications. Brownmillerite which has inherent oxygen vacancies in the lattice will be a better material for such applications.

1.2.2. Brownmillerites

Brownmillerite structured oxides have been widely studied as possible fast oxide ion conductors for use in oxygen sensors, solid oxide fuel cells, separation membranes and other electrochemical devices [97-101]. Named after the mineral Ca_2FeAlO_5 [102], brownmillerites are well known because of the variation in space group and properties

that occurs with a change in composition [103-106]. Brownmillerite has a general formula of $A_2B_{2-x}B'_xO_5$ where A is alkaline earth ion (Ca, Sr, Ba) and B/B′ is a group III or transition metal ions (e.g., Al, Ga, In, Cr, Mn, Co, Fe) [105, 107]. The charges of B′/B are generally +3 but it can be a mixture of +2, +3 and +4 when a rare earth metal atom is substituted into the lattice (e.g., $LaAMn_2O_5$, A = Ca or Sr) [108, 109]. The structure of these compounds can be derived from that of perovskite ABO_3, in which the tetravalent B cation in $A^{II}B^{IV}O_3$ perovskite or trivalent A cation in the $A^{III}B^{III}O_3$ perovskite have been completely substituted by cations one less in valency. In order to maintain charge balance, one-sixth of the anions are removed [97] and the brownmillerite structure responds to the high proportion of vacancies by ordering them in parallel rows, resulting in the alternating sequence of octahedra and tetrahedra as shown in Figure 1.5. These compounds in general adopt an orthorhombic structure with alternate layers of tilted metal centred octahedra and disordered tetrahedra piled along one of the axis [105]. The zigzag ordering of the chains of BO_4 tetrahdra layers results in the variations in the space group in these structures. The most common space groups observed in these type of oxide compounds are Pnma, Icmm and Ibm2 [104, 110]. Various factors such as ionic radius, electronic effects and Jahn–Teller distortion associated with the B-site metal atom play significant role in determining the site preferences for metals to reside in octahedral or tetrahedral layer [111, 112].

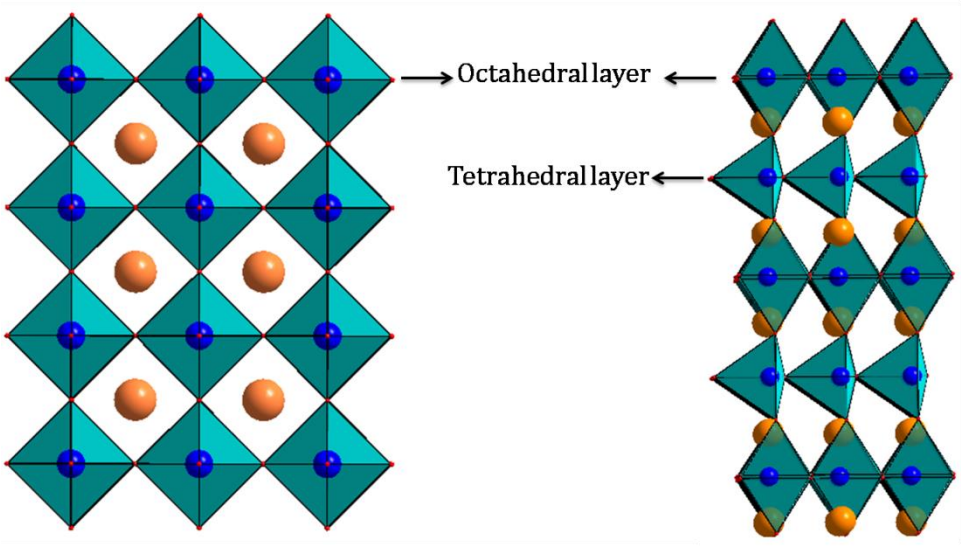

Figure 1.5. Correlation between ABO_3 perovskite and $A_2B_2O_5$ brownmillerite.

Among the family of brownmillerites, $Ba_2In_2O_5$ is well studied because of its excellent MIEC properties at high temperatures. The oxide ion conductivity for $Ba_2In_2O_5$ is more than that of YSZ at intermediate and high temperatures. An immense amount of research has been carried out on this highly oxygen deficient compound [113-116]. $Ba_2In_2O_5$ undergoes a series of phase transitions from orthorhombic structure to tetragonal above 925 °C and subsequently to a disordered cubic phase above 1040 °C. At these temperatures, the ordered oxygen vacancies in the lattice become disordered. Attempts are going on to lower down this order-disorder temperature; which will in fact lead to a material with high MIEC properties at relatively lower temperature. Similarly the random distribution of oxygen vacancies in the lattice will also help in increased oxygen adsorption site on the surface which will enhance ORR activity of these type of oxides in low temperature fuel cell.

1.3. Scope and objective of the thesis

Based on the literature surveys carried out in the previous sections, it is clear that perovskite type oxides are potential candidates for some of the emerging energy sectors such as MIEC membranes, electrode and electrolyte materials in SOFC and as cathode material for ORR in AFC. Owing to their relatively low price when compared to noble metal based catalysts, stability under harsh operating conditions (high temperatures, highly oxidizing and reducing atmosphere etc.,) and the ability to tune properties by doping in the lattice by more than 90% of the elements present in the periodic table, these type of perovskite based oxides have gained considerable attention in research community. Further research has proved that oxygen vacancies in these types of oxides play a pivotal role in all these applications. Hence oxide systems with properties similar to that of perovskite type compounds and with inherent oxygen vacancies in the lattice can be envisaged as better candidates for these applications.

Brownmillerite ($A_2B_2O_5$) type oxides which have alternate layers of octahedra and tetrahedra with oxygen vacancies orderly distributed in the two dimensional tetrahedral layers are selected as the parent material for the work carried out in this thesis. Proper doping strategies at both cationic and anionic sites are employed to tune the properties of the parent brownmillerite. The cationic substitution at the B-site with elements exhibiting redox properties will be attempted. B-site doping will help in

inducing disorder in the orderly distributed two dimensional oxygen vacancy. The randomly distributed oxygen vacancies along the lattice will enhance the catalytic activity of the compound as it will facilitate anisotropic conduction through the sample.

Further anionic substitution with nitrogen in the oxygen site will be attempted. This may lead to the change in the electronic structure of the compound which in turn will improve the conductivity of the oxide materials. Also the band gap of these compounds can be tuned by N doping; owing to the formation of N-2p impurity acceptor state above the valence band consisting of O-2p. Hence this type of anionic substitution in Fe containing brownmillerite can bring forth the presence of Fe-N active sites in the lattice, which is known to be an active site for ORR.

A series of oxygen deficient brownmillerite doped in cationic and anionic sites are synthesised and thorough structural characterizations are presented in this thesis. The potential candidature of these materials for MIEC membranes and as cathode materials for SOFC was analyzed by performing in-situ high temperature XRD under various atmospheres and by measuring the electrical conductivity at higher temperature. An in depth study of the ORR activity of these materials is done in alkaline medium.

Based on these, the following works have been carried out in the present thesis

1. Synthesis and structural characterization of cerium doped $Ba_2In_2O_5$ viz. $Ba_2In_{2-x}Ce_xO_{5+\delta}$; the stability under various atmospheres at higher temperature, oxygen uptake and detailed electrochemical analysis under alkaline medium were performed.
2. Synthesis and characterization of Zr doping in $Ba_2InCeO_{5+\delta}$ viz. $Ba_2CeIn_{1-x}Zr_xO_{5+\delta}$ was done to study the role of oxygen vacancy in the lattice for ORR under alkaline medium and conductivity at high temperatures.
3. Since the electrochemical reactions depend on the conductivity of the sample, Co doping in $Ba_2In_2O_5$ was attempted and complete structural and electrochemical characterizations were performed. Stability at higher temperatures was studied to screen the compounds as potential materials for SOFC and membrane applications.

4. N doping in $A_2Fe_2O_5$ (A=Ca, Sr & Ba) were performed, to get active Fe-N centre in the lattice. Detailed structural and electrochemical studies were performed.

1.4. Reference

1. Megaw, H. D. *Nature* **1945**, *155*, 484.
2. Maegli, A. E.; Hisatomi, T.; Otal, E. H.; Yoon, S.; Pokrant, S.; Gratzel, M.; Weidenkaff, A. *J. Mater. Chem.* **2012**, *22*, 17906.
3. Zhang, H.; Chen, G.; Li, Z.; Liu, J. *J. Rare Earth* **2007**, *25*, 293.
4. Wei, Z. X.; Wang, Y.; Liu, J. P.; Xiao, C. M.; Zeng, W. W. *Mater. Chem. Phys.* **2012**, *136*, 755.
5. Su, H.; Jing, L.; Shi, K.; Yao, C.; Fu, H. *J. Nanopart. Res.* **2010**, *12*, 967.
6. Hibbert, D. B. *Catal. Rev. Sci. Eng.* **1992**, *34*, 391.
7. Tejuca, L. G.; Fierro, J. L. G. *Properties and applications of perovskite-type oxides* CRC Press Taylor & Francis Group New York, **1993**.
8. McFarland, E. W.; Metiu, H. *Chem. Rev.* **2013**, *113*, 4391.
9. Goldschmidt, V. M.; Skr. Nor. Viedenk Akad.; Kl. I. *Mater. Naturvidensk.* **1926**, No. *8*.
10. Smyth, D. M. *Annu. Rev. Mater. Sci.* **1985**, *15*, 329.
11. Sanchez Marcano, J. G.; Tsotsis, T. T. *Catalytic Membranes and Membrane Reactors* Wiley-VCH Verlag GmbH, Weinheim, Germany, **2002**.
12. Dixon, A. G. *Int. J. Chem. React. Eng.* **2003**, *1*, R6.
13. McLeary, E. E.; Jansen J. C.; Kapteijn, F. *Micropor. Mesopor. Mat.* **2006**, *90*, 198.
14. Ozdemir, S. S.; Buonomenna, M. G.; Drioli, E. *Appl. Catal. A*, **2006**, *307*, 167.
15. Gryaznov, V. M. *Russ. Chem. Rev.* **1963**, *32*, 188.
16. Akin, F. T.; Lin, Y. S. *J. Membr. Sci.* **2002**, *209*, 457.
17. Nozaki, T.; Fujimoto, K. *AIChE J.* **1994**, *40*, 870.
18. Pei, S.; Kleefisch, M.; Kobylinski, T. P.; Faber, J.; Udovich, C. A.; Zhang-McCoy, V.; Dabrowski, B.; Balachandran, U.; Mieville, R. L.; Poeppel, R. B. *Catal. Lett.* **1995**, *30*, 201.
19. ten Elshof, J. E.; van Hassel, B. A.; Bouwmeester, H. J. M. *Catal. Today* **1995**, *25*, 397.
20. Wang, W.; Lin, Y. S. *J. Membr. Sci.* **1995**, *103*, 219.
21. Xu, S. J.; Thomson, W. J. *AIChE J.* **1997**, *43*, 2731.

22. Yang, W.; Wang, H.; Zhu, X.; Lin, L. *Topics Catal.* **2005**, *35*, 155.
23. Liu, S.; Tan, X.; Li, K.; Hughes, R. *Catal. Rev.* **2001**, *43*, 147.
24. Pe´ rez-Ramı´rez, J.; Vigeland, B. *Angew. Chem. Int. Ed.* **2005**, *44*, 1112.
25. Dong, X.; Jin, W.; Xu, N.; Li, K. *Chem. Commun.* **2011**, *47*, 10886.
26. Nernst, W. *Z. Electrochem.* **1899**, *6*, 41.
27. Takahashi, T.; Esaka, T.; Iwahara, H. *J. Solid State Chem.* **1976**, *16*, 317.
28. Bouwmeester, H. J. M.; Burggraaf, A. J. *Dense ceramic membranes for oxygen separation, in: A.J. Burggraaf, L. Cot (Eds.), Fundamentals of Inorganic Membrane Science and Technology,* Elsevier Science B.V., Amsterdam, **1996,** p.435.
29. Sunarso, J.; Baumann, S.; Serra, J. M.; Meulenberg, W. A.; Liu, S.; Lin, Y. S.; Diniz da Costa, J. C. *J. Membrane Sci.* **2008**, *320*, 13.
30. Larminie, J.; Dicks, A. *Fuel Cell Systems Explained.* John Wiley & Sons, New York, NY, USA **2000**.
31. Steele, B. C. H.; Heinzel, A. *Nature* **2001**, *414*, 345.
32. Gosselink, J. W. *Int. J. Hydrogen Energ.* **2002**, *27*, 1125.
33. Carrette, L.; Friedrich, K. A.; Stimming, U. *Fuel Cells* **2001**, *1*, 5.
34. Vielstich, W.; Lamm, A.; Gasteiger, H. A. *Handbook of Fuel Cells: Fundamentals, Technology, Applications* John Wiley & Sons, New York, NY, USA **2003**.
35. Carrette, L.; Friedrich, K. A.; Stimming, U. *Chem. Phys. Chem.* **2000**, *1*, 162.
36. Sengodan, S.; Choi, S.; Jun, A.; Shin, T. h.; Ju, Y. W.; Jeong, H. Y.; Shin, J.; Irvine, T. S.; Kim, G. *Nat. Mater.* **2015**, *14*, 205.
37. Gross, M. D.; Vohs, J. M.; Gorte, R. J. *J. Mater. Chem.* **2007**, *17*, 3071.
38. Singhal, S. C. *Solid State Ionics* **2000**, *135*, 305.
39. Liu, M.; Lynch, M. E.; Blinn, K.; Alamgir, F. M.; Choi, Y. *Mater. Today* **2011**, *14*, 534.
40. Mogensen, M.; Jensen, K. V.; Jørgensen, M. J.; Primdahl, S. *Solid State Ionics* **2002**, *150*, 129.
41. Wachsman, E. D.; Lee, K. T. *Science* **2011**, *334*, 935.
42. Wachsman, E. D.; Marlowe, C. A.; Lee, K. T. *Energy Environ. Sci.* **2012**, *5*, 5498.
43. Sengodan, S.; Yeo, H. J.; Shin, J. Y.; Kim, G. *J. Power Sources* **2011**, *196*, 3083.
44. Jun, A.; Kim, J.; Shin, J.; Kim, G. *Chem. Electro. Chem.* **2016**, *3*, 511.
45. Kim, J. H.; Manthiram, A. *J. Electrochem. Soc.* **2008**, *155*, B385.
46. Kim, G.; Wang, S.; Jacobson, A. J.; Yuan, Z.; Donner, W.; Chen, C. L.; Reimus, L.; Brodersen, P. A.; Mims, A. *Appl. Phys. Lett.* **2006**, *88*, 024103.

47. Taskin, A. A.; Lavrov, N.; Ando, Y. *Appl. Phys. Lett.* **2005**, *86*, 091910.
48. Tarancûn, A.; Skinner, J.; Richard, J.; Chater, F.; Hern,ndez-Ramrez, F.; Kilner, J. A. *J. Mater. Chem.* **2007**, *17*, 3175.
49. Choi, S.; Shin, J.; Kim, G. *J. Power Sources* **2012**, *201*, 10.
50. Dusastre, V.; Kilner, J. A. *Solid State Ionics* **1999**, *126*, 163.
51. Colomer, M. T.; Steele, B. C. H.; Kilner, J. A. *Solid State Ionics* **2002**, *147*,41.
52. Doshi, R.; Richards, V. L.; Carter, J. D.; Wang, X.; Krumpelt, M. *J. Electrochem. Soc.* **1999**, *146*, 1273
53. Ried, P.; Holtappels, P.; Wichser, A.; Ulrich, A.; Graule, T. *J. Electrochem. Soc.* **2008**, *10*, B1029.
54. Kim, G.; Wang, S.; Jacobson, A. J.; Reimus, L.; Brodersen, P.; Mims, C. A. *J. Mater. Chem.* **2007**, *17*, 2500.
55. Lu, S.; Pan, J.; Huang, A.; Zhuang, L.; Lu, J. *Proc. Natl. Acad. Sci. USA* **2008**, *105*, 20611.
56. McLean, G. F.; Niet, T.; Prince-Richard, S.; Djilali, N. *Int. J. Hydrogen Energ.* **2002**, *27*, 507.
57. De Geeter, E.; Mangan, M.; Spaepen, S.; Stinissen, W.; Vennekens, G. *J. Power Sources* **1999**, *80*, 207.
58. Deavin, O. I.; Murphy, S.; Ong, A. L.; Poynton, S. D.; Zeng, R.; Herman, H.; Varcoe, J. R. *Energ. Environ. Sci.* **2012**, *5*, 8584.
59. He, Q.; Cairns, E. J. *J. Electrochem. Soc.* **2015**, *162*, F1504.
60. Kordesch, K.; Hacker, V.; Gsellmann, J.; Cifrain, M.; Faleschini, G.; Enzinger, P.; Fankhauser, R.; Ortner, M.; Muhr, M.; Aronson, R. R. *J. Power Sources* **2000**, *86*, 162.
61. Zhang, Z.; Liu, J.; Gu, J.; Su, L.; Cheng, L. *Energ. Environ. Sci.* **2014**, *7*, 2535.
62. Stamenkovic, V. R.; Mun, B. S.; Arenz, M., Mayrhofer, K. J. J.; Lucas, C. A.; Wang, G.; Ross P. N.; Markovic, N. M. *Nat. Mater.* **2007**, *6*, 241.
63. Lim, B.; Jiang, M.; Camargo, P. H. C.; Cho, E. C.; Tao, J.; Lu, X.; Zhu Y.; Xia, Y. *Science* **2009**, *324*, 1302.
64. Fernández, J. L.; Raghuveer, V.; Manthiram A.; Bard, A. J. *J. Am. Chem. Soc.* **2005**, *127*, 13100.
65. Antoine, O.; Bultel, Y.; Durand, R. *J. Electroanal. Chem.* **2001**, *499*, 85.

66. Stamenkovic, V.; Mun, B. S.; Mayrhofer, K. J. J.; Ross, P. N.; Markovic, N. M.; Rossmeisl, J.; Greeley, J.; Nørskov, J. K. *Angew. Chem. Int. Edit.* **2006**, *45*, 2897.
67. Greeley, J.; Stephens, I. E. L.; Bondarenko, A. S.; Johansson, T. P.; Hansen, H. A.; Jaramillo, T. F.; Rossmeisl, J.; Chorkendorff, I.; Nørskov, J. K. *Nat. Chem.* **2009**, *1*, 552.
68. Stassi, A.; D'urso, C.; Baglio, V.; Di Blasi, A.; Antonucci, V.; Arico, A. S.; Castro Luna, A. M.; Bonesi, A.; Triaca, W. E. *J. Appl. Electrochem.* **2006**, *36*, 1143.
69. Nørskov, J. K.; Rossmeisl, J.; Logadottir, A.; Lindqvist, L.; Kitchin, J. R.; Bligaard, T.; Jónsson, H. *J. Phys. Chem. B* **2004**, *108*, 17886.
70. Guo, S.; Sun, S. *J. Am. Chem. Soc.* **2012**, *134*, 2492.
71. Kongkanand, A.; Kuwabata, S.; Girishkumar, G.; Kamat, P. *Langmuir* **2006**, *22*, 2392.
72. Yang, S.; Feng, X.; Wang, X.; Müllen, K. *Angew. Chem. Int. Edit.* **2011**, *50*, 5339.
73. Yu, D.; Zhang, Q.; Dai, L. *J. Am. Chem. Soc.* **2010**, *132*, 15127.
74. Liu, Z. W.; Peng, F.; Wang, H. J.; Yu, H.; Zheng, W. X.; Yang, J. *Angew. Chem. Int. Edit.* **2011**, *50*, 3257.
75. Choi, C. H.; Park, S. H.; Woo, S. I. *ACS Nano* **2012**, *6*, 7084.
76. Suntivich, J.; Gasteiger, H. A.; Yabuuchi, N.; Nakanishi, H.; Goodenough, J. B.; Shao-Horn, Y., *Nat. Chem.* **2011**, *3*, 546.
77. Yasumiti, M.; Hirosi, Y.; Hideo, T. *Chem. Lett.* **1975**, *4*, 661.
78. Bockris, J. O. M.; Otagawa, T. *J. Electrochem. Soc.* **1984**, *131*, 290.
79. Hammouche, A.; Kahoul, A.; Sauer, D. U.; De Doncker, R. W. *J. power Sources* **2006**, *153*, 239.
80. Singh, R. N.; Malviya, M.; Anindita; Sinha, A. S. K.; Chartier, P. *Electrochim. Acta* **2007**, *52*, 4264.
81. Tulloch, J.; Donne, S. W. *J. Power Sources* **2009**, *188*, 359.
82. Suntivich, J.; Gasteiger, H. A.; Yabuuchi, N.; Shao-Horn, Y. *J. Electrochem. Soc.* **2010**, *157*, B1263.
83. Sunarso, J.; Torriero, A. A. J.; Zhou, W.; Howlett, P. C.; Forsyth, M. *J Phys. Chem. C* **2012**, *116*, 5827.
84. Wang, Y.; Cheng, H. P. *J. Phys. Chem. C* **2013**, *117*, 2106.
85. Cheriti, M.; Kahoul, A. *Mater. Res. Bull.* **2012**, *47*, 135.

86. Poux, T.; Napolskiy, F. S.; Dintzer, T.; Kéranguéven, G.; Istomin, S. Y.; Tsirlina, G. A.; Antipov, E. V.; Savinova, E. R. *Catal. Today* **2012**, *189*, 83.
87. Du, J.; Zhang, T.; Cheng, F.; Chu, W.; Wu, Z.; Chen, J. *Inorg. Chem.* **2014**, *53*, 9106.
88. Gong, K.; Du, F.; Xia, Z.; Durstock, M.; Dai, L. *Science* **2009**, *323*, 760.
89. Shao, Y.; Sui, J.; Yin, G.; Gao, Y. *Appl. Catal. B-Environ.* **2008**, *79*, 89.
90. Chen, S.; Bi, J.; Zhao, Y.; Yang, L.; Zhang, C.; Ma, Y.; Wu, Q.; Wang, X.; Hu, Z., *Adv. Mater.* **2012**, *24*, 5593.
91. Liu, R.; Wu, D.; Feng, X.; Müllen, K. *Angew. Chem.* **2010**, *122*, 2619.
92. Liang, Y.; Li, Y.; Wang, H.; Zhou, J.; Wang, J.; Regier, T.; Dai, H. *Nat. Mater.* **2011**, *10*, 780.
93. Chen, Z.; Higgins, D.; Yu, A.; Zhang, L.; Zhang, J. *Energ. Environ. Sci.* **2011**, *4*, 3167.
94. Liu, J.; Li, E.; Ruan, M.; Song, P.; Xu, W., *Catalysts* **2015**, *5*, 1167.
95. Zou, F.; Jiang, Z.; Qin, X.; Zhao, Y.; Jiang, L.; Zhi, J.; Xiao, T.; Edwards, P. P. *Chem. Commun.* **2012**, *48*, 8514.
96. Wang, J.; Tafen, D. N.; Lewis, J. P.; Hong, Z.; Manivannan, A.; Zhi, M.; Li, M.; Wu, N. *J. Am. Chem. Soc.* **2009**, *131*, 12290.
97. Steele, B. C. H. *Mater. Sci. Eng. B* **1992**, *13*, 79.
98. Goodenough, J. B.; Ruiz-Diaz, J. E.; Zhen, Y. S. *Solid State Ionics* **1990**, *44*, 21.
99. Zhang G. B.; Smyth, D. M. *Solid State Ionics* **1995**, *82*, 161.
100. Adler, S. B.; Reimer, J. A.; Baltisberger, J.; Werner, U. *J. Am. Chem. Soc.* **1994**, *116*, 675.
101. Fisher, C. A. J.; Derby, B.; Brook, R. J. *Ceram. Process. Res..* **1996**, *56*, 25.
102. Colville, A. A.; Geller, S. *Acta Cryst. B* **1971**, *27*, 2311.
103. Anderson, M. T.; Vaughey, J. T.; Poeppelmeier, K. R. *Chem. Mater.* **1993**, *5*, 151.
104. Abakumov, A. M.; Rozova, M. G.; Antipov, E. V. *Russ. Chem. Rev.* **2004**, *73*, 847.
105. Haderman, J.; Abakumov, A. M.; D'Hondt, H.; Kalyuzhnaya, A. S.; Rozova, M. G.; Markina, M. M.; Mikheev, M. G.; Tristan, N.; Klingeler, R.; Bu¨chner, B.; Antipov, E. V. *J. Mater. Chem.* **2007**, *17*, 692.
106. Redhammer, G. J.; Tippelt, G.; Roth, G.; Amthauer, G. *Am. Mineral.* **2004**, *89*, 405.
107. Grenier, J. C.; Pouchard, M.; Hagenmuller, P. *J. Solid State Chem.* **1975**, *13*, 92.
108. Alonso, J. M.; Corte´s-Gil, R.; Ruiz-Gonza´lez, L.; Gonza´lez-Calbet, J. M.; Hernando, A.; Vallet-Regı´, M.; Da´vila, M. E.; Asensio, M. C. *Eur. J. Inorg. Chem.* **2007**, 3350.

109. Corte´s-Gil, R.; Hernando, M.; Ruiz-Gonza´lez, M. L.; Ce´spedes, E.; Prieto, C.; Alonso, J. M.; Vallet-Regı´, M.; Hernando, A.; Gonza´lez- Calbet, J. M. *Chem. Eur. J.* **2008**, *14*, 9038.
110. Casey, P. S.; Barker, B.; Hayward, M. A. *J. Solid State Chem.* **2006**, *179*, 1375.
111. Dunitz, J. D.; Orgel, L. E. *J. Phys. Chem. Solids* **1957**, *3*, 318.
112. Ramezanipour, F.; Cowie, B.; Derakhshan, S.; Greedan, J. E.; Cranswick, L. M. D. *J. Solid State Chem.* **2009**, *182*, 153.
113. Islam, M. S.; Davies, R. A.; Fisher, C. A. J.; Chadwick, A. V. *Solid State Ionics* **2001**, *145*, 333.
114. Yoshinaga, M.; Fumoto, T.; Hashimoto, T. *J. Electrochem. Soc.* **2005**, *152*, A1221.
115. Hashimoto, T. *J. Electrochem. Soc.* **2002**, *149*, A1381.
116. Rolle, A.; Vannier, R. N.; Giridharan, N. V.; Abraham, F. *Solid State Ionics* **2005**, *176*, 2095.

Chapter 2

Cation Doping in B site of $Ba_2In_2O_5$: Effect of Coordination Environment and Role of Oxygen Vacancies in Electrochemical Properties

Part A

Effect of B site Coordination Environment in Disordered Brownmillerites $Ba_2In_{2-x}Ce_xO_{5+\delta}$ for ORR Activity and High Temperature Conductivity

2A.1. Introduction

The need of designing oxide based materials for various energy sectors such as cathode materials in fuel cells and as mixed ionic and electronic conducting membranes for in situ separation of O_2 from air at high temperature reactors are introduced in chapter 1. Perovskite based oxygen deficient materials are well known for such applications [1-3]. Oxygen vacancies in these oxides are reported to enhance their activity [4]. Hence a stable oxide material with inherent oxygen vacancies in the lattice can be envisaged as an efficient catalyst to carry out some of these potential reactions in the energy sector. So, we focused on brownmillerite type of oxides with inherent oxygen vacancies. Brownmillerites with a general formula $A_2B_2O_5$, have oxygen vacancies which are orderly distributed in two dimensional arrays in the lattice [5]. Appropriate doping strategies in these types of compounds can lead to random distribution of oxygen vacancies in the lattice, which in turn will create isotropic ionic conduction pathways favourable for enhanced bulk diffusion properties [6]. Also incorporation of redox centre in the lattice will improve the catalytic activity of the compounds [7].

In the present chapter we have selected $Ba_2In_2O_5$ as the parent brownmillerite and cerium doping in the indium site is performed. $Ba_2In_2O_5$ is a well studied brownmillerite having a stable structure with ions in stable oxidation state and hence avoiding any untoward structural fluctuations. $Ba_2In_2O_5$, has alternate layers of InO_6 octahedra and InO_4 tetrahedra with oxygen vacancies ordered in the two dimensional tetrahedral layer [8]. They exhibit an enhanced conductivity at elevated temperature (>925 ˚C), where structural transformation from orthorhombic to tetragonal crystal system takes place. At this temperature, the ordered oxygen vacancies are randomly distributed in the lattice and hence this temperature is known as order-disorder transition temperature [9]. Doping in brownmillerites brings down the order-disorder transition temperature. The rationale behind selecting Ce as the dopant is multifold; (i) Ce(IV) will induce vacancy disorder in the structure and hence will bring down the order-disorder transformation temperature (ii) Ce is a well known redox system hence will be more tolerant to local changes in oxygen concentrations [10] and (iii) Ce will introduce redox centres which may aid electrochemical reactions [11].

So the focus of the work carried out in this chapter is the synthesis of Ce doped $Ba_2In_2O_5$ compounds and their structural characterizations. Further the stability of the materials and electrochemical characterisation under alkaline media as ORR catalyst and high temperature impedance studies are also performed.

2A.2. Experimental section

2A.2.1. Synthesis of $Ba_2In_{2-x}Ce_xO_{5+\delta}$

$Ba_2In_{2-x}Ce_xO_{5+\delta}$ series of compounds with x = 0, 0.5, 1 and 1.5 was synthesized by solid state reaction while $BaCeO_3$ was synthesized by combustion method using citric acid. For synthesizing $Ba_2In_{2-x}Ce_xO_{5+\delta}$, high purity $BaCO_3$ (99.98%, Sigma-Aldrich), In_2O_3 (99.99%, Sigma-Aldrich) and $Ce(CH_3CO_2)_3$ (99.9%, Sigma-Aldrich) were used as the starting materials. Stoichiometric amount of the reactants were weighed and ball milled at 300 rpm for 3 h in Fristsch Pulverisette 6 Planetary Mill for homogeneous mixing. The samples were then calcined at 900 ˚C for 12 h. Subsequently, they were ground in a mortar and again calcined at 1200 ˚C for 8 h at a ramp rate of 3 ˚C min^{-1}. $BaCeO_3$ was synthesized by combustion method using citric acid (99.5%, Merck) as fuel. Equimolar amount of $Ba(NO_3)_2$ (99.999%, Aldrich) and $(NH_4)_2Ce(NO_3)_6$ (99%, Merck) was added to citric acid solution and the p^H of the solution was maintained at 7. The solution was heated at 80 ˚C to obtain a gel which was later calcined at 400 ˚C to remove the organic and volatile components. The powder was ground thoroughly and calcined at 900 ˚C for 8 h to obtain $BaCeO_3$.

2A.2.2. Characterization

The basic principles of all the techniques used throughout the work are briefly discussed in the Appendix 1. The structural characterization of the samples was carried out using powder X-ray diffraction (PXRD) in a PANalytical X'pert Pro dual goniometer diffractometer operating at 40 kV and 30 mA under ambient condition. The diffraction pattern was collected using a flat holder in a Bragg-Brentano geometry from a Ni filtered Cu-Kα (1.5418 Å) radiation. An X'celerator solid state detector with a step size of 0.008˚ and a time per step of 45.72 s was used to obtain the pattern. Structural parameters of the samples were determined by Rietveld refinement on the PXRD pattern using GSAS-EXPGUI software [12]. In situ high temperature XRD (HTXRD) experiments were carried out in an Anton-Paar XRK900 reactor. The stability of the

samples at variable temperature under oxidative and inert atmosphere was studied by passing 10% O_2 in He and He gas respectively through the Anton-Paar XRK900 reactor.

Raman spectra of all the samples were recorded using Horiba JY LabRAM HR 800 which has a Czerny-Turner type spectrograph with 800 mm focal length and achromatic flat field monochromator along with mirror-based reflective optics and charge-couple device (CCD) detector. The samples were scanned over a wavelength region of 50-1000 cm^{-1}, using He-Ne (632.8 nm, 20 mW) laser.

The surface area of the samples was determined by N_2 adsorption at the temperature of liquid nitrogen using the Autosorb iQ Quantachrome system. The samples were degassed at 300 °C under vacuum for 6 h prior to the analysis to remove the adsorbed moisture on the catalyst surface. The specific surface area was calculated using the BET model at relative pressure of $P/P_0 = 0.05–0.3$.

Thermogravimetric analysis (TGA) was performed on METTLER-TOLEDO TGA/SDTA851e instrument. All the samples were preheated under helium (40 ml min^{-1}) till 120 °C and then held at that temperature for 1 h, subsequently the samples were cooled to 30 °C. The samples were then heated to 700 °C at a ramp rate of 5 °C min^{-1} under Helium (40 ml min^{-1}) and cooled to 30°C. Finally the samples were heated till 900 °C at a ramp rate of 5 °C min^{-1} under 10% O_2 balanced by helium at a flow rate of 40 ml min^{-1}.

2A.2.3. Electrochemical analysis

The electrochemical properties of the catalyst were measured by cyclic voltammetry (CV) and rotating disk electrode (RDE) technique using a Biologic electrochemical workstation (SP-300) in a conventional three-electrode test cell with Hg/HgO and platinum foil as the reference and counter electrodes respectively under room temperature. For preparing the working electrode for CV and RDE measurements, glassy carbon (GC) electrode was first polished using 0.3 μm alumina powder and then the electrode was cleaned using deionized water. The catalyst for RDE was prepared by ball-milling (300 rpm for 90 min) a mixture of 100 mg of $Ba_2In_{2-x}Ce_xO_{5+\delta}$ with 25 mg of Vulcon XC-72 carbon. A slurry of catalyst was made by sonicating (BRANSON 1510) 5 mg of the sample-carbon composite in 1 mL 3:2 ethanol-water mixture for 1 h. 10 μL

aliquot of the catalyst slurry was drop-coated on the electrode surface. Subsequently, 2 µL of 0.01 wt. % Nafion diluted with ethanol was applied on the whole surface of the electrode to yield a uniform thin film. This electrode was then dried in air and was used as the working electrode for all the electrochemical studies. An aqueous solution of 0.1 M KOH (Aldrich, ≥ 85%) was used as the electrolyte for the electrochemical studies. Kinetics of oxygen reduction reactions (ORR) on the catalyst were studied by RDE method, at a scan rate of 5 mVs^{-1} and electrode rotation rate of 400, 900, 1200, 1600, 2000 and 2500 rpm at room temperature.

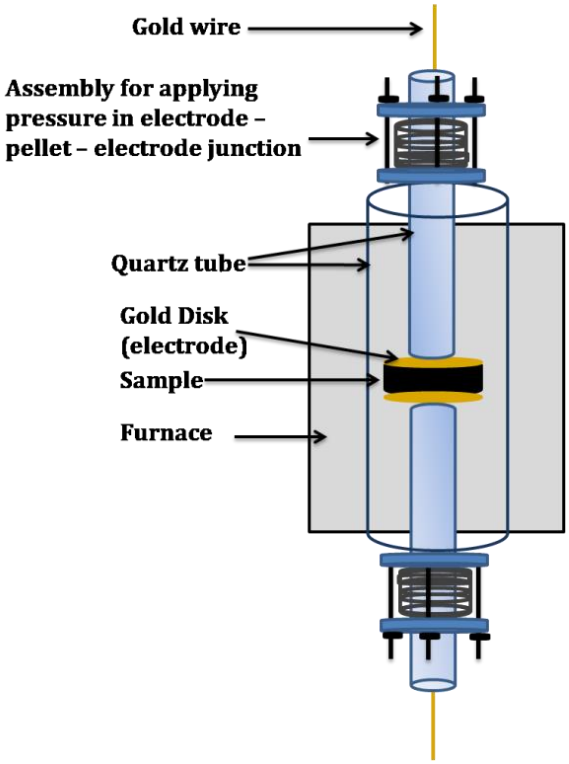

Figure 2A.1. Home-built setup for electrochemical impedance spectroscopy measurements.

The electrochemical impedance spectroscopy (EIS) under variable temperature were performed using CHI604E electrochemical analyser (CH Instruments, Inc., USA) connected with home-built electrode setup and furnace as shown in Figure 2A.1. For making pellets of the sample, 1 g of the as synthesised powder was weighed and pressed in a die of 13 mm diameter. The pellets were calcined at 900 ˚C and then used for EIS measurements. The AC impedance spectroscopy was done over a frequency range of 100 mHz to 1 MHz with an amplitude of 50 mV, in the temperature range of 300 – 700 ˚C. The dwell time at each temperature was kept 2 h to attain the equilibrium and subsequently the spectra were recorded.

2A.3. Results and discussion

2A.3.1. Synthesis and structural characterization

Synthesis of cerium doped brownmillerites viz. $Ba_2In_{2-x}Ce_xO_{5+\delta}$ (x = 0, 0.5, 1 & 1.5) was initially attempted by combustion method using citric acid. The attempt to obtain pure phase with this method failed and hence the samples were synthesised by solid state method at a final temperature of 1200 ˚C. On the other hand $BaCeO_3$ perovskite could be synthesised by combustion method using citric acid as fuel. The phase purity of all the synthesized compounds was analyzed by PXRD. Figure 2A.2 (a) represents the PXRD pattern of all the samples.

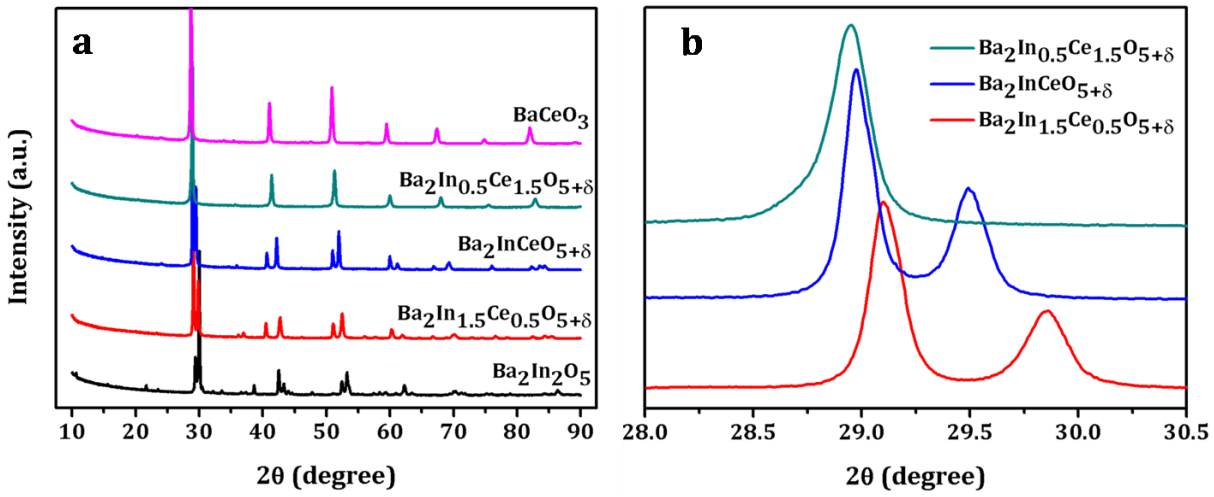

Figure 2A.2. (a) PXRD pattern of $Ba_2In_{2-x}Ce_xO_{5+\delta}$ (x = 0, 0.5, 1 & 1.5) and $BaCeO_3$ **(b)** Enlarged portion of PXRD patterns of Ce doped $Ba_2In_2O_5$.

The PXRD pattern of parent $Ba_2In_2O_5$ was identical with that of orthorhombic alpha dibarium diindium oxide (JCPDS file No. 01-074-2662) whereas that of Ce doped $Ba_2In_{1.5}Ce_{0.5}O_{5+\delta}$ matched with tetragonal $Ba_2In_2O_5$ (JCPDS file No. 01-089-9079), very small fraction of CeO_2 as impurity was observed in the PXRD pattern of $Ba_2In_{1.5}Ce_{0.5}O_{5+\delta}$. Other two Ce doped compounds viz. $Ba_2InCeO_{5+\delta}$ and $Ba_2In_{0.5}Ce_{1.5}O_{5+\delta}$ also crystallized in tetragonal system with trace amount of $BaCO_3$ impurity in the former sample. The PXRD pattern of $BaCeO_3$ matched with previously reported structure (JCPDS file No. 01-070-1429) in literature with small amount of impurities of $BaCO_3$ and CeO_2. A closer look into the PXRD patterns of Ce doped $Ba_2In_2O_5$ systems reveals that with increase in Ce concentration the 2θ difference in the tetragonal splitting decreases as evident from Figure 2A.2(b) and hence indicating a gradual merging of *a* and *c* lattice parameters. In

$Ba_2In_{0.5}Ce_{1.5}O_{5+\delta}$, the splitting is not discernible in the broad peak indicating a highly disordered structure with random distribution of O vacancies in the lattice. Also a shift towards the lower angle with increase in Ce concentration suggests an increase in the lattice parameters; this can be ascribed to the larger crystal radius of Ce when compared with In atom [13].

Structural parameters of the compounds were determined by Rietveld refinement of the PXRD pattern using GSAS EXPUGI software. Figure 2A.3 (a-e) represents the Rietveld refinement plot of $Ba_2In_{2-x}Ce_xO_{5+\delta}$ (x = 0, 0.5, 1 & 1.5) and $BaCeO_3$ respectively. Rietveld refinement on PXRD data of $Ba_2In_2O_5$ was performed using the structural parameter of alpha dibarium diindium oxide reported by Fischer et al [14]. Refinement of the PXRD pattern with these parameters proceeded smoothly and the PXRD data fitted in orthorhombic Ima2 space group. The compound had a brownmillerite structure with alternate layers of InO_6 octahedra and InO_4 tetrahedra (Figure 2A.4 (a)). Rietveld refinement of Ce doped $Ba_2In_{1.5}Ce_{0.5}O_{5+\delta}$ was carried out using the cell parameters of hydrated $Ba_2In_2O_5$; the refinement proceeded smoothly and the PXRD pattern fitted to tetragonal P4/mmm space group [15]. During the refinement, all the Ce atoms were manually assigned to the octahedral site because ionic size considerations [13] avert it from assuming tetrahedral geometry. Alternate layers in this system are disordered as evident from the availability of two equivalent atomic positions for each O atom along *ab* plane (Figure 2A.4 (b)). However, the attempts to refine the PXRD pattern of $Ba_2InCeO_{5+\delta}$ and $Ba_2In_{0.5}Ce_{1.5}O_{5+\delta}$ with the structural parameters of the hydrated $Ba_2In_2O_5$ was not fruitful. Hence a new unit cell was arrived at with $c' \sim c/2$ of the hydrated $Ba_2In_2O_5$ and atomic coordinates were modified accordingly. Rietveld refinement with these new parameters proceeded smoothly for both the systems and the data fitted into tetragonal P4/mmm space group. The oxygen vacancies were randomly distributed in the lattice and the atomic position of oxygen atom was highly disordered as evident from the Figure 2A.4 (c & d). Finally the PXRD pattern of $BaCeO_3$ was successfully refined based on the cell parameters reported by Jacobson et al [16]. $BaCeO_3$ being a perfect perovskite is expected to show an ideal cubic structure, but it deviates from the expected structure with *c* axis doubling due to octahedral tilting and crystallizes in orthorhombic Pbnm space group as shown in Figure 2A.4 (e).

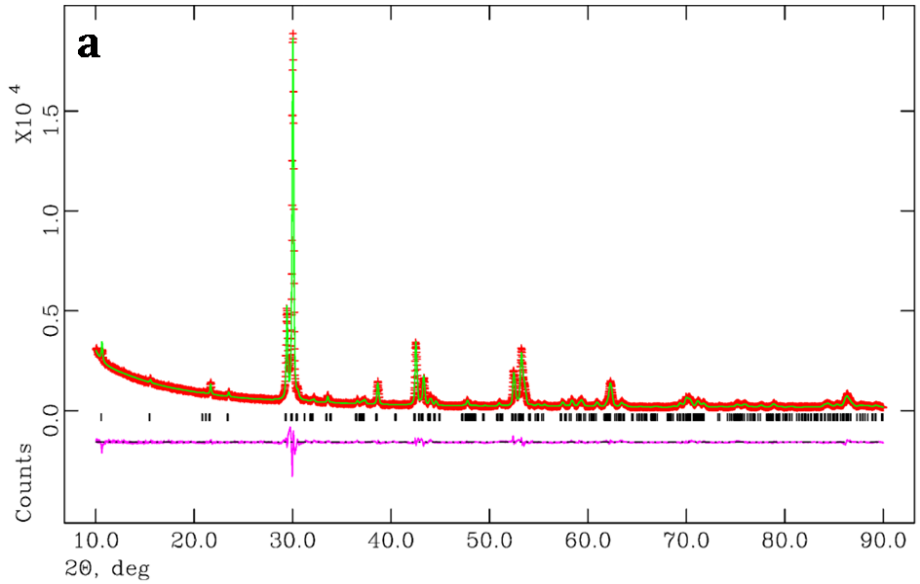
a
X10 4
1.5
1.0
0.5
0.0
Counts
10.0
20.0
30.0
40.0
50.0
60.0
70.0
80.0
90.0
2θ, deg

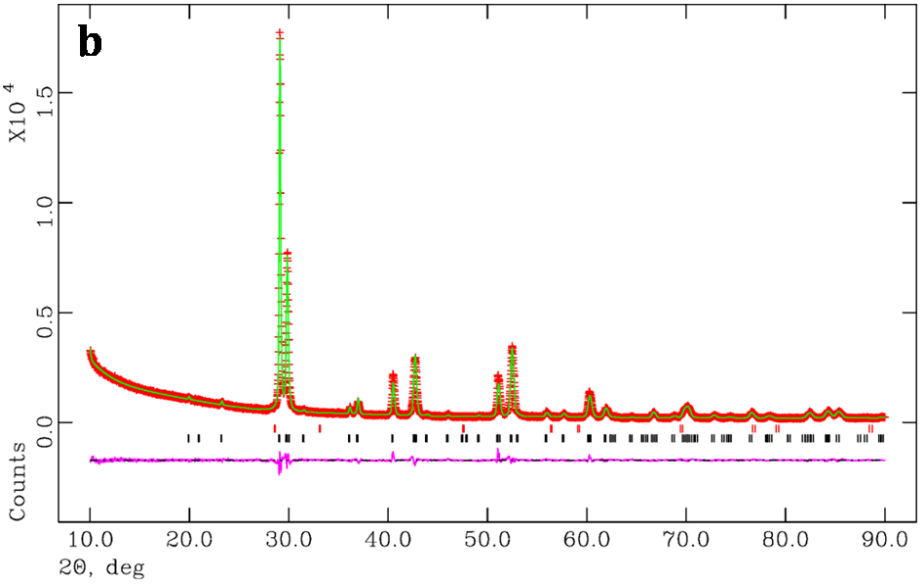
b
X10 4
1.5
1.0
0.5
0.0
Counts
10.0
20.0
30.0
40.0
50.0
60.0
70.0
80.0
90.0
2θ, deg

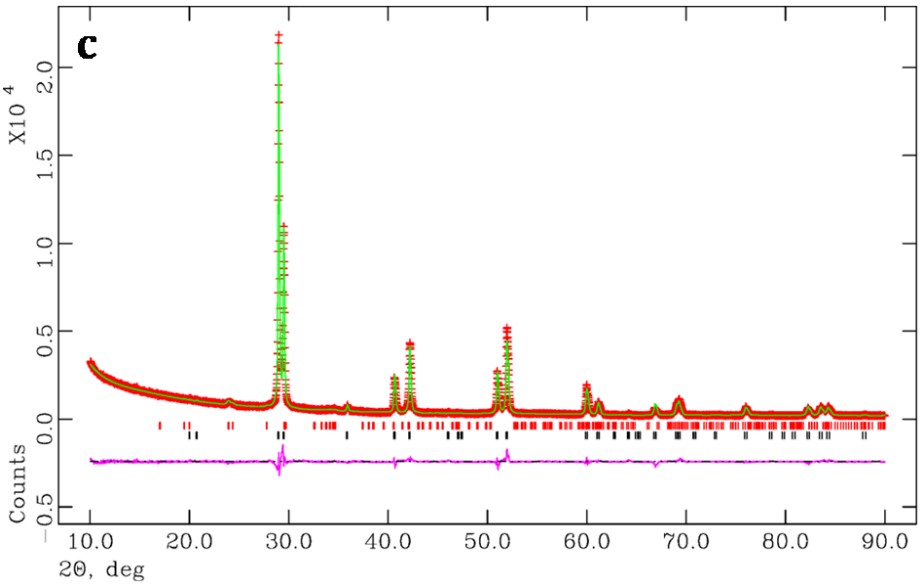
c
X10 4
2.0
1.5
1.0
0.5
0.0
0.5
Counts
10.0
20.0
30.0
40.0
50.0
60.0
70.0
80.0
90.0
2θ, deg

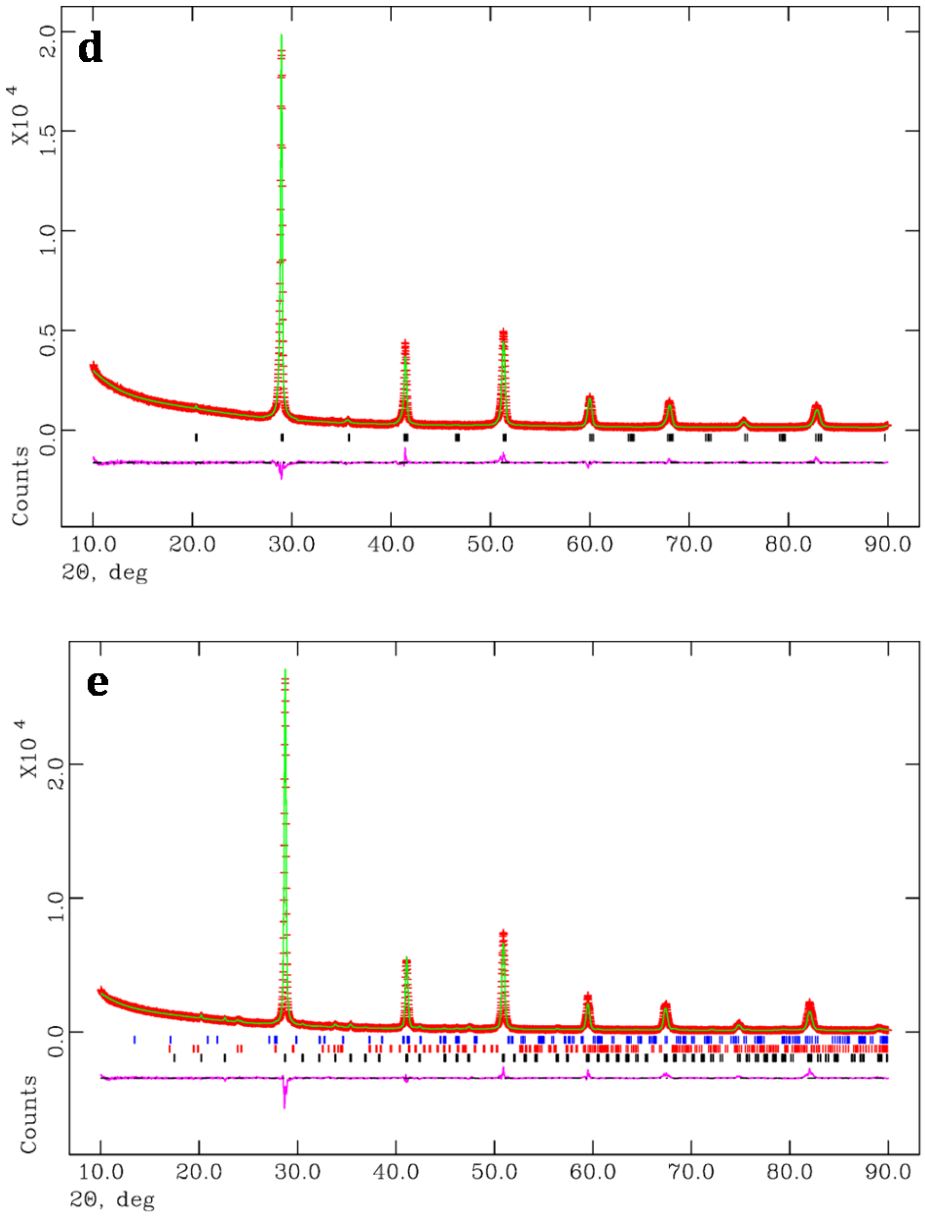

Figure 2A.3. Rietveld refinement of the PXRD pattern of **(a)** $Ba_2In_2O_5$, **(b)** $Ba_2In_{1.5}Ce_{0.5}O_{5+\delta}$, **(c)** $Ba_2InCeO_{5+\delta}$, **(d)** $Ba_2In_{0.5}Ce_{1.5}O_{5+\delta}$ and **(e)** $BaCeO_3$. Red pattern represents experimental data, green pattern is the Rietveld fit and pink pattern represents difference plot. Black vertical lines in all figures represent the expected positions for the main phase. The impurity phases are represented by red line in (b) corresponding to CeO_2; red line in (C) corresponds to $BaCO_3$ and red and blue lines in (e) corresponding to $BaCO_3$ and CeO_2 respectively.

Hence it is clear after the Rietveld refinement of PXRD data that 25 % doping of Ce in In site of $Ba_2In_2O_5$ viz. $Ba_2In_{1.5}Ce_{0.5}O_{5+\delta}$ maintains the brownmillerite structure with oxygen vacancies ordered in the alternate layers. However structures with higher concentration of Ce in $Ba_2In_2O_5$ viz. $BaIn_{0.5}Ce_{0.5}O_{2.5+\delta}$ and $BaIn_{0.25}Ce_{0.75}O_{2.5+\delta}$ tend to

attain perovskite type structure with random distribution of oxygen vacancies in the lattice.

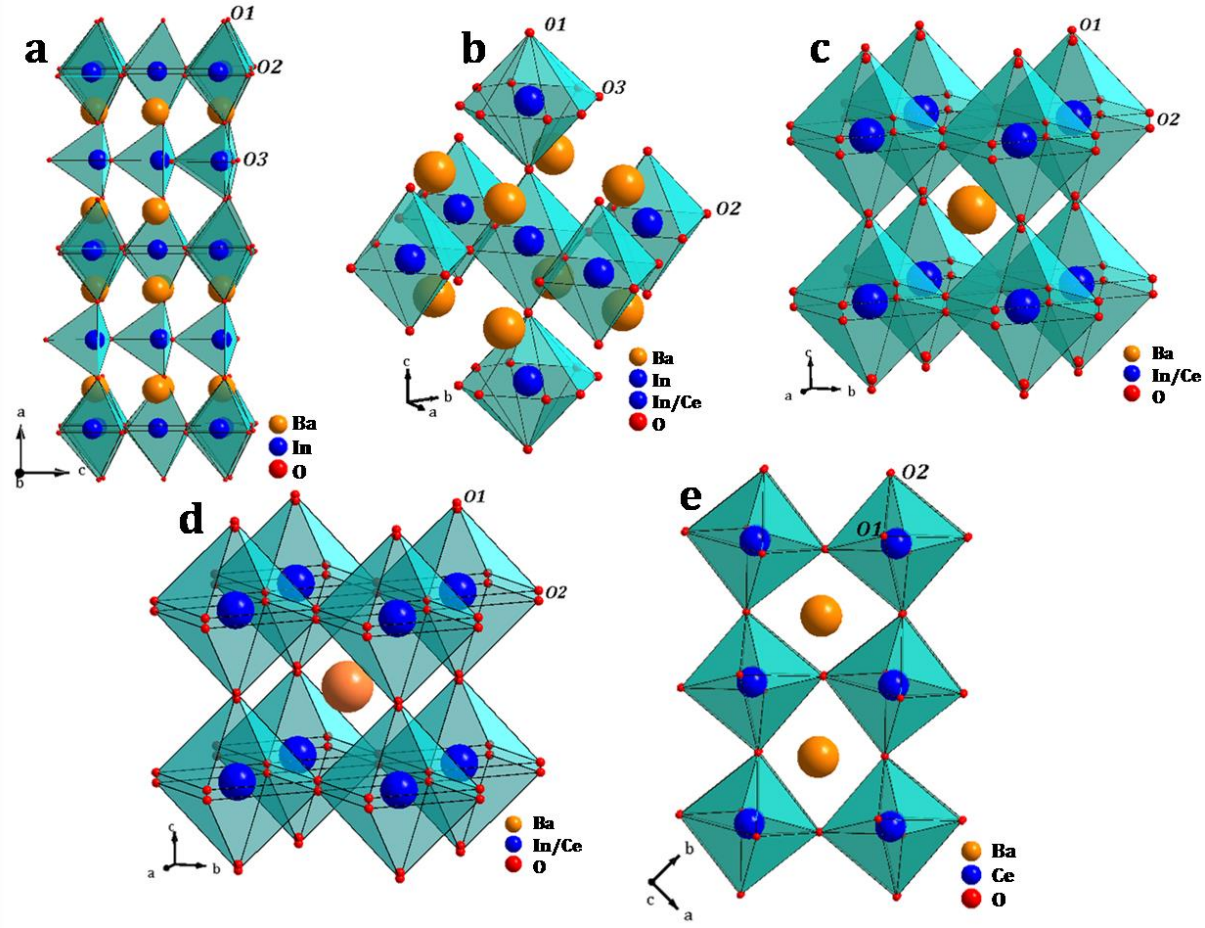

Figure 2A.4. Polyhedral representation of the structures obtained after the Rietveld refinement of PXRD patterns of **(a)** $Ba_2In_2O_5$, **(b)** $Ba_2In_{1.5}Ce_{0.5}O_{5+\delta}$, **(c)** $Ba_2InCeO_{5+\delta}$, **(d)** $Ba_2In_{0.5}Ce_{1.5}O_{5+\delta}$ and **(e)** $BaCeO_3$.

The detailed structural parameters obtained after the Rietveld refinement of $Ba_2In_{2-x}Ce_xO_{5+\delta}$ (x = 0, 0.5, 1 & 1.5) and $BaCeO_3$ are tabulated in Table 1. It can be observed from the Rietveld refinement results that the effective occupancy of O1 atom which is along the *c* direction increases gradually. This can be attributed to the fact that as Ce dopant concentration increases, the brownmillerite structure transforms to perovskite-like structure, leading to a disorder in the axial oxygen site. Finally when it reaches a perfect perovskite structure, this disorder in oxygen site is absent. Similarly, the oxygen occupancy of the equatorial oxygen atom (O2) increases from $Ba_2InCeO_{5+\delta}$ to $Ba_2In_{0.5}Ce_{1.5}O_{5+\delta}$. The disorder in the O positions is clearly visible in Figure 2A.4. Hence

the oxygen vacancies in the lattice decreases with increase in the Ce concentration, this is obvious as In(III) is replaced by Ce(III/IV) in the lattice.

Table 2A.1. Structure parameters obtained from the Rietveld refinement of $Ba_2In_{2-x}Ce_xO_{5+\delta}$ (x = 0, 0.5, 1 & 1.5) and $BaCeO_3$.

	$Ba_2In_2O_5$[a]	$Ba_2In_{1.5}Ce_{0.5}O_{5+\delta}$[b]	$BaIn_{0.5}Ce_{0.5}O_{2.5+\delta}$[c]	$BaIn_{0.25}Ce_{0.75}O_{2.5+\delta}$[d]	$BaCeO_3$[e]
χ^2	3.154	1.967	3.202	3.402	4.365
wRp(%)	7.03	5.49	6.6	6.2	8.17
Rp (%)	4.79	3.9	4.51	4.37	5.64
Space group	Ima2	P4/mmm	P4/mmm	P4/mmm	Pbnm
a (Å)	16.7777(2)	4.2466(0)	4.2902(0)	4.3448(0)	6.2229(5)
b (Å)	6.1013(1)	4.2466(0)	4.2902(0)	4.3448(0)	6.2173(6)
c (Å)	5.9731(1)	8.9298(1)	4.4434(0)	4.3682(1)	8.7859(6)
O 1 x	0.9910	0.5	0	0	0.071
y	0.2832	0.5	0	0	0.487
z	0.2491	0.244	0.5313	0.5167	0.25
Occup	1	0.8242	0.4733	0.4949	1
O 2 x	0.1424	0	0	0	-0.274
y	0.0639	0.5	0.5	0.5	0.278
z	0.0540	0.5	-0.0464	0.0296	0.041
Occup	1	0.9831	0.4238	0.4523	1
O 3 x	0.25	0.3558			
y	0.9180	0			
z	0.6398	0			
Occup	1	0.5037			
$BaCO_3$ (wt %)			4.338		1.986
CeO_2 (wt %)					2.553

[a]$Ba_2In_2O_5$: Ba(0.1103,0.0133,0.5116), In1(0,0,0.0075), In2(0.25, 0.9420, 0.0268); [b]$Ba_2In_{1.5}Ce_{0.5}O_{5+\delta}$: Ba(0,0,0.2778), In1(0.5,0.5,0.5), In2(0.5,0.5,0), Ce(0.5,0.5,0.5); [c]$BaIn_{0.5}Ce_{0.5}O_{2.5+\delta}$: Ba(0.5,0.5,0.5), In(0,0,0), Ce(0,0,0); [d]$BaIn_{0.25}Ce_{0.75}O_{2.5+\delta}$: Ba(0.5,0.5,0.5), In(0,0,0),Ce(0,0,0); [e]BaCeO3 : Ba(0.001,0.023,0.25),Ce(0,0.5,0)

In order to compare the lattice parameters of all the samples which exist in different crystal system, pseudocubic cell parameters of the samples were calculated and are plotted in figure 2A.5. The equation employed for the determination of pseudocubic lattice parameters is given in Appendix 2.

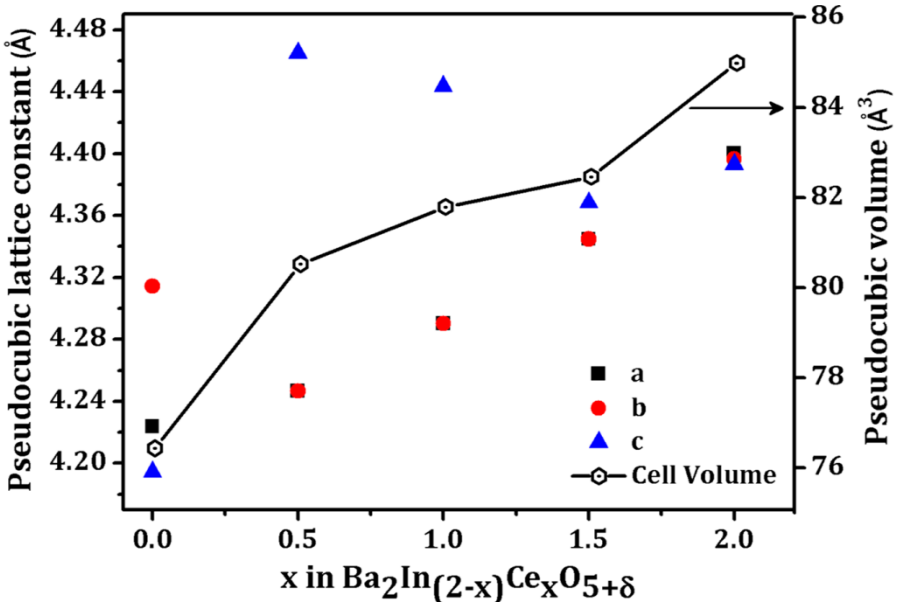

Figure 2A.5. Pseudocubic cell parameters and pseudocubic cell volume of $Ba_2In_{2-x}Ce_xO_{5+\delta}$ as a function of substitution of x; for $BaCeO_3$, x = 2.

It can be observed that with an increase in Ce concentration, the a and c lattice parameters move close to each other eventually shifting towards an ideal cubic structure. The gradual increase in the value of *a* and *b* axes can be ascribed to the larger crystal radius of Ce (1.15 Å and 1.01 Å for +3 and +4 oxidation state in octahedral coordination) than that of In (0.94 Å and 0.76 Å for octahedral and tetrahedral coordination) [13]. But along the *c* direction, the lattice constant shoots up initially on 25% Ce substitution in In site and then decreases slowly. This can be attributed to the fact that in the case of $Ba_2In_{1.5}Ce_{0.5}O_{5+\delta}$, the brownmillerite structure with octahedral and tetrahedral layers is retained and since bigger Ce atom replaces In in octahedral site, it leads to an overall increase in the Ce/In–O bond distances. But with further increase in Ce concentration, the brownmillerite structure is not retained and disorder in O1 and O2 atoms along *c* aixs is observed (Figure 2A.4 (c & d)). The distortion, as evident from distance between two equivalent O atoms along *c* axis, decreases with further increase in the Ce concentration resulting in gradual decrease in the lattice parameter along *c* direction. Similarly, the gradual increase in the pseudocubic cell

volume with increase in the Ce doping as seen in Figure 2A.5 is due to the larger crystal radius of Ce when compared with In. Interestingly, the extent of variation is very small in the substituted samples indicating that other factors like distortions, oxygen vacancies etc. play a crucial role.

Table 2A.2. Variation in the In/Ce-O-In/Ce bond angle along the *ab* plane and *c* direction.

	$Ba_2In_{1.5}Ce_{0.5}O_{5+\delta}$	$BaIn_{0.5}Ce_{0.5}O_{2.5+\delta}$	$BaIn_{02.5}Ce_{0.75}O_{2.5+\delta}$
In/Ce-O1-In/Ce (°)*	180	180	180
In/Ce-O2-In/Ce (°)#	180	169	173.17

*along c direction, #in *ab* plane

The bond angles along the *c* direction (In/Ce-O1-In/Ce) and *ab* plane (In/Ce-O2-In/Ce) for Ce doped $Ba_2In_2O_5$ systems are tabulated in Table 2A.2. It can be noticed that the bond angle, In/Ce-O1-In/Ce along *c* direction remains same in all the system. However, the bond angle along the *ab* plane, i.e. In/Ce-O2-In/Ce, initially decreases and then increases with higher substitution of In by Ce atoms. This can be correlated to a larger extent of distortion for $BaIn_{0.5}Ce_{0.5}O_{2.5+\delta}$ when compared to $BaIn_{0.25}Ce_{0.75}O_{2.5+\delta}$, as evident from the disorder in the O1 and O2 anionic site shown in Figure 2A.4. The distance between the two equivalent positions for O1 atom is 0.279 Å and that for O2 atom is 0.413 Å for $BaIn_{0.5}Ce_{0.5}O_{2.5+\delta}$ whereas in $BaIn_{0.25}Ce_{0.75}O_{2.5+\delta}$ it is 0.147 Å for O1 and 0.259 Å for O2 site. Further from Figure 2A.4, it can be observed that in $Ba_2In_{1.5}Ce_{0.5}O_{5+\delta}$, there is a disorder in O3 oxygen site in the *ab* plane. The structure is similar to that of hydrated $Ba_2In_2O_5$ where the same disorder in O3 site is observed leading to an anisotropic two dimensional layered structure with alternate layers of tetrahedra and octahedra [15].

The octahedral distortion, Δd for the Ce doped system was calculated using the following equation [17].

$$\Delta d = (1/6) \sum_{n=1,6} [(d_n - d)/d]^2$$

Where, d is the mean In/Ce – O bond distance and d_n is the individual In/Ce – O bond distance in the compound. The In/Ce – O bond distance and Δd value calculated from them are tabulated in Table 2A.3.

Table 2A.3. In/Ce-O bond distance and Δd for $Ba_2In_{1.5}Ce_{0.5}O_{5+\delta}$, $Ba_2InCeO_{5+\delta}$ and $Ba_2In_{0.5}Ce_{1.5}O_{5+\delta}$.

	$Ba_2In_{1.5}Ce_{0.5}O_{5+\delta}$	$BaIn_{0.5}Ce_{0.5}O_{2.5+\delta}$	$BaIn_{02.5}Ce_{0.75}O_{2.5+\delta}$
In/Ce – O1	2.287	2.082	2.111
In/Ce – O1		2.361	2.257
In/Ce – O2	2.125	2.155	2.176
Δd	0.001244	0.001576	0.000377

It can be observed that the octahedral distortion factor, Δd decreases with increase in Ce doping. A lower value of Δd for $BaIn_{0.25}Ce_{0.75}O_{2.5+\delta}$ indicates a more symmetric environment around the In/Ce atom in $BaIn_{0.25}Ce_{0.75}O_{2.5+\delta}$ system. This will facilitate the ionic conduction through the compound and will favor oxygen adsorption.

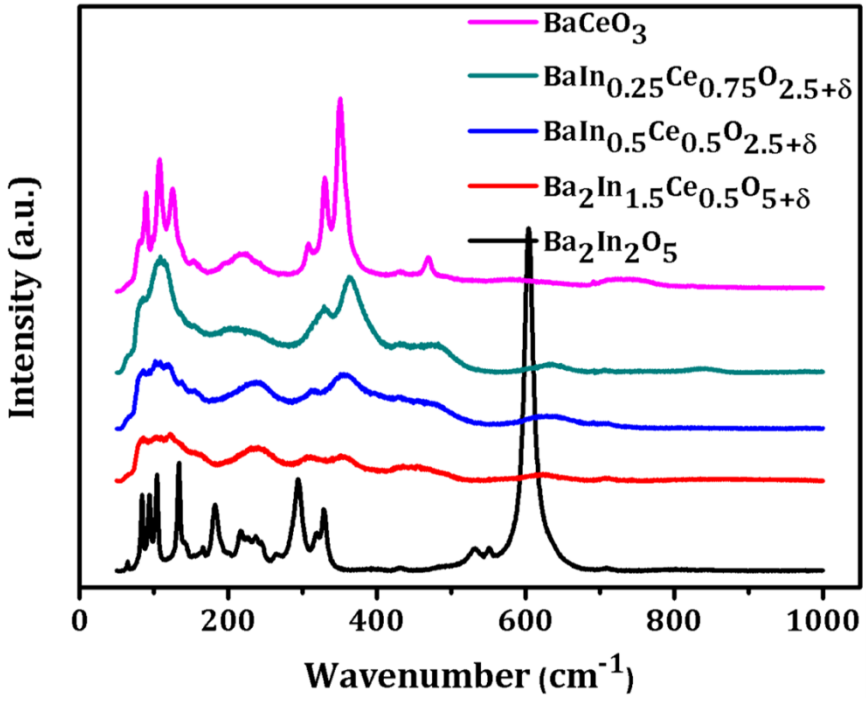

Figure 2A.6. Raman spectra of $Ba_2In_{2-x}Ce_xO_{5+\delta}$ (x = 0, 0.5, 1 & 1.5) and $BaCeO_3$.

In addition to the PXRD, Raman spectroscopy analysis was performed to get inputs on the structure. Figure 2A.6 represents the Raman spectra of $Ba_2In_{2-x}Ce_xO_{5+\delta}$ and $BaCeO_3$. Raman spectra of $Ba_2In_2O_5$ and $BaCeO_3$ matched with already reported patterns in literature [18, 19]. The bands in the low frequency region, below 300 cm^{-1} can be related to the vibrations mainly involving Ba^{2+} ions which being the heaviest atom in these compounds and hence expected to vibrate at lower wavelength. The appearance of peaks around 300–375 cm^{-1} is associated with the stretching vibration

mode of CeO_6 octahedra. With increase in the Ce concentration, intensities of these peaks increase which is a clear indication of the enhanced presence of Ce in the octahedral site. In addition to the appearance of the peaks corresponding to CeO_6 octahedra, there is a drastic reduction in the intensity of the In-O bands which appears around 600 cm^{-1}. This type of drastic reduction in the intensity is due to the disorder in the oxygen sublattice as seen with other dopants also [20].

Further, the BET surface area of the samples was measured using N_2 adsorption study and is reported in Table 2A.4. The surface area obtained for all the samples are very low which can be attributed to their synthesis procedure. In general, samples synthesized by solid state method at higher temperature have low surface area [21].

Table 2A.4. BET surface area of $Ba_2In_{2-x}Ce_xO_{5+\delta}$ (x = 0, 0.5, 1 & 1.5) and $BaCeO_3$ calculated from N_2 adsorption study.

Compound	BET surface area ($m^2 g^{-1}$)
$Ba_2In_2O_5$	5.4
$Ba_2In_{1.5}Ce_{0.5}O_{5+\delta}$	2.6
$BaIn_{0.5}Ce_{0.5}O_{2.5+\delta}$	6.0
$BaIn_{0.25}Ce_{0.75}O_{2.5+\delta}$	3.8
$BaCeO_3$	6.2

The oxygen uptake of cerium doped $Ba_2In_2O_5$ was calculated by thermogravimetric analysis under 10% O_2 in He up to 900 °C. The oxygen uptake was calculated from the amount of weight gained. The detailed calculation is given in Appendix 2. Figure 2A.7 represents the TGA profile of all the Ce doped samples under 10% O_2 in He.

For all the compounds, the oxygen uptake initially increases as evident from the figure, however a weight loss takes place around 300 °C, which can be attributed to the loss of water of hydration present in these compounds. Also it can be observed that the weight gain beyond 400 °C is steady for $Ba_2In_2O_5$ which has the highest oxygen vacancies in the lattice among the series. However, the weight gain in Ce doped systems is not that prominent, this can be attributed to the presence of Ce (IV) oxidation state in place of In (III) in the compound which in fact decreases the oxygen vacancies in the lattice. The oxygen uptake calculated from the TGA profile is tabulated in Table 2A.5.

The relation between oxygen vacancies and oxygen uptake are previously reported in literature [22, 23].

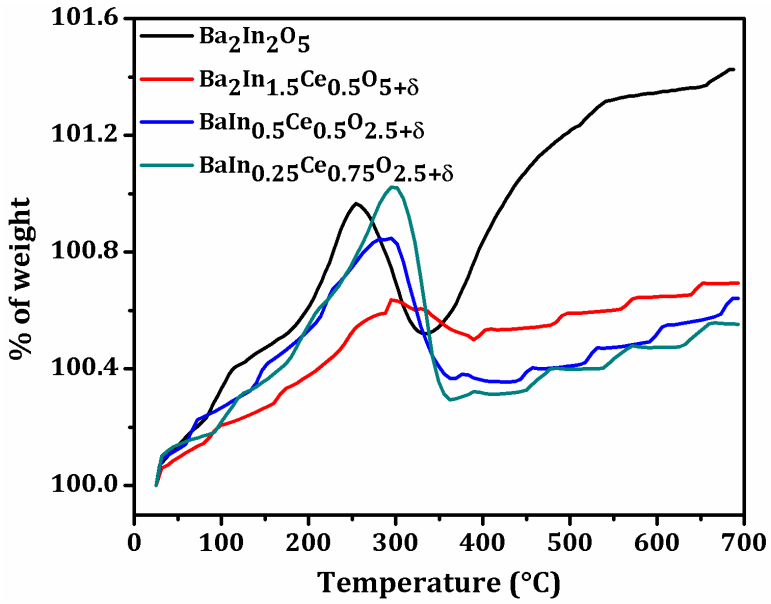

Figure 2A.7. Thermogravimetric profiles under 10% O_2 in He for $Ba_2In_2O_5$ and Ce doped $Ba_2In_2O_5$.

Table 2A.5. Oxygen uptake of Ce doped $Ba_2In_2O_5$ calculated from TGA.

Compound	Oxygen uptake (mmol g^{-1})
$Ba_2In_2O_5$	0.8
$Ba_2In_{1.5}Ce_{0.5}O_{5+\delta}$	0.42
$BaIn_{0.5}Ce_{0.5}O_{2.5+\delta}$	0.4
$BaIn_{0.25}Ce_{0.75}O_{2.5+\delta}$	0.35

Further, in order to study the stability of all the samples under different atmosphere at variable temperature, in situ HTXRD experiments were performed. Figure 2A.8 represents the PXRD pattern of all the compounds at 30 °C, 200 °C, 300°C, 400°C, 500°C and 700°C under helium and 10% O_2 in He atmosphere. The PXRD pattern of all samples were initially recorded at various temperatures under He atmosphere and then cooled to 30 °C, the gas flow was then switched to 10% O_2 in He and PXRD at variable temperature was recorded.

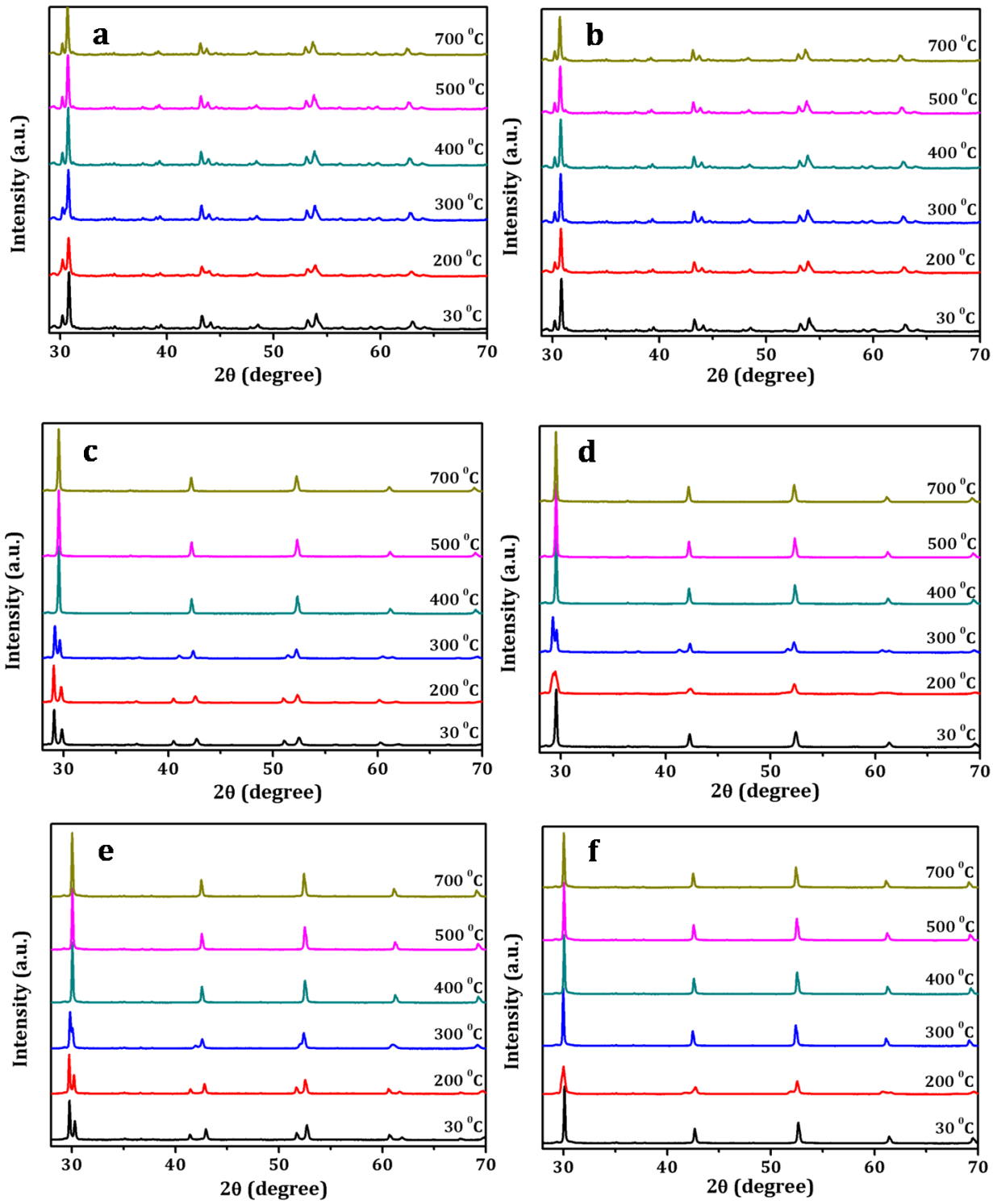
a
b
c
d
e
f
700 °C
500 °C
400 °C
300 °C
200 °C
30 °C
Intensity (a.u.)
2θ (degree)
30
40
50
60
70

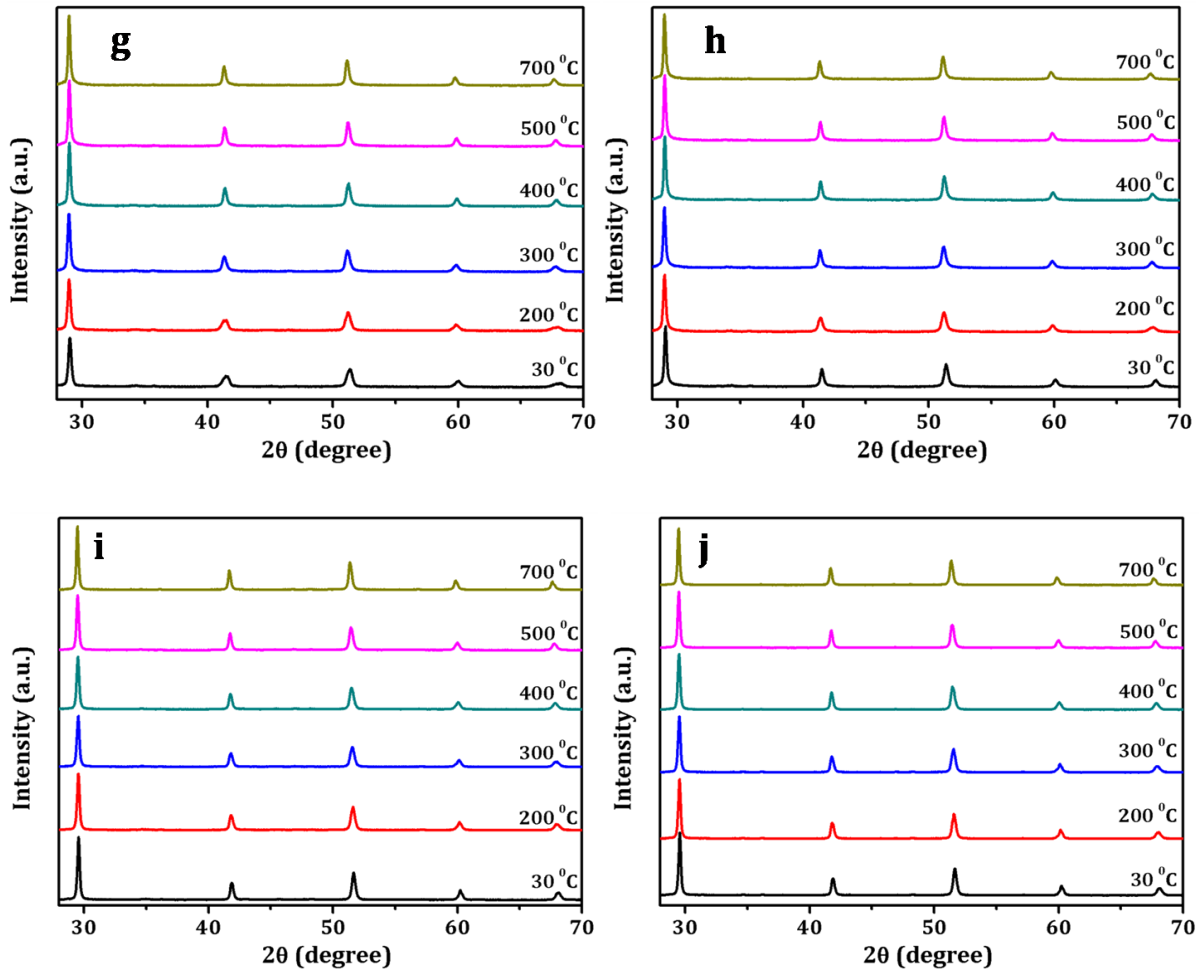

Figure 2A.8. High temperature PXRD patterns of $Ba_2In_2O_5$ **(a & b)**, $Ba_2In_{1.5}Ce_{0.5}O_{5+\delta}$ **(c & d)**, $BaIn_{0.5}Ce_{0.5}O_{2.5+\delta}$ **(e & f)**, $BaIn_{0.25}Ce_{0.75}O_{2.5+\delta}$ **(g & h)** and $BaCeO_3$ **(i & j)**. PXRD patterns in **a**, **c**, **e**, **g** & **i** are obtained under inert atmosphere (He) and **b**, **d**, **f**, **h** & **j** are obtained under oxidizing atmosphere (10% O_2 in He).

All the samples were stable under these conditions. No structural changes were observed in $Ba_2In_2O_5$ till 700 °C; it is previously reported in literature that the orthorhombic structure of $Ba_2In_2O_5$ transforms to tetragonal structure ~ 925 °C and to cubic structure ~ 1040 °C [24]. At this temperature, the orderly distributed oxygen vacancy in the two dimensional layer of brownmillerite are randomly distributed in the lattice which in fact facilitates the oxide ion conduction through the compound. Incorporation of Ce in the lattice brings down the order disorder transition temperature drastically. The structural transformation from tetragonal to cubic phase occurs after 300 °C in $Ba_2In_{1.5}Ce_{0.5}O_{5+\delta}$ and around 300 °C in $BaIn_{0.5}Ce_{0.5}O_{2.5+\delta}$ which is clearly visible in Figure 2A.8 (c & e). The cubic structure was maintained after cooling to room temperature in the same environment. Again heating the sample under 10 % O_2 in He,

the tetragonal splitting appears slowly but it disappears above 300 °C and 200 °C in $Ba_2In_{1.5}Ce_{0.5}O_{5+\delta}$ and $BaIn_{0.5}Ce_{0.5}O_{2.5+\delta}$ respectively. No appreciable changes in the PXRD patterns at higher temperatures were observed in $BaIn_{0.25}Ce_{0.75}O_{2.5+\delta}$ and $BaCeO_3$. Hence, HTXRD experiments suggest that Ce doping in $Ba_2In_2O_5$ can drastically bring down the order disorder temperature which will facilitate the conduction through these materials at a relatively lower temperature.

2A.3.2. Electrochemical characterization

Detailed electrochemical studies of these compounds were carried out by CV and RDE method under alkaline medium at room temperature and EIS technique at higher temperatures.

2A.3.2.1. ORR activity in alkaline medium

The ORR activity of these compounds under alkaline conditions was carried out using CV and RDE methods. For this a slurry made by the mixture of the sample and Vulcan XC-72 carbon was coated on glassy carbon working electrode. Cyclic voltammograms of the samples under N_2 and O_2 saturated solution at a sweep rate of 50 mV s^{-1} is shown in Figure 2A.9 (a-e). The cyclic voltammogarms of all the samples under N_2 saturated solution exhibited a nearly rectangular profile whereas after saturating the electrolyte with O_2, a distinct reduction peak was observed in the CV curve. An increase in the reduction current after O_2 saturation indicates the ORR activity of the samples.

A detailed investigation on the ORR activity of these samples was performed by RDE method. Figure 2A.10 represents the linear sweep voltammograms (LSV) of Ce doped $Ba_2In_2O_5$ and $BaCeO_3$ recorded at an electrode rotating speed of 1600 rpm in O_2 saturated 0.1 M KOH solution. The onset potential for all the Ce doped sample was around -0.06 V vs. Hg/HgO which is around 0.06 V more positive than the parent compounds viz., $Ba_2In_2O_5$ and $BaCeO_3$. Apart from this, the geometrical limiting current density also increases with increase in Ce concentration in $Ba_2In_2O_5$. However, it decreases again in the case of $BaCeO_3$, where there is no disorder in the axial and equatorial oxygen atoms.

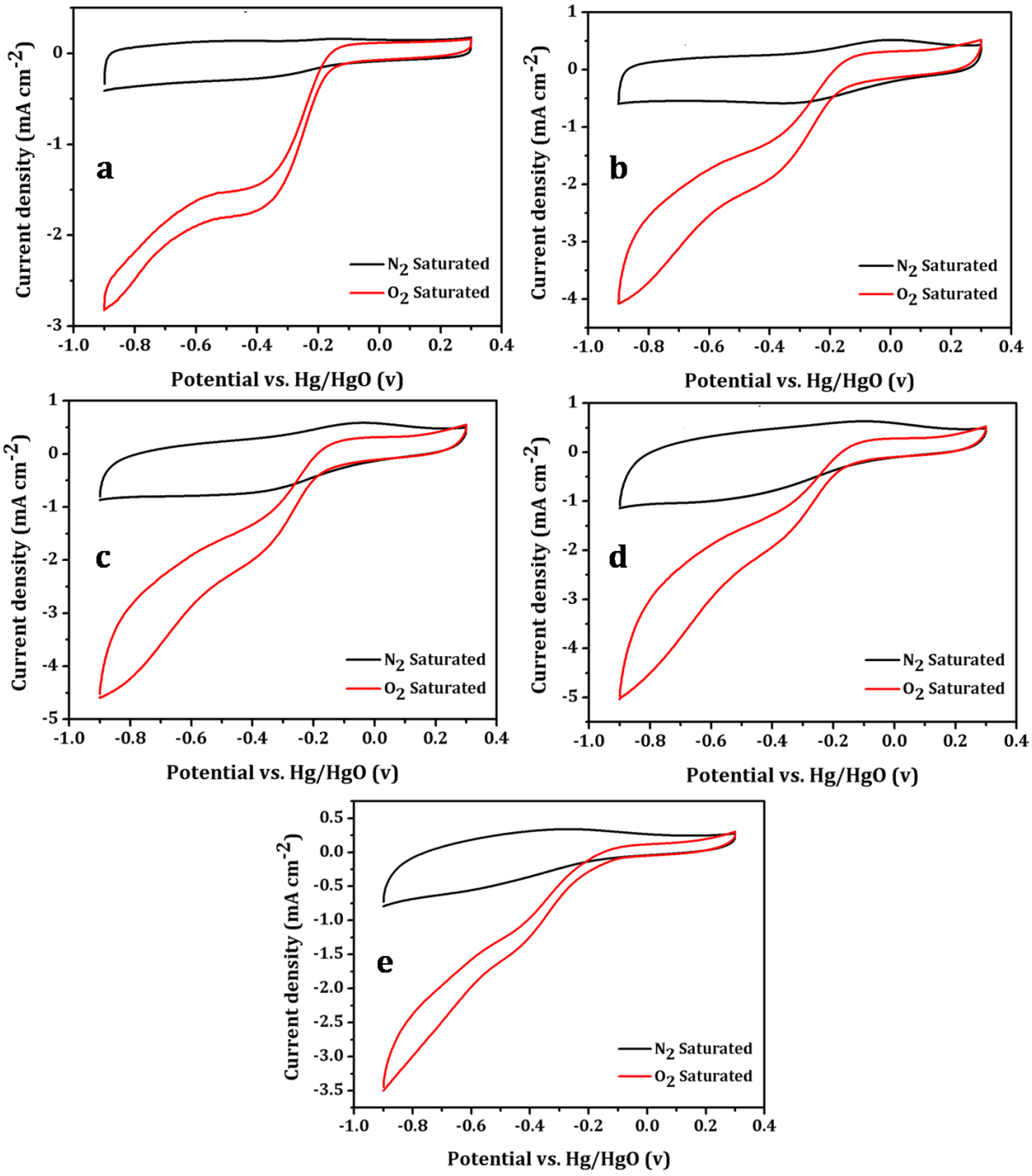

Figure 2A.9. Cyclic voltammograms of **(a)** $Ba_2In_2O_5$, **(b)** $Ba_2In_{1.5}Ce_{0.5}O_{5+\delta}$, **(c)** $BaIn_{0.5}Ce_{0.5}O_{2.5+\delta}$, **(d)** $BaIn_{0.25}Ce_{0.75}O_{2.5+\delta}$ and **(e)** $BaCeO_3$ in N_2 and O_2 saturated 0.1 M KOH at a sweep rate of 50 mV s^{-1} using Hg/HgO and Pt foil as reference and counter electrode respectively.

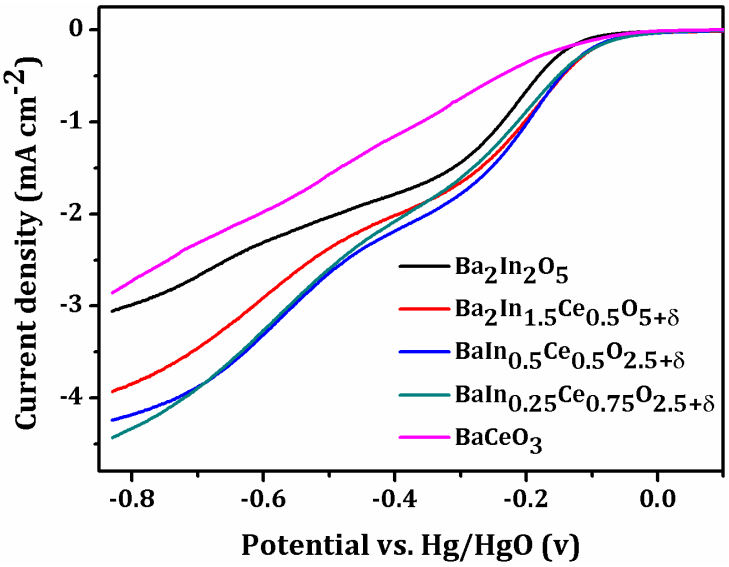

Figure 2A.10. LSVs obtained at an electrode rotating speed of 1600 rpm with a rotating disk electrode for the ORR on $Ba_2In_2O_5$, Ce doped $Ba_2In_2O_5$ and $BaCeO_3$. The experiments were performed in O_2 saturated 0.1 M KOH at a sweep rate of 5 mV s^{-1} using Hg/HgO and Pt foil as reference and counter electrode respectively.

It is important to note that as Ce concentration increases, ORR activity concomitantly increases which can be expected since Ce is an excellent redox centre. However, $BaCeO_3$, a stoichiometric perovskite without any oxygen vacancies and hence O_2 adsorption sites, exhibits very poor activity and this proves that mere presence of Ce is not enough for the material to be ORR active. Among the Ce doped compounds, $Ba_2In_{1.5}Ce_{0.5}O_{5+\delta}$, with ordered tetrahedral and octahedral layers, shows the least activity, whereas activity increases with increase in disorder. This observation can be correlated with the fact that in $Ba_2In_{1.5}Ce_{0.5}O_{5+\delta}$, the layered structure will favour only anisotropic conduction, whereas disordered structures like $BaIn_{0.5}Ce_{0.5}O_{2.5+\delta}$ and $BaIn_{0.25}Ce_{0.75}O_{2.5+\delta}$ will have enhanced isotropic conduction. Also, we observe that among $BaIn_{0.5}Ce_{0.5}O_{2.5+\delta}$ and $BaIn_{0.25}Ce_{0.75}O_{2.5+\delta}$, the latter has the least distorted octahedral environment around the In/Ce site. Such highly symmetric B site geometries are reported to play an active role in enhancing ionic conduction in doped $BaCeO_3$ compounds [22]. Hence, a synergistic influence of highly disordered yet symmetric Ce catalytic sites adjacent to oxygen vacancies can be deemed to be the important factor affecting the ORR activity of such oxides. This also suggests that, it is not only the Ce which is enhancing the ORR activity, but the peculiar structural features like extent of disorder, B site symmetry etc. also seem to have some effect.

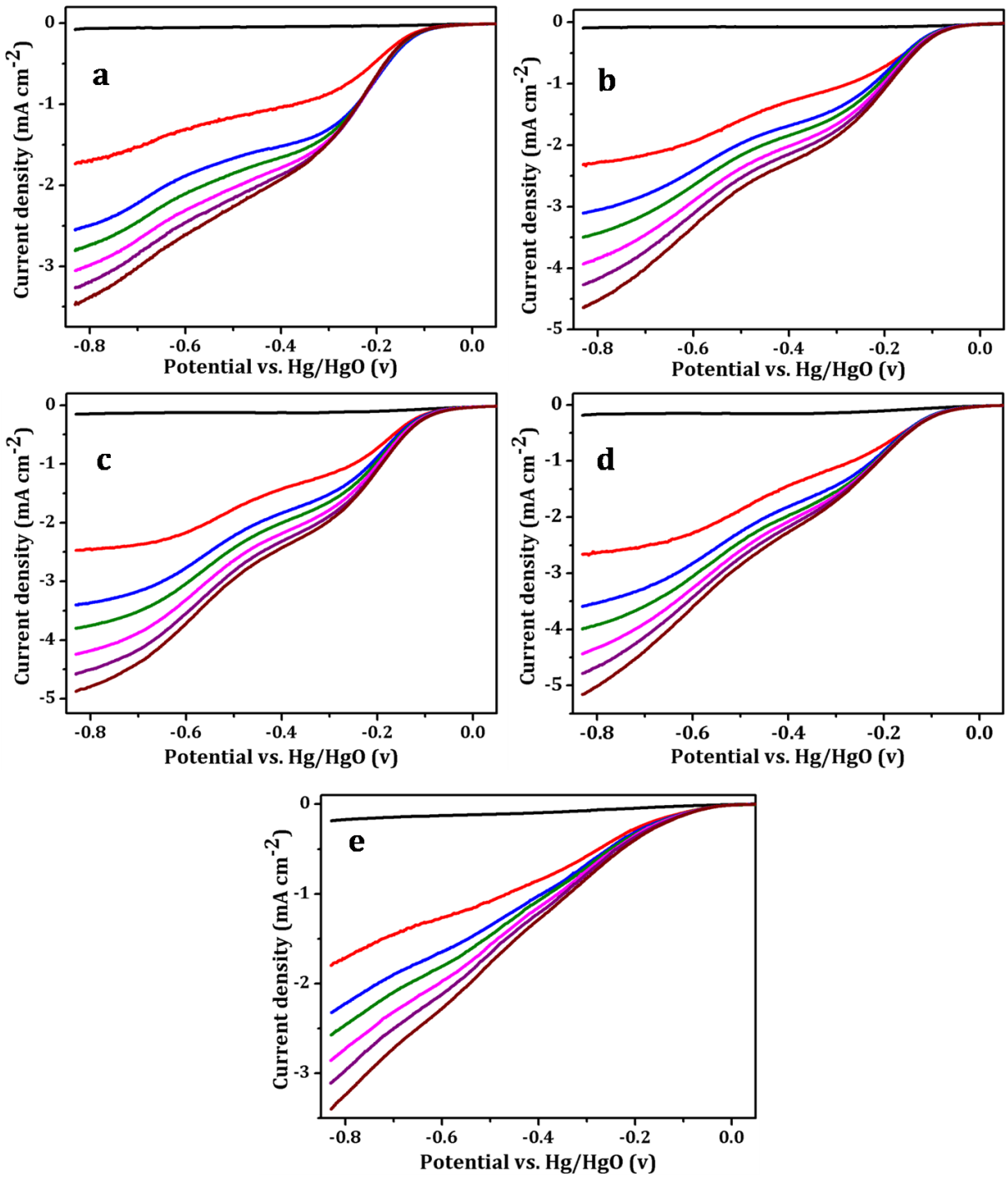

Figure 2A.11. LSVs at different electrode rotation rates (black: blank, red: 400 rpm, blue: 900 rpm, green: 1200 rpm, pink: 1600 rpm, violet: 2000 rpm and brown: 2500 rpm) for ORR on **(a)** $Ba_2In_2O_5$, **(b)** $Ba_2In_{1.5}Ce_{0.5}O_{5+\delta}$, **(c)** $BaIn_{0.5}Ce_{0.5}O_{2.5+\delta}$, **(d)**$BaIn_{0.25}Ce_{0.75}O_{2.5+\delta}$ and **(e)** $BaCeO_3$ in O_2 saturated 0.1 M KOH at a sweep rate of 5 mV s^{-1} using Hg/HgO and Pt foil as reference and counter electrode respectively.

LSVs of all the compounds at various electrode rotation rates in O_2 saturated 0.1 M KOH solution is shown in figure 2A.11 (a-e). It is evident from the figure that the

limiting current density increases with the increase in the rate of rotation of the working electrode. This can be attributed to the enhanced rate of mass transport at higher electrode rotation [25]. A close analysis of the LSV profiles of the different systems reveals that at any constant rotation rate, the limiting current density increases with increase in the Ce concentration in $Ba_2In_2O_5$ and it eventually decreases in $BaCeO_3$ where, In is completely substituted by Ce and it enters into the perovskite structure with no disorder in oxygen sites.

The kinetic parameters such as electron transfer number, kinetic current density etc., of samples were determined from Koutecky-Levich (K-L) equation [26],

$$\frac{1}{j} = \frac{1}{nFkC_{O_2}} + \frac{1}{0.62nFC_{O_2}D_{O_2}^{2/3}\upsilon^{-1/6}\omega^{1/2}}$$

Where, 'j' is the disk electrode current density, 'n' (mol^{-1}) is the number of electrons exchanged per O_2 molecule, 'F' is the Faraday constant (96500 C mol^{-1}), 'k' is the reaction rate constant, 'C_{O2}' is the bulk oxygen concentration (1.2×10^{-6} mol L^{-1}) , 'D_{O2}' is the diffusion coefficient of molecular oxygen in 0.1 M KOH solution (1.9×10^{-5} cm^2 s^{-1}), 'ν' is the kinematic viscosity of the electrolyte (0.01 cm^2 s^{-1}) and 'ω' is the electrode rotation speed in radians per second (= 2πf = 2π rpm/60).

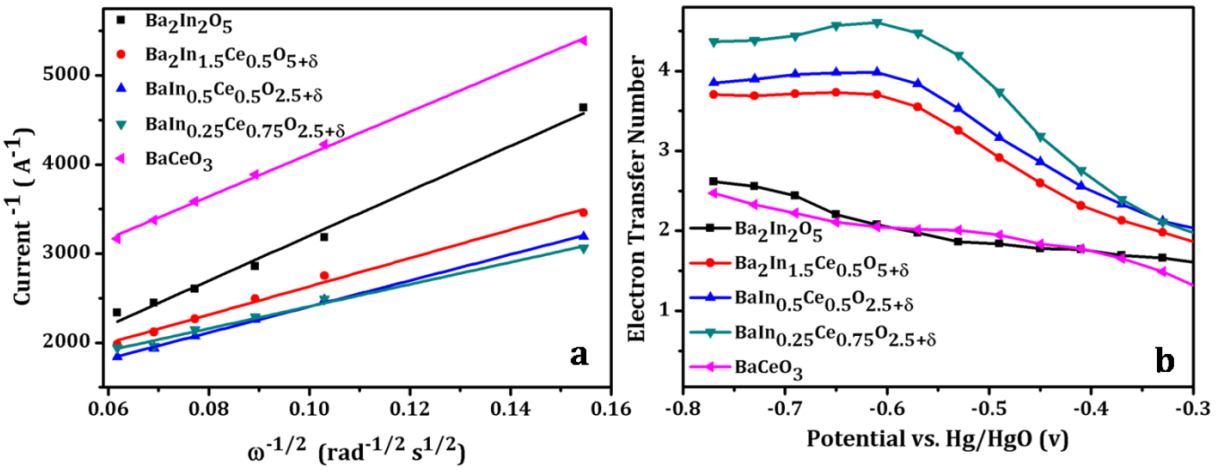

Figure 2A.12. (a) K-L plot of ORR on $Ba_2In_2O_5$, Ce doped $Ba_2In_2O_5$ and $BaCeO_3$ at a constant potential of -0.49 V and **(b)** The dependence of the electron transfer number of $Ba_2In_2O_5$, Ce doped $Ba_2In_2O_5$ and $BaCeO_3$ on various applied potential; in O_2 saturated 0.1 M KOH at a sweep rate of 5 mV s^{-1} using Hg/HgO and Pt foil as reference and counter electrode respectively.

A plot of the inverse of current (i^{-1}) as a function of inverse of the square root of the rotation rate ($\omega^{-1/2}$) is known as K-L plot. Figure 2A.12 (a) represents the K-L plot of all the samples at -0.49 V. A clear change in the slope for Ce doped $Ba_2In_2O_5$ systems when compared to that of $Ba_2In_2O_5$ and $BaCeO_3$ is visible from the figure. This suggests that the ORR mechanism which can occur either through a 2-electron pathway or 4-electron pathway, are different for the two sets. The number of electrons involved in the ORR mechanism was calculated from the slope of the K-L plot at different potential. Figure 2A.12 (b) represents the dependence of the applied potential on the electron transfer number in these samples. It is evident from the figure that, for $Ba_2In_2O_5$ and $BaCeO_3$, the number of electrons involved in the ORR is around 2 throughout the applied potential range, this indicates that the reduction of oxygen occurs through peroxide intermediate. But, in the other three samples, the electron transfer number for ORR is found to be ~ 2 at lower negative potential and ~ 4 at higher negative potential. In the intermediate region the electron transfer number is found to be ~ 3. An electron transfer number of 3 may be due to a parallel pathway involving both 2 and 4 electron mechanism [27]. This indicates that the applied potential has a significant role in deciding the kinetics of ORR reaction. The structural features mentioned in the section 2A.3.1 can be understood to play an important role in deciding the reaction pathway which is evident from the difference in the number of electrons involved for Ce doped $Ba_2In_2O_5$ and the end members i.e. $Ba_2In_2O_5$ and $BaCeO_3$. Further it can be observed that, with increase in Ce dopant concentration, the number of electrons involved in the ORR increases. The observed value of ~4.5 at higher potentials in case of $BaIn_{0.25}Ce_{0.75}O_{2.5+\delta}$ which is above the theoretical value of 4 can be attributed to parasitic current generated as a consequence of side reactions and chain reactions.

Finally the kinetic current density of all the samples was calculated. Figure 2A.13 represents the kinetic current density of all the samples. The kinetic current values (j_k), which is directly correlated to the rate constant for ORR is plotted against the corresponding potentials to analyse the current potential behaviour of the different catalysts. It can be seen that at a particular potential, the kinetic current density increases with increase in Ce concentration however it finally decreases in $BaCeO_3$.

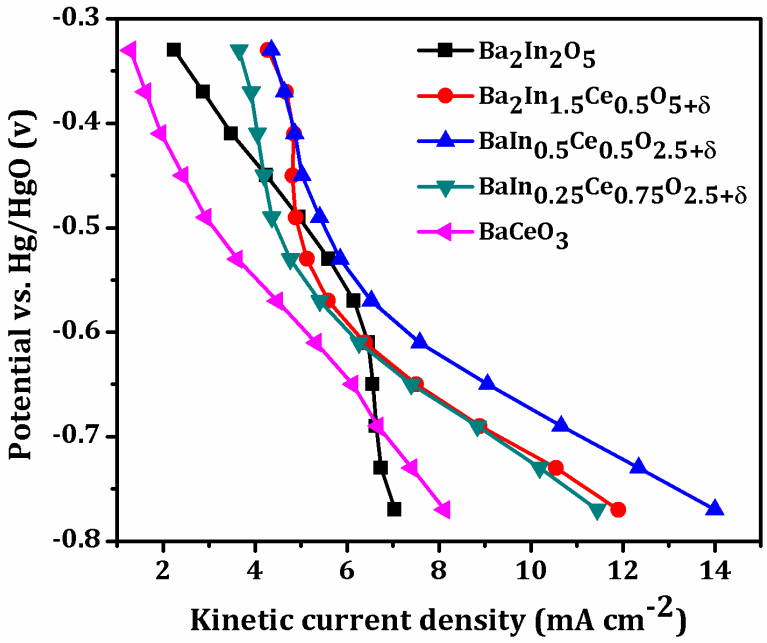

Figure 2A.13. The kinetic current density on the potential for $Ba_2In_2O_5$, Ce doped $Ba_2In_2O_5$ and $BaCeO_3$. The experiments were performed in O_2 saturated 0.1 M KOH at a sweep rate of 5 mV s^{-1} using Hg/HgO and Pt foil as reference and counter electrode respectively.

2A.3.2.2. High temperature EIS measurements

A polycrystalline sample connected with an electrode to perform impedance spectroscopy will have different regions and can be represented by the brick layer model as shown in Figure 2A.14 [28].

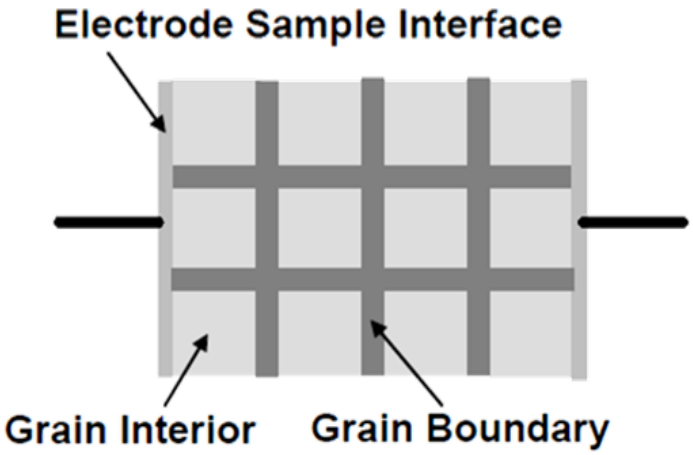

Figure 2A.14. Brick layer model representing a polycrystalline ceramic sample connected to electrode.

The analysis of the AC impedance scans obtained from such materials can be done on the basis of Bauerle model [29], where the Ac impedance spectrum of a ceramic polycrystalline sample appears in three successive semicircles associated to the bulk impedance (in the high frequency range), grain boundary impedance (at intermediate frequencies) and the charge transfer or electrode impedance (at low frequencies). The analysis of the AC impedance scans in the current work is also based on this model. In some instances, all three semicircles are not obtained; this is either due to the overlapping of the semicircles or part of the spectra being out of the range of frequencies. The impedance scans can be modelled using an equivalent circuit with a series of Randle circuit (RC) elements representing bulk, grain boundary and electrode impedance. Figure 2A.15 represents the equivalent circuit used for fitting the impedance plot.

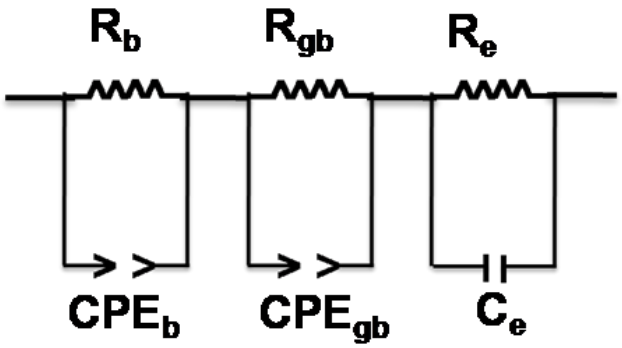

Figure 2A.15. Equivalent circuit used for representing the contribution from bulk, grain boundary and electrode interface in the total AC impedance response.

Capacitors in EIS experiments often do not behave ideally and they act like a constant phase element denoted by CPE [30]. The impedance of a capacitor is given by

$$Z_{CPE} = \frac{1}{(j\omega)^{\alpha}C}$$

Where, ω is the radial frequency, α is an empirical constant generally 0.9-1.0 (α=1 for an ideal capacitor) and C is the capacitance.

Depending upon the magnitudes of the capacitance, the RC components can be assigned to different regions of the samples. Table 2A.6 represents the capacitance values and their possible origin [31].

Table 2A.6 Capacitance value obtained for the equivalent circuit and their possible interpretation.

Capacitance (F)	Phenomenon Responsible
10^{-12}	Bulk
10^{-11}	Minor, second phase
10^{-11} to 10^{-8}	Grain boundary
10^{-10} to 10^{-9}	Bulk ferroelectric
10^{-9} to 10^{-7}	Surface layer
10^{-7} to 10^{-5}	Sample-electrode interface
10^{-4}	Electrochemical reactions

The high temperature ac impedance spectroscopy measurements of the series of compounds were performed on the sintered pellets as mentioned in section 2A.2.3. All the scans were fitted to the equivalent circuit shown in Figure 2A.15.

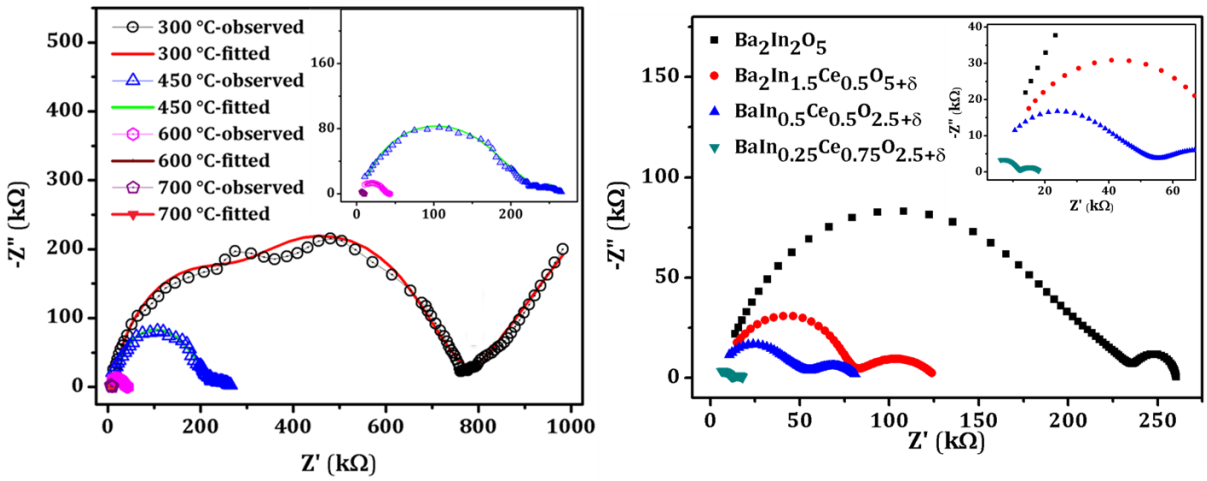

Figure 2A.16. (a) Raw and fitted AC impedance scans for $Ba_2In_2O_5$ at different temperatures and **(b)** AC impedance scans of $Ba_2In_2O_5$ and Ce doped $Ba_2In_2O_5$ at 450 °C. Inset in both the figure represents enlarged portion of high frequency region.

Figure 2A.16 (a) represents the fitted AC impedance plot obtained for the parent $Ba_2In_2O_5$ brownmillerite. With increase in the temperature, the total impedance of the materials decreased. Similar observations were seen in the other compounds of the series. The total resistance (R_b + R_{gb}) of the materials were calculated from the fitting parameters of the equivalent circuit. The total resistance of the compounds with varying temperature is tabulated in Table 2A.7.

Table 2A.7. Total resistance (R_b+R_{gb}) of the parent and Ce doped $Ba_2In_2O_5$ at variable temperature determined by EIS. Parameters were determined by fitting the experimental AC scans to the equivalent circuit shown in Figure 2A.14.

	R_b+R_{gb} (ohms)			
	300 °C	450 °C	600 °C	700 °C
$Ba_2In_2O_5$	7.8 x 10^5	2.4 x 10^5	3.7 x 10^4	9.2 x 10^3
$Ba_2In_{1.5}Ce_{0.5}O_{5+\delta}$	4.6 x 10^5	8.2 x 10^4	2.5 x 10^4	8.9 x 10^3
$BaIn_{0.5}Ce_{0.5}O_{2.5+\delta}$	4.2 x 10^5	5.5 x 10^4	1.01 x 10^4	3.3 x 10^3
$BaIn_{0.25}Ce_{0.75}O_{2.5+\delta}$	8.7 x 10^4	1.2 x 10^4	3.2 x 10^3	9.6 x 10^2

It can be observed that at a fixed temperature, with increase in Ce concentration, the impedance decreased. Figure 2A.16 (b) represents the AC impedance scans of $Ba_2In_2O_5$ and Ce doped $Ba_2In_2O_5$ samples at 450°C. The decrease in the total resistance with increasing concentration of Ce can be attributed to the presence of Ce in the lattice which will induce vacancy disorder, thereby leading to isotropic conduction.

The total conductivities of the samples were calculated from the impedance data. The detailed calculation is given in Appendix 2.

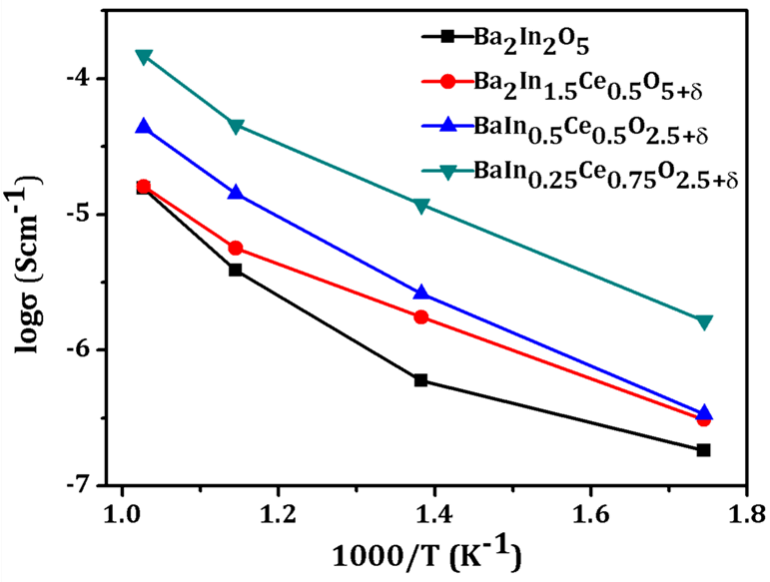

Figure 2A.17. Arrhenius plots of the total conductivities determined from the AC impedance scan of $Ba_2In_2O_5$ and Ce doped $Ba_2In_2O_5$.

The Arrhenius graphs constructed from the measured conductivity of all the samples are shown in Figure 2A.17. There is a continuous increase in the conductivity of

the sample with increase in temperature. Also with increase in Ce concentrations, the conductivity increases. The higher conductivity of Ce doped samples and the fact that the order-disorder transition temperature in these compounds are much lower than the parent brownmillerite suggests that, these materials can be used in MIEC membranes and SOFC at relatively lower temperature. The activation energy for the conduction through these materials was calculated (detailed calculation steps given in Appendix 2) from the Arrhenius plot and is tabulated in Table 2A.8.

Table 2A.8. Activation energy for the conductivity through $Ba_2In_2O_5$ and Ce doped $Ba_2In_2O_5$ calculated from the Arrhenius plot.

Compound	Activation Energy (J mol^{-1})
$Ba_2In_2O_5$	21.67
$Ba_2In_{1.5}Ce_{0.5}O_{5+\delta}$	19.12
$BaIn_{0.5}Ce_{0.5}O_{2.5+\delta}$	23.2
$BaIn_{0.25}Ce_{0.75}O_{2.5+\delta}$	21.61

The activation energy initially decreased with Ce doping but it again increases with higher concentration of Ce. This may be due to the fact that as Ce concentration increases, although the orderly distributed oxygen vacancies in the lattice is randomly distributed, but simultaneously the number of oxygen vacancies decreases due to the presence of Ce in +4 oxidation state.

2A.4. Conclusions

$Ba_2In_2O_5$ brownmillerites with Ce doped progressively in In site were synthesized by solid state method. Phase purity of the synthesised samples was determined by PXRD and the structural parameters were obtained by the Rietveld refinement of the PXRD patterns. 25 % Ce doping retained the brownmillerite structure whereas higher doping of Ce resulted in the loss of alternate layers of octahedral and tetrahedral and lead to a highly disordered perovskite like structure. Both the pseudocubic lattice parameters as well as the cell volume increased with increase in the Ce concentration. The octahedral distortion factor of Ce doped $Ba_2In_2O_5$ decreased with increase in the Ce concentration hence leading to a more symmetric environment around B site cation which will eventually ease the ionic conduction and oxygen adsorption. TGA data reveals that oxygen uptake decreases with increase in Ce doping.

All the samples were stable in both inert and 10 % O_2 in He atmosphere till 700°C as evident from the in situ high temperature PXRD measurements. The samples were tested for ORR activity in alkaline medium. An interesting structural correlation emerged with respect to activity and disorder. The end members $Ba_2In_2O_5$ brownmillerite and $BaCeO_3$ perovskite are found to have poor activity for ORR. $Ba_2In_2O_5$ has an anisotropic structure in which In occupies alternate layers of tetrahedra and octahedra consequently giving rise to oxygen vacancies ordered in the tetrahedral layer. On the contrary, $BaCeO_3$ is a stoichiometric perovskite without any oxygen vacancies or disorder, but with full occupancy of Ce in B site. Apparently, these features separately do not lead to good activity but when combined, enhance the ORR activity in the doped compounds. 75% Ce doped $Ba_2In_2O_5$; $BaIn_{0.25}Ce_{0.75}O_{2.5+\delta}$ exhibited better ORR activity among the series with a 4 electron direct reduction pathway at higher applied potentials. The high temperature EIS measurement shows that with increase in temperature, the impedance decreased. Also with increase in the Ce concentration, the total resistance (R_b+R_{gb}) of the sample decreased. This is because on Ce(IV) doping in In(III) sites, oxygen vacancies are envisaged to be reduced but with enhanced disorder. The disorder occurs when the ordered layer structure collapses into 3D octahedral network as in the case of perovskites; now the structure has random oxygen vacancies in all three directions. Such disordered structures with isotropic conduction pathways are known to be better oxide ion conductors. Arrhenius plot shows that the conductivity increases with increase in temperature and Ce concentration. These materials can be envisaged as potential candidates for MIEC membranes and as cathode materials in SOFC.

2A.5. References

1. Bouwmeester, H. J. M. *Catal. Today* **2003**, *82*, 141.
2. Shao, Z.; Haile, S. M. *Nature* **2004**, *431*, 170.
3. Suntivich, J.; Gasteiger, H. A.; Yabuuchi, N.; Nakanishi, H.; Goodenough, J. B.; Shao-Horn, Y. *Nat. Chem.* **2011**, *3*, 546.
4. Sunarso, J.; Baumann, S.; Serra, J. M.; Meulenberg, W. A.; Liu, S.; Lin, Y. S.; Diniz da Costa, J. C. *J. Membrane Sci.* **2008**, *320*, 13.
5. Anderson, M. T.; Vaughey, J. T.; Poeppelmeier, K. R. *Chem. Mater.* **1993**, *5*, 151.

6. Patrakeev, M. V.; Leonidov, I. A.; Kozhevnikov, V. L.; Kharton, V. V. *Solid State Sci.* **2004**, *6*, 907.
7. Jeen, H.; Choi, W. S.; Biegalski, M. D.; Folkman, C. M.; Tung, I. C.; Fong, D. D.; Freeland, J. W.; Shin, D.; Ohta, H.; Chisholm, M. F.; Lee, H. N. *Nat. Mater.* **2013**, *12*, 1057.
8. Berastegui, P.; Hull, S.; García-García, F. J.; Eriksson, S. G. J. *Solid State Chem.* **2002**, *164*, 119.
9. Thangadurai, V.; Weppner, W. *Ionics* **2006**, *12*, 81.
10. Mogensen, M.; Sammes, N. M.; Tompsett, G. A. *Solid State Ionics* **2000**, *129*, 63.
11. Mueller, D. N.; Machala, M. L.; Bluhm, H.; Chueh, W. C. *Nat. Commun.* **2015**, *6*, 6097.
12. Toby, B. H. *J. Appl. Crystallogr.* **2001**, *34*, 210.
13. Shannon, R. *Acta Crystallogr. Sect. A* **1976**, *32*, 751.
14. Fischer, W.; Reck, G.; Schober, T. *Mater. Sci. Forum* **2000**, *321*, 363.
15. Fischer, W.; Reck, G.; Schober, T. *Solid State Ionics* **1999**, *116*, 211.
16. Jacobson, A. J.; Tofield, B. C.; Fender, B. E. F. *Acta Crystallogr. Sect. B-Struct. Sci.* **1972**, *28*, 956.
17. Malavasi, L.; Kim, H.; Proffen, T. *J. Appl. Phys.* **2009**, *105*, 123519.
18. Karlsson, M.; Matic, A.; Knee, C. S.; Ahmed, I.; Eriksson, S. G.; Börjesson, L. *Chem. Mater.* **2008**, *20*, 3480.
19. Scherban, T.; Villeneuve, R.; Abello, L.; Lucazeau, G. *Solid State Commun.* **1992**, *84*, 341.
20. Shin, J. F.; Orera, A.; Apperley, D. C.; Slater, P. R. *J. Mater. Chem.* **2011**, *21*, 874.
21. Bell, R. J.; Millar, G. J.; Drennan, J. *Solid State Ionics* **2000**, *131*, 211.
22. Malavasi, L.; Ritter, C.; Chiodelli, G. *Chem. Mater.* **2008**, *20*, 2343.
23. Suescun, L.; Dabrowski, B.; Mais, J.; Remsen, S.; Richardson, J. W.; Maxey, E. R.; Jorgensen, J. D. *Chem. Mater.* **2008**, *20*, 1636.
24. Speakman, S. A.; Richardson, J. W.; Mitchell, B. J.; Misture, S. T. *Solid State Ionics* **2002**, *149*, 247.
25. Town, J. L.; MacLaren, F.; Dewald, H. D. *J. Chem. Educ.* **1991**, *68*, 352.
26. Wang, S.; Yu, D.; Dai, L.; Chang, D. W.; Baek, J. B. *ACS Nano* **2011**, *5*, 6202.
27. Wang, S.; Yu, D.; Dai, L. *J. Am. Chem. Soc.* **2011**, *133*, 5182.
28. Hwang, J. H.; McLachlan, D. S.; Mason, T. O. *J. Electroceram.* **1999**, *3*, 7.

29. Bauerle, J. E. *J. Phys. Chem. Solids* **1969**, *30*, 2657.
30. Barsoukov, E.; Macdonald J. R. *Impedance Spectroscopy; Theory, Experiment, and Applications, 2nd ed.* Wiley Interscience Publications, Hoboken, New Jersey, **2005**.
31. Irvine, J. T. S.; Sinclair, D. C.; West, A. R. *Adv. Mater.* **1990**, *2*, 132.

Part B

Role of Oxygen Vacancies in Electrochemical Properties: A Study on Zr Doped $BaCe_{0.5}In_{0.5}O_{3-\delta}$ Perovskite Type Oxides

2B.1. Introduction

The improved electrochemical activity of cerium doped in the indium site of $Ba_2In_2O_5$ brownmillerites has been demonstrated in Chapter 2A. Interestingly, the electrochemical activity decreases when all the In atom in the lattice is replaced by Ce, which results in $BaCeO_3$ perovskite structure. The study indicated that, the presence of not only catalytically active redox centre (cerium in the present case) but also the randomly distributed oxygen vacancies in the lattice contributes towards the enhanced activity. However the exact role of oxygen vacancies in the electrochemical properties was not very clear from the above studies. Hence to unambiguously prove the role of oxygen vacancies, the amount of catalytically active centre in the compound has to be kept constant and oxygen vacancies should be varied gradually. Aliovalent doping in the compound will result in the variation in oxygen vacancies [1]. However few criteria are to be followed while selecting the dopant for such studies; (i) the dopant should have a stable oxidation state throughout the reaction condition and (ii) it should be catalytically inert. Hence zirconium, which has a stable oxidation state of +4 was selected as the dopant in the present chapter.

$BaCe_{0.5}In_{0.5}O_{3-\delta}$ which exhibited considerable electrochemical properties as evident from the previous chapter was selected as the parent compound for doping. A series of compounds viz. $BaCe_{0.5}In_{(0.5-x)}Zr_xO_{3-\delta}$ was synthesized by gradually doping Zr in the In site. The oxygen vacancies along the series can be expected to decrease with increase in the Zr concentration, as In(III) is replaced by Zr(IV). Further the concentration of Ce was kept constant throughout the series to nullify the effect of catalytically active redox centre in the series. Hence the main focus of the work carried out in the present chapter is to study the role of oxygen vacancies on ORR activity at ambient condition and conductivity at higher temperatures.

2B.2. Experimental section

2B.2.1. Synthesis of $BaCe_{0.5}In_{0.5-x}Zr_xO_{3-\delta}$

$BaCe_{0.5}In_{0.5-x}Zr_xO_{3-\delta}$ series of compounds with x = 0.125, 0.25 & 0.375 was synthesized by solid state reaction method. High purity $BaCO_3$ (99.98%, Sigma-Aldrich), In_2O_3 (99.99%, Sigma-Aldrich), $Ce(CH_3CO_2)_3$ (99.9%, Sigma-Aldrich) and ZrO_2 (99%

Sigma Aldrich) were used as the starting materials. Stoichiometric amount of the reactants were weighed and ball milled at 300 rpm for 3 h in Fristsch Pulverisette 6 Planetary Mill for homogeneous mixing. The samples were then calcined at 900 ˚C for 12 h. Subsequently, they were ground in a mortar and again calcined at 1200 ˚C for 12 h at a ramp rate of 3 ˚C min^{-1} with intermediate grinding.

2B.2.2. Characterization

The structural characterization of the samples was carried out using PXRD. The details of the instruments and procedures used for PXRD are same as those described in chapter 2A in section 2A.2.2. Lattice parameters of the samples were calculated by Rietveld refinement on the PXRD pattern using GSAS-EXPGUI program [2]. The oxygen uptake of the compound was calculated using TGA as described in Section 2A.2.2 of Chapter 2A. Finally the stability of the compounds under He and 10 % O2 in He atmosphere at higher temperatures were examined using in situ high temperature PXRD as explained in section 2A.2.2 of Chapter 2A.

2B.2.3. Electrochemical analysis

The electrochemical properties of the catalyst were measured by Cyclic Voltammetry (CV) and Rotating Disk Electrode (RDE) technique using CHI604E electrochemical analyzer (CH Instruments, Inc., USA) in a conventional three-electrode test cell with Hg/HgO and platinum wire as the reference and counter electrodes respectively at room temperature. The working electrode preparation method and the experimental procedure for CV and RDE measurements are same as mentioned in Section 2A.2.3 in Chapter 2A. The EIS spectroscopy at higher temperatures was also performed as the procedure described in Chapter 2A in Section 2A.2.3.

2B.3. Results and discussion

2B.3.1. Synthesis and structural characterization

Zirconium doped compounds viz. $BaCe_{0.5}In_{0.5-x}Zr_xO_{3-\delta}$ (x = 0.125, 0.25 & 0.375) was synthesised by solid state method. The phase purity of all the synthesized compounds was analyzed by PXRD. Figure 2B.1 represents the PXRD pattern of all the samples.

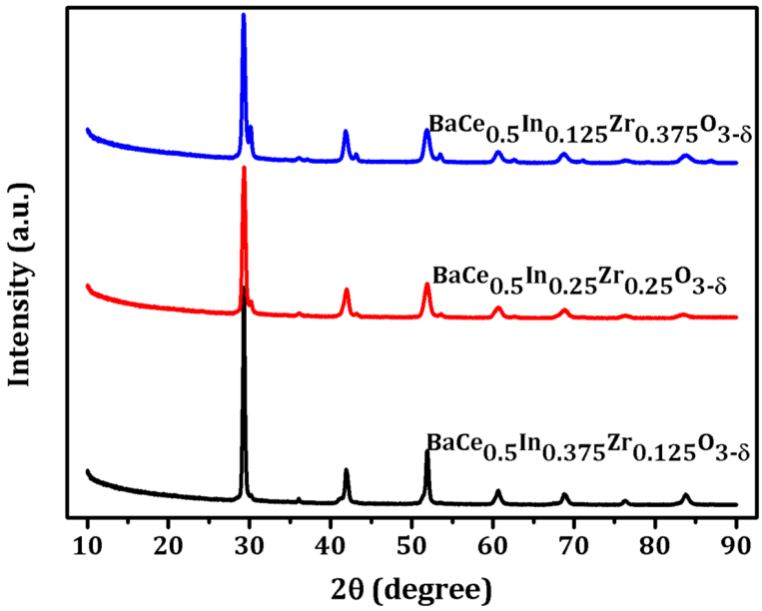

Figure 2B.1. PXRD pattern of $BaCe_{0.5}In_{0.5-x}Zr_xO_{3-\delta}$ (x = 0.125, 0.25 & 0.375).

The PXRD pattern of Zr doped $BaCe_{0.5}In_{0.5}O_{3-\delta}$ matched with that of $Ba_{0.87}K_{0.13}BiO_3$ perovskite (JCPDS file No. 01-078-2084) which crystallizes in cubic Pm-3m space group. Impurity phase corresponding to $BaIn_{0.5}Zr_{0.5}O_{3-\delta}$ (ICSD No. 159187) was observed in all the samples. Additionally, peaks corresponding to $BaCeO_3$ (JCPDS file No. 75-431) were observed in $BaCe_{0.5}In_{0.375}Zr_{0.125}O_{3-\delta}$. Structural parameters of the compounds were determined by Rietveld refinement of the PXRD pattern using GSAS EXPUGI software. Figure 2B.2 (a-c) represents the Rietveld refinement plot of $BaCe_{0.5}In_{0.5-x}Zr_xO_{3-\delta}$ (x = 0.125, 0.25 & 0.375).

Rietveld refinement on the PXRD data of Zr doped $BaCe_{0.5}In_{0.5}O_{3-\delta}$ was performed using the structural parameters of $Ba_{0.87}K_{0.13}BiO_3$ perovskite [3]. The A site occupancies in all the compounds were completely assigned to Ba and the B site occupancies were assigned as per the stoichiometric compositions. The Rietveld refinement of $BaCe_{0.5}In_{0.375}Zr_{0.125}O_{3-\delta}$ proceeded smoothly and the peaks fitted in cubic Pm-3m space group. However additional peaks corresponding to $BaIn_{0.5}Zr_{0.5}O_{3-\delta}$ and $BaCeO_3$ were present in the PXRD pattern and hence phases corresponding to these systems were also incorporated during the refinement to get better fit. The impurity phases of $BaIn_{0.5}Zr_{0.5}O_{3-\delta}$ and $BaCeO_3$ was found to be 1.8 % and 5.4 % respectively.

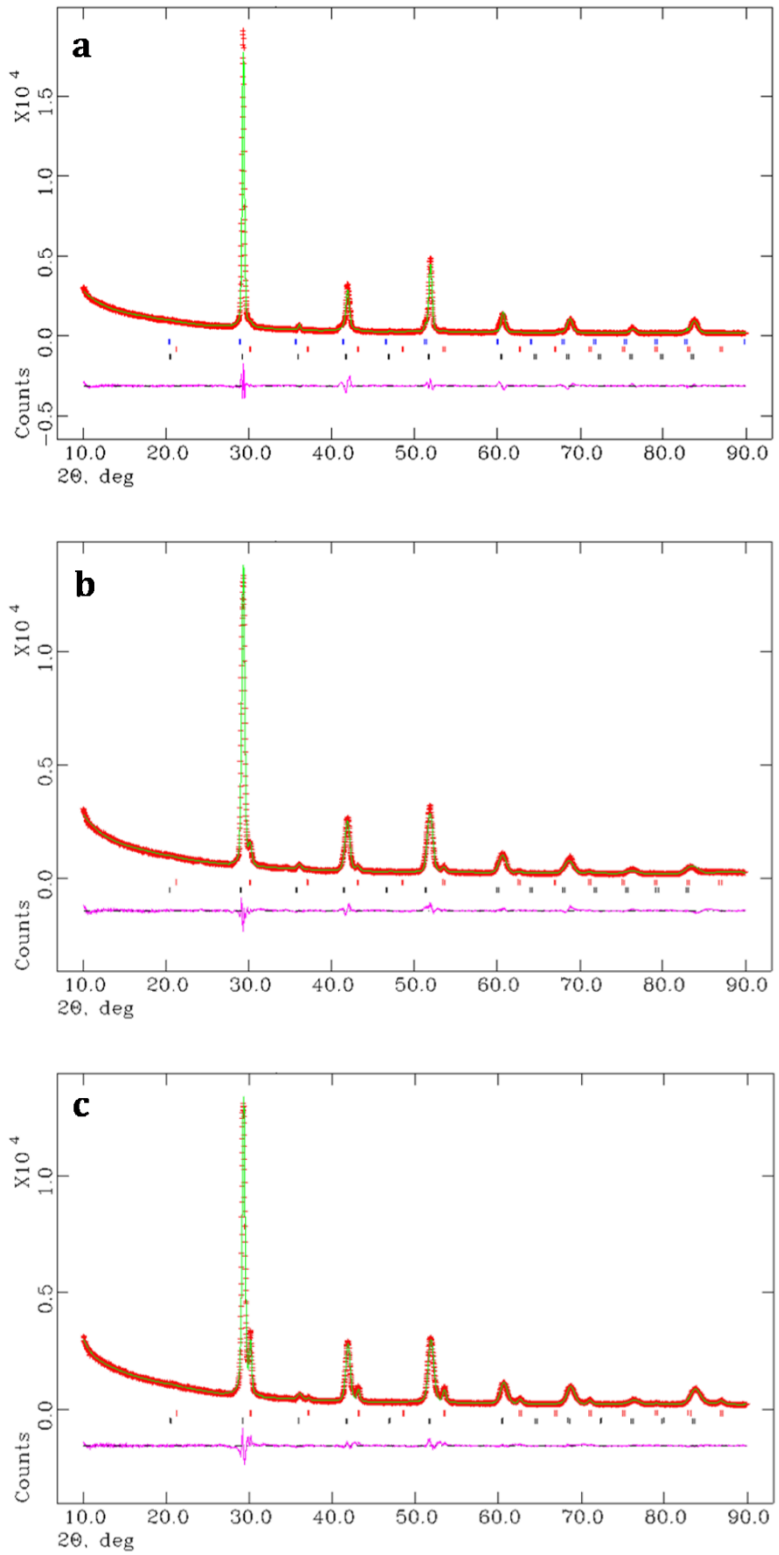

Figure 2B.2. Rietveld refinement of the PXRD pattern of **(a)** $BaCe_{0.5}In_{0.375}Zr_{0.125}O_{3-\delta}$, **(b)** $BaCe_{0.5}In_{0.25}Zr_{0.25}O_{3-\delta}$ and **(c)** $BaCe_{0.5}In_{0.125}Zr_{0.375}O_{3-\delta}$. Red pattern represents experimental data, green pattern is the Rietveld fit and pink pattern represents difference plot. Black vertical lines in all figures represent the expected positions for the main phase. The impurity phases of $BaInZrO_3$ are represented by red line and that of $BaCeO_3$ in **(a)** is represented by blue line.

Further refinement of higher concentrations of Zr in $BaCe_{0.5}In_{0.5-x}Zr_xO_{3-\delta}$ samples fitted to the same cubic Pm-3m space group. But impurity phase corresponding to $BaIn_{0.5}Zr_{0.5}O_{3-\delta}$ was present in both the systems; the quantitatively calculated amount of impurity phase was 6.7% and 10.9% for $BaCe_{0.5}In_{0.25}Zr_{0.25}O_{3-\delta}$ and $BaCe_{0.5}In_{0.125}Zr_{0.375}O_{3-\delta}$ respectively. The final stoichiometric composition of all the samples calculated (detailed calculation given in Appendix 2) after considering the amount of impurity and the occupancy of oxygen with increasing amount of Zr dopant in $BaCe_{0.5}In_{0.5-x}Zr_xO_{3-\delta}$ (x = 0.125, 0.25 & 0.375) was $BaCe_{0.48}In_{0.39}Zr_{0.13}O_{2.69}$, $BaCe_{0.54}In_{0.23}Zr_{0.23}O_{2.88}$ and $BaCe_{0.61}In_{0.086}Zr_{0.392}O_{2.9}$. For sake of clarity, the samples are named based on their intended composition ($BaCe_{0.5}In_{0.5-x}Zr_xO_{3-\delta}$ (x = 0.125, 0.25 & 0.375)) further in this chapter.

The detailed structural parameters obtained after the Rietveld refinement of $BaCe_{0.5}In_{(0.5-x)}Zr_xO_{3-\delta}$ (x = 0.125, 0.25, and 0.375) are tabulated in Table 1. The polyhedral representation of the compounds obtained from the refinement parameters is shown in Figure 2B.3. As evident from the figure the compounds have three dimensional arrays of octahedra in which oxygen vacancies are randomly distributed in the lattice.

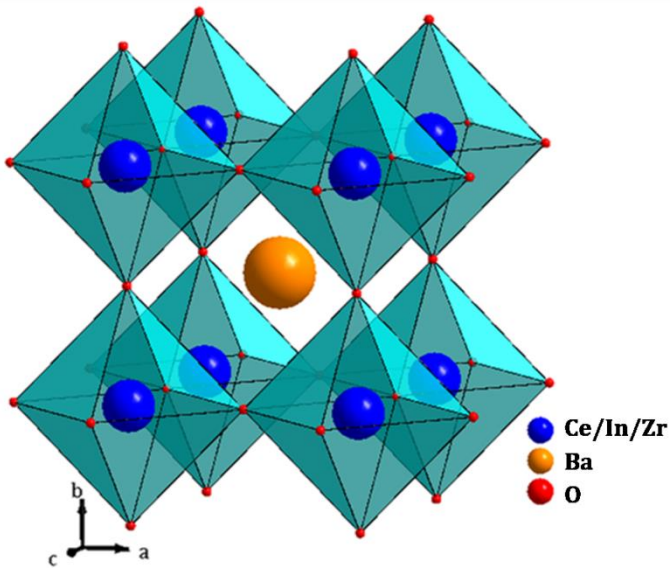

Figure 2B.3. Polyhedral representation of the structures obtained after the Rietveld refinement of PXRD patterns of Zr doped $BaCe_{0.5}In_{0.5-x}Zr_xO_{3-\delta}$.

Table 2B.1. Structural parameters obtained from the Rietveld refinement of Zr doped $BaCe_{0.5}In_{0.5}O_{3-\delta}$.

		$BaCe_{0.5}In_{0.375}Zr_{0.125}O_{3-\delta}$[a]	$BaCe_{0.5}In_{0.25}Zr_{0.25}O_{3-\delta}$[b]	$BaCe_{0.5}In_{0.125}Zr_{0.375}O_{3-\delta}$[c]
χ^2		3.993	2.818	2.643
wRp(%)		7.72	6.42	6.03
Rp (%)		5.18	4.62	4.30
Space group		Pm-3m	Pm-3m	Pm-3m
a (Å)		4.33293(3)	4.35676(4)	4.33180(4)
O	x	0.5	0	0
	y	0	0	0
	z	0	0.5313	0.5167
Occup		0.898(12)	0.961(12)	0.966(17)
$BaIn_{0.5}Zr_{0.5}O_{3-\delta}$ (wt %)		1.8	6.7	10.9
$BaCeO_3$ (wt %)		5.4		

[a]$BaCe_{0.5}In_{0.375}Zr_{0.125}O_{3-\delta}$: Ba(0.5,0.5,0.5), Ce(0,0,0), In(0,0,0), Zr(0,0,0); [b]$BaCe_{0.5}In_{0.25}Zr_{0.25}O_{3-\delta}$: Ba(0.5,0.5,0.5), Ce(0,0,0), In(0,0,0), Zr(0,0,0); [c]$BaCe_{0.5}In_{0.125}Zr_{0.375}O_{3-\delta}$: Ba(0.5,0.5,0.5), Ce(0,0,0), In(0,0,0), Zr(0,0,0)

It can be observed from the Rietveld refinement results that the effective occupancy of O atom increases gradually with increase in Zr concentration. The value of oxygen vacancies (δ) calculated from the final stoichiometric chemical formula for the series of compounds with increase in the Zr concentration are 0.31, 0.12 and 0.1 respectively. This decrease in the oxygen vacancies along the series is expected since In(III) is replaced by Zr(IV) in the lattice and in order to attain the charge balance in the compound, higher amount of oxygen is incorporated in the lattice in the anionic site.

Further it is evident that with increase in the Zr concentration, initially the cell parameter increases and then decreases as shown in Figure 2B.4. Ideally one would expect the lattice parameter to decrease with increase in the Zr concentration as the crystal radius of Zr (0.86 Å) is smaller than that of In (0.94 Å) in octahedral coordination [4]. However the discrepancy in the lattice parameter along the series can be explained by considering the stoichiometric formula obtained after the Rietveld refinement of the PXRD data. The first member of the series has impurity phases of $BaCeO_3$ (5.4 %) and $BaIn_{0.5}Zr_{0.5}O_{3-\delta}$ (1.8 %) which causes the expulsion of larger Ce atom (crystal radii of Ce in octahedral coordination is 1.15 Å) giving rise to a final composition of

$BaCe_{0.48}In_{0.39}Zr_{0.13}O_{2.69}$. This lowering in the total concentration of Ce from the ideal case causes the decrease in the lattice parameter. Further increasing the concentration of Zr dopant causes an increase in the lattice parameter along the series which can be attributed to the increased amount of Ce and a small deviation from the expected composition of this sample. But in the final compound, although the net amount of Ce atom increases, the lattice parameter decreases. This may be owing to the fact that there is a considerable increase in the Zr atom which has a smaller crystal radius than In. Similar effect was also observed in the cell volume along the series as evident from Figure 2B.4

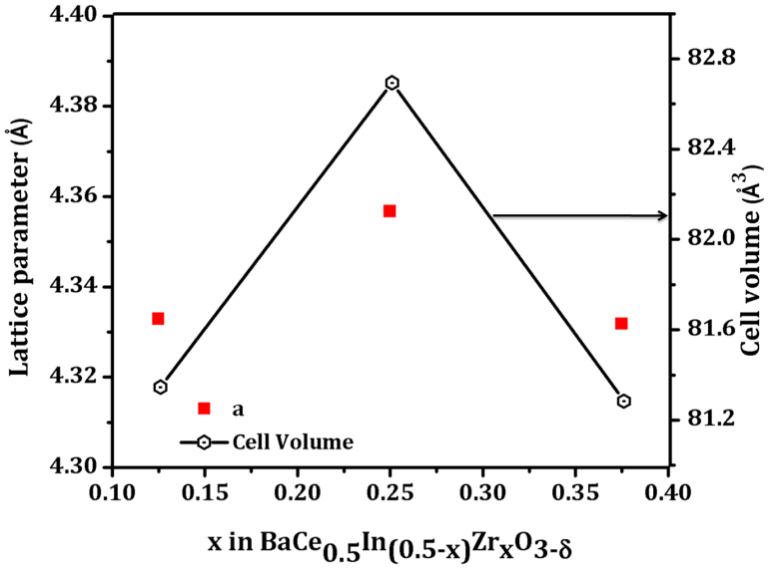

Figure 2B.4. Cell length and volume of $BaCe_{0.5}In_{0.5-x}Zr_xO_{3-\delta}$ as a function of substitution of x.

The oxygen uptake of $BaCe_{0.5}In_{0.5-x}Zr_xO_{3-\delta}$ series was calculated by thermogravimetric analysis under 10% O_2 in He up to 800 °C. The oxygen uptake was calculated from the amount of weight gained. The detailed calculation is given in Appendix 2. Figure 2B.5 represents the TGA profile of all the Zr doped samples under 10% O_2 in He. A steep increase in the oxygen uptake for all the samples were observed till 250 °C. However a fall in the profile occurs after this temperature as observed in the Ce doped $Ba_2In_2O_5$ samples in Chapter 2A. This weight loss can be attributed to the loss of water of hydration present in these systems. After this point there is a gradual increase in the oxygen uptake for the first member of the series which has the highest oxygen vacancies. However, no considerable increase in the oxygen uptake is observed

for the other two compounds which have lower oxygen vacancies as evident from the refinement data.

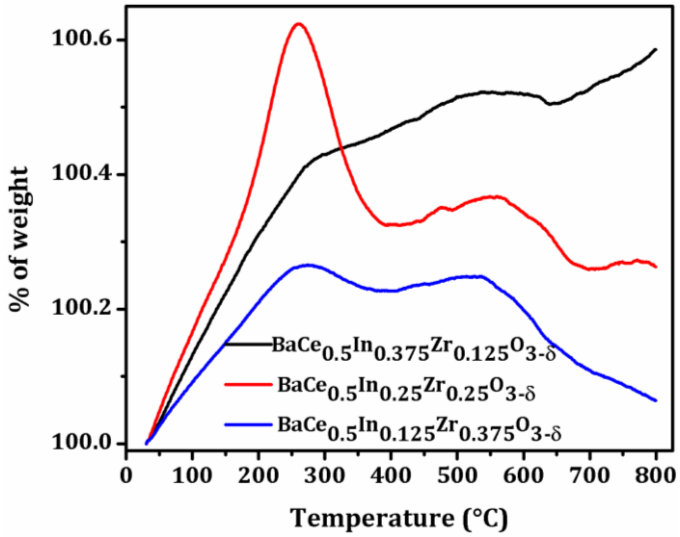

Figure 2B.5. Thermogravimetric profiles of $BaCe_{0.5}In_{0.5-x}Zr_xO_{3-\delta}$ under 10% O_2 in He.

The oxygen uptake calculated from the TGA profile is tabulated in Table 2B.2. Oxygen uptake gradually decreases with increase in the Zr concentration; this can be attributed to the presence of Zr (IV) oxidation state in place of In (III) in the compound. With increase in the Zr concentration, oxygen vacancies decreases which in fact leads to the decrease in oxygen uptake. This observation is in concordance with the oxygen vacancies obtained from the Rietveld refinement of the PXRD data. The relation between oxygen vacancies and oxygen uptake are widely studied in literature and is also explained in the section 2A.3.1 in Chapter 2A [5, 6].

Table 2B.2. Oxygen uptake of $BaCe_{0.5}In_{0.5-x}Zr_xO_{3-\delta}$ series calculated from TGA.

Compound	Oxygen uptake (mmol g^{-1})
$BaCe_{0.5}In_{0.375}Zr_{0.125}O_{3-\delta}$	0.36
$BaCe_{0.5}In_{0.25}Zr_{0.25}O_{3-\delta}$	0.17
$BaCe_{0.5}In_{0.125}Zr_{0.375}O_{3-\delta}$	0.05

Further, in order to study the stability of all the samples under different atmosphere at variable temperature, in situ high temperature PXRD experiments were performed. Figure 2B.6 represents the PXRD pattern of all the compounds at 30 °C, 100

°C, 200 °C, 300 °C, 400 °C, 500 °C, 600 °C and 700 °C under He and 10% O_2 in He atmosphere.

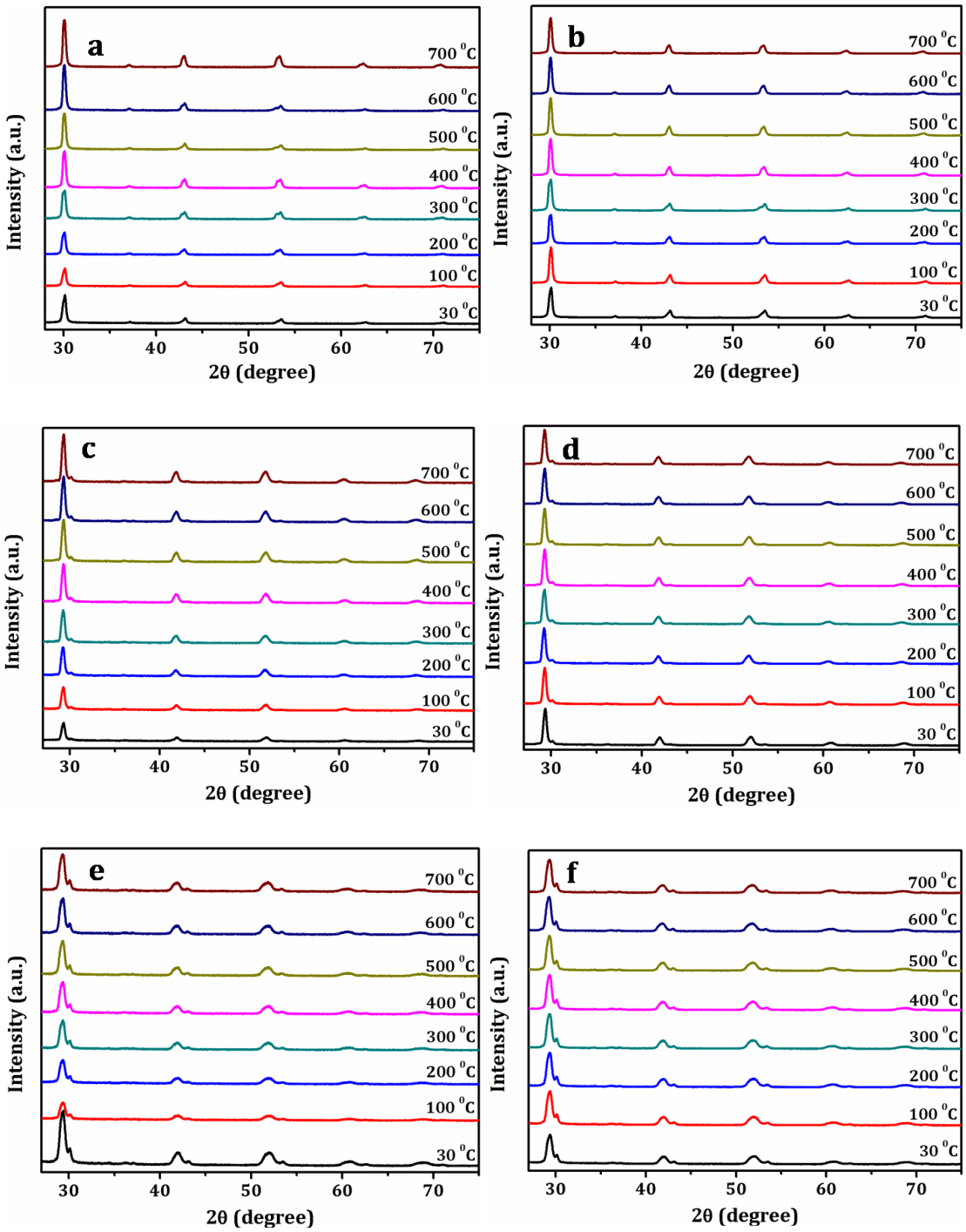

Figure 2B.6. High temperature PXRD patterns of $BaCe_{0.5}In_{0.375}Zr_{0.125}O_{3-\delta}$ **(a & b),** $BaCe_{0.5}In_{0.25}Zr_{0.25}O_{3-\delta}$ **(c & d)** and $BaCe_{0.5}In_{0.125}Zr_{0.375}O_{3-\delta}$ **(e & f)**. PXRD patterns in **a**, **c** & **e** are obtained under inert atmosphere (He) and **b**, **d** & **f** are obtained under oxidizing atmosphere (10% O_2 in He).

The PXRD pattern of the samples were initially recorded at various temperatures under He atmosphere and then cooled to 30 °C, the gas flow was then switched to 10% O_2 in He and PXRD at variable temperature was obtained. All the samples were stable under these conditions. No structural changes were observed in any of the samples till 700 °C under both the atmosphere. These can be understood by the fact that unlike in the parent compound viz. $BaIn_{0.5}Ce_{0.5}O_{3-\delta}$, where the compound exists in tetragonal structure at room temperature and transforms to higher symmetric cubic structure at higher temperature with random distribution of oxygen vacancies in the lattice, $BaCe_{0.5}In_{0.5-x}Zr_xO_{3-\delta}$ systems already exists in cubic phase with oxygen vacancies randomly distributed in the lattice.

2B.3.2. Electrochemical characterization

Detailed electrochemical studies of these compounds were carried out by CV and RDE method under alkaline medium at room temperature and EIS technique at higher temperatures to investigate the role of oxygen vacancies in the electrochemical behaviour.

2B.3.2.1. ORR activity in alkaline medium

The ORR activity of these compounds under alkaline conditions was carried out using CV and RDE methods. For this, slurry made by the mixture of the sample and Vulcan XC-72 carbon was coated on glassy carbon working electrode.

Cyclic voltammograms of the samples under N_2 and O_2 saturated solution at a sweep rate of 50 mV s^{-1} is shown in Figure 2B.7 (a-c). A distinct reduction peak was observed in the CV profile recorded after saturating the electrolyte with O_2. An increase in the reduction current after O_2 saturation indicates the ORR activity of the samples.

A detailed investigation on the ORR activity of these samples was performed by RDE method. Figure 2B.8 represents the LSV's of $BaCe_{0.5}In_{0.5-x}Zr_xO_{3-\delta}$ recorded at an electrode rotating speed of 1600 rpm in O_2 saturated 0.1 M KOH solution. The onset potential of $BaCe_{0.5}In_{0.375}Zr_{0.125}O_{3-\delta}$ and $BaCe_{0.5}In_{0.25}Zr_{0.25}O_{3-\delta}$ was around -0.09 V vs. Hg/HgO which is around 0.02 V more positive than the end member of the series viz., $BaCe_{0.5}In_{0.125}Zr_{0.375}O_{3-\delta}$.

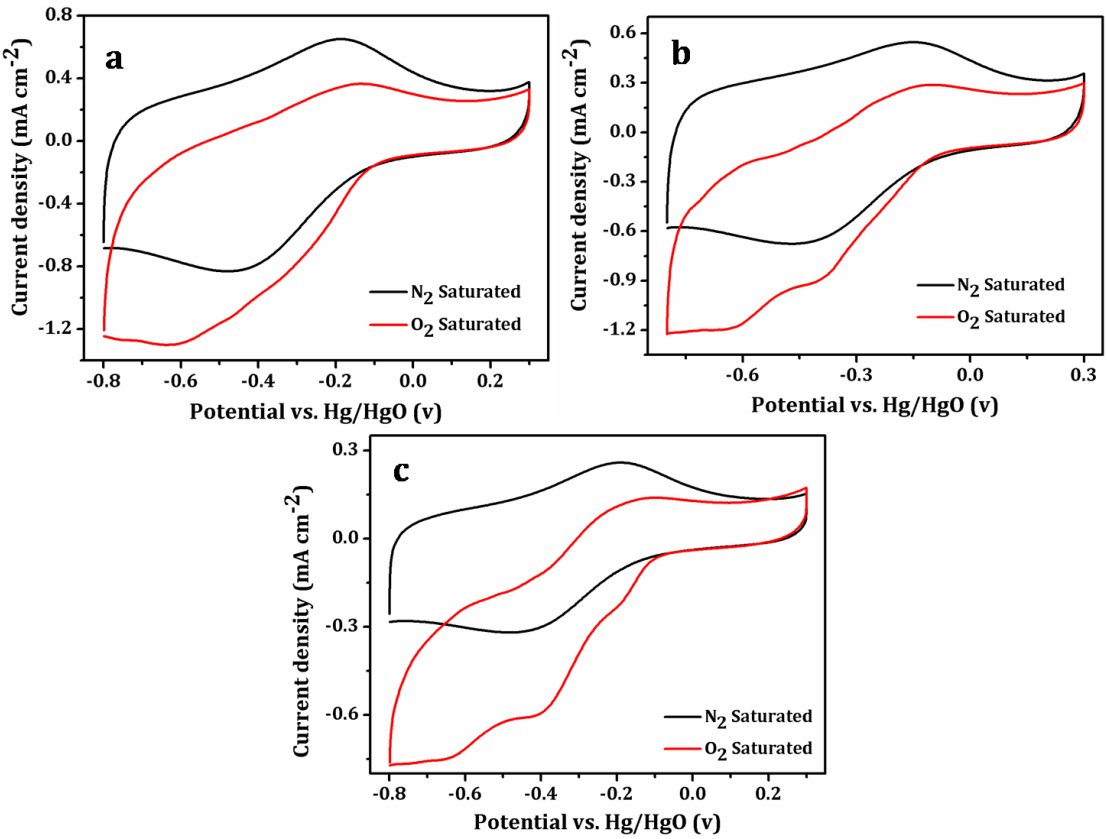

Figure 2B.7. Cyclic voltammograms of **(a)** $BaCe_{0.5}In_{0.375}Zr_{0.125}O_{3-\delta}$, **(b)** $BaCe_{0.5}In_{0.25}Zr_{0.25}O_{3-\delta}$ and **(c)** $BaCe_{0.5}In_{0.125}Zr_{0.375}O_{3-\delta}$ in N_2 and O_2 saturated 0.1 M KOH at a sweep rate of 50 mV s^{-1} using Hg/HgO and Pt wire as reference and counter electrode respectively.

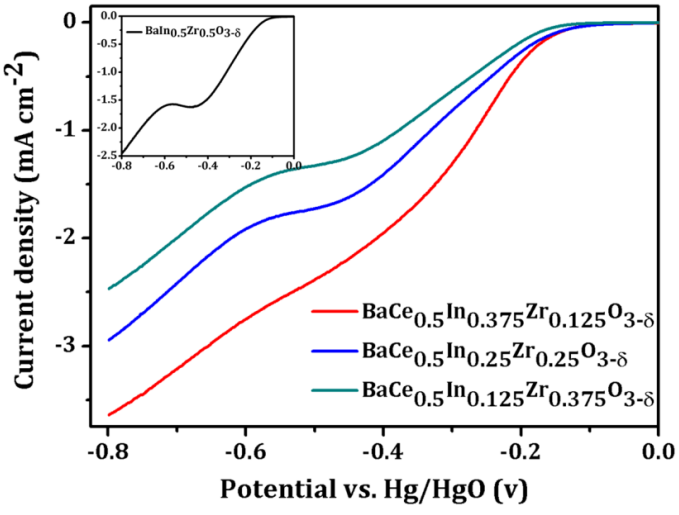

Figure 2B.8. LSVs obtained at an electrode rotating speed of 1600 rpm with a rotating disk electrode for the ORR on $BaCe_{0.5}In_{0.5-x}Zr_xO_{3-\delta}$ series of samples. Inset represents the LSV of $BaIn_{0.5}Zr_{0.5}O_{3-\delta}$ The experiments were performed in O_2 saturated 0.1 M KOH at a sweep rate of 5 mV s^{-1} using Hg/HgO and Pt wire as reference and counter electrode respectively.

Apart from this, the geometrical limiting current density also decreases with increase in Zr concentration indicating that the presence of more Zr site in the lattice does not facilitate ORR activity. Also it is worth to observe that the ORR activity increases with increase in oxygen vacancies. The parent compound, $BaCe_{0.5}In_{0.5}O_{3-\delta}$, exhibited much better onset potential (~ -0.06 V vs. Hg/HgO) and limiting current density (-4.25 mA cm^{-2} at -0.8 V vs Hg/HgO) as evident from Figure 2A.10 in Chapter 2A. Similar experiments were performed on $BaIn_{0.5}Zr_{0.5}O_{3-\delta}$ (inset in Figure 2B.8) and it was observed that the ORR activity was poor when compared to other compounds; they exhibited a 2 electron pathway which is not desirable for ORR. The decrease in the ORR activity of Zr doped samples can be attributed to the lesser number of catalytically active redox species in the lattice and a decrease in the total oxygen vacancies.

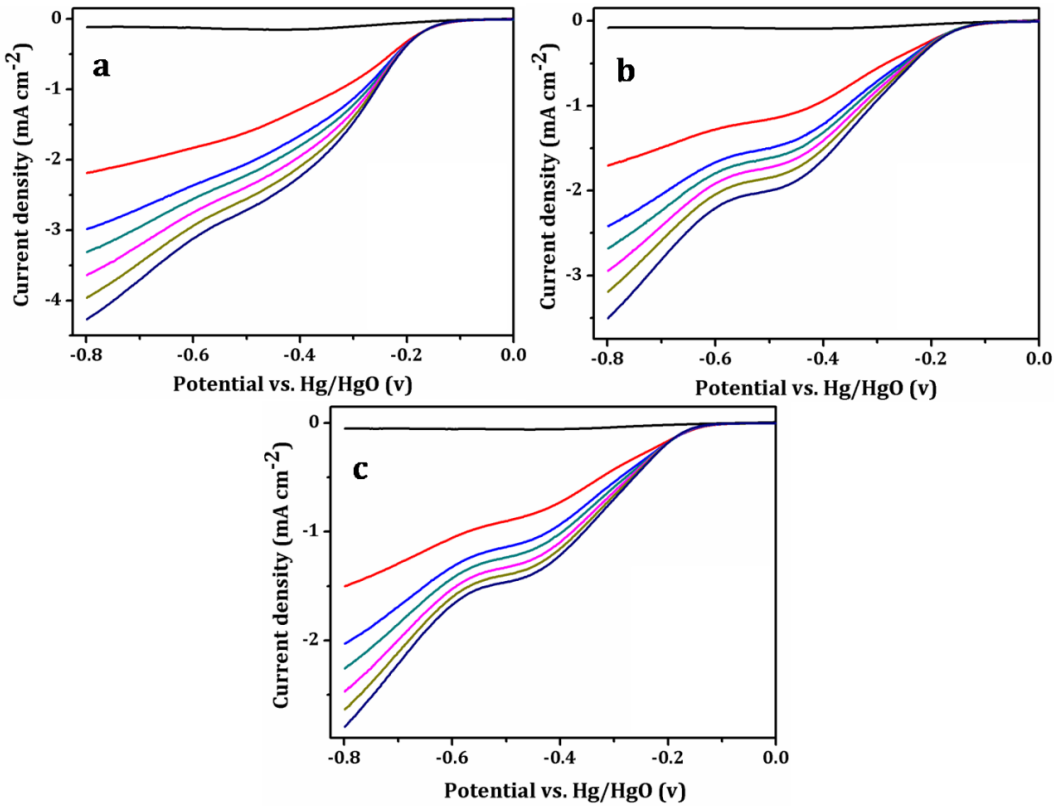

Figure 2B.9. LSVs at different electrode rotation rates (black: blank, red: 400 rpm, blue: 900 rpm, green: 1200 rpm, pink: 1600 rpm, dark yellow: 2000 rpm and navy: 2500 rpm) for ORR **(a)** $BaCe_{0.5}In_{0.375}Zr_{0.125}O_{3-\delta}$, **(b)** $BaCe_{0.5}In_{0.25}Zr_{0.25}O_{3-\delta}$ and **(c)** $BaCe_{0.5}In_{0.125}Zr_{0.375}O_{3-\delta}$. in O_2 saturated 0.1 M KOH at a sweep rate of 5 mV s^{-1} using Hg/HgO and Pt wire as reference and counter electrode respectively.

LSVs of all the compounds at various electrode rotation rates in O_2 saturated 0.1 M KOH solution is shown in figure 2B.9 (a-c). It is evident from the figure that the

limiting current density increases with the increase in the rate of rotation of the working electrode, as expected due to the enhanced rate of mass transport at higher electrode rotation [7]. A close analysis of the LSV profiles of the different systems reveals that at any constant rotation rate, the limiting current density decreases with increase in the Zr concentration in $BaCe_{0.5}In_{0.5-x}Zr_xO_{3-\delta}$. This indicates that presence of a relatively inert metal such as Zr in the lattice does not help in the electrochemical activity and also the decrease in the oxygen vacancies caused due to the doping of tetravalent ion in the place of trivalent ion in the lattice, brings down the ORR activity of the sample.

The kinetic parameters such as electron transfer number, kinetic current density etc., of samples were determined from K-L equation [8], as given in chapter 2A.

$$\frac{1}{j} = \frac{1}{nFkC_{O_2}} + \frac{1}{0.62nFC_{O_2}D_{O_2}^{2/3}\upsilon^{-1/6}\omega^{1/2}}$$

where, 'j' is the disk electrode current density, 'n' (mol^{-1}) is the number of electrons exchanged per O_2 molecule, 'F' is the Faraday constant (96500 C mol^{-1}), 'k' is the reaction rate constant, 'C_{O2}' is the bulk oxygen concentration (1.2×10^{-6} mol L^{-1}) , 'D_{O2}' is the diffusion coefficient of molecular oxygen in 0.1 M KOH solution (1.9×10^{-5} cm^2 s^{-1}), 'ν' is the kinematic viscosity of the electrolyte (0.01 cm^2 s^{-1}) and 'ω' is the electrode rotation speed in radians per second (= 2πf = 2π rpm/60).

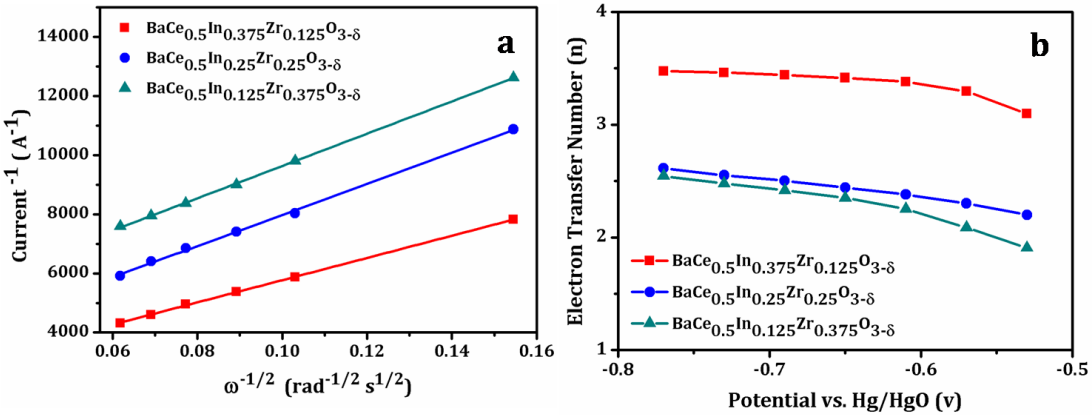

Figure 2B.10. (a) K-L plot of ORR on $BaCe_{0.5}In_{0.5-x}Zr_xO_{3-\delta}$ series at a constant potential of -0.65 V and **(b)** The dependence of the electron transfer number of $BaCe_{0.5}In_{0.5-x}Zr_xO_{3-\delta}$ series on various applied potential; in O_2 saturated 0.1 M KOH at a sweep rate of 5 mV s^{-1} using Hg/HgO and Pt wire as reference and counter electrode respectively.

A plot of the inverse of current (i^{-1}) as a function of inverse of the square root of the rotation rate ($\omega^{-1/2}$) is known as K-L plot. Figure 2B.10 (a) represents the K-L plot of all the samples at -0.65 V. The slope of $BaCe_{0.5}In_{0.25}Zr_{0.25}O_{3-\delta}$ and $BaCe_{0.5}In_{0.125}Zr_{0.375}O_{3-\delta}$ are almost same indicating a similar ORR mechanism for these two samples. Whereas there is a small change in the slope of $BaCe_{0.5}In_{0.375}Zr_{0.125}O_{3-\delta}$ sample indicating a different ORR mechanism in this compound when compared to other two systems. In fact this was observed when the number of electrons involved in the ORR mechanism was calculated from the slope of the K-L plot at different potential. Figure 2B.10 (b) represents the dependence of the applied potential on the electron transfer number in these samples. It is evident from the figure that the number of electrons involved in the ORR for $BaCe_{0.5}In_{0.375}Zr_{0.125}O_{3-\delta}$ is ~ 3.5 indicating that reaction pathways involving both 2-electron peroxide intermediate and 4-electorn hydroxide species occur simultaneously, with 4-electron pathway predominating. On the other hand in the compounds with higher concentrations of Zr viz., $BaCe_{0.5}In_{0.25}Zr_{0.25}O_{3-\delta}$ and $BaCe_{0.5}In_{0.125}Zr_{0.375}O_{3-\delta}$ ORR proceeds mainly through a 2 electron peroxide mechanism as evident from the electron transfer number of ~2.5.

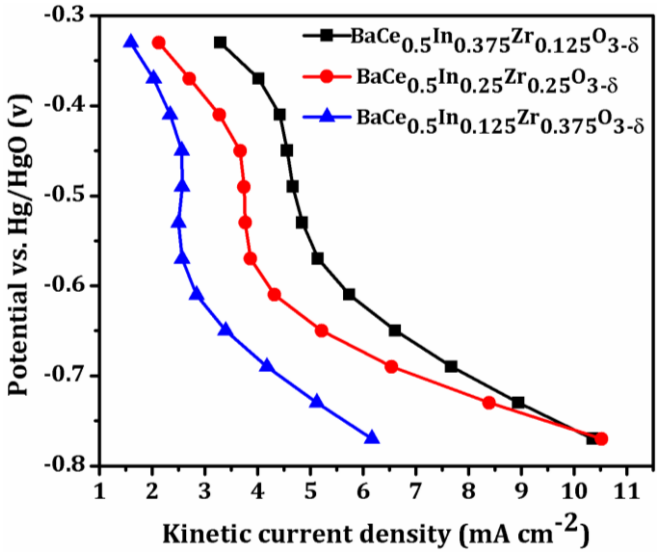

Figure 2B.11. The kinetic current density at various applied potential for $BaCe_{0.5}In_{0.5-x}Zr_xO_{3-\delta}$ series of compounds. The experiments were performed in O_2 saturated 0.1 M KOH at a sweep rate of 5 mV s^{-1} using Hg/HgO and Pt wire as reference and counter electrode respectively.

Figure 2B.11 represents the kinetic current density of all the samples. The kinetic current values (j_k) which is directly correlated to the rate constant for ORR is plotted against the corresponding potentials to analyse the current potential behaviour of the

different catalysts. It can be seen that at a particular potential the kinetic current density increases with decrease in Zr concentration.

So in brief it can be observed that the ORR activity of Zr doped in the In site of $BaCe_{0.5}In_{0.5}O_{3-\delta}$ decreases with increase in the concentration of Zr. These results can be explained on the basis of oxygen vacancies present in the compounds. It was observed from the Rietveld refinement and TGA data that with increase in the Zr concentration, oxygen vacancies in the compound decreases. The presence of oxygen vacancies in the lattice of oxide materials can facilitate the adsorption of oxygen species on the surface of the catalyst which is an important step in ORR [9]. Hence a decrease in concentration of such sites will bring down the ORR activity of the sample also as seen in the series with increase in the Zr concentration. Further on comparing Zr doped samples with the parent $BaCe_{0.5}In_{0.5}O_{3-\delta}$ catalyst, latter exhibited better ORR activity. In all these samples, although the concentration of Ce is almost same, the amount of oxygen vacancies in the lattice decreases on doping Zr(IV) in In(III) site. These observations further support the fact that oxygen vacancies play a pivotal role in ORR activity.

2B.3.2.2. High temperature EIS measurements

The high temperature EIS measurements were performed on these samples to measure the conductivity of the samples. The polycrystalline ceramic samples were considered as the Brick layer model [10] and the AC impedance scans obtained from such materials were analyzed on the basis of Bauerle model [11] as explained in Section 2A.3.2.2 in Chapter 2A. The impedance scans can be modelled using an equivalent circuit and depending upon the magnitudes of the capacitance, each RC component was assigned to different regions in the sample [12]. The high temperature ac impedance spectroscopy measurements of the series of compounds were performed on the sintered pellets as mentioned in section 2A.2.3 in Chapter 2A.

Figure 2B.12 (a) represents the experimental and fitted AC impedance plot obtained from the equivalent circuit shown in the figure for $BaCe_{0.5}In_{0.375}Zr_{0.125}O_{3-\delta}$ at different temperature indicating that the equivalent circuit used to fit the scans matches with the experimental data. Further it was observed that at a fixed temperature, with increase in Zr concentration, the impedance increased.

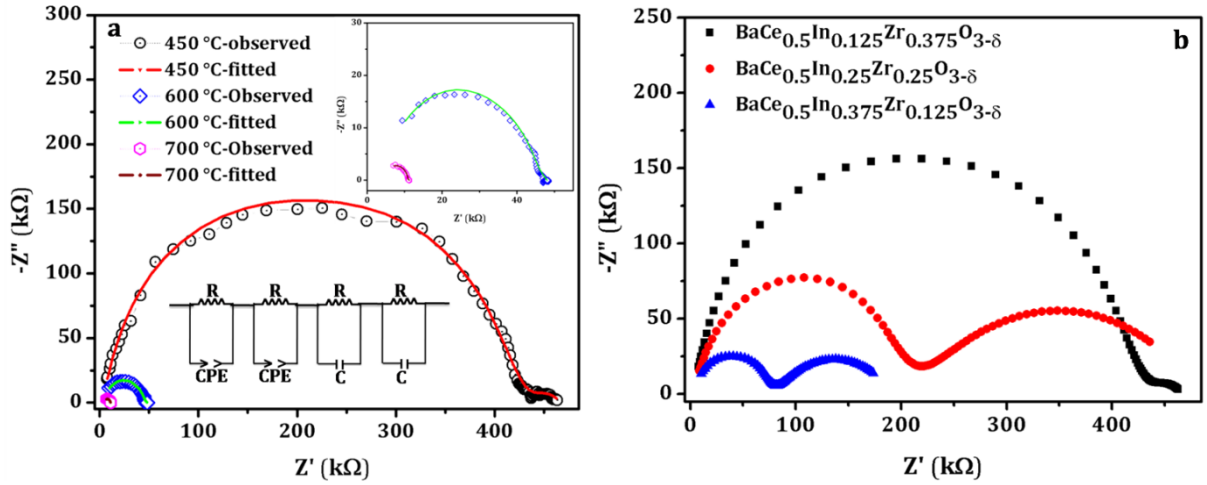

Figure 2B.12. (a) Observed and fitted ac impedance scans for $BaCe_{0.5}In_{0.375}Zr_{0.125}O_{3-\delta}$ at different temperatures with the equivalent circuit used to fit the data, inset shows the enlarged portion indicating the impedance scans at 600 °C and 700 °C ;**(b)** AC impedance scans of $BaCe_{0.5}In_{0.5-x}Zr_xO_{3-\delta}$ series at 450 °C.

Figure 2B.12 (b) represents the ac impedance scans of $BaCe_{0.5}In_{(0.5-x)}Zr_xO_{3-\delta}$ series of samples at 450 °C. The increase in the total resistance with increasing concentration of Zr can be attributed to the fact that, the presence of higher concentration of Zr in the lattice will reduce the randomly distributed oxygen vacancies in the lattice which in turn will decrease the conduction through the sample. The total resistance of the materials were calculated from the fitting parameters of the equivalent circuit and is tabulated in Table 2B.3.

Table 2B.3. Total resistance (R_b+R_{gb}) of $BaCe_{0.5}In_{0.5-x}Zr_xO_{3-\delta}$ series of compounds at variable temperature determined by EIS. Parameters were determined by fitting the experimental AC scans to the equivalent circuit.

	R_b+R_{gb} (ohm)			
	300 °C	450 °C	600 °C	700 °C
$BaCe_{0.5}In_{0.375}Zr_{0.125}O_{3-\delta}$	6.17×10^5	6.17×10^4	1.49×10^4	4.84×10^3
$BaCe_{0.5}In_{0.25}Zr_{0.25}O_{3-\delta}$	1.33×10^6	1.65×10^5	3.44×10^4	5.9×10^3
$BaCe_{0.5}In_{0.125}Zr_{0.375}O_{3-\delta}$	2.03×10^6	2.75×10^5	3.95×10^4	6.21×10^3

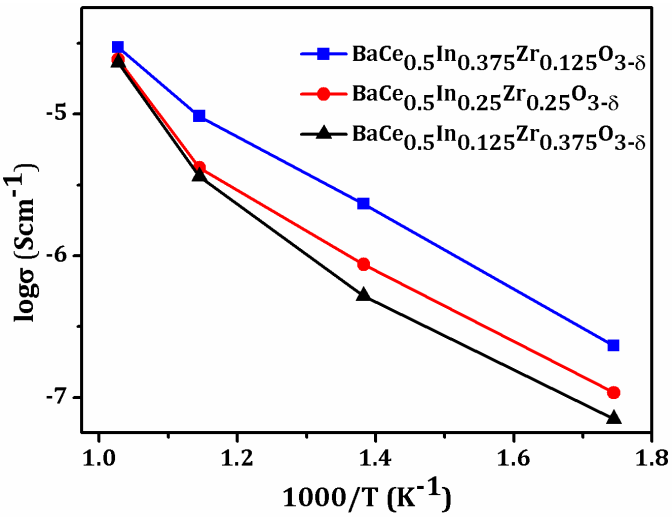

Figure 2B.13. Arrhenius plots of the total conductivities determined from the AC impedance scan of $BaCe_{0.5}In_{0.5-x}Zr_xO_{3-\delta}$ series.

The total conductivities of the samples were calculated (detailed calculation given in Appendix 2) from the impedance data. The Arrhenius graphs constructed from the measured conductivity of all the samples are shown in Figure 2B.13. There is a continuous increase in the conductivity of the sample with increase in temperature. But the conductivity decreases with decrease in the oxygen vacancies or increase in the Zr concentration. The activation energy for the conductivity in these samples was calculated from the Arrhenius plot and is tabulated in Table 2B.4. The activation energy required for the conductivity increases with increase in the Zr concentration. This can be attributed to the lower amount of oxygen vacancies present in these compounds which will in turn lead to the decrease in the anisotropic conduction in the lattice through the oxygen vacancies.

Table 2B.4. Activation energy for the conductivity through $BaCe_{0.5}In_{0.5-x}Zr_xO_{3-\delta}$ series of compounds calculated from the Arrhenius plot.

Compound	Activation energy (J mol^{-1})
$BaCe_{0.5}In_{0.375}Zr_{0.125}O_{3-\delta}$	23.8
$BaCe_{0.5}In_{0.25}Zr_{0.25}O_{3-\delta}$	25.82
$BaCe_{0.5}In_{0.125}Zr_{0.375}O_{3-\delta}$	27.84

2B.4. Conclusions

Zirconium doped in the Indium site of $BaCe_{0.5}In_{0.5}O_{3-\delta}$ brownmillerite series were synthesized by solid state method. Phase purity of the synthesised samples was determined by PXRD and the structural parameters were obtained by the Rietveld refinement of the PXRD patterns. It was observed that the synthesized samples crystallizes in cubic perovskite phase in Pm-3m space group with a general formula of $BaCe_{0.5}In_{(0.5-x)}Zr_xO_{3-\delta}$. Impure phases of $BaIn_{0.5}Zr_{0.5}O_{3-\delta}$ were observed in all the samples in addition to this, peaks corresponding to $BaCeO_3$ were observed in $BaCe_{0.5}In_{0.375}Zr_{0.125}O_{3-\delta}$. Rietveld refinement parameters revealed that the oxygen vacancies decreased with increase in the Zr concentration. The lattice parameter initially increased and then decreased as the concentration of Zr along the series increased. This is attributed to the fact that the expulsion of Ce from the lattice in the form of $BaCeO_3$ in the starting compound of the series leads to the lowering of lattice constant. TGA data also revealed that oxygen uptake decreases with increase in Zr doping indicating that the total oxygen vacancies in the compound decreases with increase in Zr concentration. All the samples were stable in both inert and 10 % O_2 in He atmosphere till 700 °C as evident from the in situ high temperature PXRD measurements. The samples were tested for ORR activity in alkaline medium. The ORR activity decreased with increase in the Zr concentration; in other words, with decrease in oxygen vacancies ORR activity also decreased. High temperature impedance also increased with increase in Zr concentration. Arrhenius plot was plotted for the conductivities of the samples calculated from the total resistance. It was observed that the conductivity of a compound increases with increase in temperature and the conductivity improves with the presence of oxygen vacancies in the lattice. Finally it was observed that samples having least oxygen vacancies exhibited higher activation energy for conduction. Hence it can be concluded form these studies that oxygen vacancies in the lattice play pivotal role in electrochemical properties of oxide materials.

2B.5. References

1. Cuesta, A.; Aranda, M. A. G.; Sanz, J.; de la Torre, A. G.; Losilla, E. R. *Dalton Trans.* **2014**, *43*, 2176.
2. Toby, B. H. *J. Appl. Crystallogr.* **2001**, *34*, 210.

3. Wignacourt, J. P.; Swinnea, J. S.; Steinfink, H.; Goodenough, J. B. *App. Phys. Lett.* **1988**, *53*, 1753.
4. Shannon, R. *Acta Crystallogr. Sect. A* **1976**, *32*, 751.
5. Suescun, L.; Dabrowski, B.; Mais, J.; Remsen, S.; Richardson, J. W.; Maxey, E. R.; Jorgensen, J. D. *Chem. Mater.* **2008**, *20*, 1636.
6. Speakman, S. A.; Richardson, J. W.; Mitchell, B. J.; Misture, S. T. *Solid State Ionics* **2002**, *149*, 247.
7. Town, J. L.; MacLaren, F.; Dewald, H. D. *J. Chem. Educ.* **1991**, *68*, 352.
8. Wang, S.; Yu, D.; Dai, L.; Chang, D. W.; Baek, J. B. *ACS Nano* **2011**, *5*, 6202.
9. Suntivich, J.; Gasteiger, H. A.; Yabuuchi, N.; Nakanishi, H.; Goodenough, J. B.; Shao-Horn, Y. *Nat. Chem.* **2011**, *3*, 546.
10. Hwang, J. H.; McLachlan, D. S.; Mason, T. O. *J. Electroceram.* **1999**, *3*, 7.
11. Bauerle, J. E. *J. Phys. Chem. Solids* **1969**, *30*, 2657.
12. Irvine, J. T. S.; Sinclair, D. C.; West, A. R. *Adv. Mater.* **1990**, *2*, 132.

Chapter 3

Cobalt Doped $Ba_2In_2O_5$ Brownmillerite: An Excellent Electrochemical Catalyst with Improved Conductivity and ORR Activity

3.1. Introduction

From chapter 2 it is evident that B site doping with catalytically active elements and oxygen vacancies in the lattice of brownmillerite play a pivotal role in both high temperature and low temperature electrochemical properties. Further in designing materials for electrochemical applications, one of the important properties that have to be taken into account is the conductivity of the compounds. Hence doping by metals which can enhance the conductivity in the lattice of the sample will further improve the electrochemical activity of the compounds. Some of the transition metal oxides have shown excellent conductivity owing to the unique nature of the outer d-electrons and narrow electronic bands because of the small overlap between the metal d and the oxygen p orbital [1]. Hence doping indium site of $Ba_2In_2O_5$ with transition metal can be envisaged to improve their low and high temperature conductivity. Cobalt was selected due to its ability to enhance conductivity and also its redox nature which will make the catalyst tolerant to local changes in the oxygen concentration [2, 3]. Moreover incorporation of cobalt in the lattice will also induce oxygen vacancy disorder in the brownmillerite lattice.

So the focus of this chapter is to synthesize cobalt doped $Ba_2In_2O_5$ compounds and their detailed structural characterisations using PXRD and XPS. Further the electrochemical properties of these materials are correlated with the structure by aid of various techniques such as CV, RDE, and high temperature EIS measurement.

3.2. Experimental section

3.2.1. Synthesis of $Ba_2In_{2-x}Co_xO_{5+\delta}$

All the samples with composition $Ba_2In_{2-x}Co_xO_{5-\delta}$ (x = 0.5, 1 & 1.5) were synthesized by solid state method. High purity $BaCO_3$ (99.98%, Sigma-Aldrich), In_2O_3 (99.99%, Sigma-Aldrich) and $CoCO_3$ (Co 43-47%, Sigma-Aldrich) were used as the starting materials. Stoichiometric amount of the starting materials were weighed and ball milled at 300 rpm for 3 h in Fristsch Pulverisette 6 Planetary Mill for homogeneous mixing. The samples were then calcined at 900 ˚C for 12 h. Subsequently, they were ground in a mortar and again calcined at 1300 ˚C for 18 h at a slow heating rate with intermediate grinding.

3.2.2. Characterization

The characterization of the synthesised samples was carried out using various physico-chemical techniques. The phase purity of all the samples was determined by PXRD. The details of the instruments and procedures used for PXRD are same as those described in section 2A.2.2 of chapter 2A. Lattice parameters of the samples were calculated by Rietveld refinement on the PXRD pattern using GSAS-EXPGUI program [4]. Oxidation state of cobalt in the samples was studied using XPS measurements carried out on a VG Micro Tech ESCA 300 instrument at a pressure of > 1 x 10^{-9} Torr with pass energy of 50 eV, with electron take off angle 60˚ and the overall resolution was ~ 0.1 eV. All binding energies were referenced to the C 1s peak (284.8 eV) arising from adventitious carbon. The specific surface area of the compounds was determined by N_2 adsorption using BET model as explained in section 2A.2.2 of chapter 2A. The oxygen uptake of the compound was calculated using TGA. The details of the instruments and procedures used for TGA experiments are same as those described in section 2A.2.2 of chapter 2A. Finally the stability of the compounds under He and 10% O_2 in He atmosphere at higher temperatures were examined using in situ high temperature PXRD as mentioned in section 2A.2.2 of chapter 2A.

3.2.3. Electrochemical analysis

The electrochemical properties of the catalyst for ORR were measured by CV and RDE assembly using a CHI604E electrochemical analyzer (CH Instruments, Inc., USA) in a conventional three-electrode test cell with Hg/HgO and platinum wire as the reference and counter electrodes respectively at room temperature. The catalyst was prepared by ball-milling (300 rpm for 90 min) a mixture of sample and Vulcan XC-72 carbon in the ratio of 4:1. Slurry of the catalyst was prepared by ultrasonically mixing 5.0 mg of the sample - carbon composite in 960 µL of isopropanol - water (3:1) solution and 40 µL of 5 wt % Nafion solution for 30 min in order to get a homogeneous suspension. For preparing the working electrode for CV and RDE measurements, glassy carbon (GC) electrode was first polished using 0.05 µm alumina and then the electrode was cleaned using Milli-Q water. 4 µL of the catalytic slurry was loaded onto the surface of the GC electrode of 3 mm diameter (0.0707 cm^2 geometrical area) using a micropipette. The slurry was allowed to dry over-night at room temperature in ethanol

atmosphere to obtain a thin homogeneous catalyst film. The final catalyst loading on the electrode surface was 283 μg cm^{-2}. An aqueous solution of 0.1 M KOH (Aldrich, ≥ 85%) was used as the electrolyte for normal CV and RDE studies. Kinetics of oxygen reduction reactions of the catalyst were studied by using RDE technique in 0.1 M KOH using a three-electrode cell assembly at a scan rate of 5 mV s^{-1} at 400, 900, 1200, 1600, 2000 and 2500 rpm at room temperature.

The electrochemical impedance spectroscopy (EIS) under variable temperature was performed using CHI604E electrochemical analyzer (CH Instruments, Inc., USA) assembled with home-built electrode setup and furnace. The detailed procedure used for the EIS measurements are same as those described in section 2A.2.3 of chapter 2A. The EIS spectrum was recorded in between 300 ˚C and 600 ˚C.

3.3. Results and Discussion

3.3.1. Synthesis and structural characterization

$Ba_2In_{2-x}Co_xO_{5-\delta}$ series of compounds with x = 0.5, 1 and 1.5 was synthesized by solid state reaction. The phase purity of the synthesized compounds was determined from PXRD. Figure 3.1 (a) represents the PXRD patterns obtained for all the synthesized compounds.

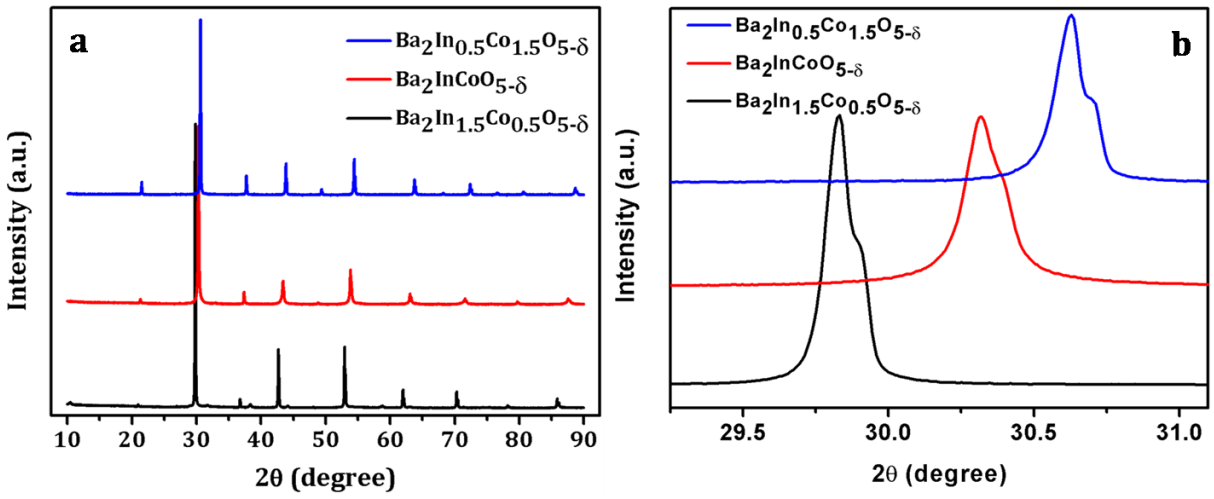

Figure 3.1. (a) PXRD pattern of $Ba_2In_{2-x}Co_xO_{5+\delta}$ (x = 0.5, 1 & 1.5) **(b)** Enlarged portion of PXRD patterns of Co doped $Ba_2In_2O_5$. The shoulder peaks are due to Kα2 radiations.

No impurity phases were observed in any of the samples. The PXRD pattern of $Ba_2In_{1.5}Co_{0.5}O_{5-\delta}$ revealed that the compound crystallizes in tetragonal system, whereas further doping in indium site of $Ba_2In_2O_5$ with cobalt leads to the formation of cubic perovskite structure. Again a closer look into the PXRD patterns of the Co doped $Ba_2In_2O_5$ reveals that, with increase in the Co concentration, there is a gradual shift in the peaks towards higher 2θ as evident from Figure 3.1 (b). This shift in the peaks indicates a decrease in the lattice parameters with increase in Co concentration, which can be attributed to the lower crystal radius of cobalt when compared with that of indium [5].

The detailed structural parameters of the compounds were determined by Rietveld refinement of the PXRD patterns using GSAS-EXPGUI software. The Rietveld refinement plot of the compounds is shown in Figure 3.2.

Rietveld refinement of the PXRD pattern of $Ba_2In_{1.5}Co_{0.5}O_{5-\delta}$ was carried out using the structural parameters of hydrated $Ba_2In_2O_5$ in P4/mmm space group (JCPDS file No. 01-089-9079) [6]. The In-Co ratio in B site was manually assigned as 75% and 25% of the occupancy respectively and the refinement with these parameters proceeded smoothly. Alternate layers in this compound are disordered as evident from the availability of two equivalent atomic positions for each O atom along *ab* plane (Figure 3.3 (a)). However, refinement of the patterns of compounds with higher concentrations of Co with the same model was not fruitful. Hence a model of cubic perovskite, $BaZrO_3$ (JCPDS file No. 01-074-1299) was selected since the PXRD pattern of this model matches with that of $Ba_2In_{2-x}Co_xO_{5-\delta}$ (x = 1 & 1.5), with small shift in 2θ values [7]. Rietveld refinement with these parameters proceeded smoothly and both the systems crystallized in cubic perovskite structure with a composition of $BaIn_{0.5}Co_{0.5}O_{3-\delta}$ for x = 1 and $BaIn_{0.25}Co_{0.75}O_{3-\delta}$ for x = 1.5. The brownmillerite structure was not retained anymore in these compounds and the oxygen vacancies were distributed randomly in the structure. These structures are similar to that of $BaInO_{2.5}$ (JCPDS file No. 01-077-1462) cubic system. The oxygen occupancies in both the systems were almost same. The structural parameters obtained after refinement of cobalt doped $Ba_2In_2O_5$ compounds are tabulated in Table 3.1 and the polyhedral representation of the structures obtained are shown in Figure 3.3.

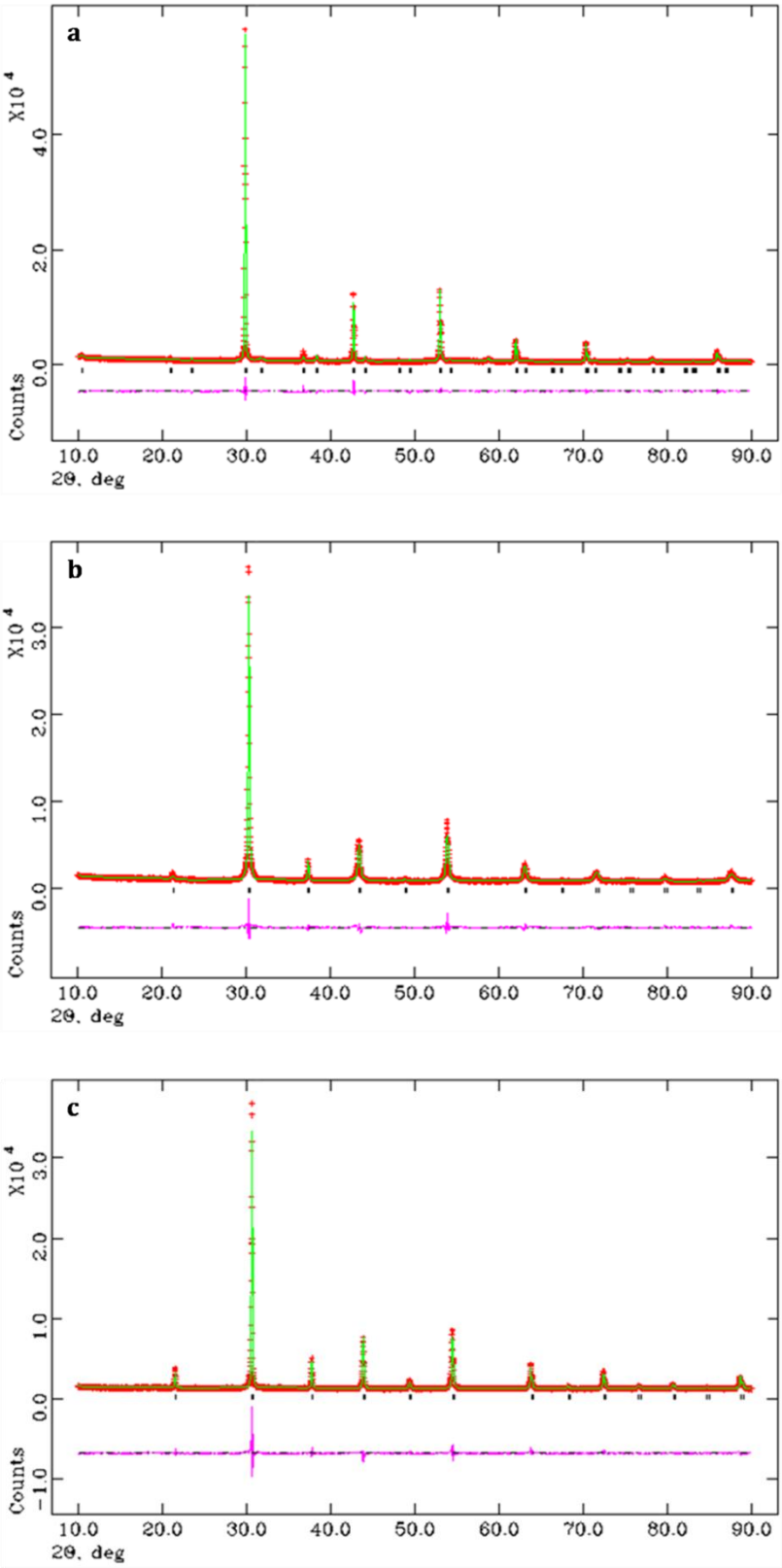

Figure 3.2. Rietveld refinement of the PXRD pattern of **(a)** $Ba_2In_{1.5}Co_{0.5}O_{5-\delta}$, **(b)** $Ba_2InCeO_{5-\delta}$ and **(c)** $Ba_2In_{0.5}Ce_{1.5}O_{5-\delta}$. Red pattern represents experimental data, green pattern is the Rietveld fit and pink pattern represents difference plot. Black vertical lines in all the figures represent the expected positions for the main phase.

Table 3.1. Structural parameters obtained from the Rietveld refinement of $Ba_2In_{2-x}Co_xO_{5+\delta}$ (x = 0.5, 1 & 1.5).

		$Ba_2In_{1.5}Co_{0.5}O_{5-\delta}$ [a]	$BaIn_{0.5}Co_{0.5}O_{3-\delta}$ [b]	$BaIn_{0.25}Co_{0.75}O_{3-\delta}$ [c]
χ^2		4.372	4.199	3.756
wRp(%)		6.79	5.92	4.92
Rp (%)		4.75	4.33	3.18
Space group		P4/mmm	Pm-3m	Pm-3m
a (Å)		4.2253(0)	4.1633(0)	4.1200(0)
b (Å)		4.2253(0)	4.1633(0)	4.1200(0)
c (Å)		8.4621(1)	4.1633(0)	4.1200(0)
O 1	x	0.5	0.5	0.5
	y	0.5	0	0
	z	0.266	0	0
Occup		0.8687	0.8176	0.8187
O 2	x	0		
	y	0.5		
	z	0.5		
Occup		0.7715		
O 3	x	0.3272		
	y	0		
	z	0		
Occup		0.4032		

[a] $Ba_2In_{1.5}Co_{0.5}O_{5-\delta}$: Ba(0,0,0.277), In1 (0.5,0.5,0.5), In2(0.5,0.5,0), Co1 (0.5,0.5,0.5), Co2(0.5,0.5,0); [b] $BaIn_{0.5}Co_{0.5}O_{3-\delta}$: Ba(0.5, 0.5,0.5), In(0,0,0), Co(0,0,0); [c] $BaIn_{0.25}Co_{0.75}O_{3-\delta}$: Ba(0.5, 0.5,0.5), In(0,0,0), Co(0,0,0)

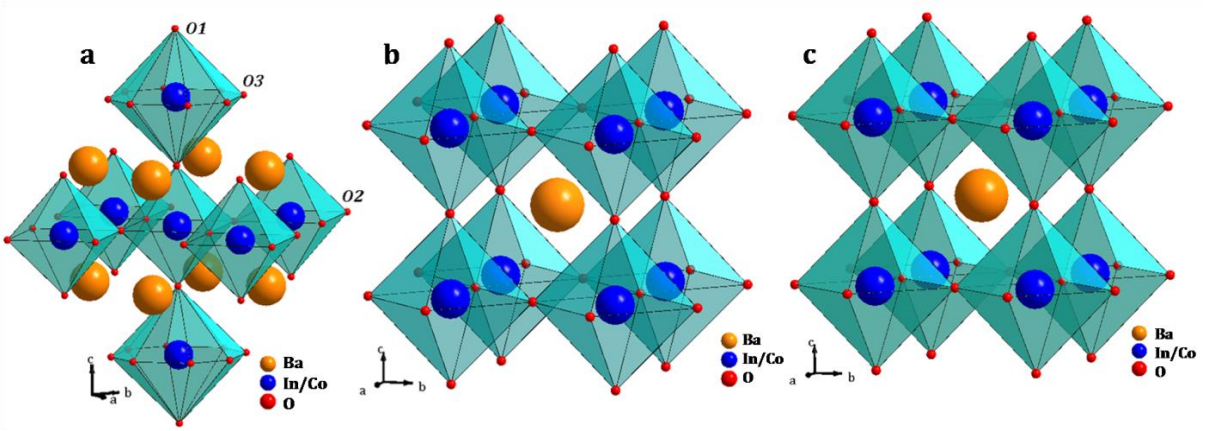

Figure 3.3. Polyhedral representation of the structures obtained after the Rietveld refinement of PXRD patterns of (a) $Ba_2In_{1.5}Co_{0.5}O_{5-\delta}$, (b) $BaIn_{0.5}Co_{0.5}O_{3-\delta}$ and (c) $BaIn_{0.25}Co_{0.75}O_{3-\delta}$.

The lattice parameters of Co doped $Ba_2In_2O_5$ with variation in the Co concentration is depicted in Figure 3.4. For comparison with other cubic systems, the pseudocubic lattice parameter of tetragonal $Ba_2In_{1.5}Co_{0.5}O_{5-\delta}$ was calculated as described in Appendix 2. It is evident from the plot that cell length and cell volume decrease with increase in Co concentration. This can be attributed to the smaller crystal radius of Co (0.72 Å and 0.68 Å for tetrahedral and octahedral coordination) when compared to In (0.76 Å and 0.94 Å for tetrahedral and octahedral coordination) [5]. This trend is in accordance with the shift observed in the peaks in PXRD pattern.

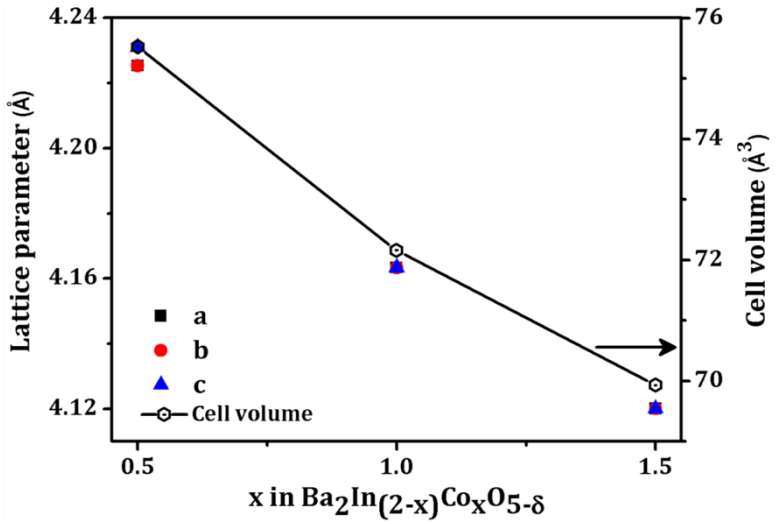

Figure 3.4. Cell length and volume of $Ba_2In_{2-x}Co_xO_{5-\delta}$ as a function of substitution of x.

In order to determine the oxidation state of the metals, XPS measurements were performed on the compounds. Figure 3.5 shows the XP spectra obtained over the range 772.5 eV to 800 eV.

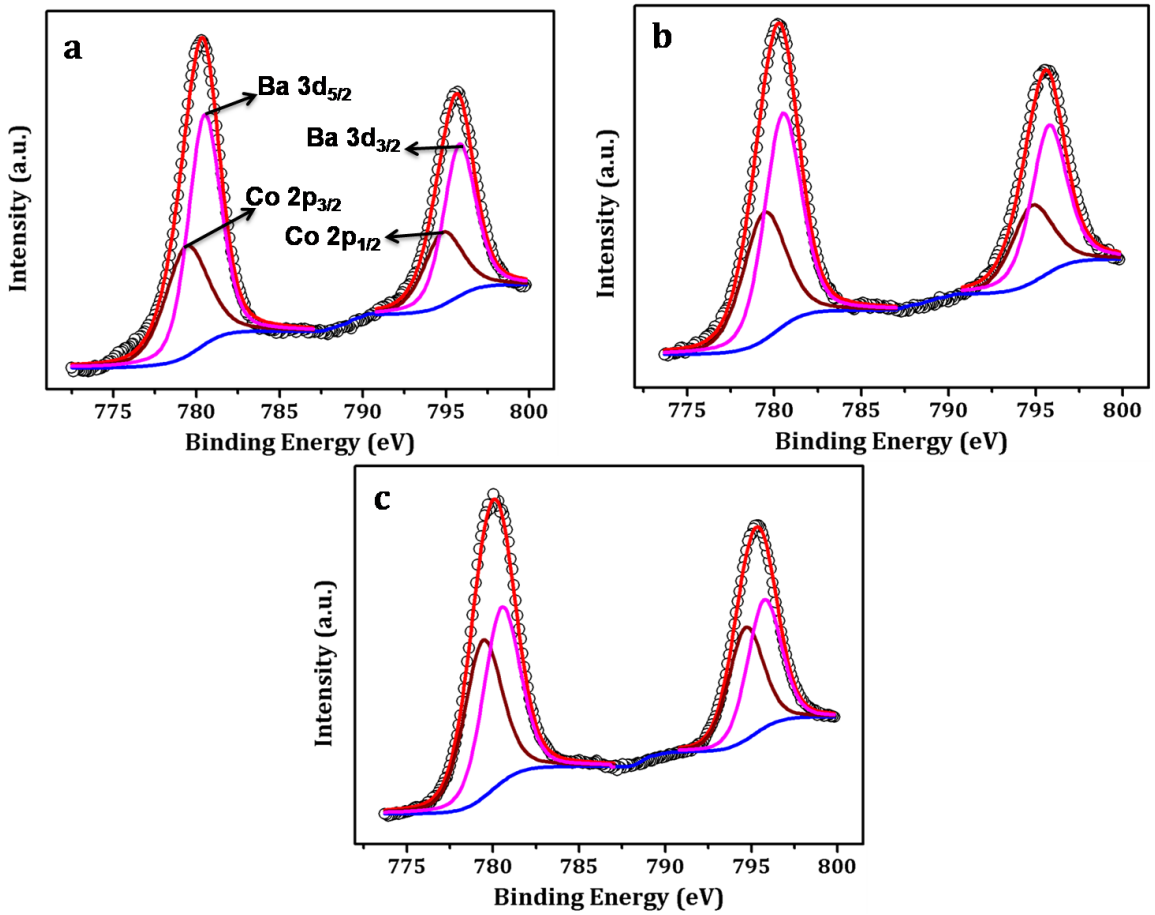

Figure 3.5. XP spectra of Ba 3d and Co 2p in **(a)** $Ba_2In_{1.5}Co_{0.5}O_{5-\delta}$, **(b)** $BaIn_{0.5}Co_{0.5}O_{3-\delta}$ and **(c)** $BaIn_{0.25}Co_{0.75}O_{3-\delta}$. Data in black circles, fitted spectra in red, deconvoluted peaks of Co and Ba in brown and pink respectively and baseline is represented in blue.

In this region the Co $2p_{3/2}$ and Ba $3d_{5/2}$ peaks overlap around 780 eV and Co $2p_{1/2}$ and Ba $3d_{3/2}$ peaks overlap around 796 eV; however, individual peaks could be extracted through deconvolution [8]. Ba^{2+} peak lies at slightly higher binding energy when compared to Co ions. The spin orbit splitting of Co $2p_{3/2}$ and Co $2p_{1/2}$ in all the compounds were found to be around 15.3 eV indicating Co in +3 oxidation state. Also the absence of satellite features around 786 eV discards the chances of Co^{2+} on the surface [7]. Hence the presence of Co in +3 oxidation state in these compounds can be confirmed from the XPS studies.

Further, the BET surface area of all the samples was measured using N_2 adsorption study. It was observed that the surface area of the samples ranged between 0.1 to 0.6 $m^2\ g^{-1}$ as expected from high temperature solid state synthesis method employed for the preparation of the samples. The BET surface area of the samples is tabulated in Table 3.2.

Table 3.2. BET surface area of Co doped $Ba_2In_2O_5$ calculated from N_2 adsorption study.

Compound	BET surface area (m^2/g)
$Ba_2In_{1.5}Co_{0.5}O_{5-\delta}$	0.182
$BaIn_{0.5}Co_{0.5}O_{3-\delta}$	0.26
$BaIn_{0.25}Co_{0.75}O_{3-\delta}$	0.526

The oxygen uptake of cobalt doped $Ba_2In_2O_5$ was calculated by thermogravimetric analysis under 10% O_2 in He up to 600 °C. The oxygen uptake was calculated from weight gain. The detailed calculation is given in Appendix 2. Figure 3.6 represents the TGA profile of all the Co doped samples under 10% O_2 in He. There is a steady increase in the oxygen uptake for all the samples till ~400 °C. However no considerable gain after this temperature was observed and the weight decreases slowly at higher temperature.

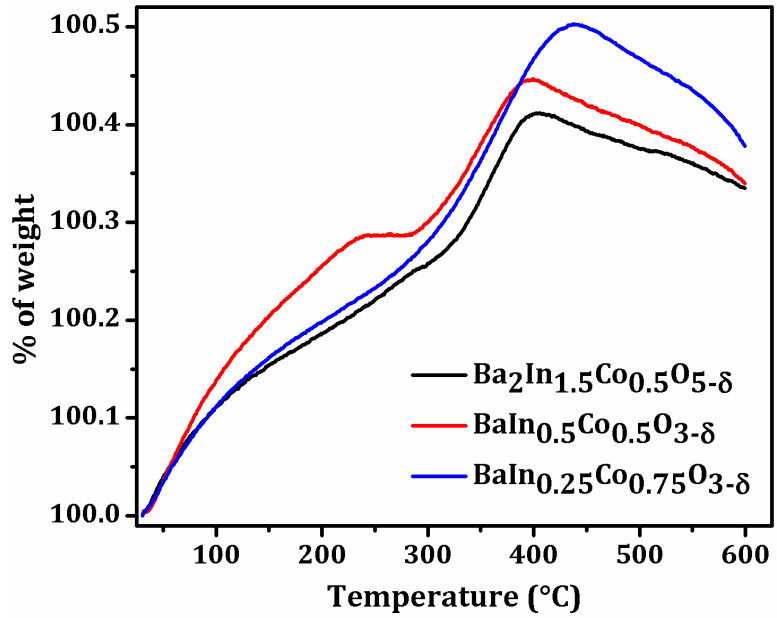

Figure 3.6. Thermogravimetric profiles under 10% O_2 in He for Co doped $Ba_2In_2O_5$.

Table 3.3. Oxygen uptake of Co doped $Ba_2In_2O_5$ calculated from TGA.

Compound	Oxygen uptake (mmol/g)
$Ba_2In_{1.5}Co_{0.5}O_{5-\delta}$	0.21
$BaIn_{0.5}Co_{0.5}O_{3-\delta}$	0.21
$BaIn_{0.25}Co_{0.75}O_{3-\delta}$	0.23

The oxygen uptake calculated from the TGA profile is tabulated in Table 3.3. Oxygen uptake of the series of compounds are almost similar; this can be due to the fact that Co (III) is substituted in place of In (III) in the compound and hence will not alter the oxygen vacancies present in the compound. Oxygen uptake is directly correlated to the oxygen vacancies in the compound [9, 10]. XPS studies have already revealed that Co is in +3 oxidation.

Further the stability of Co doped $Ba_2In_2O_5$ samples under inert and 10% O_2 in He atmosphere at variable temperature was studied by in situ high temperature PXRD experiments. Figure 3.7 represents the PXRD pattern of all the compounds at 30 °C, 100 °C, 200 °C, 300 °C, 400 °C, 500 °C and 600 °C under helium and 10% O_2 in He atmosphere.

The PXRD pattern of the samples were initially recorded at various temperatures under He atmosphere and then cooled to 30 °C, the gas flow was then switched to 10% O_2 in He and again the PXRD at variable temperature was obtained. In the case of $Ba_2In_{1.5}Co_{0.5}O_{5-\delta}$, the splitting of the peaks above 200 °C under He atmosphere was observed, which remained even after heating the same sample under 10% O_2 in He till 600 °C. Whereas in the case of other two compounds viz., $BaIn_{0.5}Co_{0.5}O_{3-\delta}$ and $BaIn_{0.25}Co_{0.75}O_{3-\delta}$ no appreciable change was observed in the PXRD patterns at variable temperatures under inert and 10% O_2 atmosphere.

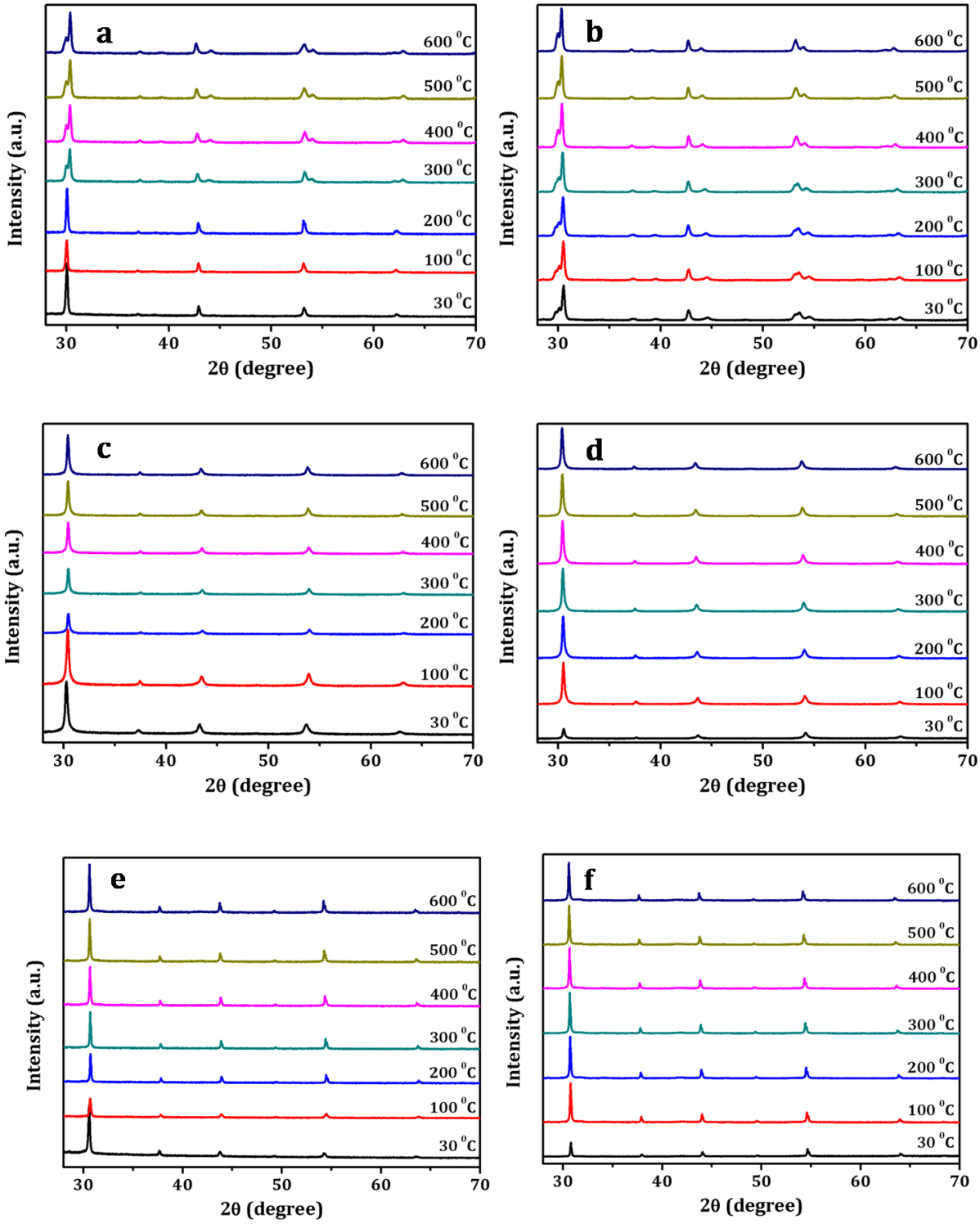

Figure 3.7. High temperature PXRD patterns of $Ba_2In_{1.5}Co_{0.5}O_{5-\delta}$ **(a & b)**, $BaIn_{0.5}Co_{0.5}O_{3-\delta}$ **(c & d)** and $BaIn_{0.25}Co_{0.75}O_{3-\delta}$ **(e & f)**. PXRD patterns in a, c & e are obtained under inert atmosphere (He) and b, d & f are obtained under oxidizing atmosphere (10% O_2 in He).

3.3.2. Electrochemical characterization

Detailed electrochemical studies on Co doped $Ba_2In_2O_5$ compounds were carried out by CV and RDE method under alkaline medium at room temperature to study the potential candidature of these materials toward ORR. EIS measurements with these compounds were carried out at higher temperatures to study their applicability in SOFC.

3.3.2.1. ORR activity in alkaline medium

The detailed electrochemical studies on the series of compounds for ORR activity was carried out in alkaline medium using CV and RDE methods. All the studies were performed in 0.1 M KOH solution under ambient temperature in a conventional three-electrode test cell with Hg/HgO and platinum wire as the reference and counter electrodes respectively.

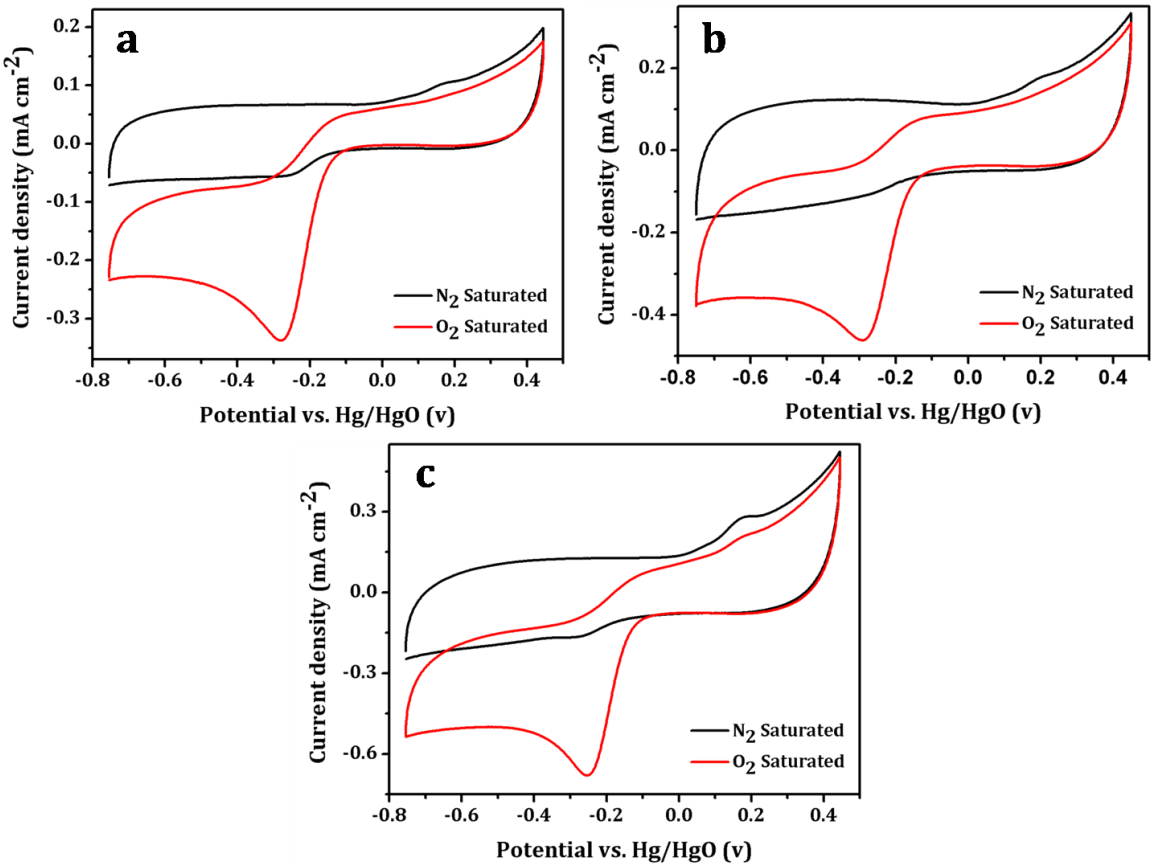

Figure 3.8. Cyclic voltammograms of **(a)** $Ba_2In_{1.5}Co_{0.5}O_{5-\delta}$, **(b)** $BaIn_{0.5}Co_{0.5}O_{3-\delta}$ and **(c)** $BaIn_{0.25}Co_{0.75}O_{3-\delta}$ under N_2 and O_2 saturated 0.1 M KOH solution at a sweep rate of 20 mV s^{-1} using Hg/HgO and Platinum wire as the reference and counter electrode respectively.

All the samples were mixed with Vulcan XC-72 to improve the electrical conductivity of the compounds. The catalyst slurry was coated on glassy carbon electrode which was used as working electrode.

The cyclic voltammogram of all the samples were recorded in N_2 saturated 0.1 M KOH at a sweep rate of 20 mV s^{-1} and then under O_2 saturation at the same sweep rate. Figure 3.8 represents the voltammograms of all the samples recorded under both N_2 and O_2 saturated solution. No characteristic peaks are observed under N_2 saturated solution, whereas a clear reduction peak can be seen in all the samples under O_2 saturated solution. An increase in the reduction current after purging O_2 in the solution indicates the ORR activity of the samples.

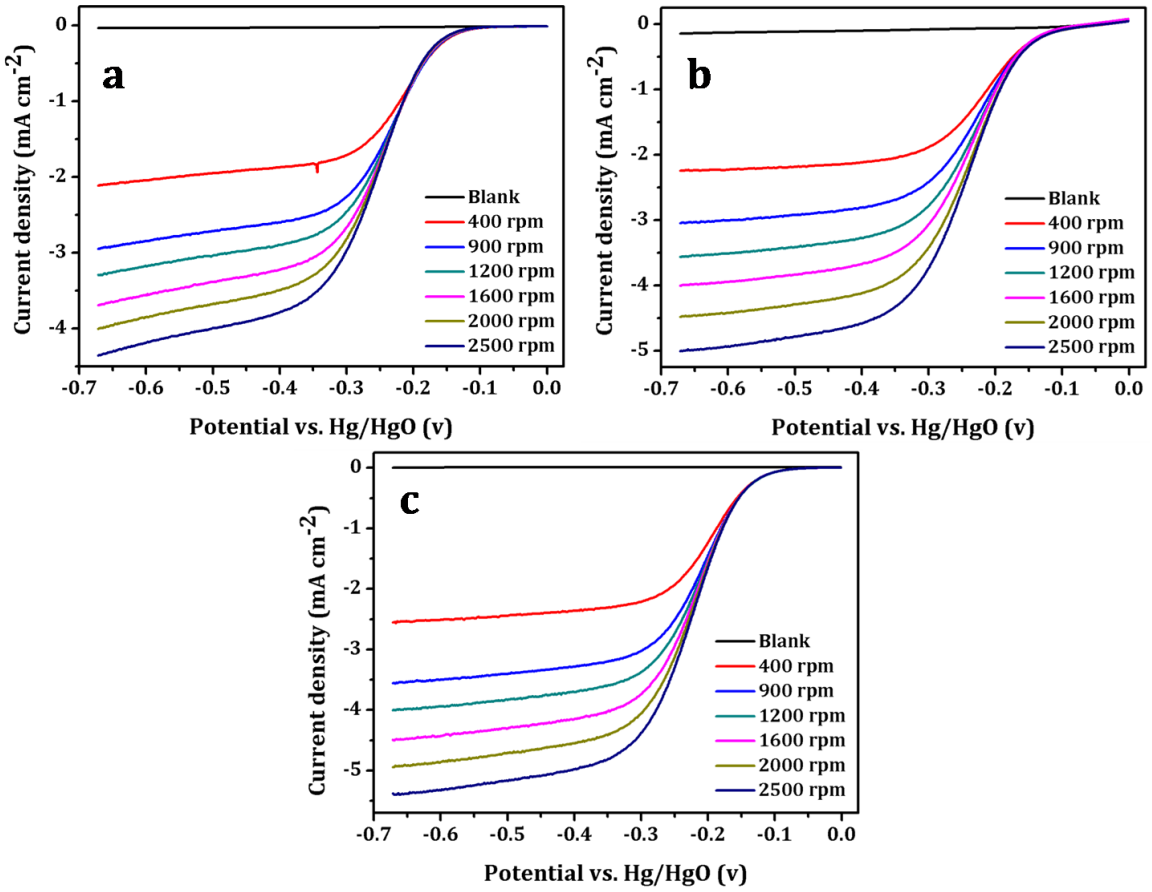

Figure 3.9. LSV's at different electrode rotation rate for ORR using **(a)** $Ba_2In_{1.5}Co_{0.5}O_{5-\delta}$, **(b)** $BaIn_{0.5}Co_{0.5}O_{3-\delta}$ and **(c)** $BaIn_{0.25}Co_{0.75}O_{3-\delta}$. The experiments were performed in O_2 saturated 0.1 M KOH at a sweep rate of 5 mV s^{-1} using Hg/HgO and platinum wire as the reference and counter electrodes respectively.

A detailed investigation on the ORR activity of the samples was performed by RDE method. Figure3.9 represents the LSV's of all the samples at different electrode rotation rates in O_2 saturated 0.1 M KOH solution. It is clear from the figure that the limiting current density increases with increase in the rate of electrode rotation; this can be attributed to the enhanced rate of mass transport at higher electrode rotation rate [11].

Figure 3.10 represents the linear sweep voltammograms (LSV) of Co doped $Ba_2In_2O_5$ along with the parent brownmillerite at an electrode rotation rate of 1600 rpm. It is evident from the figure that there is an improvement in the ORR activity with increase in the Co concentration. The onset potential of Co doped samples is more positive than the parent $Ba_2In_2O_5$ which was observed to be around -0.12 V vs Hg/HgO. $Ba_2In_{1.5}Co_{0.5}O_{5-\delta}$ exhibited an onset potential of -0.11 V which is 10 mV more than the onset potential of parent $Ba_2In_2O_5$. However, $BaIn_{0.5}Co_{0.5}O_{3-\delta}$ and $BaIn_{0.25}Co_{0.75}O_{3-\delta}$ exhibited an onset potential of -0.09 V and -0.08 V which is 30 mV and 40 mV higher than that of parent $Ba_2In_2O_5$.

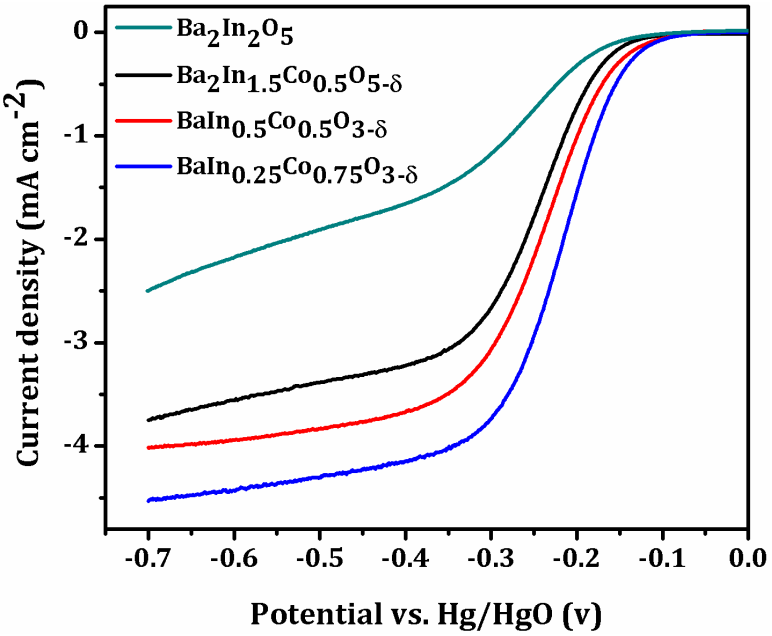

Figure 3.10. Linear sweep voltammograms obtained at an electrode rotating speed of 1600 rpm with a rotating disk electrode for the ORR on $Ba_2In_2O_5$ and Co doped $Ba_2In_2O_5$. The experiments were performed in O_2 saturated 0.1 M KOH at a sweep rate of 5 mV s^{-1} using Hg/HgO and platinum wire as the reference and counter electrodes respectively.

It is evident from the figure that with increase in Co concentration, the limiting current density increases, this can be attributed to the ability of cobalt to enhance the conductivity of the catalyst. The improved ORR activity when compared to the parent brownmillerite and with increase in cobalt concentration can be attributed to the presence of catalytically active Co atoms in the B site. It is well known that the transition metals in such oxides are responsible for ORR activity. Interestingly, Co doping in $Ba_2In_2O_5$ gives a better voltammogram with distinct mass transport region; this type of behaviour is not visible in the brownmillerite systems studied in Chapter 2A & 2B and some of the other oxide system [12-14]. This observation can be correlated to the studies carried out by Suntivich et. al. where the authors have observed that an e_g filling of 1 in Co^{3+} ion in $LaCoO_3$ enhances the ORR activity. Similar configuration can be expected in our case also since Co is mainly in Co^{3+} state as evident from XPS studies. Too little e_g – filling leads to strong B-O_2 bonding whereas too high e_g – filling leads to very weak B-O_2 bonding; both the situations are not desirable for good ORR activity. Whereas moderate e_g - filling will lead to an ideal state where the bond strength between the B-site cation and O_2 will neither be too strong nor too weak leading to maximum activity as evident from Sabatier's principle [15].

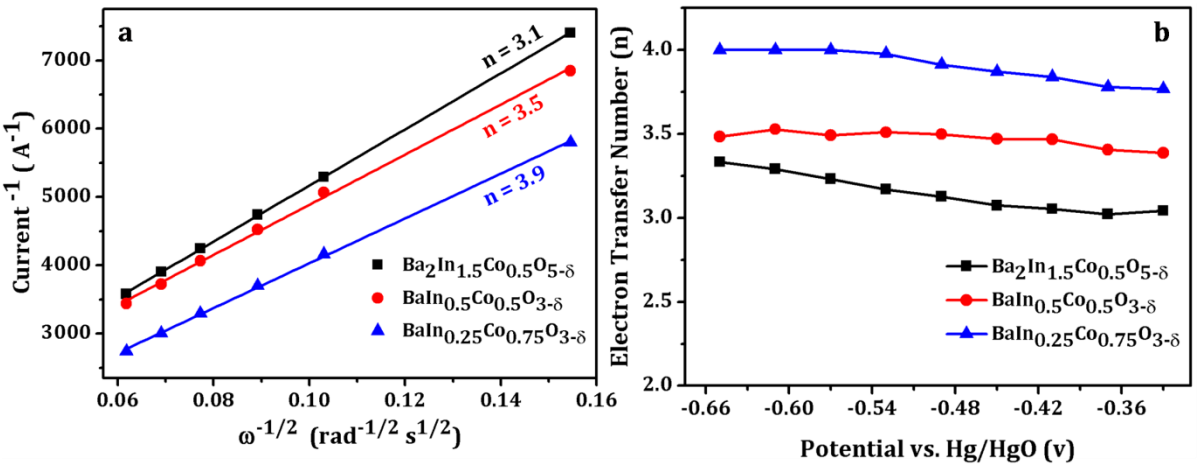

Figure 3.11. (a) K-L plot of ORR on Co doped $Ba_2In_2O_5$ compounds at a constant potential of -0.49 V and **(b)** The dependence of the electron transfer number of Co doped $Ba_2In_2O_5$ on various applied potential; in O_2 saturated 0.1 M KOH at a sweep rate of 5 mV s^{-1} using Hg/HgO and Pt wire as reference and counter electrode respectively.

The kinetic parameters such as electron transfer number, kinetic current densities etc., of samples were determined from Koutecky-Levich (K-L) equation as

explained in section 2A.3.2.1 of Chapter 2A [16]. A comparison of the KL plot of the various samples at -0.49 V is shown in Figure 3.11 (a). It is evident from the figure that the slope of the K-L plot changes along the series. This suggests that the number of electrons involved in the ORR in the series changes with Co concentration. In fact at this potential, the number of electrons involved for ORR on $Ba_2In_{1.5}Co_{0.5}O_{5-\delta}$ was found to be ~3 whereas that for $BaIn_{0.5}Co_{0.5}O_{3-\delta}$ was ~3.5 and for $BaIn_{0.25}Co_{0.75}O_{3-\delta}$ the value was ~3.9. The number of electrons (4 or 2) involved in the ORR mechanism decides whether the reaction proceeds through a 4-electron direct hydroxide pathway or 2-electron peroxide intermediate pathway. Direct reduction of oxygen to hydroxide via 4-electron pathway is more efficient and desirable in ORR [17]. Hence $BaIn_{0.25}Co_{0.75}O_{3-\delta}$ with an electron transfer number ~4 exhibits better ORR kinetics among the series of compounds.

The number of electrons involved in the ORR mechanism for all the samples at different potential was calculated from the K-L equation and is plotted in Figure 3.11 (b). It is clear from the figure that the number of electrons involved in the ORR for $BaIn_{0.25}Co_{0.75}O_{3-\delta}$ is in between 3.7 and 4 indicating that the ORR in this system mainly proceeds via 4-electron mechanism involving direct hydroxyl formation. But on the other hand it is observed that the number of electrons involved in ORR on $Ba_2In_{1.5}Co_{0.5}O_{5-\delta}$ is between 3 and 3.3. A value around 3 can be attributed to the simultaneous reaction involving both 2-electron peroxide intermediate pathway and 4-electorn direct pathway [18]. It is worth to note that ORR on $BaIn_{0.5}Co_{0.5}O_{3-\delta}$ (n = ~3.5) also proceeds through both 2 and 4 electron pathway but 4-electron direct reduction is more predominant. Further kinetic current density at various potential was calculated and is represented in Figure 3.12. It can be seen that at a particular potential, the kinetic current density increases with increase in Co concentration.

From these observations, it is clear that the incorporation of cobalt in indium site of $Ba_2In_2O_5$ improves the ORR activity of the sample. The ORR activity of $Ba_2In_{1.5}Co_{0.5}O_{5-\delta}$ is considerably enhanced from that of the parent $Ba_2In_2O_5$ although both systems have oxygen vacancies ordered in the alternate layers. Hence the increase in the activity is solely attributed to the incorporation of active Co sites in the brownmillerite lattice. Further incorporation of Co viz., $BaIn_{0.5}Co_{0.5}O_{3-\delta}$ and $BaIn_{0.25}Co_{0.75}O_{3-\delta}$ results in the loss

of brownmillerite structure and formation of cubic perovskite structure where the oxygen vacancies are randomly distributed in the lattice.

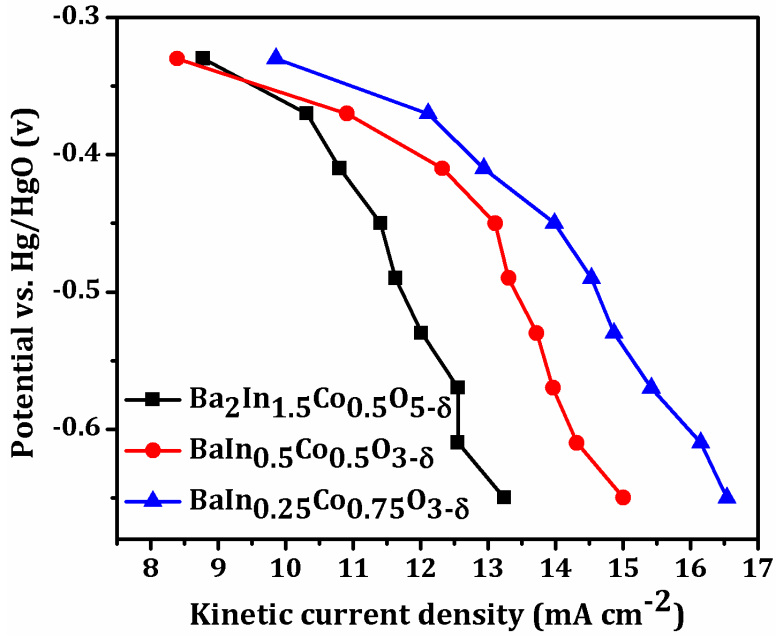

Figure 3.12. The kinetic current density at different potential for Co doped $Ba_2In_2O_5$. The experiments were performed in O_2 saturated 0.1 M KOH at a sweep rate of 5 mV s^{-1} using Hg/HgO and Pt wire as reference and counter electrode respectively.

The enhancement in the ORR activity is due to the concentration of cobalt but a role of random distribution of vacancies which will help in the O_2 adsorption cannot be ruled out. The role of oxygen vacancy in ORR is already reported in literature and chapter 2 [19]. Interestingly it can be observed that the composition $BaIn_{0.25}Co_{0.75}O_{3-\delta}$ with the highest Co concentration exhibits the best ORR activity with an electron transfer number ~4, more positive onset potential and highest limiting current density among the series.

3.3.2.1. High temperature EIS measurements

The EIS studies on the Co doped $Ba_2In_2O_5$ pellets were performed by considering it as polycrystalline ceramic sample as explained in Section 2A.3.2.2 of Chapter 2A. The analysis of the EIS spectrum was done on the basis of Bauerle model where the AC impedance spectra of a ceramic polycrystalline sample appears in three successive semicircles associated to the bulk impedance (in the high frequency range), grain boundary impedance (at intermediate frequencies) and the charge transfer or electrode

impedance (at low frequencies) [20]. The AC scans were fitted using the equivalent circuit shown in figure 3.13.

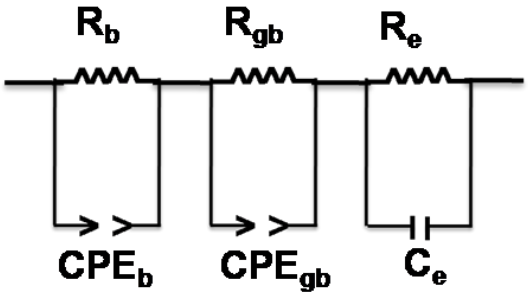

Figure 3.13. Equivalent circuit used for representing the contribution from bulk, grain boundary and electrode interface in the total AC impedance response.

The high temperature AC impedance spectroscopy measurements of the series of compounds were performed on the sintered pellets. Figure 3.14 represents the AC impedance plot obtained for the $BaIn_{0.5}Co_{0.5}O_{3-\delta}$. Similar patterns were obtained for the other two compounds.

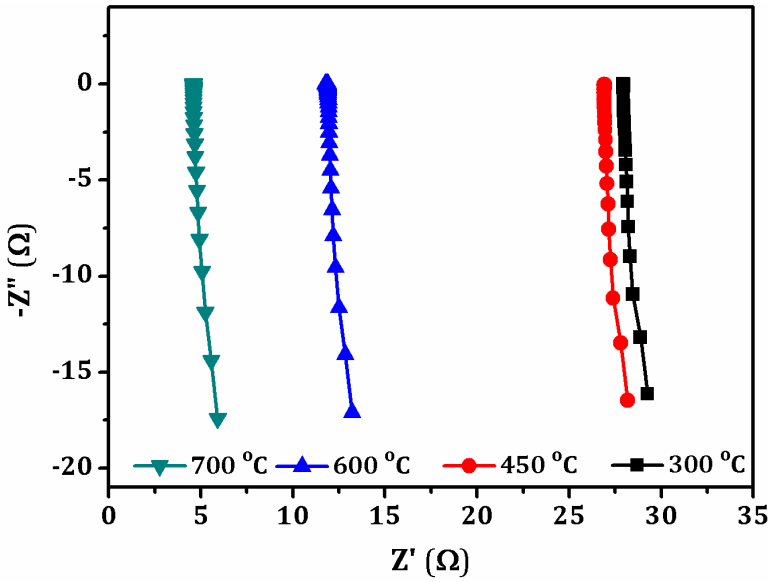

Figure 3.14. AC impedance scans for $BaIn_{0.5}Co_{0.5}O_{3-\delta}$ at different temperatures.

At the outset it can be observed that the impedance of Co doped samples is much lesser, when compared to the Ce and Zr doped $Ba_2In_2O_5$ systems explained in chapter 2. It can be further observed that EIS experiments on Co doped sample showed inductive contribution in the AC impedance scan. This can be attributed to the parasitic inductance of the external wiring of the testing setup [21]. The contribution from the

inductance was subtracted from the measured data in order to get the sample resistance. For this, the same experiment was repeated with sintered pellet by shorting the cell for which the pellet was wrapped in a thin Pt strip [22]. Figure 3.15 shows the scheme which explains the method employed to subtract the inductance effect.

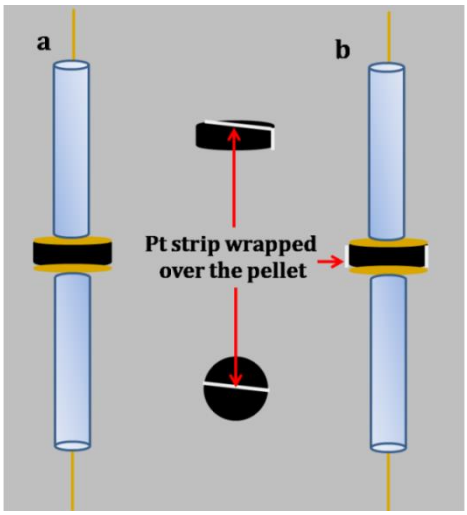

Figure 3.15 (a) The normal set up employed to measure EIS with sintered pellet (black colour) in between two electrodes and **(b)** Set up used after shorting the circuit, pellets are wrapped in Pt strip (white colour).

The impedance data obtained after shorting the cell was subtracted from the data obtained for the pellet alone (detailed procedure is given in Appendix 2) and the Nyquist plot was plotted. Figure 3.16 shows the Nyquist plot obtained for $BaIn_{0.5}Co_{0.5}O_{3-\delta}$ at 300 °C after removing the contribution from the inductance.

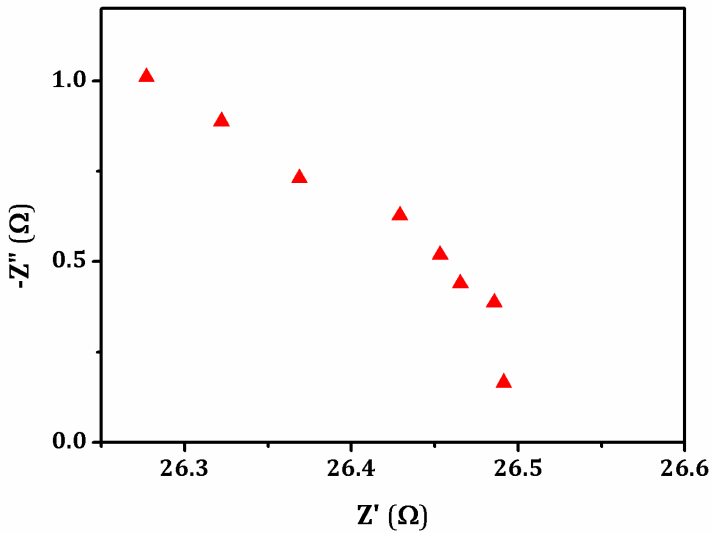

Figure 3.16. AC impedance of $BaIn_{0.5}Co_{0.5}O_{3-\delta}$ at 300 °C after subtracting the inductance effect.

A lesser number of points at the higher frequency range can be attributed to the fact that the maximum frequency employed for the experiments was 1 MHz. The spectrum was fitted with equivalent circuit as explained in section 2A.3.2.2 in Chapter 2A. The total resistance (R_b + R_{gb}) of the materials were calculated from the fitting parameters of the equivalent circuit. The total resistance of the compounds with varying temperature is tabulated in Table 3.4.

Table 3.4. Total resistance (R_b+R_{gb}) of the Co doped $Ba_2In_2O_5$ at variable temperature determined by EIS.

	R_b+R_{gb} (ohm)			
	300 °C	450 °C	600 °C	700 °C
$Ba_2In_{1.5}Co_{0.5}O_{5-\delta}$	9.3 x 10^3	1.04 x 10^3	195	89
$BaIn_{0.5}Co_{0.5}O_{3-\delta}$	26.45	21.92	11.88	4.6
$BaIn_{0.25}Co_{0.75}O_{3-\delta}$	5.86	2.97	1.84	1.4

From the values, it is clear that the impedance of a compound decreases with increase in temperature and with Co concentration along the series. The decrease in the impedance along the series can be attributed to the presence of Co in the lattice which will favour conductivity. The total conductivity of the sample was calculated from the resistance and Arrhenius graph was plotted as shown in Figure 3.17.

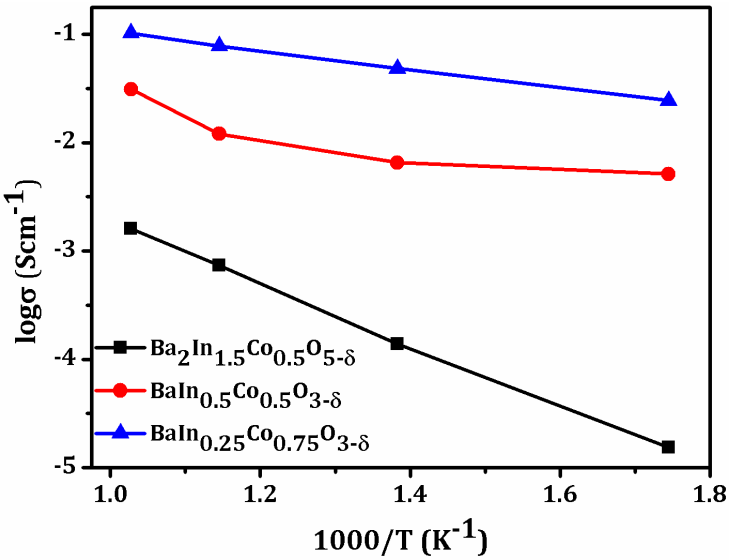

Figure 3.17. Arrhenius plots of the total conductivities determined from the AC impedance scan of Co doped $Ba_2In_2O_5$.

It can be observed that there is an increase in the conductivity of the sample with increase in temperature. Also with increase in Co concentrations, the conductivity increases as expected due to the increased amount of Co in the lattice. The activation energy for the conduction through these compounds was calculated from Arrhenius plot and is tabulated in Table 3.5. Although the oxygen vacancies are almost similar in all the three compounds, it can be observed that the activation energy decreases drastically after the first member of the series. This can be attributed to the fact that the oxygen vacancies are ordered in $Ba_2In_{1.5}Co_{0.5}O_{5-\delta}$ due to its brownmillerite structure; however vacancies are randomly distributed in the samples with higher concentration of Co doping. This will result in anisotropic conduction through the compounds.

Table 3.5. Activation energy for the conductivity through Co doped $Ba_2In_2O_5$ series of compounds calculated from the Arrhenius plot.

Compound	Activation energy (J mol^{-1})
$Ba_2In_{1.5}Co_{0.5}O_{5-\delta}$	23.47
$BaIn_{0.5}Co_{0.5}O_{3-\delta}$	8.13
$BaIn_{0.25}Co_{0.75}O_{3-\delta}$	7.15

Interestingly the conductivity of the Co doped systems are much better than Ce and Zr doped systems and are comparable with other perovskite type oxides which are used as cathode materials in the SOFC. Also the fact that these compounds are stable under inert and oxidative atmosphere at higher temperatures makes them a potential material for high temperature energy applications.

3.4. Conclusions

$Ba_2In_2O_5$ brownmillerites with Co doped progressively in In site were synthesized. $Ba_2In_{1.5}Co_{0.5}O_{5-\delta}$, with the least concentration of Co, retained the brownmillerite structure with disorder in O3 site in the two dimensional alternate layer along ab plan. But higher concentrations of Co in In site of $Ba_2In_2O_5$ viz., $BaIn_{0.5}Co_{0.5}O_{3-\delta}$ and $BaIn_{0.25}Co_{0.75}O_{3-\delta}$ leads to the loss of brownmillerite structure and the compound attains perovskite structure with oxygen vacancy distributed randomly in the lattice. Both the cell length and cell volume gradually decreased with increase in Co concentration owing to the smaller crystal radius of Co when compared to In. XPS studies revealed that Co exists in +3 oxidation state in all the compounds. The oxygen uptake calculated from

TGA was almost same for all the samples. The compounds were stable under both inert and 10 % O_2 in He at higher temperatures as evident from high temperature PXRD measurements. The compounds were tested for ORR activity under alkaline medium and interestingly all the samples exhibited far better ORR activity when compared to the parent $Ba_2In_2O_5$ brownmillerite. They also exhibited well defined linear sweep voltammogram which was not observed in the parent $Ba_2In_2O_5$ as well as Ce and Zr doped $Ba_2In_2O_5$ systems. The enhanced activity of Co doped samples is attributed to the presence of catalytically active Co in lattice. Among the doped system with increase in Co concentration, the ORR activity increases which can be correlated to both Co concentration and the random distribution of oxygen vacancy in the higher Co doped systems. Moreover, the Co concentrations are found to have an impact on the reaction pathway. The parent brownmillerite exhibited a 2 electron reaction pathway which proceeds through peroxide intermediate. But for $Ba_2In_{1.5}Co_{0.5}O_{5-\delta}$, the number of electrons involved in the ORR was found to be ~3 indicating that both 2-electron peroxide intermediate pathway and 4-electorn direct pathway occur simultaneously. But with increasing Co concentration, 4-electron direct pathway predominates with an electron transfer number of ~3.5 and ~3.85 for $BaIn_{0.5}Co_{0.5}O_{3-\delta}$ and $BaIn_{0.25}Co_{0.75}O_{3-\delta}$ respectively. The composition $BaIn_{0.25}Co_{0.75}O_{3-\delta}$ with the highest Co concentration exhibited the best ORR activity among the series. The high temperature EIS measurements were performed on sintered pellets. All the samples showed contribution from inductive effect of the external wiring. Impedance of the samples were calculated by subtracting the contribution from inductance effect. Impedance of the sample decreased with increase in the temperature. Also with increase in the Co concentration, the total resistance (R_b+R_{gb}) of the sample decreased. Arrhenius plot shows that the conductivity increases with increase in temperature and Co concentration. This trend can be attributed to the presence of Co in the lattice which enhances the conductivity of the sample.

3.5. References

1. Rao, C. N. R. *Annu. Rev. Phys. Chem.* **1989**, *40,* 291.
2. Zhang, J.; Liu, F.; Cheng, J. P.; Zhang, X. B. *ACS Appl. Mater. Interfaces* **2015**, *7*, 17630.

3. Petitto, S. C.; Marsh, E. M.; Carson, G. A.; Langell, M. A. *J. Mol. Catal. A: Chem.* **2008**, *281*, 49.
4. Toby, B. H. *J. Appl. Crystallogr.* **2001**, *34*, 210.
5. Shannon, R. *Acta Crystallogr. Sect. A* **1976**, *32*, 751.
6. Fischer, W.; Reck, G.; Schober, T. *Solid State Ionics* **1999**, *116*, 211.
7. Ahmed, I.; Eriksson, S. G.; Ahlberg, E.; Knee, C. S.; Karlsson, M.; Matic, A.; Engberg, D.; Börjesson, L. *Solid State Ionics* **2006**, *177*, 2357.
8. Fischer, W.; Reck, G.; Schober, T. *Solid State Ionics* **1999**, *116*, 211.
9. Malavasi, L.; Ritter, C.; Chiodelli, G. *Chem. Mater.* **2008**, *20*, 2343.
10. Suescun, L.; Dabrowski, B.; Mais, J.; Remsen, S.; Richardson, J. W.; Maxey, E. R.; Jorgensen, J. D. *Chem. Mater.* **2008**, *20*, 1636.
11. Town, J. L.; MacLaren, F.; Dewald, H. D. J. *Chem. Educ.* **1991**, *68*, 352.
12. Wu, Z. S.; Yang, S.; Sun, Y.; Parvez, K.; Feng, X.; Müllen, K. *J. Am. Chem. Soc.* **2012**, *134*, 9082.
13. Zhang, Y.; Fugane, K.; Mori, T.; Niu, L.; Ye, J. *J. Mater. Chem.* **2012**, *22*, 6575.
14. Fabbri, E.; Mohamed, R.; Levecque, P.; Conrad, O.; Kötz, R.; Schmidt, T. J. *ACS Catal.* **2014**, *4*, 1061.
15. Suntivich, J.; Gasteiger, H. A.; Yabuuchi, N.; Nakanishi, H.; Goodenough, J. B.; Shao-Horn, Y. *Nat. Chem.* **2011**, *3*, 546.
16. Wang, S.; Yu, D.; Dai, L.; Chang, D. W.; Baek, J. B. *ACS Nano* **2011**, *5*, 6202.
17. Ge, X.; Sumboja, A.; Wuu, D.; An, T.; Li, B.; Goh, F. W. T.; Hor, T. S. A.; Zong, Y.; Liu, Z. *ACS Catal.* **2015**, *5*, 4643.
18. Wang, S.; Yu, D.; Dai, L. *J. Am. Chem. Soc.* **2011**, *133*, 5182.
19. Du, J.; Zhang, T.; Cheng, F.; Chu, W.; Wu, Z.; Chen, J. *Inorg. Chem.* **2014**, *53*, 9106.
20. Bauerle, J. E. *J. Phys. Chem. Solids* **1969**, *30*, 2657.
21. Vladikova, D.; Kilner, J. A.; Skinner, S. J.; Raikova G.; Stoynov, Z. *Electrochim. Acta*, **2006**, *51*, 1611.
22. Jankovic, J.; Wilkinson, D. P.; Hui, R. *J. Electrochem. Soc.* **2011**, *159*, B109.

Chapter 4

N-Doping in $A_2Fe_2O_5$: A Strategy for Improving ORR Activity of Brownmillerites

4.1. Introduction

The role of brownmillerite based oxide materials having inherent oxygen vacancies in ORR activity are explained in Chapter 2 and Chapter 3. Cation doping in the B site of the brownmillerite was performed and their ORR activity was investigated. The next aim was to study the effect of anion doping in these stable oxygen deficient oxide materials for the ORR activity.

Heteroatom doped carbon morphologies have shown immense potential as metal-free highly active electrocatalysts to replace noble metals, including platinum [1]. Among the heteroatoms, nitrogen doped systems are widely studied [2, 3]. These systems exhibit excellent ORR activity owing to their unique electronic properties resulting from the conjugation between the nitrogen lone pair electrons and graphene π system [4]. A detailed understanding of the active sites and the role of nitrogen atom is yet to be achieved; however, widely accepted mechanism is that a net positive charge is created on the carbon atoms adjacent to nitrogen in the matrix, which readily attracts electrons from the anode and also facilitates the O_2 adsorption in the ORR process [2]. Further development has shown that N and transition metal (Fe & Co) co-doped carbon morphologies exhibit better ORR activity under both acidic and alkaline condition [5-7]. Among the transition metals, Fe containing systems were widely studied. Very recently Zitolo et al has demonstrated that the active sites in Fe-N-C systems are porphyrinic FeN_4C_{12} moieties. Further it was observed that the ORR activity can be enhanced on pyrolysis under ammonia because of the incorporation of highly basic N-group in Fe-N-C structure [8]. In general it is observed that Fe-N-C site is active for ORR and enhances the activity of the catalyst [9, 10].

Further studies have revealed that N-doping in metal oxides improve the ORR activity of the compounds. A very recent study reveals that CoO films synthesized under N_2 atmosphere exhibit higher ORR activity than their N-free counterparts. Even though N doping is not unambiguously proved, the enhancement in the activity has been attributed to the Co-N_x active sites which may be present in the catalyst [11]. Hence, it can be anticipated that catalyst systems incorporating the advantageous features of oxides with substantial oxygen vacancies and transition metal-N interaction in a single stable structure will have desirable ORR activity.

So the focus of the work carried out in this chapter is the incorporation of nitrogen in the lattice of Fe containing brownmillerite. We have incorporated Fe-N sites in stable and oxygen deficient brownmillerite and studied their ORR activity in alkaline medium. Iron containing $A_2Fe_2O_5$ (A = Ca, Sr & Ba) brownmillerites are synthesised and subsequently nitrogen doping in anionic site was achieved.

4.2. Experimental section

4.2.1. Synthesis of $A_2Fe_2O_5$ (A = Ca, Sr & Ba) and N-doped $A_2Fe_2O_5$

Brownmillerties viz., $Ca_2Fe_2O_5$ (CFO), $Sr_2Fe_2O_5$ (SFO) and $Ba_2Fe_2O_5$ (BFO) were synthesised by solid state method. High purity $CaCO_3$ (≥99 %, Sigma Aldrich), $SrCO_3$ (99.995%, Sigma Aldrich), $BaCO_3$ (99.98%, Sigma Aldrich) and Fe_2O_3 (99.98%, Sigma Aldrich) were used as the starting materials. For CFO, stoichiometric amounts of $CaCO_3$ and Fe_2O_3 were mixed and calcined at 500 ˚C for 2 h followed by 950 ˚C for 16 h. Whereas in the case of SFO and BFO, the stoichiometric amount of starting materials were mixed and calcined under N_2 atmosphere for 18 and 24 h respectively with intermediate grinding. For nitrogen doping, the pristine samples were heated under ammonia gas flow at 800 ˚C for 6 h. Ammonia gas was synthesized in-situ by drop wise addition of NaOH (1 M) to NH_4Cl (4 M) solution and the gas was carried by a flow of N_2 (20 mL/min) into the tubular furnace. The gas was passed through CaO just before entering the furnace in order to trap the moisture present in the mixture. Hereafter nitrogen doped $Ca_2Fe_2O_5$, $Sr_2Fe_2O_5$ and $Ba_2Fe_2O_5$ are mentioned as CFO-N, SFO-N and BFO-N respectively.

4.2.2. Characterization

The phase purity of all these samples was determined by PXRD. The details of the instruments and procedures used for PXRD are same as those described in section 2A.2.2 of Chapter 2A. Neutron diffraction experiments were carried out at room temperature with the help of Focusing Crystal Diffractometer at Dhruva reactor using a wavelength of 1.48 Å. The scattered neutrons in this diffractometer were detected using an array of four 3He linear position sensitive detectors covering a range of 6˚–120˚. Lattice parameters from the neutron diffraction data were calculated by Rietveld refinement method by using GSAS-EXPGUI program [12]. UV-vis spectra of the samples in reflectance mode were recorded using Cary 5000 UV-vis-NIR spectrophotometer in a

solid sample holder. Oxidation state of the elements and the presence of nitrogen in the doped samples were studied using XPS measurements. Instruments and procedures used for XPS measurements are same as those described in section 3.2.2 of Chapter 3. X ray absorption spectroscopy (XAS) measurements of the samples at Fe K-edge were carried out in transmission mode at the scanning extended X-ray absorption fine structure (EXAFS) Beamline (BL-9) at the Indus-2 Synchrotron Source (2.5 GeV, 100 mA) at the Raja Ramanna Centre for Advanced Technology (RRCAT), Indore, India [13, 14]. The analysis of the EXAFS data has been carried out using the standard procedure [15, 16] using the IFEFFIT software package [17]. The current-voltage (I-V) measurements were carried out in Keithley Semiconductor Characterization System 4200-SCS instrument. For making the substrate for I-V curve measurement, 10 mg of the sample was taken in 1 ml isopropyl alcohol and sonicated for 10 min. 200 μL of the solution was drop casted on an inter digitated Au micro electrode and it was dried at 60 ˚C for 30 min. The current in a potential range of -100 to +100 V was measured under ambient condition in a 2 probe setup.

4.2.3. Electrochemical analysis

The electrochemical properties of the catalysts were measured by cyclic voltammetry (CV) and rotating disk electrode (RDE) assembly using a CHI604E electrochemical analyser (CH Instruments, Inc., USA); and rotating ring disk electrode (RRDE) assembly using CHI760E bipotentiostat (CH Instruments, Inc., USA) in a conventional three-electrode test cell with Hg/HgO and platinum wire as the reference and counter electrodes, respectively under room temperature. The details of the electrode preparation method are same as those described in section 3.2.3 of Chapter 3. The number of electrons involved in the reaction and the yield of peroxide was calculated by RRDE measurement at 1600 rpm inO_2 saturated 0.1 M KOH solution. The disk electrode was scanned at a rate of 5 mV s^{-1} and the ring potential was kept at 0.55 V vs. Hg/HgO. The stability of the samples was evaluated by potentially cycling the catalyst at a scan rate of 50 mVs^{-1} in 0.1 M KOH for 5000 cycles.

4.3. Results and discussion

4.3.1. Synthesis and structural characterization

Parent CFO, SFO and BFO were synthesized by solid state synthesis method and nitrogen doping was achieved by passing ammonia gas through the synthesized samples at 800 ˚C for 6 h. At the outset it was observed that the colour of the samples changed after nitrogen doping. Figure 4.1 represents the photographs of parent and N-doped samples. This type of change in colour after N-doping can be attributed to modulations in band gaps [18].

Figure 4.1 Photographic images of parent and N-doped CFO, SFO and BFO.

The phase purity of all the samples was confirmed by PXRD. Figure 4.2 represents the PXRD pattern of pristine and N-doped samples.

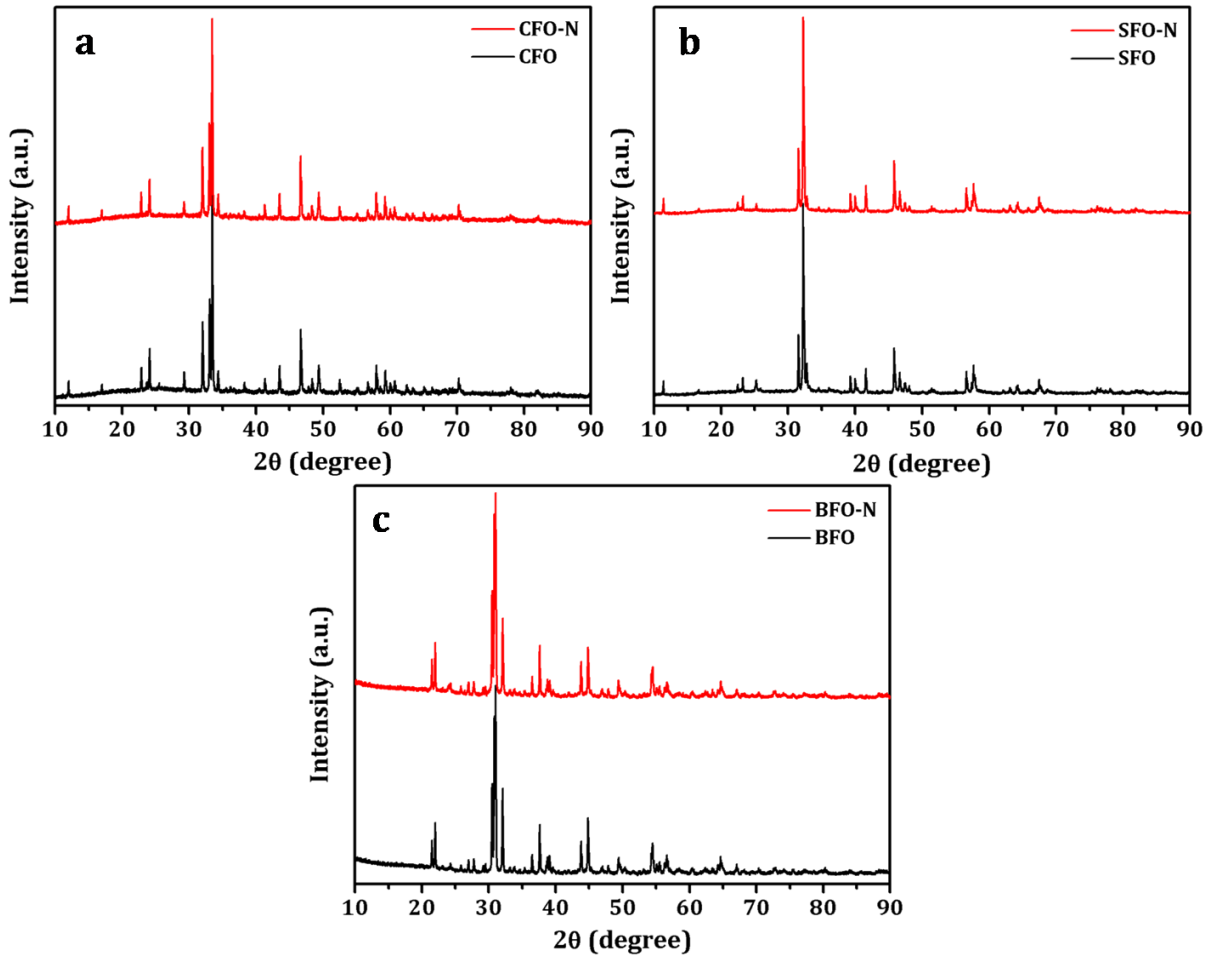

Figure 4.2 PXRD patterns of parent and N-doped brownmillerites **(a)** CFO & CFO-N **(b)** SFO & SFO-N and **(c)** BFO & BFO-N.

The PXRD pattern of CFO matches with already reported pattern (JCPDS file No. 01-071-2264) and the compound crystallises in orthorhombic structure. SFO also crystallizes in orthorhombic system and the PXRD pattern matches with previously reported structure (JCPDS file No.01-070-0836). Whereas BFO crystallize in monoclinic system and the structure matches with that reported by Clemens et al [19]. The PXRD patterns of nitrogen doped samples (Figure 4.2) matches with its parent brownmillerite indicating that the crystal structure is retained after nitrogen doping.

The detailed structural parameters of the compounds were obtained by Rietveld refinement of the PXRD patterns using GSAS-EXPGUI software. Rietveld refinement of CFO, SFO and BFO was carried out using previously reported structural parameters.

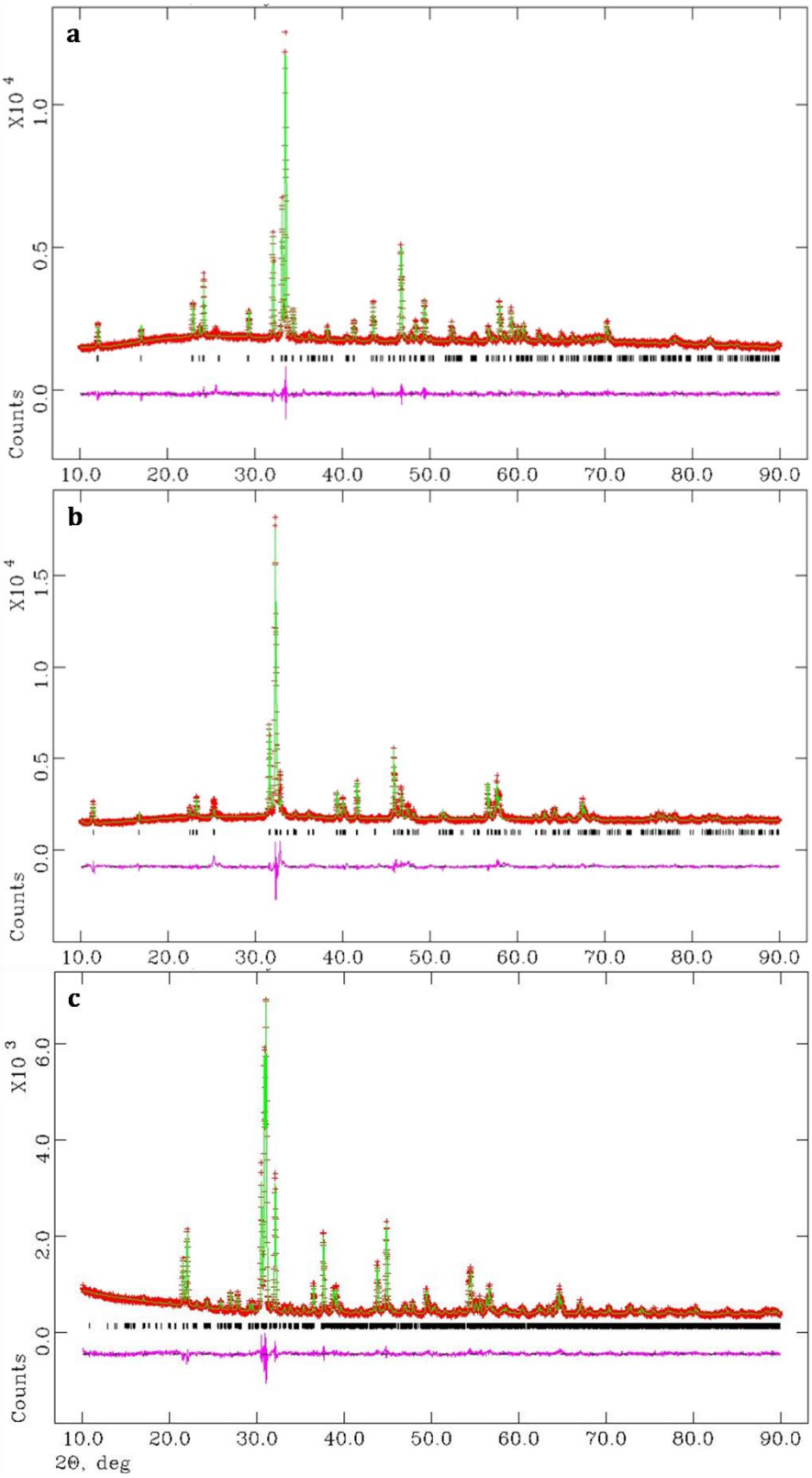

Figure 4.3 Rietveld refinement plots of the PXRD patterns of **(a)** CFO, **(b)** SFO and **(c)** BFO. Red pattern represents experimental data, green pattern is the Rietveld fit and pink pattern represents difference plot. Black vertical lines in all the figures represent the expected positions for the main phase.

Refinement of the PXRD patterns with these parameters proceeded smoothly and the Rietveld refinement plots of the parent brownmillerites obtained are represented in Figure 4.3. The structural parameters obtained after the refinement are tabulated in Table 4.1.

Table 4.1 Structure parameters obtained from the Rietveld refinement of CFO, SFO and BFO.

	CFO	SFO	BFO
χ^2	1.274	3.291	1.357
wRp (%)	2.65	4.23	4.97
Rp (%)	2.02	2.84	3.94
Space group	P n m a	I c m m	P1 21/c 1
a (Å)	5.4290(0)	5.6715(0)	6.9705(0)
b (Å)	14.7980(1)	15.5734(2)	11.7245(1)
c (Å)	5.6010(0)	5.5270(0)	23.4359(2)

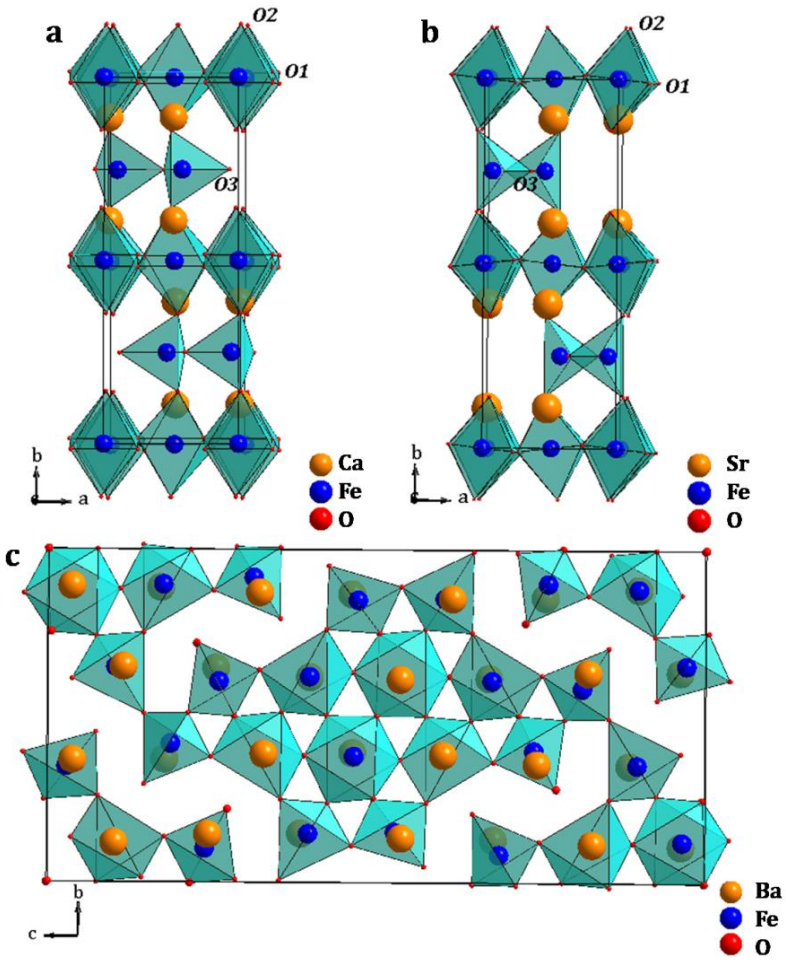

Figure 4.4 Polyhedral representation of the structures obtained after the refinement for **(a)** CFO, **(b)** SFO and **(c)** BFO.

The polyhedral representations of CFO, SFO and BFO are shown in Figure 4.4. CFO and SFO crystallize in orthorhombic brownmillerite structure with alternate layers of FeO_6 and FeO_4 polyhedra. The oxygen vacancies in these structures are orderly distributed in the two dimensional FeO_4 tetrahedral layer in the *ac* plane. BFO on the other hand crystallizes in a complex monoclinic structure with Fe atom having 6, 5 and 4 coordination number viz., FeO_6 octahedral, FeO_5 square pyramidal and FeO_4 tetraherdal geometries with oxygen vacancies ordered in rhombic type pattern in the *bc* plane [19]. Hence in all the brownmillerite structures, the oxygen vacancies are orderly distributed in two dimensional layers.

Further characterizations are explained on the basis of brownmillerite $Ca_2Fe_2O_5$ (CFO) and its nitrogen doped counterpart CFO-N.

Neutron diffraction data of CFO-N was collected to get a better insight into the position of oxide and nitride ions in the compound. Rietveld refinement on the neutron diffraction data were performed with already reported crystallographic data of CFO. Three different models were selected; in the first model all the anionic sites were assigned to oxygen atoms, in the second all the anionic sites were exclusively assigned to nitrogen and in the third one for each anionic sites, both oxygen (90% of the occupancy) and nitrogen (10% of the occupancy) were assigned before starting refinement [20]. The occupancies were refined with a constraint that the total occupancy of each anionic site was equal to 1.

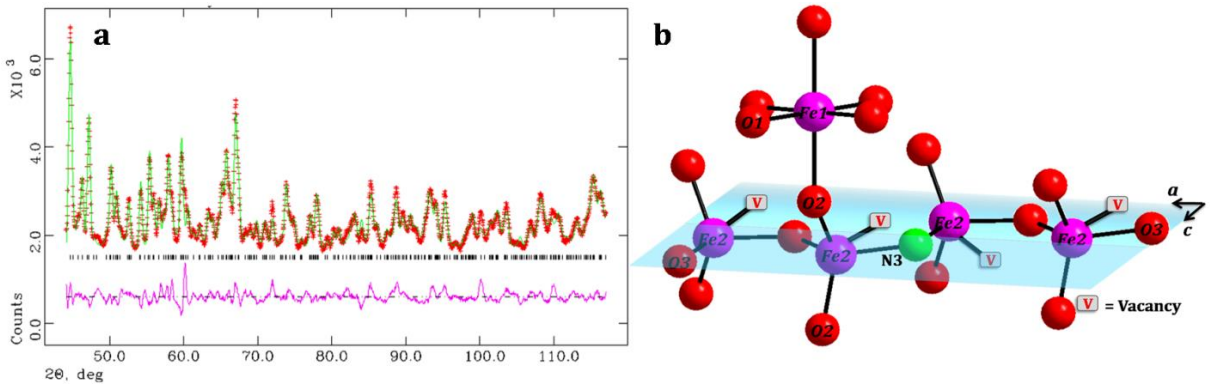

Figure 4.5 (a) Rietveld refinement plot obtained from the neutron diffraction data of CFO-N and **(b)** Ball and stick model of CFO-N obtained from the Rietveld refinement data. "V" represents possible positions of inherent vacancies available in the tetrahedral layer of the brownmillerite in the ac plane.

Of the three models used for the refinement, the third one with both oxygen and nitrogen in the anionic site produced the best fit with a χ^2 of 7.454 when compared to oxygen only (χ^2 of 10.01) and nitrogen only (χ^2 of 14.8) models. This arrives at a substitution of 7 atom% of O with N. The detailed results obtained from the Rietveld refinement on the neutron diffraction data of CFO-N is given in Table 4.2.

Table 4.2 Rietveld refinement parameters of neutron diffraction data of CFO-N.

Atom	Fractional Coordinate			Occ.	Uiso
	X	Y	Z		
Ca	0.4789(20)	0.1092(5)	0.0288(16)	1	0.0154(12)
Fe	0	0	0	1	0.0143(14)
Fe	-0.0561(12)	0.25	-0.0679(12)	1	0.0154(15)
O1	0.2702(20)	-0.0167(4)	0.2257(16)	0.994(35)	0.0179(13)
O2	0.0268(13)	0.1422(4)	0.0721(11)	0.914(34)	0.0259(14)
O3	0.6032(22)	0.25	-0.1286(20)	0.821(48)	0.0120(16)
N1	0.2702(20)	-0.0167(4)	0.2257(16)	0.005(35)	0.0179(13)
N2	0.0268(13)	0.1422(4)	0.0721(11)	0.085(34)	0.0259(14)
N3	0.6032(22)	0.25	-0.1286(20)	0.178(48)	0.0120(16)

a = 5.4224(3), b = 14.7896(6), c = 5.5941(3); Space group = Pnma; χ^2 =5.496, wRp = 4.8, Rp = 3.7

From the occupancy parameters, it is clear that O3, the apex oxygen of FeO_4 tetrahedra is more labile for N substitution, when compared to octahedral oxygen atoms. This interesting observation also points to the fact that N is in close proximity to the oxygen vacancies which in fact occupy the uncoordinated sites of the FeO_4 tetrahedra. Hence a catalytic complex V_o-Fe-N can be envisaged in this novel material as shown in Figure 4.5(b). Neutron diffraction studies therefore confirm the incorporation of N in the lattice of $Ca_2Fe_2O_5$ brownmillerite.

Band gap of both parent and N-doped CFO were calculated from Tauc plot. The detailed calculation is given in Appendix 2. Figure 4.6 represents the Tauc plot of CFO and CFO-N. It is evident from the Tauc plot that there is a slight reduction in the band gap of CFO after N-doping. CFO-N has a band gap of 2.18 eV, which is 0.08 eV lesser than the parent CFO. This reduction in the band gap can be attributed to the fact that in N-doped oxides, N 2p orbitals present impurity acceptor states above the valence bands

consisting of O 2p orbitals and thereby reducing the band gap [21]. Hence the reduction in band gap reveals N doping in CFO.

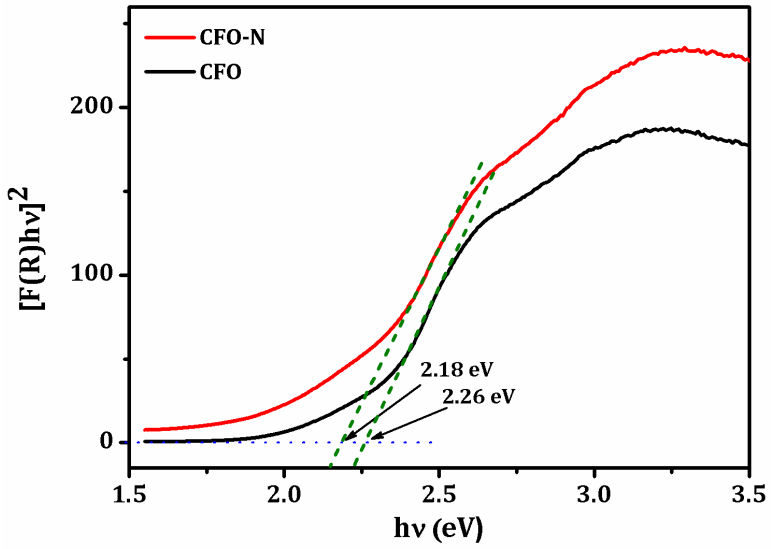

Figure 4.6 Tauc plot of CFO and its N-doped counterpart CFO-N.

XPS measurements were carried out to further confirm the presence of nitrogen in the doped samples. Very broad peak spanning from 395 to 402 eV was observed for N1s XP spectra as shown in Figure 4.7(a).

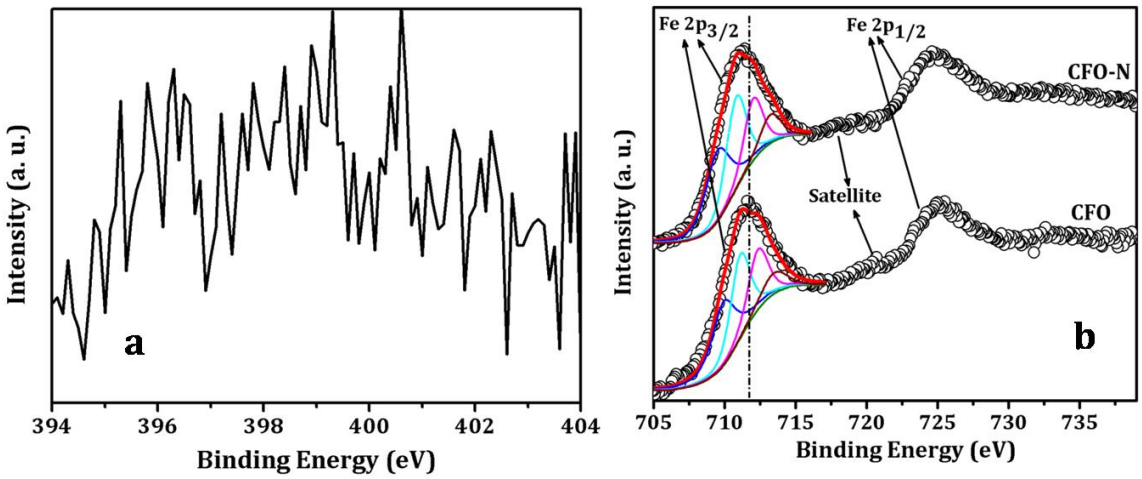

Figure 4.7 (a) N 1s XP spectra of CFO-N and **(b)** Fe 2p XP spectra of CFO and CFO-N. Deconvolution of Fe $2p_{3/2}$ was performed considering Gupta and Sen model. Data in black circles, fitted spectra in red, deconvoluted peaks in blue, cyan, pink and brown.

This indicates nitrogen is in multiple bonding sites with varying chemical environments [22]. Also a small contribution from the molecularly adsorbed N_2 (~400 eV and ~402

eV) cannot be avoided since reactions were done under N_2 atmosphere [23]. The signal to noise ratio of the spectra was very poor which may be because of low loading of nitrogen in the lattice as evident from the neutron diffraction studies. This is expected since we employed NH_3 diluted with N_2 for the synthesis.

However, a better insight was obtained from Fe 2p XP spectra of CFO and CFO-N as represented in Figure 4.7(b). The Fe $2p_{3/2}$ peak for CFO and CFO-N was observed at 711.6 and 711.3 eV respectively. The spin orbit splitting of Fe 2p component for CFO and CFO-N was found to be 13.3 and 13.2 eV respectively. Also the satellite peak appeared around 8 eV above the binding energy of Fe $2p_{3/2}$ indicating the presence of Fe in +3 oxidation state [24]. The XPS data of early transition metals with high spin unpaired electrons show multiplet structure for the 2p spectra due to spin-orbital and electrostatic interactions [25, 26]. Based on the Gupta-Sen model and studies conducted by Grosvenor et al., the high spin Fe^{3+} species can be fitted to four main peaks [27]. We have followed the same procedure and the Fe 2p spectra obtained could be successfully fitted into four multiples, indicating the presence of Fe in +3 oxidation state in the compounds. A closer look into the spectra reveals that there is a slight shift of around 0.3 eV towards lower binding energy of the Fe 2p peak in nitrogen doped samples. This can be attributed to the fact that when N replaces O in the FeO_x geometry, owing to the lower electronegativity of N than O, there is a red shift of the Fe 2p peaks [28].

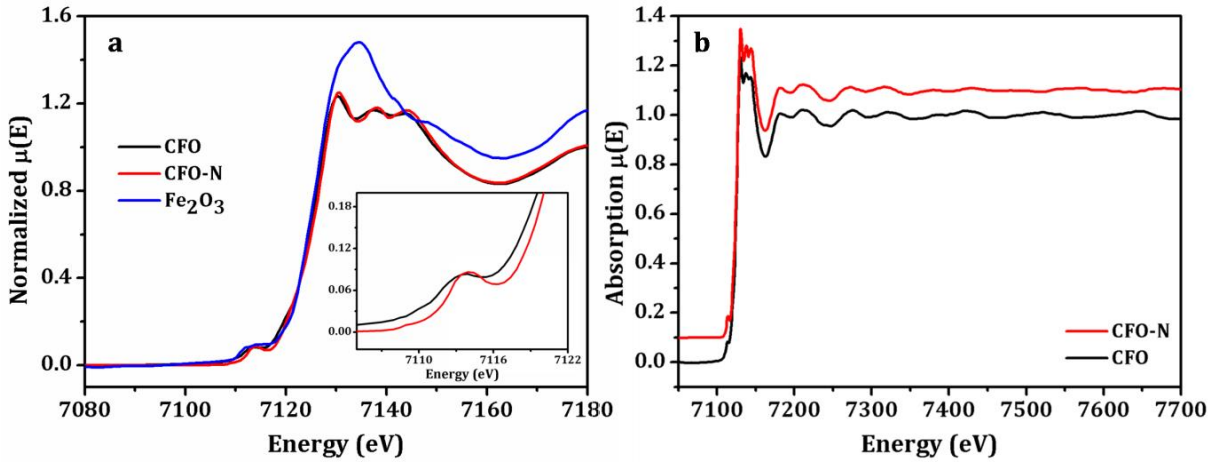

Figure 4.8(a) Normalized Fe K-edge XANES spectra from CFO, CFO-N and Fe_2O_3. Inset represents the enlarged portion of the pre-edge region of CFO and CFO-N. **(b)** EXAFS spectra of CFO and CFO-N at the K-edge of Fe.

Further XAS measurements were carried out to study the incorporation of nitrogen in brownmillerite lattice. Figure 4.8 (a) represents the X-ray absorption near edge structure (XANES) spectra measured at Fe K-edge for CFO, CFO-N and Fe_2O_3. The spectra obtained for CFO was similar to that reported in the literature [29]. The absorption edges of Fe in the CFO and CFO-N samples lie close to that of the Fe_2O_3 standard indicating that the oxidation state of Fe in CFO and CFO-N are same as that of Fe_2O_3 standard i.e. in +3 oxidation state. The Fe K-edge XANES spectra of the CFO and CFO-N samples have similar features. Therefore, it can be inferred that no appreciable change occurs in the CFO lattice due to N doping. But a closer look into the pre-edge region of XANES (inset in Figure 4.8(a)) shows a small shift in the peaks. Since the pre-edge is quite sensitive to the coordination number and orbital geometry, this change can be attributed to the perturbation in the covalent mixing of 3d orbital with ligand valance orbital [30]. Figure 4.8 (b) represents the experimental EXAFS (μ(E) vs. E) spectra of CFO and CFO-N samples measured at Fe K-edge. The detailed step involved in the fitting of the experimental data is given in Appendix 2.

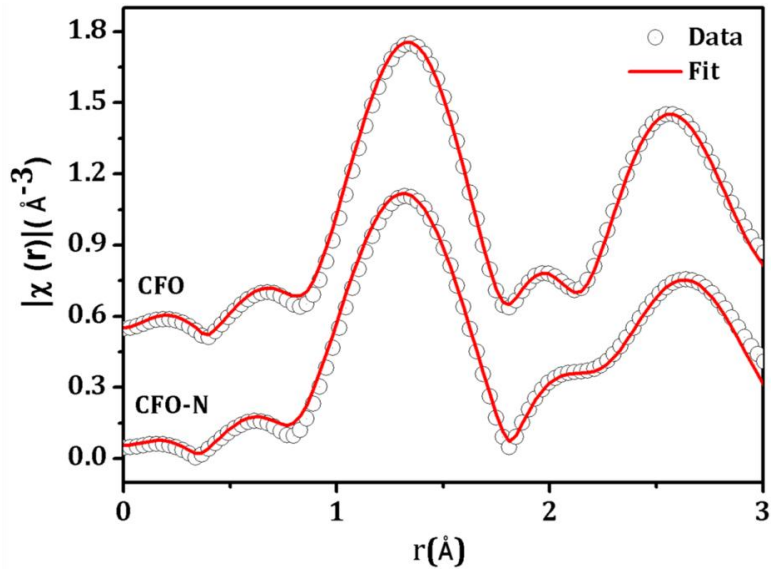

Figure 4.9 Fourier transformed EXAFS spectra of CFO and CFO-N at the Fe K-edge (scatter points) and theoretical fit (solid line).

The experimental χ(r) vs. r plots of CFO and CFO-N samples at Fe K-edge was fitted with theoretically simulated χ(r) vs. r plots generated assuming the brownmillerite structure of CFO. The structural parameters for the CFO are obtained from the reported crystal data. There are two nonequivalent Fe sites present in a unit

cell represented as Fe1 and Fe2. Following the above structure, the experimental data have been fitted assuming three Fe-O shells at 1.84(4×) Å, 1.96(4×) Å, 2.12(2×) Å and two Fe-Ca shells at 3.06(6×) Å and 3.31(4×) Å. Due to the limitation in number of fitting parameters set by Nyquist criterion, Fe-N paths are not explicitly considered during fitting of N doped sample, instead the changes in the Fe-O bond distances are studied carefully to predict the effect of doping. Figure 4.9 shows the experimental χ(r) vs. r plots of the CFO and CFO-N samples at Fe-K edge along with the best fit theoretical plots.

Table 4.3 Local Structural Parameters for CFO and CFO-N calculated by EXAFS measurements at Fe K-Edge

Path	Theoretical		CFO			CFO-N		
R Factor			0.0014			0.0023		
	r (Å)	N	r (Å)	N	σ2	r (Å)	N	σ2
Fe1-O1	1.84	4	1.88(1)	4	0.001(1)	1.85(1)	4	0.001(1)
Fe2-O1	1.96	4	2.05(1)	4	0.006(2)	2.02(1)	4	0.003(1)
Fe2-O2	2.12	2	2.31(2)	2	0.005(2)	2.30(1)	2	0.003(2)

The results obtained from the fitting of EXAFS data have been tabulated in Table 4.3. From the EXAFS results it can be seen that the Fe1-O1 (tetragonal Fe site) and Fe2-O1 (octahedral Fe site) bond lengths are slightly lower in CFO-N sample than that in the CFO, this might be a result of nitrogen doping. EXAFS and DFT studies carried out on N-doped TiO_2 systems by Ceotto et al [31] and Sahoo et al [32] to predict the location of N-dopant suggests that, interstitial doping of N in TiO_2 lattice increases both the equatorial and axial Ti-O bond distances while, substitutional doping does not change the bond distances significantly. In the present system also no considerable increase in the equatorial or axial bonds are observed. Also any extra peak that may correspond to the Fe-N bond is not observed in the spectra. Therefore, the chances of N occupying interstitial positions may be excluded hence the EXAFS results indicates that N substitutes O in the lattice.

Finally the current-voltage measurements on the parent and N-doped samples were performed to understand the effect of doping on the electrical properties of the samples. Figure 4.10 represents the I-V curves of CFO and CFO-N. The conductivity of CFO-N was found to be 3.07 x 10^{-8} S cm^{-1}, which is 100 times higher than that of the

parent brownmillerite. This can be attributed to the change in the electronic structure after the incorporation of N in the lattice of brownmillerite.

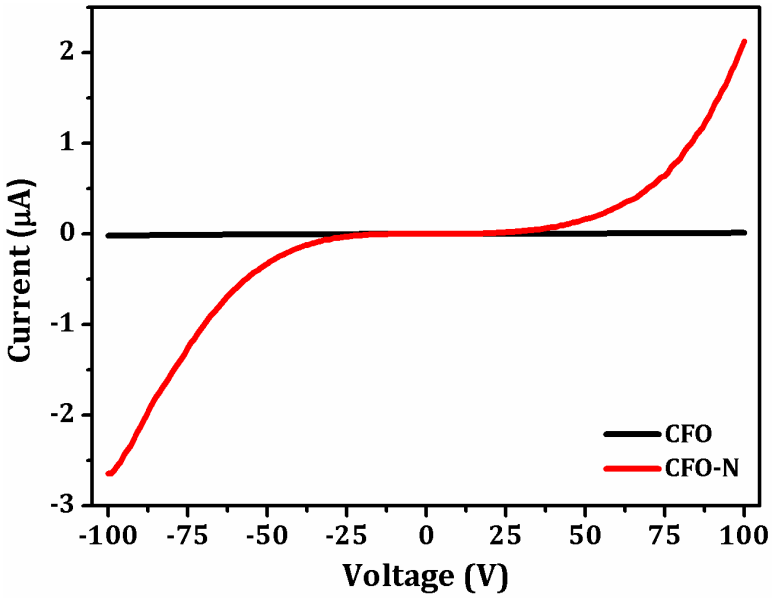

Figure 4.10 Current-voltage curves of CFO and CFO-N.

Thus a string of results comprising the neutron diffraction data, the change in the colour of the N-doped samples along with the reduction in band gap observed from the Tauc plot, XPS and XAS data enable us to conclude that the N-doping in the $Ca_2Fe_2O_5$ was successful and brings forth the existence of active Fe-Nx sites in the samples.

4.3.2. Electrochemical characterization

The electrocatalytic activity of CFO and CFO-N was initially screened by CV technique. To improve the conductivity of these synthesised samples, they were mixed with Vulcan XC-72. The CV of both the samples was recorded in N_2 and O_2 saturated 0.1 M KOH solution at a sweep rate of 50 mV s^{-1}. Figure 4.11 represents the cyclic voltammogram of CFO and CFO-N; both the samples exhibited a nearly rectangular CV curve in N_2 saturated. Interestingly, a distinct reduction peak ~ -0.21 V in O_2 saturated electrolyte was observed for both the samples. An increase in the reduction current after O_2 saturation indicates the ORR activity of both the samples. A reduction hump ~ -0.46 V could be due to redox reactions like $Fe^{+3/+2}$ from the electrocatalyst. Also it is worth to note that a capacitive behaviour is observed in CV profile, which may be due to anion-based intercalation pseudocapacitance as a result of presence of anion vacancy in the lattice [33].

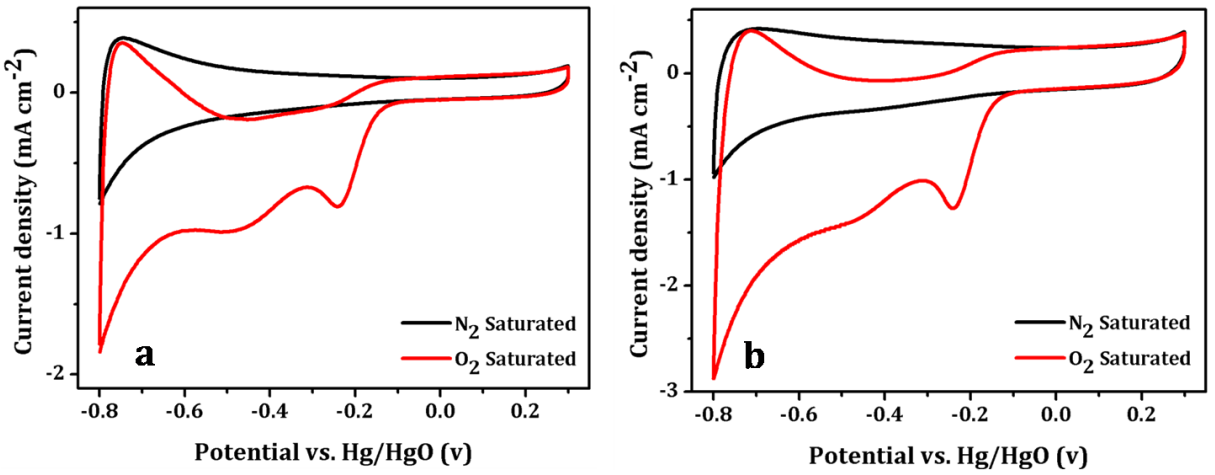

Figure 4.11 Cyclic voltammograms of **(a)** CFO and **(b)** CFO-N recorded in O_2 and N_2 saturated 0.1 M KOH solution at a sweep rate of 50 mVs^{-1} using Hg/HgO and Pt wire as the reference and counter electrode respectively.

A more detailed investigation on the ORR activity of the samples was performed by RDE and RRDE method. Figure 4.12 represents the LSV's of parent and N-doped CFO samples recorded at various electrode rotation rates in O_2 saturated 0.1 M KOH solution in an RDE electrode setup. The current density increases with increase in the rate of rotation due to enhanced rate of mass transport at higher electrode rotation [34].

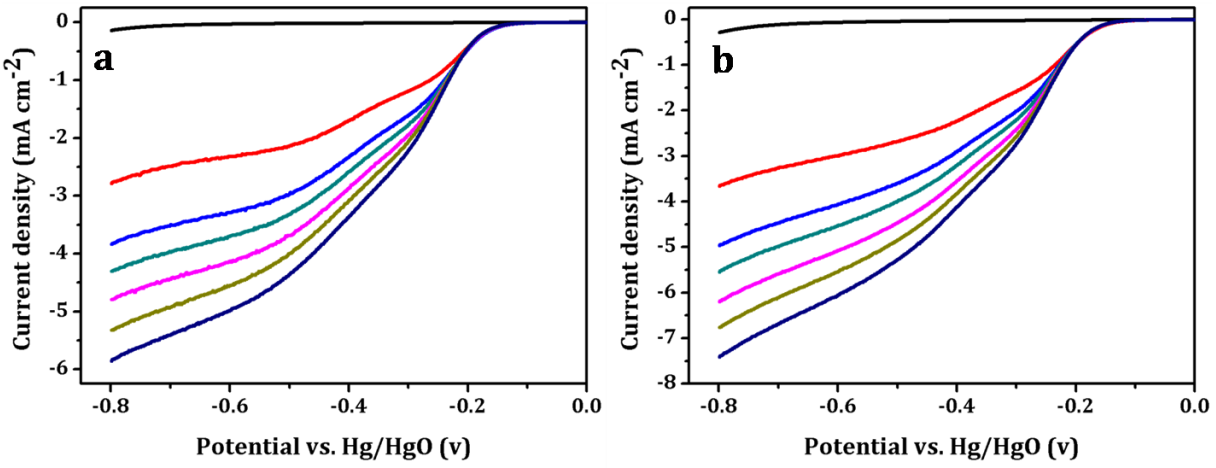

Figure 4.12 LSVs at different electrode rotation rates (black: blank, red: 400 rpm, blue: 900 rpm, green: 1200 rpm, pink: 1600 rpm, dark yellow: 2000 rpm and navy blue: 2500 rpm) for ORR on **(a)** CFO and **(b)** CFO-N. The experiments were performed in O_2 saturated 0.1 M KOH at a sweep rate of 5 mV s^{-1} using Hg/HgO and Pt wire as the reference and counter electrode respectively.

The voltammograms obtained on the disk and ring electrodes of RRDE in O_2 saturated 0.1 M KOH electrolyte at 1600 rpm is shown in Figure 4.13 (a). The disk current reflects the ORR activity of the sample whereas the ring current indicates the amount of peroxide formed during ORR on the electrode.

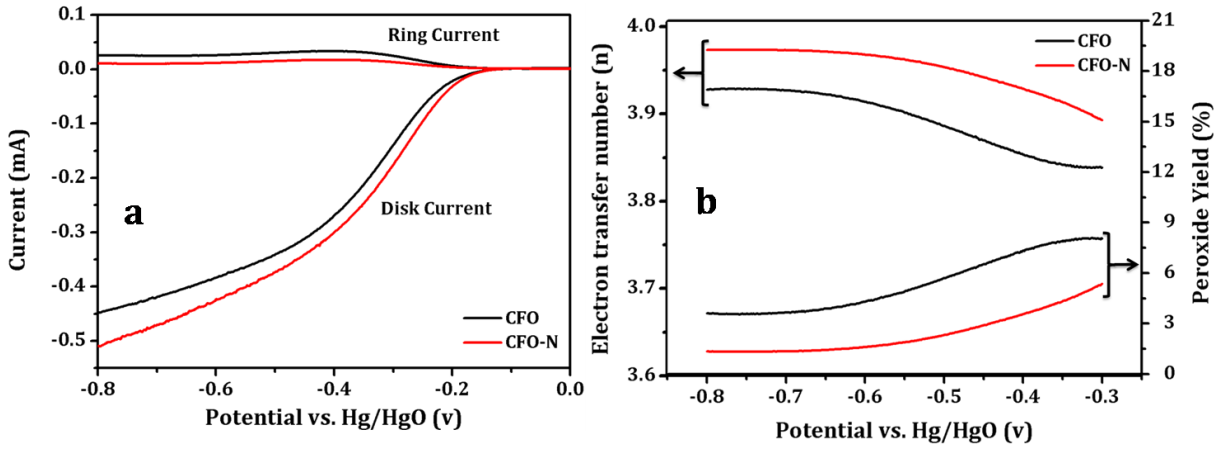

Figure 4.13 (a) RRDE voltammograms recoded on the disk and ring electrodes at an electrode rotating speed of 1600 rpm and **(b)** Electron transfer number and the percentage of peroxide generated at different potentials calculated from RRDE data. The experiments were performed in O_2-saturated 0.1 M KOH at a sweep rate of 5 mV s^{-1} using Hg/HgO and Pt wire as the reference and counter electrode respectively.

A positive shift of 10 mV in the onset potential of CFO-N was observed when compared to the parent CFO having onset potential at -0.16 V Vs Hg/HgO, also the cathodic current for CFO-N was higher than the parent CFO throughout the potential window indicating better electrocatalytic activity of N-doped CFO. The increased activity of N-doped sample can be attributed to the presence of Fe-N_x active sites and improved conductivity of CFO-N which will favour the transfer of charges from the catalyst to oxygen [35]. Further it can be observed that a current plateau characteristic for diffusion controlled region was not well defined in both the samples. This can be attributed to the fact that ORR is under a mixed kinetic-diffusion control over the whole potential range. Similar observations are previously reported on some of the non-Pt systems including Fe containing oxide systems [5, 36-38]. The lack of well defined mass transport region in Fe containing perovskite system can be correlated to the study conducted by Suntivich et al, where the authors have correlated the intrinsic ORR activity of perovskites (ABO_3) of first row transition elements (B) as a function of the e_g-filling of B site cations [39]. They observed a volcano shape for the ORR activity as a

function of the e_g-filling of B site cations; with the most active ORR ions (Mn, Ni & Co) placed near the peak of the volcano. Ease of adsorption and desorption of O_2 on B, through B-O_2 bond strengths, is connected to e_g - filling. Fe containing perovskites are placed at the base of the volcano plot (with $e_g > 1.5$) and hence has poorer adsorption-desorption capability. Hence this can be the reason for poor diffusion-controlled behaviour of most of the Fe containing oxides manifesting lack of well defined voltammograms.

From Figure 4.13 (a) it is evident that the ring current, which is indicative of the yield of peroxide species formed during the reaction, is slightly more for the parent CFO brownmillerite. The number of electrons (n) involved in the reaction pathway and the percentage of peroxide generated were calculated from the RRDE data using the below equation [40]

$$n = 4 \times \frac{I_D}{I_D + {I_r}/{N}}$$

$$\%HO_2^- = 200 \times \frac{{I_r}/{N}}{I_D + {I_r}/{N}}$$

Where I_D is disk current, I_r is ring current and N = 0.38 is current collection efficiency of Pt ring. The collection efficiency (N) was calculated by using simple reversible couple of ferrocyanide/ferricyanide system [41] as reported by Patil et al [42].

As evident from Figure 4.13 (b), it can be observed that for CFO, the number of electrons involved in the reaction is around 3.9 and that for CFO-N is around 3.95. This suggests that in both the compounds, ORR proceeds mainly through a four electron pathway. Further it can be observed that the peroxide yield is lesser for the N-doped sample when compared to the parent CFO brownmillerite which has a maximum of 8 % peroxide relative to the total product.

Stability of both the samples was evaluated by potentially cycling the catalyst at a scan rate of 50 mVs^{-1} in 0.1 M KOH for 5000 cycles. Figure 4.14 represents the LSV's taken before and after the stability test. It is evident from the figure that in both cases there is a decrease in the cathodic current after 5000 cycles. The decrease in the activity

can be attributed to the carbon corrosion and probably the weakening of carbon-oxide interface during potential cycling [43-45]. Interestingly it can be observed that the drop in the onset potential is prominent for CFO (~ 30 mV) whereas it is almost same for CFO-N indicating a better stability of N-doped sample.

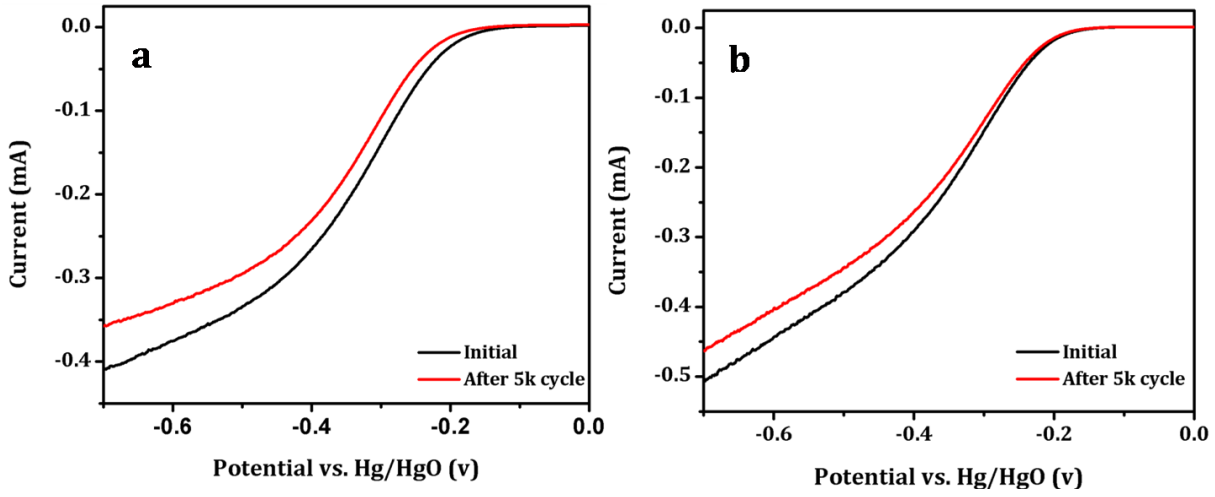

Figure 4.14 LSV's of **(a)** CFO and **(b)** CFO-N recorded before and after 5000 cycles. The experiments were performed in O_2-saturated 0.1 M KOH at a sweep rate of 5 mV s^{-1}.

Hence it can be observed that the incorporation of N in the brownmillerite lattice enhances the ORR activity of the catalyst. This is evident from the electrochemical characterizations performed using CV, RDE and RRDE which indicates an improved oxygen reduction activity in N-doped brownmillerite with a 10 mV positive shift in the onset potential and also a 4-electron reduction pathways with lower H_2O_2 production in CFO-N. N-doped brownmillerite sample also exhibited better stability.

To further establish the enhanced ORR activity of N-doped brownmillerites, structural and electrochemical analyses were carried out in other two brownmillerite systems viz., SFO and BFO along with their N-doped counterparts; SFO-N and BFO-N. Neutron diffraction data revealed that in SFO-N 10% of anionic sites were occupied by nitrogen atoms. However exact percentage of N in BFO-N could not be calculated owing to its complex structure which has 18 anionic sites. Further from Tauc plot (Figure 4.15 a & b) it was observed that as seen in CFO/CFO-N system, there was a reduction in the band gap after N-doping in SFO and BFO. Also a shift in the Fe 2p XP spectra (Figure 4.15 c & d) towards lower binding energy was observed for N-doped sample. Finally the electrical conductivity measurement (Figure 4.15 e & f) revealed that N-doped samples

exhibited higher conductivity than the parent SFO and BFO. Hence these results enable us to conclude that N-doping in the lattice of brownmillerites was successful and brings forth the existence of active Fe-N_x site in the compound.

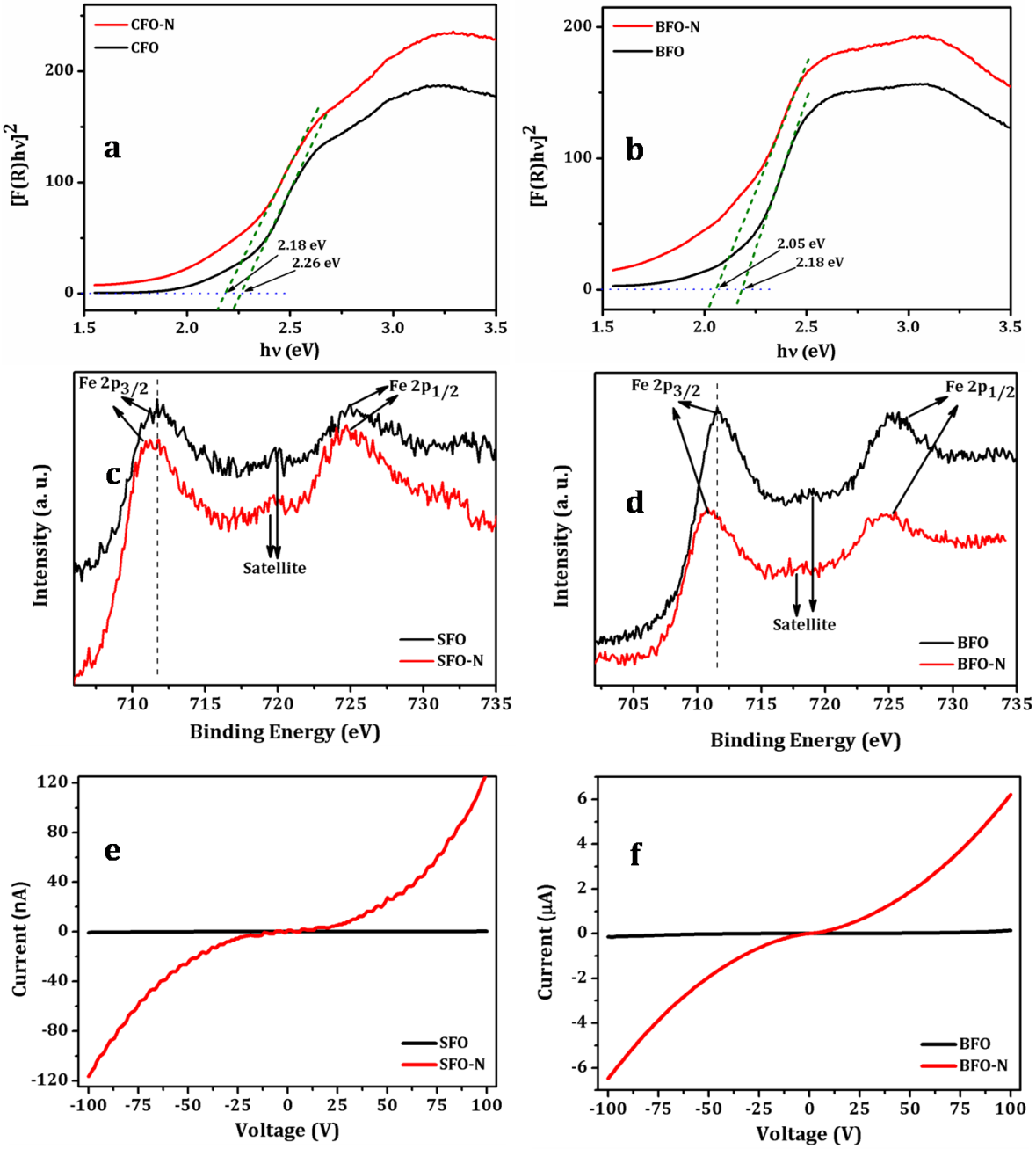

Figure 4.15 Tauc plot of **(a)** SFO & SFO-N and **(b)** BFO & BFO-N; Fe 2p XP spectra of **(c)** SFO & SFO-N and **(d)** BFO & BFO-N; Current-voltage curves of **(e)** SFO & SFO-N and **(f)** BFO & BFO-N.

The electrochemical results obtained in these systems were similar to that of CFO/CFO-N system. The results obtained from CV and RDE analysis of SFO/SFO-N and BFO/ BFO-N system are shown in Figure 4.16.

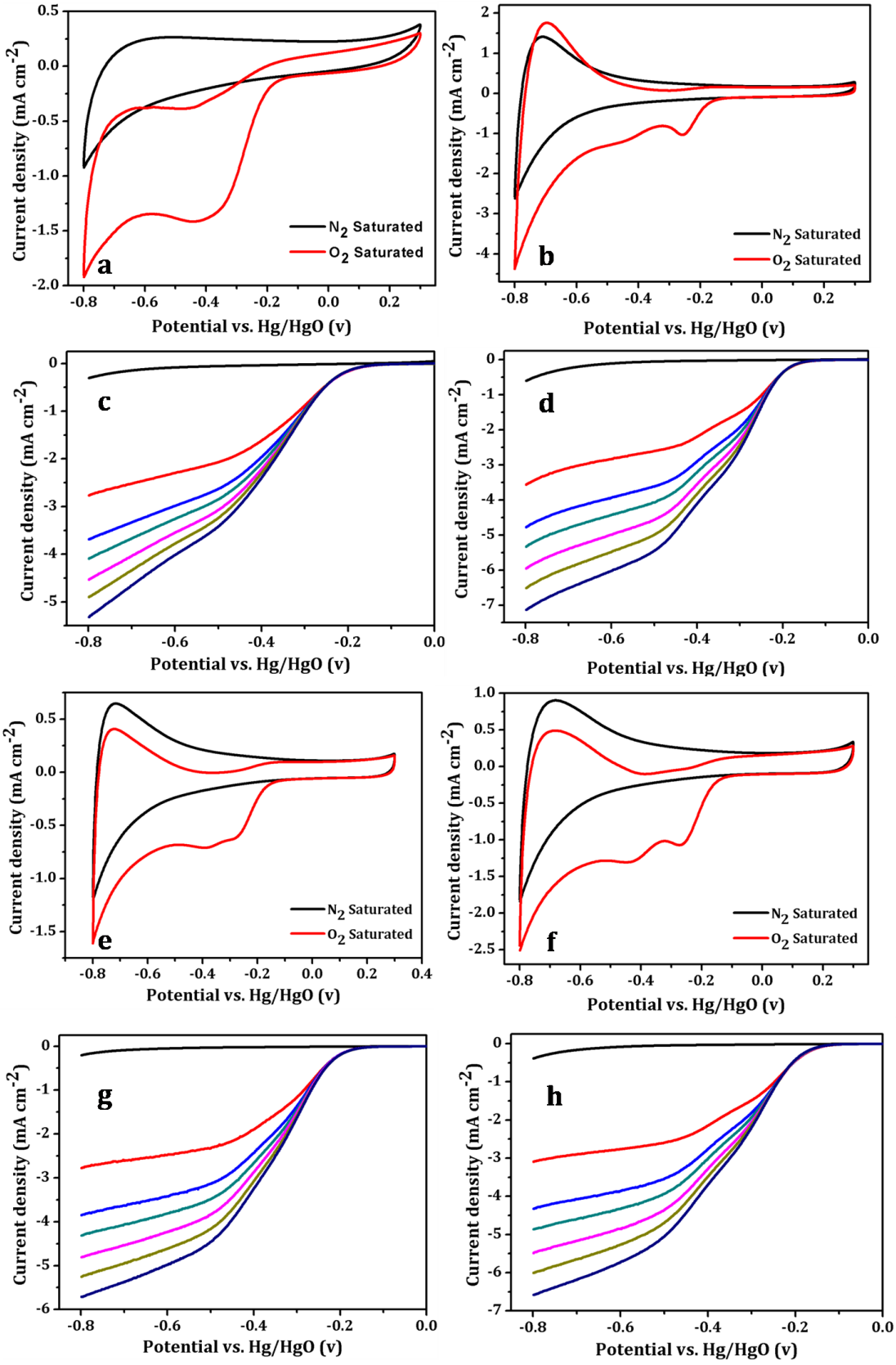

Figure 4.16 CV of **(a)** SFO, **(b)**SFO-N, **(e)** BFO & **(f)** BFO-N; LSV's at different electrode rotation rates (black: blank, red: 400 rpm, blue: 900 rpm, green: 1200 rpm, pink: 1600 rpm, dark yellow: 2000 rpm and navy blue: 2500 rpm) for ORR on **(C)** SFO, **(d)** SFO-N **(g)** BFO & **(h)**BFO-N.

In these samples also, N-doped materials exhibited better ORR activity than parent brownmillerites. The onset potential for SFO-N and BFO-N was 20 mV and 30 mV more positive than the parent SFO and BFO respectively. Although all these samples exhibits a near 4-electron reduction pathway but N-doped samples showed enhanced current density when compared to the parent brownmillerite.

Finally to understand the effect of structural parameters, if any, on the electrochemical activity, similar tests were conducted on N doped Fe_2O_3 synthesized by the same procedure. Fe_2O_3 is a simple binary oxide with each Fe atoms bonded to six oxygen atom and forming an octahedral geometry without any oxygen vacancies [46]. Figure 4.17 represents the LSV of CFO-N, SFO-N, BFO-N and Fe_2O_3-N. Although the onset potential of Fe_2O_3-N was close to that of other N-doped brownmillerite systems, a detailed study on the reaction kinetics showed that the ORR mechanism proceeds initially by a 2 electron pathway and later by a 4 electron pathway in Fe_2O_3-N. This variation in behaviour of simple Fe_2O_3 compared to brownmillerites indicates a contribution from the structural parameters like oxygen vacancies, which may act as oxygen absorption sites facilitating catalysis.

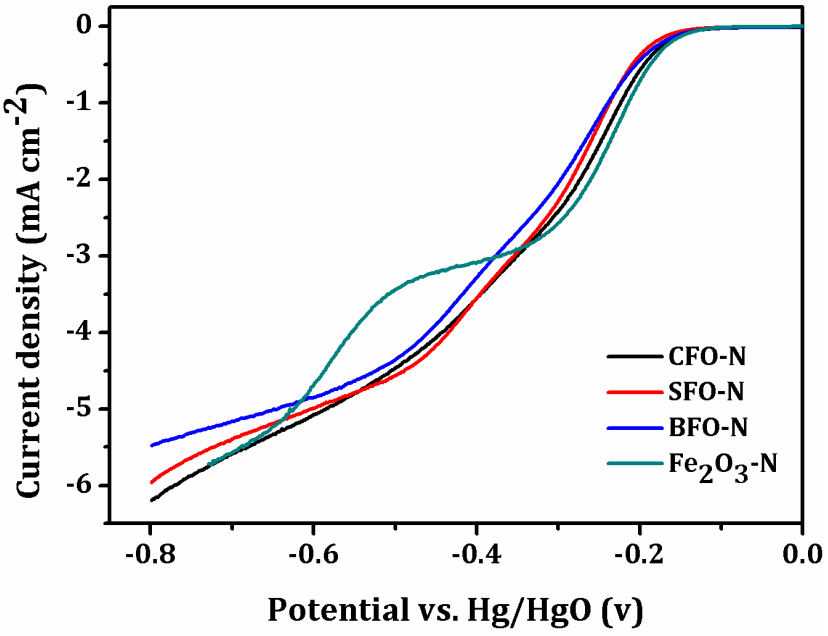

Figure 4.17 LSV's obtained at an electrode rotating speed of 1600 rpm with a rotating disk electrode for the ORR on CFO-N, SFO-N, BFO-N & Fe_2O_3-N. The experiments were performed in O_2-saturated 0.1 M KOH at a sweep rate of 5 mV s^{-1} using Hg/HgO as the reference electrode.

It is known from literature that on doping, N ions substitute oxide ions or exist in interstitial sites. From the neutron diffraction experiments along with XPS and XAS studies in the present system, the presence of N in the lattice is confirmed. The presence of catalytically active Fe-N_x site along with the presence of O_2 adsorption sites in the form of inherent oxygen vacancies enhances the ORR activity.

4.4. Conclusions

In summary, ORR activity of a brownmillerites $A_2Fe_2O_5$ (A = Ca, Sr & Ba) is compared with its N-doped counterpart. Oxides were synthesized by solid state method and further N-doping was achieved by passing ammonia through them. N-doping could be discerned by visual comparison consequent to colour changes in the sample. Rietveld refinement of neutron diffraction data with different models shows the presence of nitrogen in the structure as evident from the lowest χ^2 obtained for the model containing both O and N in anionic site. Oxygen site in the layer containing inherent oxygen vacancies in these systems are more labile for N substitution. Hence, creation of catalytic complexes of structure V_O-Fe-N is unambiguously proved. XPS shows broad peaks for N1s but a closer look into the Fe 2p XP spectra revealed a slight reduction in the binding energy of Fe in the doped compounds, attributed to the lower electronegativity of N in the proximity of Fe. XAS studies further confirm the presence of N in the lattice. An enhancement in the electrical conductivity of N-doped samples was also observed. N-doped brownmillerites exhibited enhanced ORR activity with positive shift in the onset potential and higher cathodic current than the parent brownmillerites. The enhancement in the activity is assigned to the presence of nitrogen in the proximity of Fe species forming a Fe-N_x active centre and also due to the higher electrical conductivity of N-doped samples which favors the transfer of charges from catalyst to oxygen. Further modification in the brownmillerite by B site doping with ORR active transition metals will lead to the disorder in the oxygen vacancy and will also bring positive shift in the overpotential. This type of shift in the overpotential on B-site doping is observed in previous chapters. Hence the current work can be envisaged as a potential strategy for improving the ORR activity of brownmillerite and other perovskite based oxide systems for future fuel cell technology.

4.5. References

1. Zhao, Z.; Li, M.; Zhang, L.; Dai, L.; Xia, Z. *Adv. Mater.* **2015**, *27*, 6834.
2. Gong, K.; Du, F.; Xia, Z.; Durstock, M.; Dai, L. *Science* **2009**, *323*, 760.
3. Chen, S.; Bi, J.; Zhao, Y.; Yang, L.; Zhang, C.; Ma, Y.; Wu, Q.; Wang, X.; Hu, Z. *Adv. Mater.* **2012**, *24*, 5593.
4. Liu, R.; Wu, D.; Feng, X.; Müllen, K. *Angew. Chem.* **2010**, *122*, 2619.
5. Wu, Z. S.; Yang, S.; Sun, Y.; Parvez, K.; Feng, X.; Müllen, K. *J. Am. Chem. Soc.* **2012**, *134*, 9082.
6. Parvez, K.; Yang, S.; Hernandez, Y.; Winter, A.; Turchanin, A.; Feng, X.; Müllen, K. *ACS Nano* **2012**, *6*, 9541.
7. Liang, Y.; Li, Y.; Wang, H.; Zhou, J.; Wang, J.; Regier, T.; Dai, H. *Nat. Mater.* **2011**, *10*, 780.
8. Zitolo, A.; Goellner, V.; Armel, V.; Sougrati, M. T.; Mineva, T.; Stievano, L.; Fonda, E.; Jaouen, F. *Nat. Mater.* **2015**, *14*, 937.
9. Chen, Z.; Higgins, D.; Yu, A.; Zhang, L.; Zhang, J. *Energ. Environ. Sci.* **2011**, *4*, 3167.
10. Liu, J.; Li, E.; Ruan, M.; Song, P.; Xu, W. *Catalysts* **2015**, *5*, 1167.
11. Yu, H.; Li, Y.; Li, X.; Fan, L.; Yang, S. *Chem. Eur. J.* **2014**, *20*, 3457.
12. Toby, B. H. *J. Appl. Crystallogr.* **2001**, *34*, 210.
13. Poswal, A. K.; Agrawal, A.; Yadav, A. K.; Nayak, C.; Basu, S.; Kane, S. R.; Garg, C. K.; Bhattachryya, D.; Jha, S. N.; Sahoo, N. K. *AIP Conf. Proc.* **2014**, *1591*, 649.
14. Basu, S.; Nayak, C.; Yadav, A. K.; Agrawal, A.; Poswal, A. K.; Bhattacharyya, D.; Jha, S. N.; Sahoo, N. K. *J. Phys Conf. Ser.* **2014**, *493*, 012032.
15. Koningsberger, D. C.; Prins, R. *Chemical Analysis, X-ray Absorption: Principles, Applications, Techniques of EXAFS SEXAFS, and XANES,* John Wiley & Sons, New York, **1988**, Vol. 91.
16. Kelly, S. D.; Hesterberg, D.; Ravel, B. *In Methods of Soil Analysis, Part 5-Mineralogical Methods; Ulery, A. L., Drees, L. R., Eds.* Soil Science Society of America: Madison, WI, **2008**, pp 367−464.
17. Newville, M.; Ravel, B.; Haskel, D.; Rehr, J. J.; Stern, E. A.; Yacoby, Y. *Physica B* **1995**, *208*, 154.
18. Meng, F.; Hong, Z.; Arndt, J.; Li, M.; Zhi, M.; Yang, F.; Wu, N. *Nano Res.* **2012**, *5*, 213.

19. Clemens, O.; Gröting, M.; Witte, R.; Perez-Mato, J. M.; Loho, C.; Berry, F. J.; Kruk, R.; Knight, K. S.; Wright, A. J.; Hahn, H.; Slater, P. R. *Inorg. Chem.* **2014**, *53*, 5911.
20. Wu, O. Y.; Parkin, I. P.; Hyett, G. *J. Solid State Chem.* **2012**, *190*, 169.
21. Wang, J.; Tafen, D. N.; Lewis, J. P.; Hong, Z.; Manivannan, A.; Zhi, M.; Li, M.; Wu, N. *J. Am. Chem. Soc.* **2009**, *131*, 12290.
22. Zou, F.; Jiang, Z.; Qin, X.; Zhao, Y.; Jiang, L.; Zhi, J.; Xiao, T.; Edwards, P. P. *Chem. Commun.* **2012**, *48*, 8514.
23. Asahi, R.; Morikawa, T.; Ohwaki, T.; Aoki, K.; Taga, Y. *Science* **2001**, *293*, 269.
24. Dhankhar, S.; Gupta, K.; Bhalerao, G.; Shukla, N.; Chandran, M.; Francis, B.; Tiwari, B.; Baskar, K.; Singh, S. *RSC Advances* **2015**, *5*, 92549.
25. Gupta, R. P.; Sen, S. K. *Phys. Rev. B* **1974**, *10*, 71.
26. Gupta, R. P.; Sen, S. K. *Phys. Rev. B* **1975**, *12*, 15.
27. Grosvenor, A. P.; Kobe, B. A.; Biesinger, M. C.; McIntyre, N. S. *Surf. Interface Anal.* **2004**, *36*, 1564.
28. Min Ji, S.; Borse, P. H.; Gyu Kim, H.; Won Hwang, D.; Suk Jang, J.; Won Bae, S.; Sung Lee, J. *Phys. Chem. Chem. Phys.* **2005**, *7*, 1315.
29. Grosvenor, A. P.; Greedan, J. E. *J Phys. Chem. C* **2009**, *113*, 11366.
30. Westre, T. E.; Kennepohl, P.; DeWitt, J. G.; Hedman, B.; Hodgson, K. O.; Solomon, E. I. *J. Am. Chem. Soc.* **1997**, *119*, 6297.
31. Ceotto, M.; Lo Presti, L.; Cappelletti, G.; Meroni, D.; Spadavecchia, F.; Zecca, R.; Leoni, M.; Scardi, P.; Bianchi, C. L.; Ardizzone, S. *J Phys. Chem. C* **2012**, *116*, 1764.
32. Sahoo, M.; Yadav, A. K.; Jha, S. N.; Bhattacharyya, D.; Mathews, T.; Sahoo, N. K.; Dash, S.; Tyagi, A. K. *J Phys. Chem. C* **2015**, *119*, 17640.
33. Mefford, J. T.; Hardin, W. G.; Dai, S.; Johnston, K. P.; Stevenson, K. J. *Nat. Mater.* **2014**, *13*, 726-732.
34. Town, J. L.; MacLaren, F.; Dewald, H. D. J. *Chem. Educ.* **1991**, *68*, 352.
35. Liu, H.; Li, J.; Xu, X.; Wang, F.; Liu, J.; Li, Z.; Ji, J. *Electrochim. Acta* **2013**, *93*, 25.
36. Fabbri, E.; Mohamed, R.; Levecque, P.; Conrad, O.; Kötz, R.; Schmidt, T. J. *ACS Catal.* **2014**, *4*, 1061.
37. Ryabova, A. S.; Napolskiy, F. S.; Poux, T.; Istomin, S. Y.; Bonnefont, A.; Antipin, D. M.; Baranchikov, A. Y.; Levin, E. E.; Abakumov, A. M.; Kéranguéven, G.; Antipov, E. V.; Tsirlina, G. A.; Savinova, E. R. *Electrochim. Acta* **2016**, *187*, 161.
38. Zhang, Y.; Fugane, K.; Mori, T.; Niu, L.; Ye, J. *J. Mater. Chem.* **2012**, *22*, 6575.

39. Suntivich, J.; Gasteiger, H. A.; Yabuuchi, N.; Nakanishi, H.; Goodenough, J. B.; Shao-Horn, Y. *Nat. Chem.* **2011**, *3*, 546.
40. Sunarso, J.; Torriero, A. A. J.; Zhou, W.; Howlett, P. C.; Forsyth, M. *J Phys. Chem. C* **2012**, *116*, 5827.
41. Hancock, C. A.; Ong, A. L.; Slater, P. R.; Varcoe, J. R. *J. Mater. Chem. A* **2014**, *2*, 3047-3056.
42. Patil, I. M.; Lokanathan, M.; Ganesan, B.; Swami, A.; Kakade, B. *Chem. Eur. J.* **2017**, *23*, 676.
43. Wang, L.; Yu, P.; Zhao, L.; Tian, C.; Zhao, D.; Zhou, W.; Yin, J.; Wang, R.; Fu, H. *Sci. Rep.* **2014**, *4*, 5184.
44. Sakthivel, M.; Bhandari, S.; Drillet, J. F. *ECS Electrochem. Lett.* **2015**, *4*, A56-A58.
45. Zhang, Z.; Liu, J.; Gu, J.; Su, L.; Cheng, L. *Energ. Environ. Sci.* **2014**, *7*, 2535-2558.
46. https://en.wikipedia.org/wiki/Iron(III)_oxide

Chapter 5

Summary and Conclusions

5.1. Summary

Chapter 1 presents a general introduction on the current scenario of energy demands and the consequence of using conventionally available fossil fuels and hence the need of a scientifically possible, environmentally acceptable and technologically promising alternative source of energy. The chapter emphasizes on new materials to meet the challenges in the field of energy. Among the vast families of materials, oxide based compounds in particular, perovskites have gained considerable attention owing to their unique structure and a wide window available for doping, thereby tuning the properties of the compound. The chapter describes the structural composition of perovskites and discusses some of the important applications of perovskite type oxides such as MIEC membranes, cathode and electrolyte materials in SOFC and as cathode materials for ORR in AFC. The role of oxygen vacancies in these applications is highlighted. A comprehensive review of literature on the ORR activity of perovskites and other non noble metal based systems such as N and metal doped carbon morphologies are discussed. The chapter briefly describes brownmillerites which are stable and structurally similar to perovskites but have inherent oxygen vacancies in the lattice. Finally the scope and objective of the thesis are mentioned.

Chapter 2A describes the synthesis of Ce doped $Ba_2In_2O_5$ viz $Ba_2In_{2-x}Ce_xO_{5+\delta}$. Structural parameters of the samples were obtained by the Rietveld refinement of the PXRD data. The compound retained brownmillerite structure for x = 0.5, however higher concentration of cerium in the lattice (x = 1 & 1.5) resulted in the loss of alternate layer of octahedra and tetrahedra and led to a highly disordered perovskite like structure with oxygen vacancies randomly distributed in the lattice. The lattice parameter increased with increase in the Ce concentration owing to higher crystal radii of Ce when compared to In. The octahedral distortion factor of the samples decreased with increase in the Ce concentration. Further Ce doping brings down the order-disorder temperature in the compounds as evident from HTXRD experiments. TGA data reveals that oxygen uptake decreases with increase in the Ce concentration which is attributed to the presence of Ce in +4 oxidation state. Parent $Ba_2In_2O_5$ with oxygen vacancies ordered in the alternate layers exhibited poor ORR activity. The ORR activity

increased with increase in Ce concentration in the In site. However, $BaCeO_3$, which is a stoichiometric perovskite without any oxygen vacancies or disorder, but with full occupancy of Ce in B site exhibited poor activity for ORR. Hence the presence of Ce and oxygen vacancies in the lattice separately does not lead to good activity but when combined, enhance the ORR activity in the doped compounds. The high temperature EIS measurements showed that with increase in cerium concentration and temperature, the impedance of the compounds decreases. The high temperature conductivity results and HTXRD data suggests that these compounds can be used as MIEC membranes and as cathode materials in SOFC at relatively lower temperature.

Chapter 2B describes the progressive doping of Zr in the In site of $BaCe_{05}In_{0.5}O_{3-\delta}$, while keeping the concentration of Ce constant in the lattice. By doping Zr(IV) in the In(III) site, the oxygen vacancies in the compounds are gradually decreased. Rietveld refinement on PXRD data indicated that the compounds crystallize in cubic perovskite phase in Pm-3m space group. Impurity phase of $BaIn_{0.5}Zr_{0.5}O_{3-\delta}$ was observed in all compounds whereas that of $BaCeO_3$ was observed in $BaCe_{0.5}In_{0.375}Zr_{0.125}O_{3-\delta}$. TGA data revealed that oxygen uptake decreases with increase in Zr doping indicating that the total oxygen vacancies in the compound decreases with increase in Zr concentration. HTXRD experiments under inert and oxidative atmosphere suggest that the compounds are stable under both these conditions till 700 °C. The ORR activity decreased with increase in the Zr concentration; in other words, with decrease in oxygen vacancies ORR activity also decreased. Similar behavior was observed in high temperature EIS experiments. Hence it can be summarized form these studies that oxygen vacancies in the lattice play pivotal role in electrochemical properties of oxide materials.

Chapter 3 reports cobalt doping in the indium site of $Ba_2In_2O_5$ which enhanced the conductivity of these oxide materials. Lower concentration of Co doping viz., $Ba_2In_{1.5}Co_{0.5}O_{5-\delta}$, retained the brownmillerite structure; however, higher concentrations of Co doped compounds viz., $BaIn_{0.5}Co_{0.5}O_{3-\delta}$ and $BaIn_{0.25}Co_{0.75}O_{3-\delta}$ crystallized in perovskite like structure with oxygen vacancy distributed randomly in the lattice. The lattice parameter decreased with increase in the Co concentration owing to the lower crystal radii of Co when compared to that of In. XPS studies revealed that Co existed in

+3 oxidation state. The oxygen uptake in all the samples was almost same indicating that the oxygen vacancies are almost same in the compounds. HTXRD measurements showed that the compounds were stable upto 600 °C. Co doped samples exhibited much better ORR activity when compared to the parent $Ba_2In_2O_5$ brownmillerite as well as Ce and Zr doped systems. Among the series of compounds, the sample with highest concentration of Co exhibited the best ORR activity. The high temperature EIS measurements performed on sintered pellets showed contribution from inductive effect. The conductivity at higher temperatures improved with Co doping.

Chapter 4 describes the synthesis of nitrogen doped $A_2Fe_2O_5$ (A = Ca, Sr & Ba) brownmillerites. N-doping in the brownmillerites was achieved by passing ammonia gas through them. N-doping led to the change in the color of the pristine samples; however, PXRD data indicated that the structure remained intact after N-doping. Rietveld refinement of neutron diffraction data with different models shows the presence of nitrogen in the structure as evident from the lowest χ^2 obtained for the model containing both O and N in anionic site. Oxygen site in the layer containing inherent oxygen vacancies in these systems were more labile for N substitution. Hence, presence of catalytic active complex viz., V_O-Fe-N is unambiguously proved. Although XPS data of N1s was poor owing to the low loading of N in the lattice, a closer look into the Fe 2p XP spectra revealed a slight reduction in the binding energy of Fe in the doped compounds which is attributed to the lower electronegativity of N in the proximity of Fe. XAS studies further confirmed the presence of N in the lattice. Electrical conductivity measurements revealed that N-doped samples exhibited better conductivity. N-doped brownmillerites exhibited enhanced ORR activity with positive shift in the onset potential and higher cathodic current than the parent brownmillerites. The enhancement in the activity is assigned to the presence of nitrogen in the proximity of Fe, forming a Fe-N_x active centre and also due to the higher electrical conductivity of N-doped compounds which favors the transfer of charges from catalyst to oxygen. Hence N-doping can be envisaged as a potential strategy for improving the ORR activity of brownmillerite and other perovskite based oxide systems for future fuel cell technology.

5.2. Conclusions

- Cerium doped $Ba_2In_2O_5$ was synthesized. Doping in the B site led to the disorder in the oxygen vacancies in the lattice.
- All the samples were stable under inert and oxidative condition at higher temperature. Also the order-disorder transition temperature of brownmillerites came down after Ce doping.
- The presence of both Ce and oxygen vacancies in the lattice enhanced the ORR activity of the compounds in alkaline medium however these features when present separately do not lead to good activity.
- The conductivity of the samples at higher temperature improved with Ce doping.
- $BaCe_{0.5}In_{0.5-x}Zr_xO_{3-\delta}$ with varying oxygen vacancies were synthesized to study the effect of oxygen vacancy in ORR and high temperature conductivity.
- ORR activity and high temperature conductivity decreased with decrease in oxygen vacancies in the lattice.
- Co doping in $Ba_2In_2O_5$ was performed to improve the conductivity of the compound.
- XPS studies revealed the presence of Co(III) in place of In(III) which was also evident form almost same oxygen uptake in all the Co doped samples.
- Sample with highest doping of Co exhibited better ORR activity due to the better catalytic effect of Co and its high conductivity.
- Incorporation of Fe-N site in brownmillerite was achieved and was unambiguously proved using neutron diffraction and XAS measurements.
- ORR activity of $A_2Fe_2O_5$ brownmillerites enhanced after N-doping.
- Presence of V_o-Fe-N site is envisaged to increase the electrocatalytic activity of N-doped brownmillerite.

List of Publications

1. Nitrogen Doping in Oxygen-Deficient $Ca_2Fe_2O_5$: A Strategy for Efficient Oxygen Reduction Oxide Catalysts; **Chamundi P. Jijil**, Moorthi Lokanathan, Sundaresan Chithiravel, Chandrani Nayak, Dibyendu Bhattacharyya, Shambu Nath Jha, P.D. Babu, Bhalchandra Kakade and R. Nandini Devi. *ACS Appl. Mater. Interfaces* **2016**, *8*, 34387.
2. Effect of B Site Coordination Environment in the ORR Activity in Disordered Brownmillerites $Ba_2In_{2-x}Ce_xO_{5+\delta}$; **Chamundi P. Jijil**, Siddheshwar N Bhange, Kurungot Sreekumar, and R. Nandini Devi. *ACS Appl. Mater. Interfaces* **2015**, *7*, 3041.
3. Disordered Brownmillerite $Ba_2InCeO_{5+\delta}$ with Enhanced Oxygen Reduction Activity; **Chamundi P. Jijil**, Sreekuttan Maraveedu Unni, Kurungot Sreekumar, and R. Nandini Devi. *Chem. Mater.* **2012**, *24*, 2823.
4. In situ Encapsulation of Ultra Small Ceria Nanoparticles Stable at High Temperatures in the Channels of Mesoporous Silica; Sumona Ghosh, **Chamundi P. Jijil**, R. Nandini Devi. *Micropor. Mesopor. Mat*. **2012**, *155*, 215.
5. Cobalt doped $Ba_2In_2O_5$ Brownmillerites: an Efficient Electrocatalyst for Oxygen Reduction in Alkaline Media; **Chamundi P. Jijil**, Indrajit M. Patil, Bhalchandra Kakade and R. Nandini Devi. *Manuscript communicated,* **2016**.

Contributions to Symposia/Conference

1. Poster & oral presentation in International Symposium on Solid State Chemistry held at JNCASR, Bangalore, India during December 01-03, 2016. (Title: Designing Efficient Oxygen Reduction Catalyst: via. N-Doping in $Ca_2Fe_2O_5$ Brownmillerite)
2. Oral presentation in 3rd Indo-French Bilateral Symposium on Catalysis for Sustainable & Environmental Chemistry held at CSIR-NCL, Pune, India during October 29-31, 2014. (Title: Disordered Brownmillerites $Ba_2In_{2-x}Ce_xO_{5+\delta}$ as catalysts for oxygen reduction reaction)
3. Oral presentation in 21st National Symposium On Catalysis "Catalysts For Sustainable Development" (CATSYMP-21) held at CSIR-IICT, Hyderabad, India during February 10-13, 2013. (Title: Disordered Brownmillerite as an Effective ORR Catalyst)
4. Poster presentation in National Science Day Celebration-2012 held at CSIR-NCL, Pune, India during February 27-28, 2012. (Title: Novel Disordered $Ba_2InCeO_{5+\delta}$ Brownmillerite With enhanced oxygen reduction activity)
5. Poster presentation in the International conference on Membranes: Environmental and Biological Applications (ICM 2011) held at Hotel Windsor Castle, organized by CEET and MG University, Kottayam, Kerala, India during September 16-19, 2011. (Title: Synthesis and Oxide Ion Conductivity of Ce Doped $Ba_2In_2O_5$)
6. Poster presentation in National Science Day Celebration-2011 held at CSIR-NCL, Pune, India during February 24-25, 2011.
7. Poster presentation in 20th National Symposium On Catalysis "Catalysis for Energy Conversion and Conservation of Environment" (CATSYMP-20) held at IIT Madras, India during December 19-22, 2010. (Title: Synthesis and oxide ion conductivity of doped $Ba_2In_2O_5$).

Appendix 1

Physicochemical Characterizations

Various physicochemical techniques were used for the characterization of the brownmillerite type materials studied in this thesis. The principles of techniques used in the present study like; powder diffraction using laboratory X-rays or neutron and its Rietveld refinement, XPS, XAS, Raman spectroscopy, UV-visible spectroscopy, Surface area analysis using N_2 adsorption, CV, RDE, RRDE and Impedance spectroscopy are discussed in details in the following sections.

1. Powder Diffraction

The structure of an idealized crystal lattice consists of periodic arrangement of atom which can be understood clearly by single crystal analysis. However, because of the unavailability of suitable single crystals in many cases and to extract information on the bulk material, alternative technique such as powder diffraction is routinely used. Moreover it can be used for the determination of microstructural properties, disorder in materials, studies of macroscopic stresses in components, and texture of polycrystalline samples.

X-rays are electromagnetic waves having wavelengths of the order of 1 Å, which is comparable with the spacing between lattice planes in crystals. XRD, based on wide-angle elastic scattering of X-rays is the most important and common tool to determine the structure of the materials characterized by the long range ordering. XRD involves the measurement of the intensity of X-rays scattered from electrons bound to atoms. Waves scattered at atoms at different positions arrive at the detector with a relative phase shift. Therefore, the measured intensities yield information about the relative atomic positions. The diffraction patterns give information about structure formation, phase purity, degree of crystallinity, and unit cell parameters of the materials. The formation of a structural phase can be confirmed by comparing the powder diffraction patterns with that of pure reference phases distributed by International Center for Diffraction Data (ICDD).

The use of Bragg's equation is the easiest way to get to the structural information in powder diffraction, the derivation of which considers X-ray diffraction as a reflection of X-rays by sets of lattice planes. As the X-rays penetrate deeply, additional reflections occur at thousands of consecutive parallel planes. The overlap of the scattered X-rays occur since all are reflected in the same direction. The Braggs equation is, $n\lambda = 2d\sin\theta$, where d is the interplanar spacing of parallel lattice planes and 2θ is the diffraction angle, which is the angle between the incident and diffracted X-ray beams.

Sharp intensities emerge from the sample only at the special angles where Bragg's equation holds. For crystalline materials, the destructive interference results in a completely destruction of intensity in all the other directions. In the modern flat-plate powder X-ray diffractometer, which is used most commonly in industrial and academic laboratories, the divergent incident beam is allowed to reflect from the sample and converges at a fixed radius from the sample position. This configuration is commonly referred to as "Bragg–Brentano" geometry (shown in Figure 1).

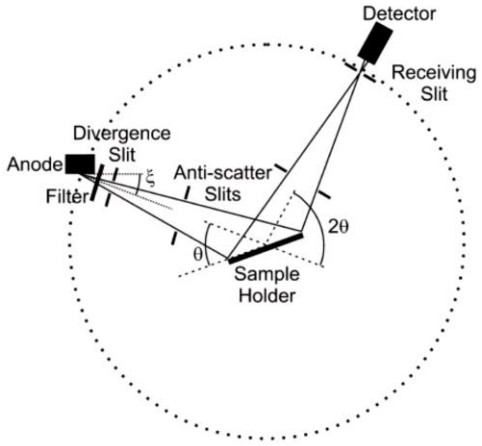

Figure 1. Schematic representation of Bragg-Brentano geometry used for XRD.

Powder diffraction experiments, exploits X-rays from a laboratory generator or from a high energy storage ring (synchrotron radiation), or neutrons produced in a reactor or spallation source. The typical wavelength used lies in the range 0.1 – 5 Å, comparable with the spacing between lattice planes in crystals. Data can be collected in transmission or reflection modes, depending on the absorption of radiation by the sample. A brief

description of the different sources used for the powder diffraction experiments are given here.

1.1. Laboratory X-ray Sources

In a standard laboratory instrument, X-rays are produced in a sealed - tube source where electrons, accelerated by a potential difference of up to 60 kV, is bombard with a metal anode inside a vacuum tube. This results in the formation of a characteristic radiation spectrum composed of discrete peaks arising from the filling of vacant level in the inner shell (created from the ejection of electron by the incoming high energy electron) by a higher atomic level electron. The emission of an X-ray photon is characterized by the difference in energy between the two levels. A higher resolution copper X-ray spectrum consists of components labeled as $K_{\alpha 1}$ (1.54056 Å) and $K_{\alpha 2}$(1.54439 Å). The most commonly used target element is Cu but Mo, Cr, Fe, Co, Ag and W are also used for special applications. Cu tube is the most common choice for routine analysis, which gives X-rays of shortest wavelength above 1 Å. Also relatively high power can be applied to the target because of the good thermal conductivity of copper.

Table1. Approximate principle emission lines for various anode targets.

Anode	Cu	Mo	Cr	Fe	Co	Ag	W
$\lambda(K_\alpha)$ Å	1.54	0.71	2.29	1.94	1.79	0.56	0.21

1.2. Neutron Scattering

Neutron radiation of sufficient intensity can be provided at research reactors and spallation neutron sources. A neutron even though uncharged has a magnetic moment as a result of its spin (spin of 1/2) and therefore it can approach the nucleus of atoms closely. This result in scattering of neutrons by nuclear forces or via spin - spin interactions with both nuclear magnetic moments and unpaired electrons in magnetic atoms or ions. The scattering cross section, σ, measured in barns (1 barn = 10^{-28} m^2) is used to describe the scattering of a neutron by a nucleus which is defined as equal to the effective area presented by the nucleus to the incoming neutron. The scattering occurs isotropically as

the range of the neutron - nucleus interaction is tiny compared to the wavelength of the neutron making the nucleus essentially a point scatterer.

In the case of X-ray diffraction, the photons are scattered by the interaction of electron cloud of the material and this means that in presence of heavier atoms, it may be difficult to detect lighter atoms. However, most atoms have neutron scattering lengths of approximately equal in magnitude (as shown in Table 2) and hence neutron diffraction techniques are used to detect light elements and also to distinguish nearby elements.

Table 2. Scattering cross section for X-rays and neutrons.

Element		$_{1}$**H**	$_{6}$**C**	$_{25}$**Mn**	$_{26}$**Fe**	$_{28}$**Ni**	$_{46}$**Pd**	$_{67}$**Ho**	$_{92}$**U**
σ_{coh}	X-ray	0.66	24	416	450	522	1406	2986	5631
(barn)	Neutron	1.76	5.55	1.75	11.22	13.30	4.39	8.06	8.90

The properties of a radiation source can be characterized by parameters such as spectral flux and brightness. Flux is the number of photons travelling through unit area in unit time. The spectral brightness is defined as photon flux density in phase space about a certain frequency. This means the number of photons per unit time per unit area per unit solid angle

$$\text{Spectral flux} = \text{Photons } s^{-1}(0.1\% \text{ bandwidth})^{-1}$$

$$\text{Brightness} = \text{Photons } s^{-1}\, \text{mrad}^{-2}\, (0.1\%\text{bandwidth})^{-1}$$

A comparison of brightness and flux of X-rays and neutrons from various sources is given in the following table.

Table 3. Brightness and flux for generalized X-ray and neutron sources.

Source type	Brightness ($s^{-1}m^{-2}ster^{-1}$)	Divergence ($mrad^2$)	Flux ($s^{-1}m^{-2}$)
Neutron reactor source	10^{15}	10x10	$1x10^{11}$
X-ray tube	10^{20}	0.5x10	$5x10^{14}$
Synchrotron bending magnet	10^{27}	0.1x5	$5x10^{20}$
Synchrotron undulator	10^{33}	0.01x0.1	$1x10^{24}$

1.3. Rietveld refinement

Rietveld refinement is a technique devised by Hugo Rietveld for use in the characterization of crystalline materials. Rietveld method is a powerful technique that makes use of the entire powder pattern instead of analyzing individual, non - overlapped, diffraction peaks for crystal structure refinement. The advantage of this method is that it calculates the entire powder pattern of a crystalline model, including various experimental and sample dependent effects. Rietveld method essentially tries to fit a structural model based on a number of crystal structure parameters to the experimental diffraction data. This model utilizes a least-squares approach where various parameters such as lattice parameters, atomic positions and parameters such as peak shape, background, scale factors, peak broadening, that describe the experimental and sample conditions, are allowed to vary to reach an agreement between the calculated and measured diffraction profiles. However to employ this method, a good initial knowledge of the structure is needed which is refined by small adjustments. The method can be utilized to refine several powder or single crystal diffraction data such as reactor neutron data, laboratory X-ray powder diffraction data, synchrotron powder diffraction data, time-of-flight neutron data from pulsed spallation sources, and to refinements of magnetic structures. Rietveld analysis is carried out mostly for the determination of the structural parameters, but increasingly, the method is also used to determine relative amounts of the crystallographic phases, the preferred orientation, residual stress, crystallite size etc. This method further helps to quantitatively detect small amounts of polymorphic phases which are of great interest especially for pharmaceutical research and in the concrete business. Currently various softwares are available for the Rietveld refinement such as GSAS, GSAS-EXPGUI, Fullprof, TOPAS, JANA2000, Rietan etc.

2. X-ray photoelectron spectroscopy

X-ray Photoelectron Spectroscopy (XPS) or Electron Spectroscopy for Chemical Analysis (ESCA) is based on the principle that when X-rays hit atoms, electrons are ejected. It is a typical surface sensitive technique as electrons that are generated in the top few atomic layers (mean free path ~1.5 nm) are detected, even though the absorption length of

the X-rays is about 100-1000 nm. The technique provides quantitative information about the elemental composition of the surface of all kinds of solid material like insulators, conductors, polymers etc. The sample material is irradiated with mono energetic soft x-rays causing electrons to be ejected. The measurement of kinetic energies of these ejected photoelectrons helps in the identification of the elements in the sample as each element produces a characteristic set of XPS peaks at characteristic binding energy values. All elements except H and He can be detected. Moreover the relative concentrations of elements can be determined from the photoelectron intensities. The most important advantage of XPS is its ability to obtain information on chemical states from the variations in binding energies, or chemical shifts, of the photoelectron lines. Most modern instruments have detection limits for most of the elements in the parts per thousand ranges. Detection limits of parts per million (ppm) are possible under special conditions such as concentration at top surface or very long collection time.

In XPS, soft X-rays with energies range from 200-2000 eV are used. The development of synchrotron radiation sources has enabled high resolution studies with much wider and more complete energy range (5-5000 eV). A sample placed in ultra-high vacuum is irradiated with photons of energy, hν. Electrons of the atoms on the surface absorb the photons and leave the atom by using some of its energy to overcome the coulomb attraction of the nucleus, reducing its KE by its initial state BE. The kinetic energy of the ejected electron is related to the energy of the X-ray photon as

$$KE = h\nu - BE - \Phi$$

Where, BE represents the binding energy of the atomic orbital from which the electron are ejected and Φ is the spectrometer work function which is an adjustable instrumental correction factor that accounts for the few eV of KE loss of the photoelectron as it becomes absorbed by the instrument's detector. An electron energy analyzer measures the kinetic energy distribution of the emitted photoelectrons and a photoelectron spectrum can thus be recorded.

The number of detected electrons is a measure for the elemental concentration. Atomic concentrations can be obtained by dividing the peak areas by standard sensitivity

factors and normalizing to 100%. For bulk materials the surface concentrations can be determined with a 20% inaccuracy. However, in most cases, the surface composition varies as a function of depth, where the signal of an element in a lower layer will be attenuated more strongly than that in the top layer. In such cases either angle-resolved measurements or model calculations are performed to extract quantitative information.

Electrons travelling through a material have a relatively high probability of experiencing inelastic collisions with locally bound electrons as a result of which, they suffer energy loss contributing to the background of the spectrum rather than a specific peak. Due to this inelastic scattering process, the flux of photoelectrons emerging from the sample is much attenuated. Consequently, in some cases the satellite peaks emerge on both the high and low BE side of the main peaks. These peaks give valuable information about the defect complex or the different charge states present, if any. Thus, significant qualitative and quantitative information about the chemical state of elements present in various materials can be obtained from XPS analysis. Apart from this, XPS is a versatile *in-situ* analysis tool for understanding the growth kinetics. However, many limitations are associated with this technique. First, high vacuum condition is needed to run these experiments and hence samples must be dried properly. Sometimes, this drying may impact few subtle systems resulting in many chemical transformations in the sample. Beam-induced damage and carbon contamination from XPS chamber are few other limitations of XPS.

3. X-ray absorption spectroscopy

Through a photoelectric process, the x-rays can be absorbed by all matter. Thereby the energy of the X-ray photon is used to excite a core-electron and the atom is left in an excited state with an empty electron orbital (a core hole). The excited electron is called photo-electron and the kinetic energy of this electron $E_{K.E.,}$ equals the difference of the energy from the photon and the binding energy of the electron $E_{B.E.}$ ($E_{K.E.} = E_{phot} - E_{B.E.}$). The probability that an X-ray photon is absorbed by the radiated material is given by the absorption coefficient μ and it can be observed that μ increases strongly when the X-ray

energies equal the binding energies $E_{B.E.}$ of a core-electron of an element in the investigated material.

These step-like features in an absorption spectrum are called absorption edges. X-ray absorption spectra measured at condensed matter show oscillations just above the absorption edge. These oscillations are called X-ray absorption fine structure and result from the fact that in condensed matter all atoms are embedded in a defined structure with neighboring atoms at specified distances. The absorption spectrum contains information on the structure of the investigated material. The information content depends on the x-ray energy with respect to the binding energy of the electron and thus the spectrum can be divided into two parts: the X-ray absorption near edge structure (XANES) and the extended X-ray absorption fine structure (EXAFS).

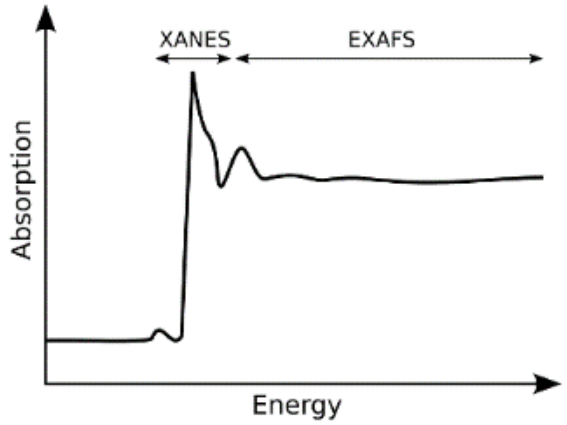

Figure 2. X-ray absorption spectrum.

The near edge structure extends up to 50 eV above the absorption edge. In this energy region the core electron is excited to an unoccupied bound state, so that the shape of the absorption edge depends on the density of states closely above the Fermi level. Therefore, the oxidation state and binding geometry affect the XANES part of the spectrum. The region from 50 eV-1000 eV above an absorption edge is called EXAFS. This part of the spectrum contains information on the types and number of neighbor atoms to the absorbing atom.

In order to take care of the oscillations in the absorption spectra, it has been converted to absorption function defined as follows

$$\chi(E) = \frac{\mu(E) - \mu_0(E)}{\Delta\mu_0(E_0)}$$

Where, E_0 absorption edge energy, $\mu_0(E_0)$ is the bare atom background and $\Delta\mu_0(E_0)$ is the step in $\mu(E)$ value at the absorption edge. The energy dependent absorption coefficient $\chi(E)$ has been converted to the wave number dependent absorption coefficient using relation,

$$K = \sqrt{\frac{2m(E - E_0)}{\hbar^2}}$$

Where, m is the electron mass.

$\chi(k)$ is weighted by k to amplify the oscillation at high and the χ(k)k functions are Fourier transformed in R space to generate the $\chi(R)$ versus R spectra in terms of the real distances from the center of the absorbing atom. The set of EXAFS data analysis available in within IFEFFIT software package have been widely used for EXAFS data analysis. This includes background reduction and Fourier transform to derive the $\chi(R)$ versus R spectra from the absorption spectra (using ATHENA software), generation of the theoretical EXAFS spectra starting from an assumed crystallographic structure and finally fitting of experimental data with the theoretical spectra using ARTEMIS software.

4. Raman Spectroscopy

Raman spectroscopy is a powerful tool to analyze structural, morphological and electronic properties of materials at a local level. When light encounters molecules in air, the predominant mode of scattering is elastic scattering, called Rayleigh scattering. It is also possible for the incident photons to interact with the molecules in such a way that energy is either gained or lost so that the scattered photons are shifted in frequency. Such

inelastic scattering is called Raman scattering. Like Rayleigh scattering, the Raman scattering depends upon the polarizability of the molecules. For polarizable molecules, the incident photon energy can excite vibrational modes of the molecules, yielding scattered photons, which are diminished in energy by the amount of the vibrational transition energies. A spectral analysis of the scattered light under these circumstances will reveal spectral satellite lines below the Rayleigh scattering peak at the incident frequency. Such lines are called "Stokes lines". If there is significant excitation of vibrational excited states of the scattering molecules, then it is also possible to observe scattering at frequencies above the incident frequency. These lines, generally weaker, are called anti-Stokes lines, (Figure 3). Since the Raman Effect depends upon the polarizability of the molecule, it can be observed for molecules, which have no net dipole moment and therefore produce no pure rotational spectrum. This process can yield information about the moment of inertia and hence the structure of the molecule.

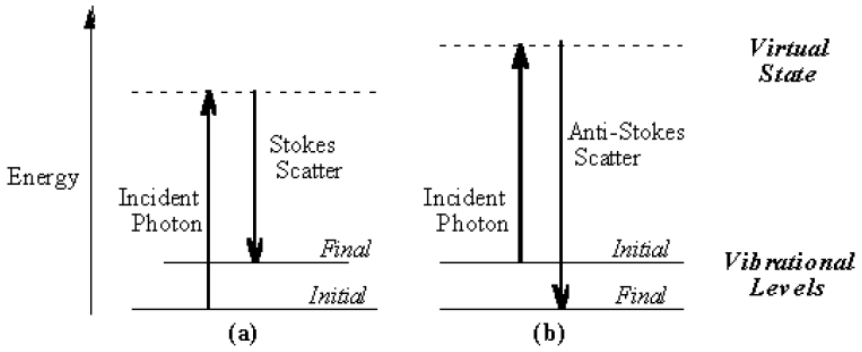

Figure 3. Energy level diagram for Raman scattering.

In Raman scattering, an intense monochromatic light source (laser) can give scattered light, which includes one or more "sidebands" that are offset by rotational and/or vibrational energy differences. Since the sideband frequencies contain information about the scattering medium, which could be useful for identification. Moreover, the Raman bands are the characteristics of the structure and give valuable information about the structure, size and crystal surface area. However, the main limitations of Raman spectroscopy are its inherently low intensity compared to that of the elastically scattered

laser intensity and interference from fluorescence due to the electronic excitation of the molecule by the laser.

5. UV-visible Spectroscopy

Absorption spectroscopy in the visible region has long been an important tool to the analyst. Appearance of colour arises from the property of the coloured material to absorb selectively and reflect its complementary colour which falls within the visible region of the electromagnetic spectrum. Absorption of energy leads to a transition of electron from ground state to an excited state which is governed by the following equation

$$\Delta E = h\nu = hc/\lambda$$

Where, h represents Planck's constant, ν is the frequency of radiation, c is the velocity of light and λ is the radiation wavelength. Thus from the equation it seems that the UV-energy is quantized and hence a single discrete line should be obtained from a single electronic spectrum. However, this is not the case in reality as excitation of electronic energy levels would also involve excitation of the embedded vibrational and rotational energy levels of an atom, thus giving rise to a broad absorption band. The intensity of the absorption band depends on three factors namely (a) transition probability, (b) population of states and (c) concentration or path length.

Almost all relationships between intensities of incident and transmitted radiation with the concentration and path-length is governed by Beer-Lambert's law which is given as

$$I = I_0 \exp(-\kappa cl)$$

$$\log (I_0/I) = A = \kappa cl$$

where, I = Intensity of the emitted radiation, I_0 = Intensity of the incident radiation, κ = constant, c = concentration and l = path length. A is known as the absorbance or the optical density and κ, the constant generally represented as ε, known as the molar absorption coefficient.

In a dual beam spectrophotometer, light from either the visible or ultraviolet source enters the grating monochromator before it reaches the filter. Broad band filters contained in a filter wheel are automatically indexed into position at the required wavelengths to reduce the amount of stray light and unwanted orders from the diffraction grating. The light from the source is alternatively split into one of the two beams by a rotating mirror called a chopper; one beam is passed through the sample and the other through the reference. The detector alternately sees the beam from the sample and then the reference. Its output which ideally would be an oscillating square-wave gives the ratio of I to I_o directly i.e. the reference correction is made automatically.

Array-detector spectrophotometers allow rapid recording of absorption spectra. Dispersing the source light after it passes through a sample allows the use of an array detector to simultaneously record the transmitted light power at multiple wavelengths. These spectrometers use photodiode arrays as the detector. The light source is a continuum source such as a tungsten lamp. All wavelengths pass through the sample. The light is dispersed by a diffraction grating after the sample and the separated wavelengths fall on different pixels of the array detector. The resolution depends on the grating, spectrometer design, and pixel size, and is usually fixed for a given instrument.

Diffuse reflectance UV-Vis measurements were performed on a spectrophotometer with Teflon pellet as the reference material.

6. Thermogravimetry Analysis

In termogravimetric analysis (TGA) the weight change of a material is monitored as a function of temperature at a controlled rate. Information about any weight changes associated with thermally induced transformations can be obtained from TGA. The change in weight as a function of temperature is the characteristic feature of a material; since these are associated with some physical and chemical changes over a wide range of temperature.

Thermogravimetric curves (thermograms) provide information regarding the thermal stability, desorption, absorption, sublimation, vaporization, oxidation, reduction and decomposition of materials under a variety of conditions. Moreover, thermal stability

of many materials in presence of different atmospheres can be studied along with the kinetics. TGA is also a good technique to measure the oxygen storage capability of any solid oxide materials.

7. Adsorption Isotherm and BET Method for surface area measurement

When a gas or vapor phase is brought into contact with a solid, part of it remains on the outside attached to the surface. In some cases the gas molecules (referred as adsorbate) are attached to the solid surface (refered as adsorbent) by a weak Vander Waals attraction. This type of adsorption known as physisorption (physical adsorption), can be utilized to characterize materials allowing for the determination of specific surface area, pore size distribution and pore volume.

The specific surface area of a powder is determined by measuring the amount of adsorbate gas corresponding to a monomolecular layer on the surface usually at the temperature of liquid nitrogen. The amount of gas adsorbed can be measured by a volumetric or continuous flow procedure. The most common adsorbate used is nitrogen; however, other adsorbates like Ar, CO, CO_2, O_2 are also used in some instances.

In 1938, S. Brunauer, P. H. Emmett, and E. Teller put forward a theory known as Brunauer–Emmett–Teller (BET) theory to explain the physisorption of gas molecules on a solid surface which forms the basis for the technique for the determination of the specific surface area of a material. The theory is based on the following hypotheses:

(a) Gas molecules physically adsorb on a solid in layers infinitely.

(b) There is no interaction between each adsorption layer.

(c) The Langmuir theory can be applied to each layer.

(d) Uppermost layer is in equilibrium with vapor phase.

(d) First layer adsorption is governed by the heat of adsorption while heat of condensation can use for higher layers.

With these assumptions, the following equation known as BET equation is derived.

$$1/\{v[(p_o/p)-1]\} = [(c-1)/v_m c]\ (p/p_o) + (1/v_m c),$$

where, p and p_o are the equilibrium and the saturation pressure of adsorbates at the temperature of adsorption, v is the volume of adsorbed gas, v_m is the monolayer adsorbed gas quantity and c is the BET constant given as

$$c = \exp[(E_1-E_L)/RT],$$

where, E_1 is the heat of adsorption for the first layer, and E_L is that for the second and higher layers and is equal to the heat of liquefaction.

The BET Equation is an adsorption isotherm and a straight line can be plotted (only in the p/p_o range 0.05-0.35) known as BET plot with the factor $1/v[(p_o/p)-1]$ on the y-axis and p/p_o on the x-axis. The value of "v_m" and "c" can be calculated from the values of slope (A) and Y-intercept (I) using the equations,

$$v_m = 1/(A+I) \text{ and } c = 1+ (A/I)$$

The BET method is widely used for the calculation of surface areas of solids in heterogeneous catalysis where the number of active sites depends on the surface area which in turn related to particle size, particle morphology, surface texturing and porosity.

The total surface area (S_{total}) and the specific surface area ($S_{BET)}$ are then given by,

$$S_{total} = (v_m N s)/V \ \ \& \ \ S_{BET} = S_{total}/\ a,$$

Where, "N" is the Avogadro's number, "s" the adsorption cross section of the adsorbing species, "V" the molar volume of the adsorbate gas, and "a" the mass of the solid sample or adsorbent.

The single-point method may be employed directly for a series of powder samples of a given material for which the material constant C is much greater than unity.

8. Electrochemical Characterizations

Several electrochemical techniques, like cyclic voltammetry (CV), rotating disk electrode (RDE), rotating ring disk electrode (RRDE) and impedance spectroscopy (EIS) are commonly used to study different electrochemical processes (faradaic and non-faradaic) associated with a material. These tools can be effectively used to study the behavior of electroactive species diffusing to an electrode surface, interfacial phenomena at an electrode surface and bulk properties of materials in or on the electrodes. However, adequate precautions have to be taken with the cleanliness of the electrode surface and also with the stability of the materials under electric field in order to get correct information.

8.1. Cyclic Voltammetric Analysis

Cyclic Voltammetry **(**CV) is the most commonly used potential controlled electrochemical technique which is routinely used to investigate the electrochemical properties of materials. This technique offers a fast location of the redox potentials of electroactive species. In CV, generally three-electrode systems are used even though two-electrode systems can also be used. In three-electrode systems, the potential is applied between WE and reference electrode (RE) while the current is measured in between the WE and the counter electrode (CE). To tackle with large currents, normally counter electrode will be with very high surface area. In CV, the potential of the WE is cycled linearly with time between two potential ends at which the oxidation and reduction of the sample occurs. Here, the potential is scanned at a particular scan rate and the current-time curve is plotted. As the scan rate is constant and the initial and switching potential are known, time can be converted into potential. The resulting current-potential plot is known as cyclic voltammogram.

8 .2. Rotating Disc Electrode Analysis

The rotating disc electrode (RDE) is a useful tool for following the electrochemical reactions that involves mass transport. This is an effective tool to precisely quantify the electrocatalytic activity of materials, especially electrocatalysts for ORR. In this

technique, a WE which can rotate in a pre-determined rate is generally used and this rotation brings the reactant gases to the electrode surface in a controlled manner. The flux of the gas to the electrode surface is determined by various parameters such as intrinsic properties of the electrolyte, rotation rate of the WE etc. Thus, in this technique, a convective transport is induced by the rotation of the WE. Here, the total measured current (i) will be the sum of kinetic current (i_k) and mass transport limited current (i_d) and it can be adjusted to the simple Koutecky-Levich equation as,

$$\frac{1}{j} = \frac{1}{j_k} + \frac{1}{j_d} = \frac{1}{j_k} + \frac{1}{BC_0\omega^{1/2}} = \frac{1}{j_k} + \frac{1}{0.62nFAD_0^{2/3}C_0^{*}v^{-1/6}\omega^{1/2}}$$

where, 'n' is the number of transferred electrons per oxygen molecule, 'F' is the Faraday constant, 'D_0' is the diffusion coefficient of the electrolyte, 'C_o*' is the concentration of dissolved oxygen in the electrolyte, 'υ' is the kinematic viscosity of the electrolyte, 'ω' is the angular velocity of the electrode. Thus, a plot of 1/j versus $1/\omega^{1/2}$ will give a straight line whose intercept corresponds to $1/j_k$ and slope corresponds to $1/BC_0$. At infinite rotation speeds, current can be considered as kinetic current free from external mass transfer limitation. From the kinetic current, the apparent rate constant 'k' can be evaluated using oxygen solubility and diffusion coefficient and from the slope the number of electrons transferred also can be calculated.

8.3. Electrochemical Impedance Spectroscopy

Electrochemical impedance spectroscopy (EIS) is a very versatile electrochemical tool to characterize intrinsic electrical properties of any material and its interface. This is a steady state method measuring the current response to the application of an AC voltage as a function of the frequency. The basis of impedance spectroscopy is the analysis of the impedance (resistance of alternating current) of the observed system with respect to the applied frequency and applied signal. An important advantage of EIS over other techniques is the possibility of using tiny ac voltage amplitudes exerting a very small perturbation on the system. EIS provides quantitative information about the conductance, dielectric coefficient and some interfacial properties. EIS data for electrochemical cells are most often

represented in Nyquist and Bode plots. Bode plots refer to representation of the impedance magnitude (or the real or imaginary components of the impedance) and phase angle as a function of frequency. Because both the impedance and the frequency often span orders of magnitude, they are frequently plotted on a logarithmic scale. Bode plots explicitly show the frequency-dependence of the impedance of the device under test. A complex plane or Nyquist plot depicts the imaginary impedance, which is indicative of the capacitive and inductive character of the cell, versus the real impedance of the cell. Nyquist plots have the advantage that activation-controlled processes with distinct time-constants show up as unique impedance arcs and the shape of the curve provides insight into possible mechanism or governing phenomena.

Appendix 2

1. Determination of pseudocubic lattice parameters

A. For $Ba_2In_2O_5$

$a' = c/\sqrt{2}$, $b' = b/\sqrt{2}$, $c' = a/4$

B. For $Ba_2In_{1.5}Ce_{0.5}O_{5+\delta}$

$a' = a$, $b' = b$, $c' = c/2$

C. For $BaIn_{0.5}Ce_{0.5}O_{2.5+\delta}$ and $BaIn_{0.25}Ce_{0.75}O_{2.5+\delta}$

$a' = a$, $b' = b$, $c' = c$

D.For $BaCeO_3$

$a' = a/\sqrt{2}$, $b' = b/\sqrt{2}$, $c' = c/\sqrt{2}$

E. For $Ba_2In_{1.5}Co_{0.5}O_{5-\delta}$

$a' = a$, $b' = b$, $c' = c/2$

2. Determination of oxygen uptake from TGA profile

Let, x = Initial weight (in g) of the sample (after cooling the sample in He at 30 °C)

y= Final weight (in g) of the sample (900 °C in 10% O_2 in He atmosphere)

So the oxygen uptake (in g) during the TGA experiment = weight gained = (y – x)

Number of moles of oxygen gained = (y – x)/16 = z

Amount of oxygen uptake per gram of the sample = z/x

3. Determination of Conductivity of pellets form the impedance data

If, t = thickness of the pellet,

A = Cross sectional area of the pellet = $\pi \times r^2$ (where, r = radius of the pellet)

and R = total resistance of the pellet = $R_g + R_{gb}$ (where, R_g = grain and R_{gb} = grain boundary resistance)

Then, conductivity = t / (R x A)

4. Calculation of activation energy from Arrhenius plot

We know the Arrhenius equation,

$k = Ae^{-(Ea/RT)}$

Taking logarithm on both side,

$\ln k = -E_a/RT + \ln A$

This is the equation for straight line (y = mx + c)

Where, y = ln k

x = 1/T

m = slope (can be obtained from the Arrhenius plot for conductivity)

c = intercept

Therefore, Activation energy, E_a = - slope x R

Where, R = 8.314 J mol K^{-1}

5. Determination of stoichiometric composition of $BaCe_{0.5}In_{0.5-x}Zr_xO_{3-\delta}$ (with x = 0.125)

% composition obtained after Rietveld refinement

92.8% of $BaCe_{0.5}In_{0.375}Zr_{0.125}O_{2.694}$

1.8% of $BaIn_{0.5}Zr_{0.5}O_{3-\delta}$

5.4% of $BaCeO_3$

Amount of impurity of each element

Ba: 0.018 + 0.054 = 0.072

In: 0.009

Zr: 0.009

Ce: 0.054

Final composition of individual element after accounting for the impurities

Ba: 1 – 0.072 = 0.928

Ce: 0.5 – 0.054 = 0.446

In: 0.375 - 0.009 = 0.366

Zr: 0.125 – 0.009 = 0.116

O: 92.8% of 2.694 = 2.5

Multiplying these final compositions with 1.078(to make the amount of Ba to 1) the following stoichiometric composition is arrived

$BaCe_{0.48}In_{0.39}Zr_{0.12}O_{2.695}$

Similarly the other two compositions were calculated.

6. Procedure for plotting the Nyquist plot after removing the inductive effect.

Nyquist plot is a plot between the imaginary (-Z'') and real part (Z') of the impedance.

In samples exhibiting inductive effect,The EIS data is first collected let's say it has –A'' as imaginary part of impedance and A' as real part.

Then the pellet is wrapped with a Pt strip for shorting the circuit and EIS data of the pellet wrapped with Pt strip is recorded, let's say it has –B'' and B' as imaginary and real part of impedance.

Now for each frequency, the real and imaginary part of the data obtained for the pellet wrapped in Pt strip is subtracted from the original data to get the actual impedance of the pellet ,

Let –C'' and C' be the imaginary and real part of the impedance of the sample after removing the inductive effect, then

$$-C'' = -A'' - (-B'')$$

and $$C' = A' - B'$$

7. Calculation of band gap from Tauc plot

To calculate band gap from UV-Vis spectrophotometer, following steps were followed

A. %R of the samples were obtained from the instrument
B. R was calculated from %R
C. Kubelka Munk transformation was performed using the equation,

$$K.M. = (1-R)^2/2R$$

D. Energy of the wavelength (λ) was calculated as ,

$$h\nu = 1240.78 / \lambda$$

E. Multiply Kubelka Munk factor with energy to obtain (K.M x hν)
F. Using the following expression proposed by Tauc, Davis and Mott, the band gap can be obtained

$$(K.M \times h\nu)^{1/n} = A(h\nu - E_g)$$

G. For direct transition, n = ½
H. Using Kubelka Munk function, $(K.M \times h\nu)^2$ is plotted against hν
I. A line is drawn tangent to the point of inflection on the curve, and the hν value at the point of intersection of the tangent line and the horizontal axis is the band gap E_g value

8. EXAFS data fitting procedure

The analysis of the EXAFS data has been carried out by following the standard procedure and using the IFEFFIT software package. This includes data reduction and Fourier transform to derive the $\chi(r)$ versus r plots from the absorption spectra, generation of the theoretical EXAFS spectra starting from an assumed crystallographic structure and finally fitting of the experimental $\chi(r)$ versus r data with the theoretical ones using the FEFF 6.0 code. The bond distances and disorder (Debye-Waller) factors (σ^2), which give the mean-square fluctuations in the distances, have been used as fitting parameters. The goodness of the fit in the above process is generally expressed by the R_{factor} which is defined as:

9. $$R_{factor} = \sum \frac{[\mathrm{Im}(\chi_{dat}(r_i) - \chi_{th}(r_i)]^2 + [\mathrm{Re}(\chi_{dat}(r_i) - \chi_{th}(r_i)]^2}{[\mathrm{Im}(\chi_{dat}(r_i)]^2 + [\mathrm{Re}(\chi_{dat}(r_i)]^2} \qquad (1)$$

where, χ_{dat} and χ_{th} refer to the experimental and theoretical $\chi(R)$ values respectively and Im and Re refer to the imaginary and real parts of the respective quantities. The fitting has been carried out in the r range of 1-3 Å and the number of fitting parameters which can be varied freely during fitting has been decided following the Nyquist criterion $N_{Free} = (2\Delta k \Delta r / \pi) + 1$.